PNNL FY 2020 Sibling Pin Testing Results

Spent Fuel and Waste Disposition

Prepared for
US Department of Energy
Spent Fuel and Waste Science and Technology

Pacific Northwest National Laboratory
RW Shimskey, JR Allred, SE Asmussen, SK Cooley, RC Daniel, MK Edwards, JGH Geeting, ZF Huber, PJ MacFarlan, LI Richmond, AM Westesen, BE Westman and BD Hanson

March 5, 2021
M2SF-21PN010201055
M2SF-20PN010201036
PNNL-31036

SUMMARY

The Office of Spent Fuel and Waste Disposition within the U.S. Department of Energy Office of Nuclear Energy (DOE-NE) established the Spent Fuel and Waste Science and Technology campaign to conduct research and development activities related to storage, transportation, and disposal of spent nuclear fuel and high-level radioactive waste. DOE-NE, in partnership with the Electric Power Research Institute, developed the High Burnup Spent Fuel Data Project to perform a large-scale demonstration and laboratory-scale testing of high burnup fuels (exceeding 45 gigawatt-days per metric ton of uranium. Under this project, 25 sibling pins (aka sister rods)— having the same design, power histories, and other characteristics—were removed from assemblies at the North Anna Nuclear Power Station and sent to Oak Ridge National Laboratory (ORNL) in January 2016. ORNL performed detailed nondestructive examination (NDE) of all 25 rods. The NDE consisted of visual examinations, gamma and neutron scanning, profilometry and rod length measurements, and eddy current examinations. Upon completion of the NDE, 10 of the sibling pins were delivered to Pacific Northwest National Laboratory (PNNL) in the NAC International, Inc., legal-weight truck cask in September 2018 for destructive examination. Each rod was individually drawn into the hot cell, where it was punctured to determine the end-of-life (EOL) rod internal pressure (RIP), internal volume, and isotopic composition of the gas within the rod. This information was compared to estimated total quantities expected based on the specific rod design and utility-provided irradiation histories and discussion in Shimskey et al. (2019a). After gas puncture, each of the ten received rods was cut into four segments and placed into storage in inerted storage tubes. Afterward, PNNL began preliminary gas communication studies using the bottom segment of rod 6U3L08, as discussed in Shimskey et al. (2019b) with results comparable to those of tests performed by ORNL.

This report discusses PNNL's progress in Phase 1 testing as outlined in Saltzstein et al. (2018). The hydraulic resistance of segments cut from the Phase 1 sibling pins (rods F35K13, 5K7K9, 5K7P2, 6U3L8, and 6U3M3) was evaluated using gas communication results from this fiscal year (FY) and FY 2019 along with rod puncture data collected during testing in FY 2018. Interpreted using a single hydraulic flow channel, testing measured hydraulic diameters that spanned 71 to 97 µm. Rod F35K13 (Zirc-4) showed the largest hydraulic diameter and rods 6U3L8 and 6U3M3 (ZIRLO) showed the smallest diameter, with rod 5K7K9 and 5K7P2 (M5) results falling between. Smaller variation in hydraulic diameter, approximately 17 µm on average, was observed along the length of an individual fuel rod. The middle two rod segments typically showed the smallest diameter and greatest hydraulic resistance to gas flow. Variation in hydraulic diameter with test pressure (between EOL RIP and 5 MPa) was small (below 2 µm) and generally fell within the range expected for nominal expansion of the cladding under pressure.

Once gas communication testing was completed, the Phase 1 segments were sectioned into subsamples for physical property testing and post-irradiation examination samples, maintaining axial and circumferential orientation on the rod. Each sample was notched to mark the end of the sample closest to the bottom of the rod and aligned with the initial gas puncture. Dissolution of the samples started shortly afterward, and fuel was removed from rods 6U3L8 and 5K7P2. The custom dissolution system worked well with no issues observed dissolving the fuel from 6 in. samples in nitric acid at 65°C in between 26 and 98 hours. The measured outer diameter of samples before and after the fuel was dissolved were found to be statistically different. Rod 6U3/L8 (ZIRLO) demonstrated an approximately 9 µm decrease in outer diameter after dissolution whereas rod 5K7P2 (M5) exhibited a 4 µm decrease.

Post-irradiation examination has started with samples from the top of rod 6U3L8 and bottom section of F35K13. As expected, the hydrogen concentration for the bottom 100 mm of F35K13 has very little hydride content (50–70 ppm H) with a very small oxide layer, while the top segment of 6UL3L8 has significantly higher hydride content with a readily apparent oxide layer. Microhardness testing is being performed on these samples in the as-received condition and will be compared to samples that undergo

radial hydride treatment to determine if annealing of radiation damage occurs during those short times at temperatures of 400°C.

The Instron test frame has now been installed and incorporated with the digital strain imaging system used for the burst system. Evaluations of the testing systems for burst, tensile, and bend testing at room temperature and at 200°C using digital imaging have been completed and the equipment is deemed ready for radiological testing.

ACKNOWLEDGEMENTS

The work reported here was performed at Pacific Northwest National Laboratory (PNNL) and supported by the U.S. Department of Energy Spent Fuel and Waste Science and Technology (SFWST) Storage and Transportation program of the Office of Nuclear Energy (NE-81). The authors are thankful for the leadership of Ned Larson in NE-81.

We thank the SFWST Storage and Transportation control account leadership of Sylvia Saltzstein at Sandia National Laboratories. We also thank the reviewers at Sandia National Laboratories, Argonne National Laboratory, and Oak Ridge National Laboratory.

This work would not have been possible without the expertise of Randy Thornhill and his vast experience working with commercial spent nuclear fuel. The Shielded Facility Operations team members Franciska Steen, Jake Bohlke, Bob Orton, Jason Cartwright, Dustin Blundon, Jordon Condray, Jarrod Turner, and Jeff Chenault were invaluable, and their dedication and long hours are greatly appreciated.

We are thankful to the project support team of Alma Contreras, Lisa Middleton-Smith, Emily Wilson, Janet Wilson, and Chrissy Charron.

Lastly, we are thankful for the expertise of Susan Tackett, Jessica Wisse, and Maura Zimmerschied in editing and formatting this report.

This page is intentionally left blank.

CONTENTS

This page is intentionally left blank.

LIST OF FIGURES

LIST OF TABLES

This page is intentionally left blank.

REVISION HISTORY

REVISION	COMMENTS	ISSUE DATE
Draft as M3SF-20PN010201038 / M3SF-21PN010201056	Initial release for programmatic review	October 30, 2020

This page is intentionally left blank.

ACRONYMS

ALARA	as low as reasonably achievable
ANL	Argonne National Laboratory
ASTM	ASTM International, formerly American Society for Testing and Materials
BET	Brunauer Emmet Teller (method for surface area determination)
CY	calendar year
d_i	inner diameter
d_o	outer diameter
DE	destructive examination
DF	decontamination factor
DIC	digital image correlation
DIW	deionized water
DOE	U.S. Department of Energy
EOL	end-of-life
EPRI	Electric Power Research Institute
FEM	finite element model
FY	fiscal year
GEA	gamma energy analysis
GS	grid spacer
GWd	gigawatt-day
HB	higher burnup
HBU	high burnup
HLRF	High-Level Radiochemistry Facility
ICP-MS	inductively coupled plasma mass spectrometry
ID	identification
LB	lower burnup
MTU	metric tons of uranium
ND	no detection
NDE	nondestructive examination
NDIR	nondispersive infrared
NE	Office of Nuclear Energy
NIST	National Institute of Standards and Technology
OM	optical microscope

ORNL	Oak Ridge National Laboratory
PDE	partial differential equation
PID	proportional, integral, derivative (control)
PIE	post-irradiation examination
PNNL	Pacific Northwest National Laboratory
POMB	point of maximum bulge
psia	pounds per square inch absolute
psig	pounds per square inch gauge
RHT	radial hydride treatment
RIP	rod internal pressure
RPD	relative percent difference
RSD	relative standard deviation
RT	room temperature
SD	standard deviation
SEM	scanning electron microscope
SFWST	Spent Fuel and Waste Science and Technology
SHE	standard hydrogen electrode
SNF	spent nuclear fuel
SS	stainless steel
UTS	ultimate tensile strength
VDC	volts direct current
VSG	virtual strain gauge
WDH	width, depth, height

SYMBOLS

A	cross-sectional area
A_1	initial cross-sectional area
A_2	final cross-sectional area
a_{bend}	length between support and load pin
C_1	pretest circumference
C_2	test circumference at burst location, excluding the opening
D_{after}	measured dose after process step
D_{before}	measure dose before process step
d_i	inner diameter
d_h	hydraulic diameter
$d_{h,e}$	effective hydraulic diameter
d_o	outer diameter
d_{o1}	initial outside diameter
d_{o2}	test outside diameter
DF	decontamination factor
E	Young's Modulus (modulus of elasticity)
e1	error in strain reported
F	force
$f_{f,c}$	Fanning Friction Factor
G	mass flow
g	mass flux
g_c	critical mass flux
h	wall thickness
I	inertia
K_m	permeability of a medium
K_p	Darcy Permeability
k	measured stiffness
k_c	theoretical stiffness at the mid-span of the sample in elastic region
L	length
L_{bend}	length of the support span
L_{gl}	axial gauge length of extensometer
M	bending moment
n	undefined number (of segments)

P/P_0	relative pressure
p	pressure
p_a	atmospheric pressure
p_b	internal pressure during burst testing
p_e	equilibrium pressure
p_k	generic chamber pressure
p_r	internal rod pressure
p_1	high pressure
p_1^0	initial upstream pressure
p_2	low pressure
p_2^c	critical downstream pressure
p_2^0	initial downstream pressure
R_m	Individual Gas Constant
rC	volume expansion (into chamber C)
rCB	volume expansion (into chambers B and C)
Re	Reynolds Number
Re_c	critical Reynolds Number
r_i	inner radius of tube
r_o	outer radius of tube
$r_{r,i}$	inner rod radius
t	time
t_0	time scale
T_o	flow temp
V_r	internal rod volume
V_1	upstream volume
V_2	downstream volume
x	position
y_1	volume fraction for upstream chamber
y_2	volume fraction for downstream chamber
α	scaling constant
Δd_h	change in hydraulic diameter
Δd_r	change in rod diameter
ΔL_z	measured axial elongation
Δp_r	difference in internal and external pressure

Δp	pressure difference
Δp_0	change in gas communication test pressure
δ_{bend}	midspan deflection of bend
δ_c	theoretical mid-span deflection
δ_r	wall thickness
δ_{z1}	initial axial distance between two points
δ_{z2}	axial distance between two points during test
$\delta_{\theta 1}$	initial distance between two points in the hoop direction
$\delta_{\theta 2}$	distance between two points in hoop direction during test
ϵ	porosity
ε_z	axial strain
ε_θ	hoop strain
Λ_c	scaled critical friction coefficient
μ	gas viscosity
ν	Poisson's Ratio
ζ_c	critical pressure ratio
ρ	radius of curvature
σ_z	axial stress
σ_θ	hoop stress
τ	scaled time
τ_m	maximum shear stress
ϕ	scaled pressure
ϕ^o	initial scaled pressure
in.	inch
IR	infrared
LCL	lower confidence limit
LECO	The LECO Corporation
M	mole/liter
STD	standard deviation
TC	thermal conductivity
TCE	total circumferential elongation

TRADEMARKS

Airmo®	Airmo is a trademark and brand of Airmo, Inc., in the United States and in other countries.
M5®	Registered trademark of Framatome (formerly AREVA NP) registered in the United States and in other countries
ZIRLO®	Registered trademark of Westinghouse Electric Company LLC in the United States and in other countries

PNNL FY 2020 SIBLING PIN TESTING RESULTS

1. INTRODUCTION

The Office of Spent Fuel and Waste Disposition within the U.S. Department of Energy Office of Nuclear Energy (DOE-NE) established the Spent Fuel and Waste Science and Technology (SFWST) campaign to conduct research and development activities related to storage, transportation, and disposal of spent nuclear fuel (SNF) and high-level radioactive waste. The initial emphasis of the program is on uranium oxide fuel from commercial light-water reactors. Because limited information is available about the properties of high burnup (HBU) fuel (exceeding 45 gigawatt-days per metric ton of uranium [GWd/MTU]) and because much of the fuel currently discharged from commercial reactors exceeds this burnup threshold, this program is particularly focused on HBU fuels.

DOE-NE, in partnership with the Electric Power Research Institute (EPRI), developed the High Burnup Spent Fuel Data Project to perform a large-scale demonstration and laboratory-scale testing of HBU fuels (EPRI 2014). Under this project, a storage cask (TransNuclear TN-32B) licensed by the U.S. Nuclear Regulatory Commission was loaded in November 2017 with 32 HBU assemblies from the pressurized water reactors at Dominion's North Anna Nuclear Power Station in Mineral, Virginia. Before the Research Project Cask was loaded, 25 HBU fuel rods were removed from assemblies and sent to Oak Ridge National Laboratory (ORNL) in January 2016. These are referred to as sibling pins (aka sister rods) because they have the same design and similar characteristics (e.g., power histories). ORNL performed detailed nondestructive examination (NDE) of all 25 rods (Montgomery et al. 2018). The NDE consisted of visual examinations, gamma and neutron scanning, profilometry and rod length measurements, and eddy current examinations. Upon completion of the NDE, 10 of the sibling pins were sent to Pacific Northwest National Laboratory (PNNL) in September 2018 for destructive examination (DE). Phase 1 of the DE testing at PNNL, ORNL, and Argonne National Laboratory (ANL) is described in the test plan visualization in Figure 1-1 (Saltzstein et al. 2018).

PNNL has completed gas puncture testing, gas analysis, and sectioning of the ten received sibling pins as discussed in Shimskey et al. (2019a), and initiated gas communication testing as discussed in Shimskey et al. (2019b). This report documents PNNL's progress in support of Phase 1 testing since then. Section 2 discusses the results of gas communication testing of the Phase 1 sectioned rods and results. Section 3 discusses the sectioning of the Phase 1 rods into individual samples for post-irradiation examination (PIE) and physical property testing and how orientation of the segments was maintained to make sure that locations of the cut samples were traceable to the positions on the parent rod. Section 4 discusses the methodology of dissolving fuel from cut samples of the sibling pins and observations made during this process. Section 5 discusses the progress of PIE of the Phase 1 sibling pins, showing results from the bottom of the F35/K13 and the top of the 6U3L08 rods. Section 6 discusses the preparation and qualification of the burst system, Instron test frame, and camera system for digital strain imaging for physical property testing of the sibling pins in FY 2021.

1.1 Quality Assurance

This work has been assigned a Quality Rigor Level 3 by SFWST. As such, the work is done in accordance with the PNNL laboratory-wide Quality Assurance Program; PNNL's program is compliant with DOE Order 414.1 and with a graded approach based on the American Society of Mechanical Engineers Nuclear Quality Assurance Standard, NQA-1-2000, Part I, Part II (Subpart 2.7), and Part IV (Subpart 4.2). Program procedures are written to follow ASTM International (ASTM) consensus standards, as applicable, with modifications made to account for safety and working with radioactive samples. Measuring and test equipment (e.g., balances, pressure transducers, thermocouples, standard volumes, data acquisition systems, etc.) for quality-affecting data are calibrated by a qualified supplier with standards traceable to the National Institute of Standards and Technology (NIST) or other nationally

or internationally recognized standard. Other systems (e.g., optical microscope, scanning electron microscope, optical micrometers, etc.) use standards traceable to NIST or other nationally or internationally recognized standards to verify system outputs. Data and project reports are reviewed by an independent technical reviewer.

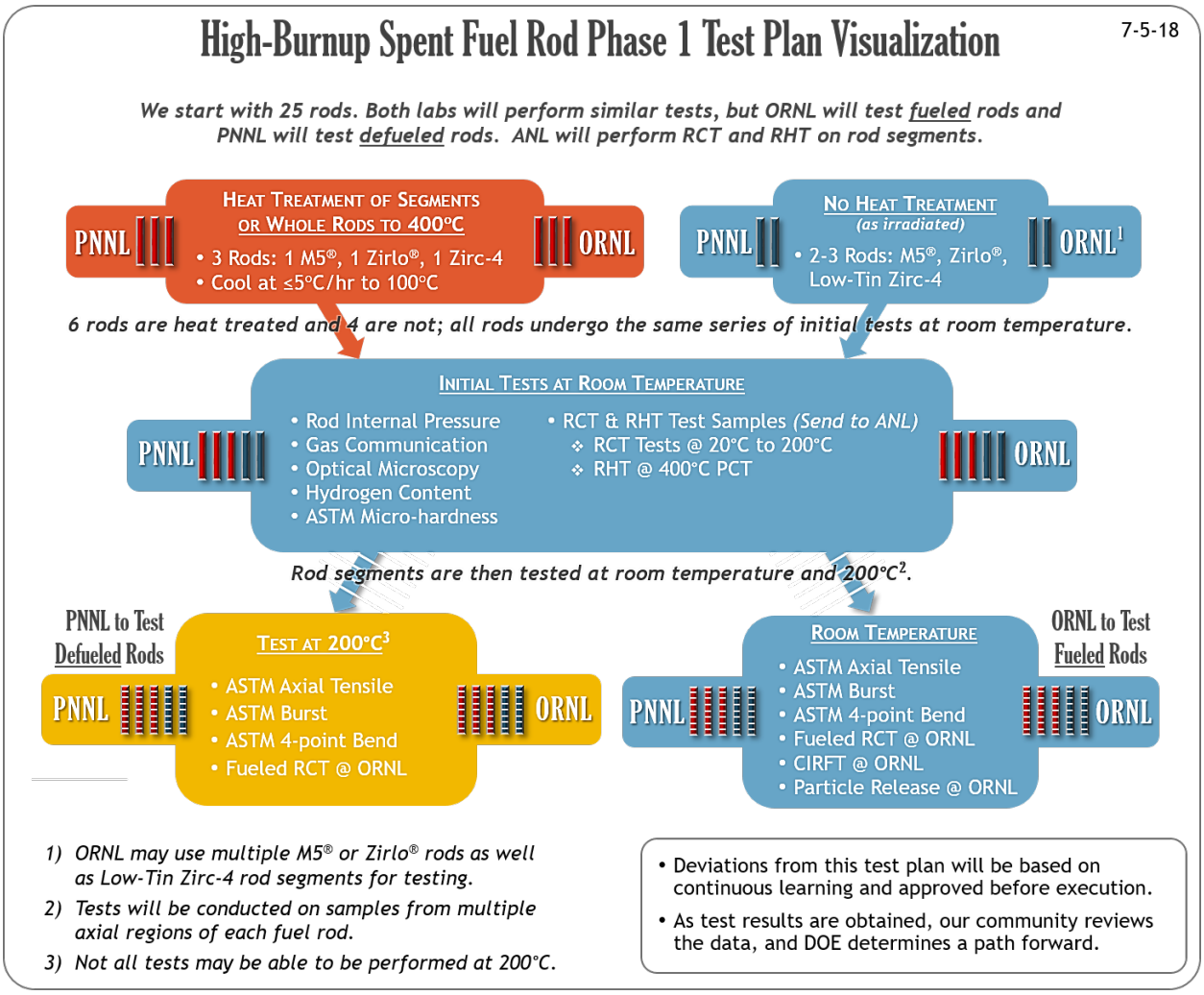

Figure 1-1. Phase 1 Test Plan Visualization (Saltzstein et al. 2018).

Note: RHT is radial hydride treatment, RCT is ring compression test, CIRFT is cyclic integrated reversible bending fatigue test.

1.2 Sample Identification

Table 1-1 identifies the cladding type, rod identification, burnup, and decay time (as of June 2020) of the ten sibling pins at PNNL. Throughout this report, the PNNL rod identification is used to identify samples. After rod puncture, each rod was segmented into approximately quarter-lengths. The upper quarter, containing the rod plenum, is identified as Segment 1 and the bottom quarter, containing the end plug, is identified as Segment 4. Thus, a sample taken from Segment 1 of rod 6U3/L8 will have the designation UL-1. After gas communication testing, each segment of the five rods composing Phase 1 (see Figure 1-1 and Table 1-1) was sectioned into test specimens as discussed in Section 3.

Per the test plan for Phase 1 (Saltzstein et al. 2018), PNNL will test defueled cladding, after the fuel has been dissolved according to the process discussed in Section 4. Two of the sibling pins are being tested as

received with no heat treatment before they are tested. The other three sibling pins will be tested after each physical property specimen is repressurized to the same room temperature, end-of-life (EOL) rod internal pressure (RIP) as reported in Shimskey et al. (2019a) and then heated to 400°C to simulate vacuum drying. This process is referred to as radial hydride treatment (RHT). All five of the sibling pins tested under Phase 1 will have axial tube tensile, 4-point bend, and burst testing performed both at room temperature and at 200°C, representative of cladding temperatures that may exist during transportation.

Table 1-1. PNNL Sister Rod Characteristics.

Clad Type	Assembly/Rod Identification	PNNL Rod Identification	~ Rod-Average Burnup (GWd/MTU)	Cooling Time (yr) (as of 6/2020)	Phase 1 Plan
M5®	5K7/C5	KC	57	11.23	
M5®	5K7/K9	KK	54	11.23	400°C
M5®	5K7/P2	KP	51	11.23	No heat
M5®	30A/P2	AP	49	9.72	
ZIRLO®	6U3/M3	UM	57	13.21	400°C
ZIRLO®	6U3/O5	UO	58	13.21	
ZIRLO®	6U3/P16	UP	50	13.21	
ZIRLO®	6U3/L8	UL	55	13.21	No heat
ZIRLO®	3F9/P2	FP	49	16.08	
Zircaloy-4	F35/K13	FK	58	31.26	400°C

Each rod has been divided into three zones: the lower burnup top and bottom ends, the middle high burnup portion, and the segments that were under grid spacers. If a zone contains sufficient material, three samples will be tested at room temperature (one each for axial tube tensile, four-point bend, and burst tests) and three samples will be tested at 200°C (again, one each for axial tube tensile, four-point bend, and burst tests). A sectioning diagram for each rod was prepared before it was segmented to accommodate this plan (see Appendix D). Typically, there is not enough material in the lower burnup zone for six samples, so the 200°C four-point bend test will not be performed in that zone. Thus, 17 physical property tests will be performed on each rod. Each sample will be 6 in. long.

The cladding dimensions inner diameter (d_i), outer diameter (d_o), and wall thickness must be known to calculate the hoop stress for RHT. Similarly, the hydride distribution, total hydrogen content, and oxide layer thickness are important parameters affecting physical properties. A 0.5 in. sample is cut on each side of the 6 in. physical property sample so these dimensions and parameters can be measured on an as-received sample.

Each segment was sectioned according to a sectioning diagram (see Appendix D), an example of which is shown in Figure 1-2. The segments were sectioned starting at the bottom of the segment and moving up. So, the first sample, closest to the top of Segment 2, from Segment UL-1is identified as UL-1-1 and the last sample, closest to the plenum, from Segment 1 is identified as UL-1-10. The segment shown in Figure 1-2 is UL-3 from the high burnup zone. The samples denoted by blue, such as UL-3-1, are the 6 in. physical properties samples; the samples denoted by red, such as UL-3-10, are the PIE samples; the samples denoted by green, such as UL-3-7, were to account for cut loss; and the remainder are archive samples.

ZIRLO Alloy Cut Plans

Legend	
	No Zone
	Zone 1: Lower Burnup/Pin Bottom
	Zone 2: Higher Burnup/Pin Middle
	Zone 3: Lower Burnup/Pin Top
	Pin Puncture/Plenum Section (No Testing)
	PIE Testing (Metallography/H Determination)
	Physical Property (Including Spares)
	Argonne Sample for Ring Compression
	Archive
	Bottom Plug (No Testing)

Abbreviation	
GS	Grid Spacer
HB	Higher Burnup
LB	Lower Burnup
ANL	Argonne National Laboratory
RHT	Reorientation Heat Treated

Rod 6U3/L8; PNNL ID UL
Burnup ~55 GWd/MTU
11.21 years cooling
Phase 1 - No heat treatment
Rod length = 3890 mm = **153.150** inches

For Planning Purposes Only

Nominal Elevation from Bottom			
in	**Zone**	**Sample ID**	
77.5		UL-3-15	
77.0			
76.5			
76.0			
75.5			HB #4 **Axial Tube Tensile 200°C**
75.0			
74.5			
74.0			
73.5			
73.0			
72.5			
72.0			
71.5		UL-3-14	Metallography/total hydrogen
71.0		UL-3-13	
70.5			
70.0			
69.5			
69.0			GS #4 **Burst Room Temperature**
68.5			
68.0			
67.5			
67.0			
66.5			
66.0			
65.5			
65.0		UL-3-12	Metallography/total hydrogen
64.5		UL-3-11	
64.0			
63.5			
63.0			
62.5			HB #5 **Burst Room Temperature**
62.0			
61.5			
61.0			
60.5			
60.0			
59.5			
59.0			
58.5		UL-3-10	Metallography/total hydrogen
58.0		UL-3-9	
57.5			
57.0			
56.5			
56.0			HB #6 **Burst 200°C**
55.5			
55.0			
54.5			
54.0			
53.5			
53.0			
52.5			
52.0		UL-3-8	Metallography/total hydrogen
51.5		UL-3-7	Reserve or Cut loss
51.0		UL-3-6	Metallography/total hydrogen
50.5		UL-3-5	
50.0			
49.5			
49.0			
48.5			GS #3 **Burst 200°C**
48.0			
47.5			
47.0			
46.5			
46.0			
45.5			
45.0			
44.5		UL-3-4	Metallography/total hydrogen
44.0		UL-3-3	
43.5			Reserve or Cut loss
43.0			
42.5		UL-3-2	Metallography/total hydrogen
42.0		UL-3-1	
41.5			
41.0			
40.5			
40.0			
39.5			HB #7 **4 pt Bend Room Temperature**
39.0			
38.5			
38.0			
37.5			
37.0			**UL Segment 3 = 78.0-36.5 41.5**
36.5			

Figure 1-2. Sample Cut Plan Layout for Segment UL-3 from Rod 6U3L08.
Note: Elevations are nominal and approximate (see discussion in Section 3.3)

2. GAS COMMUNICATION

Gas communication testing of the sibling pins involves evaluating the rate of gas transmission through the axial length of the spent fuel rods. It provides (1) a rough measure of the time scale and gas flow rates associated with depressurization under rod breach scenarios and (2) information regarding the internal microstructure of the SNF. Communication testing is done in two steps: (1) a 3–4 ft rod segment is mounted into the gas communication testing apparatus (described in Section 2.1), and (2) the rate of change in pressure within fixed-volume reservoirs upstream and downstream of the rod is monitored to infer the hydraulic resistance to flow.

In general, the pressure reservoir volumes selected for testing are larger than is prototypical of plenum or interstitial SNF rod volumes. This facilitates measurable changes in pressure across easily resolvable time scales (minutes to hours) and renders the underlying physics amenable to analysis by analytic functions. As a result, the time scales measured for gas transmission in gas communication do not necessarily correlate directly to those expected in actual gas release/rod depressurization scenarios. Rather, the results must be interpreted through first-principles analysis to derive metrics by which transmission rates under prototypical storage and release conditions can be evaluated for scaling and to support safety-basis analyses.

This section describes the experimental and analytical methods used to quantify the gas transmission properties of the sibling pins. Section 2.1 describes the gas communication test apparatus, conduct of test operations, and test fuel segment requirements. Section 2.2 presents the technical basis and first-principles equations for analyzing upstream and downstream gas reservoir pressures. Section 2.3 presents gas communication testing results for rods F35K13, 5K7K9, 5K7P2, 6U3L8, and 6U3M3 (hereafter abbreviated as rods FK, KK, KP, UL, and UM, respectively). These gas communication test results are further supplemented by estimates of hydraulic resistance derived from rod puncture testing reported in Shimskey et al. (2019a). Section 2.4 provides a short summary of anomalies observed during gas communication testing (such as migration of fuel within the cladding during testing). Finally, Section 2.5 provides a summary and discussion of key findings from gas communication testing. Analysis of particles released during the depressurization portion of the gas communication test is still underway and will be reported in the future.

2.1 Test Apparatus

The gas communication device consists of two communication chambers on a movable track to secure Airmo® grippers on opposite ends of a sibling pin segment (Figure 2-1). The inlet side of the system is connected to an isolation valve attached to a gas manifold in the back of the hot cell by a high-pressure gas line using helium as the gas source. A small gas reservoir (10 mL) is connected between the isolation valves and the inlet grip to represent the rod plenum. In the current testing, the free volume of inlet piping between the isolation valve and the Airmo gripper was measured with a 9.5 mm length of rod inserted into the grip. The opposite end (the outlet side) is connected to a second isolation valve to allow the rod segment to either pressurize or vent to the hot cell. A filter is located between the rod segment and the second isolation valve to capture particles as the rod vents into the hot cell. Each communication chamber has a transducer to measure pressure at each end of the rod segment. Optical micrometers located at approximately 1/3 and 2/3 the length of the sibling pin segment are placed on the movable track to measure circumferential rod growth during pressurization. Figure 2-2 shows the system operating in the hot cell with the discharge toward the window.

The sequence of testing operations is outlined in Figure 2-3. The order of operations was the following:

1. Load the rod segment into the gas communication system with the system depressurized.
2. Close both isolation valves and pressurize the inlet line to the test pressure.
3. Open the inlet isolation valve to allow the rod to pressurize.

4. Once the inlet and outlet transducers reach equilibrium, the inlet isolation valve is closed, and a leak test is performed on the system prior to venting.
5. Open the outlet isolation valve, allowing the rod segment to vent through the outlet filter.
6. Once the rod segment is vented, the filter assembly is removed from the cell to collect the filter. The test is either repeated with another filter assembly or the segment is removed, and the inlet line is vented.

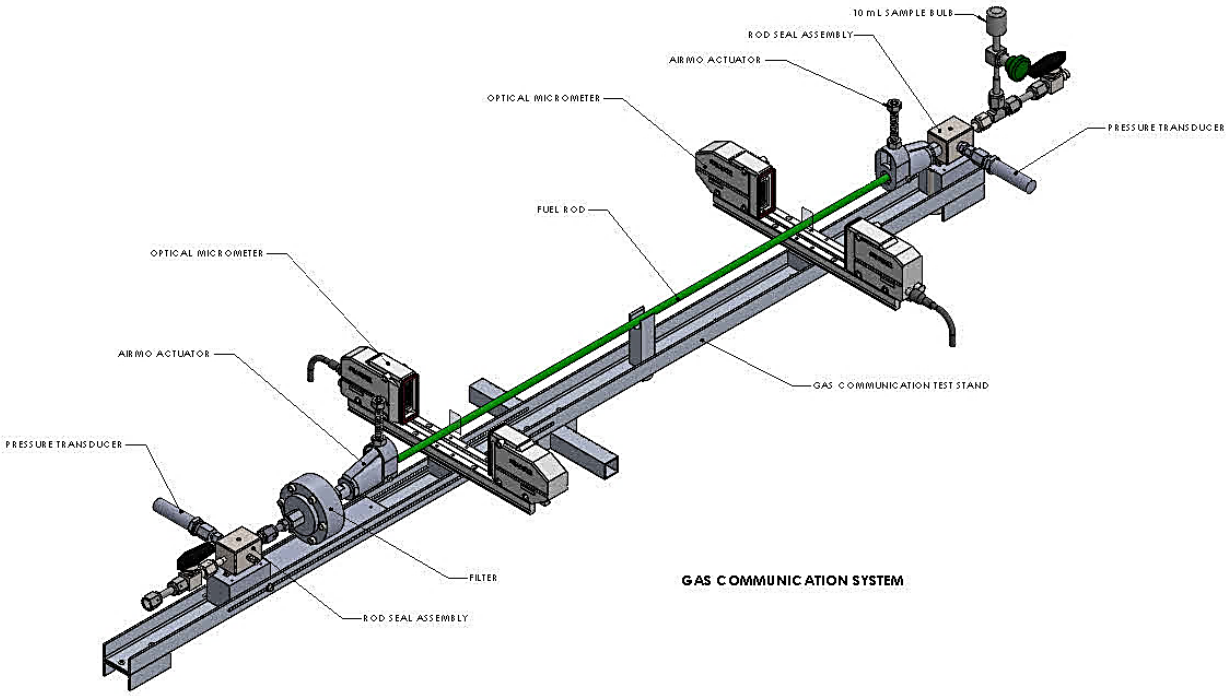

Figure 2-1. Gas Communication Apparatus.

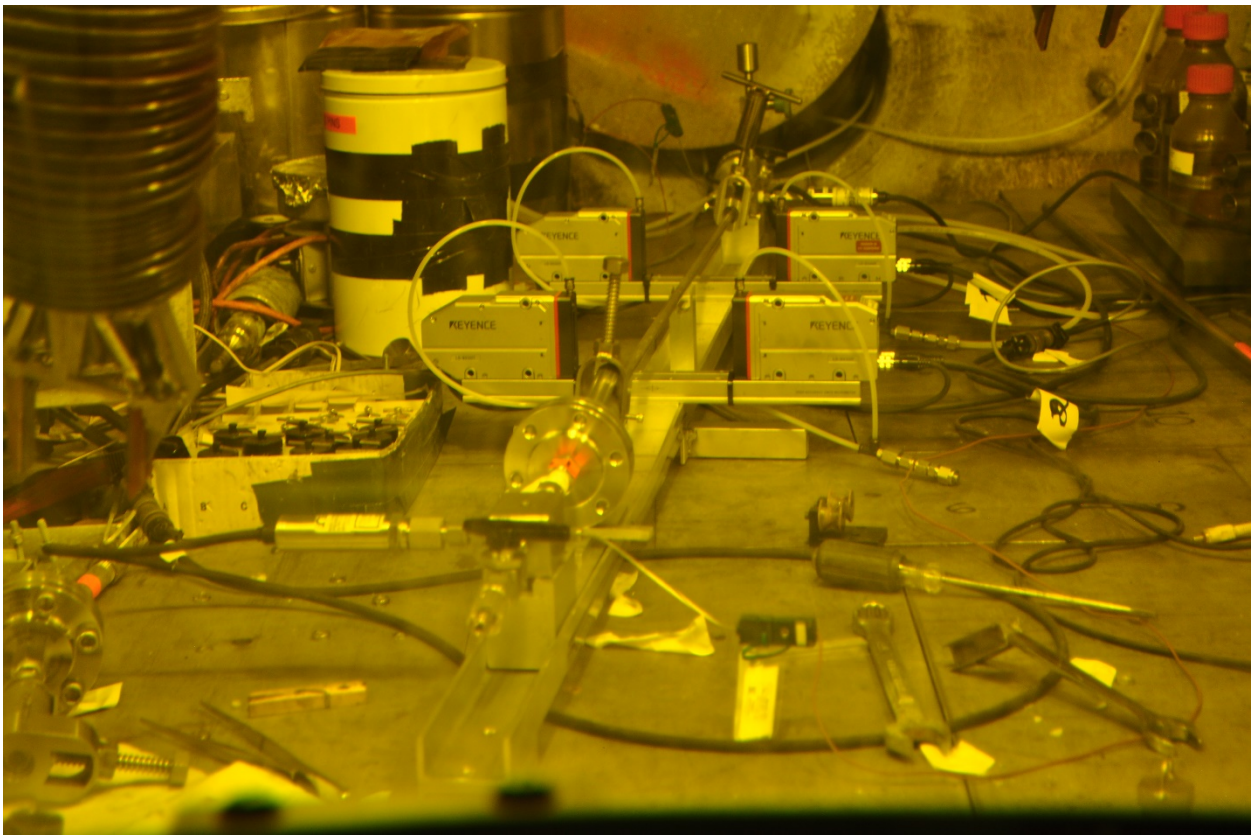

Figure 2-2. Gas Communication System Operating in PNNL Hot Cell.

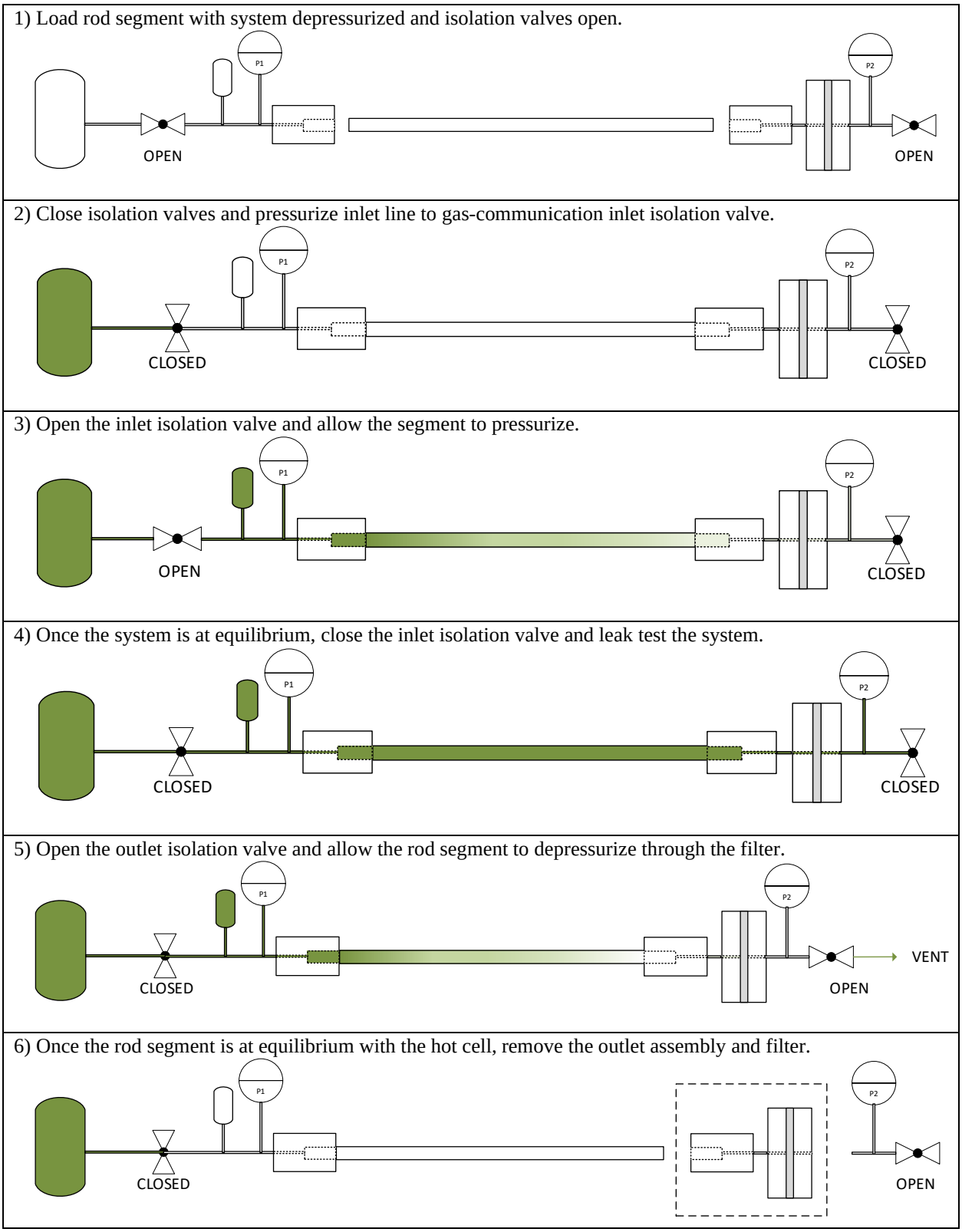

Figure 2-3. Pressurization and Depressurization Sequence of Gas Communication Test.

2.2 Technical Basis

A detailed description of the technical basis that underpins analysis of hydraulic resistance in the gas communication system outlined in Section 2.1 has already been reported in Shimskey et al. (2019b). As such, the full development of gas communication testing will not be presented herein. Rather, development of the technical basis in the current report is limited to a brief description of the equations for unsteady, compressible, friction-limited flow that can be used to extend the analysis to unsteady pressure release from rods in rod breach scenarios and to quickly develop the equations presented in Shimskey et al. (2019b).

2.2.1 Equations Governing Pseudo-Steady Laminar Gas Flow

The space- and time-dependent pressure dynamics of laminar, Darcy friction-limited isothermal flow of an ideal gas through a pseudo-single-channel porous medium are governed by the following nonlinear partial differential equation (PDE):

$$\frac{\partial p}{\partial t} = \frac{K_p}{2\mu\varepsilon}\,\nabla^2(p^2) \tag{2.1}$$

where p is pressure, t is time, μ is gas viscosity, ϵ is porosity of the medium[a], and K_p is the Darcy permeability of the channel defined by

$$K_p = \frac{d_h^2}{32} \tag{2.2}$$

Note: in other formulations, the porosity may be grouped with the permeability. More generally, one can define the permeability of the medium K_m based on the superficial rod flow area) using Equation (2.3):

$$K_m = \frac{d_h^2}{32}\left(\frac{d_h}{d_i}\right)^2 \tag{2.3}$$

where d_i is the inner diameter of the cladding (assumed to be 7937.5 μm).

Hydraulic resistance is characterized through a hydraulic diameter d_h that is characteristic of the most resistive flow channels along the length of the fuel rod. For isothermal, steady (or pseudo-steady), unidirectional flow along a rod hydraulic channel of length L separating two pressure reservoirs of fixed volume, Equation (2.1) integrates to the following:

$$G = \frac{\pi d_h^4}{256\mu R_m T_o}\left(\frac{p_1^2 - p_2^2}{L}\right) \tag{2.4}$$

where G is mass flow, R_m is the individual gas constant, and T_o is the flow temperature. The subscripts "1" and "2" are used to denote the properties (in this case, pressure) of the upstream (high pressure) and downstream (low pressure) reservoirs, respectively.

Although Equation (2.4) is strictly valid only for reservoirs at fixed pressure, it can be used to approximate, with good accuracy, mass flow rates under pseudo-steady flow conditions; that is, Equation (2.4) may be used in systems where the time scale associated with pressure equilibration within the rod is short relative to that associated with the change in upstream and downstream chamber pressures. The current test system as configured in Section 2.1 and with fuel rods with rod hydraulic diameters on the order of 10^2 μm satisfies the requirements for pseudo-steady flow. As such, Equation (2.4) may be used as-is to predict a time-dependent mass flow using time-dependent upstream and downstream pressure values.

[a] In the current context, medium porosity includes the gas-containing volume formed by cracks in the fuel, inter-pellet spacing, and pellet-cladding spacing. Medium porosity is included in the single-flow-channel equation, Equation 2.1, to properly account for rod internal volume and gas storage capacity.

Equation (2.4) only provides the rate of mass transfer of gas from the upstream to the downstream chamber. Upstream and downstream pressure are governed by equations (2.5) and (2.6):

$$\frac{dp_1}{dt} = -\frac{GR_mT_o}{V_1} \tag{2.5}$$

$$\frac{dp_2}{dt} = \frac{GR_mT_o}{V_2} \tag{2.6}$$

Here, V_1 and V_2 are the upstream and downstream chamber volumes, respectively. In the two-chamber model construct, equations (2.5) and (2.6) are not independent, because the total system gas content is constant. Rather, they are related by Equation (2.7):

$$y_1p_1^o + y_2p_2^o = y_1p_1 + y_2p_2 = p_e \tag{2.7}$$

where p_1^o and p_2^o are the initial upstream and downstream pressures, respectively, p_e is the ultimate equilibrium pressure of the two-chamber system, and y_1 and y_2 are volume fractions:

$$y_1 = \frac{V_1}{V_1+V_2} \quad \text{and} \quad y_2 = \frac{V_2}{V_1+V_2} \tag{2.8}$$

Rod pressurization (balance) and depressurization (decay) pressure dynamics may both be interpreted using equations (2.4) through (2.8); however, the specific system configuration may lead to different phenomenological behaviors for upstream and downstream pressure. For example, in rod pressurization testing, both the upstream and downstream volumes are finite, causing both p_1 and p_2 to vary with time and requiring evaluation of two equations from equations (2.4) to (2.6) to fully solve the problem. In contrast, the downstream volume in depressurization testing (namely the hot cell) is virtually infinite, which transforms equations (2.6) and (2.7) to $p_2 = p_e =$ a constant.

The parametric complexity associated with the pressure dynamics problem may be reduced somewhat through use of scaled coordinates. Specifically, the pressure dynamics for both balance and decay testing (as well as upstream and downstream pressure) may be reduced to a single first-order differential equation using scaled coordinates. First, we define, for a generic chamber pressure p_k (where k = 1 or 2), a scaled pressure ϕ and time τ such that

$$\phi = \alpha_i^{(j)} + \left(1 - \alpha_k^{(j)}\right)\left(\frac{p_k}{p_e}\right) \quad \text{and} \quad \tau = \frac{t}{t_o^{(j)}} \tag{2.9}$$

Appropriate selection of the constants $\alpha_k^{(j)}$ and $t_o^{(j)}$ (see Eq. 2.11 and 2.12) reduce the scaled system pressure dynamics to

$$\frac{d\phi}{d\tau} = \frac{1}{2}(1 - \phi^2) \tag{2.10}$$

In the scaled equations above, the superscript (j) is included to differentiate α and t_o for pressurization (balance) and depressurization (decay) testing because they are not equivalent. There is no need to distinguish between scaled p_1 and p_2 in the resultant ϕ because selection of proper scaling renders them identical. (i.e., scaling yields $\phi_1 = \phi_2 = \phi$) The analytical solution of Equation (2.10) is shown in Equation (2.11):

$$\phi = \frac{1-\theta e^{-\tau}}{1+\theta e^{-\tau}} \quad \text{with} \quad \theta = \frac{1-\phi^o}{1+\phi^o} \tag{2.11}$$

where ϕ^o is simply the initial value of ϕ corresponding to p_i^o. Analysis of pressurization and depressurization scales find the scaled form given by Equation (2.10) results when

$$\alpha_1 = \frac{y_1}{y_2}, \quad \alpha_2 = \frac{y_2}{y_1}, \text{ and} \quad t_o = \left[\frac{128\,\mu\, y_1\, y_2\, (V_1+V_2)\, L}{\pi d_h^4}\right]\frac{1}{p_e} \tag{2.12}$$

for pressurization and

$$\alpha_1 = 0, \qquad \alpha_2 = \infty, \text{ and} \qquad t_o = \left[\frac{128\,\mu\,V_1\,L}{\pi d_h^4}\right]\frac{1}{p_e} \tag{2.13}$$

for depressurization. Comparison of these expressions shows that depressurization dynamics are a limiting case of the general two-chamber dynamics for $V_2 \to \infty$.

With knowledge of the gas communication test system geometry (V_1 and/or V_2 and rod segment length L), least squares analysis can be used to scale the rate and magnitude of change in upstream and downstream pressure measurements (p_1 and p_2, respectively) in accordance with Equation (2.11) to determine the appropriate equilibrium pressure p_e and time scale t_o. The latter can be used in combination with equation (2.12) [for pressurization] or Equation (2.13) [for depressurization] to infer the hydraulic diameter d_h from the system geometry, equilibrium pressure, and gas viscosity μ. Finally, channel and media permeability, K_p and K_m, can be calculated by equations (2.2) and (2.3).

2.2.2 Exclusion of Choked and/or Turbulent Flow

Equation (2.4) and its derivatives are premised on the assumption that flow is both laminar and unchoked. Two measures used to assess the flow regime are the Reynolds number Re for onset of turbulence and the critical downstream-to-upstream pressure ratio ζ_c for onset of choked flow. Reynolds number is calculated thus:

$$\mathrm{Re} = \frac{g d_h}{\mu} \tag{2.14}$$

where g is the mass flux:

$$g = \frac{4G}{\pi d_h^2} \tag{2.15}$$

Because the analysis here treats porous flow through a virtual capillary, there is no clear threshold for turbulent flow onset in a porous medium. The current analysis uses $\mathrm{Re} \geq 2500$ as turbulent and excludes regions meeting that condition from analysis.

The critical pressure ratio ζ_c for choked flow is evaluated through the following implicit relationship

$$\frac{1}{\zeta_c} = \frac{\Lambda_c - \ln \zeta_c}{1 - \zeta_c} \tag{2.16}$$

where Λ_c is a scaled critical friction coefficient defined as follows:

$$\Lambda_c = \frac{4 f_{f,c}\, L}{d_h} \tag{2.17}$$

Here, $f_{f,c}$ is the Fanning friction factor and is assessed at the critical Reynolds number for choked flow onset (Re_c) using standard engineering correlations for friction factor [e.g., that of Churchill (1977)]. Calculation of Re_c requires knowledge of the critical mass flux g_c defined by Eq. (2.18):

$$g_c = p_1 \left(\frac{\zeta_c}{R_m T_o}\right)^{\frac{1}{2}} \tag{2.18}$$

An initial guess value of ζ_c (e.g., 0.5) can be used to iteratively converge to the actual ζ_c for the given system configuration. Then, the critical downstream pressure p_2^c below which flow is choked is

$$p_2^c = p_1 \zeta_c^{1/2} \tag{2.19}$$

That is, when $p_2 \leq p_2^c$, flow will be choked and should be excluded from analysis.

Equations (2.14) and (2.16) should make clear that determination of both Re and ζ_c and exclusion of data falling in turbulent or choked flow regions requires knowledge of d_h. d_h can be determined from measured pressure evolution in an iterative process that starts by fitting all available data and using the

resultant best-fit d_h to assess and exclude data suspected of falling in either turbulent or choked flow regions. The pared-down data set is then used to reassess the best-fit d_h and associated flow regime exclusions. The process repeats until convergence.

2.2.3 Fitting of Gas Puncture Data

To supplement and improve confidence in the current gas communication testing results, the hydraulic properties of flow within full-length rods were assessed; this was done using both the gas communication data collected in calendar year (CY) 2019 and CY 2020 (using the analysis methods described in Sections 2.2.1 to 2.2.2) and using rod puncture measurements collected during end-of-life (EOL) rod internal pressure (RIP) and rod internal volume testing done in CY 2018. In rod puncture testing, the pressurized gas inside the rod is expanded incrementally into evacuated expansion segments of known volume. Each expansion is accompanied by a rapid intra-chamber equilibration of pressure and a secondary slower equilibration of pressure that results from transport from the pores in the fuel into the downstream volumes. Equilibration is controlled by the hydraulic resistance of the fuel and can provide a secondary measure of d_h and K_p (or K_m). However, evaluation of the hydraulic properties from rod puncture data is complicated by several experimental factors:

- There is no clearly defined "upstream volume." Strictly, the upstream volume is equivalent to the accessible porous volume of the rod itself (and possibly the plenum in cases where the rod is punctured on a fuel-containing portion, as was the case for rod FK).
- Upstream pressure is not measured. No pressure sensor was installed on the end of the rod opposite puncture (nor could it be without affecting the integrity of the EOL pressure and volume determinations).
- Exact information of the fueled rod void volumes and hydraulic channel dimensions is unknown. Specifically, experimental values on the spatial distribution of porous volume and cracks that allow flow within the rod are unknown (and could show rod-to-rod variability).

Of these three points, the first and final are the most significant and derive from limited knowledge about the internal structure of the fuel. To facilitate analysis of pressure evolutions measured during rod puncture analysis, assumptions with respect to the location of the "upstream" volume within the fuel must be made.

First, if the gas is assumed to be uniformly distributed along the rod itself, solution of the downstream pressure dynamics requires solving the fully time dependent, nonlinear PDE posed by Equation (2.1). For unidirectional flow, Equation (2.1) becomes

$$\frac{\partial p(x,t)}{\partial t} = \frac{K_p}{2\mu\varepsilon}\frac{\partial^2[p^2(x,t)]}{\partial x^2} \tag{2.20}$$

and is governed by the following initial and boundary conditions for unchoked flow:

$$p(x,0) = p_r^{(j)} \tag{2.21}$$

$$p(L,t) = p_2(t) \qquad \text{and} \qquad \left.\frac{\partial p(x,t)}{\partial x}\right|_{x=0} = 0 \tag{2.22}$$

Here, the puncture is assumed to occur at $x = L$. If flow becomes choked, the downstream pressure conditions must be modified such that

$$\left.\frac{\partial p(x,t)}{\partial x}\right|_{x=L} = -\frac{\mu\sqrt{R_m T_o}}{2K_p}\left(\frac{d_h}{d_i}\right)^2 \tag{2.23}$$

where (as before) d_i is the diameter of the cladding. Equation (2.22) recognizes that peak mass flow (and therefore the location where flow will choke) corresponds to the rod puncture location. Solution of equations (2.19) through (2.22) requires iterative solution of a nonlinear PDE for a given d_h. Iterative

guesses of d_h would then need to be made to converge to a solution that provides the best fit of the measured downstream pressure response. While such an approach can be readily implemented using available numerical PDE solvers such as FEnICS[b] or COMSOL,[c] independently verifying the final calculation would be difficult within current project quality guidelines.[d]

A simpler assumed geometry that lends itself to an analytical solution starts by assuming that the upstream volume resides entirely at the closed end of the rod. Under this assumption, a pseudo-steady gas transport regime can be assumed, which renders the pressure evolution problem equivalent to gas communication pressurization (balance) testing. Then, pressure dynamics are governed by equations (2.11) and (2.12). As noted before, only downstream pressure p_2 is monitored during testing. While a lack of measured upstream pressure does not preclude determination of hydraulic parameters, it renders determination of upstream volume entirely dependent on downstream pressure analysis. In contrast, standard pressurization (balance) gas communication can employ variation in both upstream and downstream pressure to assess system volumes accurately. In practice, determinations of d_h and $K_p$from rod puncture data must rely on EOL rod internal volume and pressure measurements determined by the double-expansion method coupled with estimates (based on visual selection from the pressure evolution data) of initial and equilibrium downstream pressure.

The need to select a "starting" point for downstream pressurization is complicated (or perhaps confounded) by an initial rapid pressure change driven not by release/transmission of gas from cracks and inter-pellet spaces within the fueled section of the rod itself but rather by equilibration of the downstream chambers connected by expansion (e.g., the rod plenum to expansion volume *C* for the first expansion). To evaluate pressure dynamics governed purely by gas release from "porous" volume within the fueled sections of the rod, the initial dynamics governed by chamber equilibration must be explicitly excluded. Of course, release from pores and chamber equilibration occur simultaneously. However, because chamber equilibration is fast (or assumed to be fast where the puncture diameter is much larger than the hydraulic diameter of the fuel), the initial pressure rise attributable to fueled rod porosity during chamber equilibration is assumed to be negligible. These assumptions lead to increased uncertainty in the analysis. Likewise, the uncertainty in the EOL pressure and volume derived from expansion testing lead to further increases in the uncertainty associated with rod-puncture–derived d_h and K_p. Rough, order-of-magnitude estimates place d_h uncertainty on the same order as volume uncertainty (approximately 5%). Finally, evaluations of d_h and K_p are generally limited to the first two volume expansions measured during rod puncture, namely volume expansions rC (where the as-received rod internal pressure expands into system Volume C - ~15 mL) and rCB (where the pressure contained in expansion rC is allowed to expand into system Volume B - ~205 mL).[e] These two expansions were selected because they involve relatively large changes in downstream pressure, which increases the pressure change signal relative to the noise in the signal (±0.1 psia). Further expansions are generally limited by two factors: first, certain expansions yield minor increases in relative expansion volume (e.g., expansion involving segments E and F – see Figure 4-2 in Shimskey et al. 2019a) and second, later expansions fall below 10% of full scale of the pressure transducer; (these have been generally excluded from EOL evaluations because of poor accuracy of the 0 to 500 psia sensor at pressures below 50 psia).

2.2.4 Assessing Overall Rod Resistance from Segment-Based Analyses

Section 2.2.2 and Section 2.2.3 provide the technical basis for evaluating rod hydraulic parameters, namely d_h, for rod segments tested as part of CY 2019–2020 gas communication studies (Section 2.1)

[b] https://fenicsproject.org/

[c] https://www.comsol.com/

[d] Equations (2.20) through (2.23) are not ultimately used but are reported herein to provide a basis for future considerations in case there is reason to evaluate more complex rod internal structure on release dynamics.

[e] For a more complete discussion of gas puncture expansion terminology (e.g., rC, rCB, etc.), see Shimskey et al. 2019a

and for full-length rods tested during CY 2018 rod puncture testing that supported determination of EOL rod internal pressure and volume. The results of these analyses, discussed in Section 2.3, demonstrate segment-to-segment variability in the evaluated d_h. In seeking (1) to compare segment-based results derived from gas communication testing to the full-rod measurements developed from rod puncture testing, and (2) more generally to evaluate the total rod hydraulic resistance for safety-basis analyses, a means of combining d_h values for rod segments into a single representative value for the entire length of the original rod is needed. For pseudo-steady flow processes, Equation (2.4) holds for any rod segment j of length L_j such that

$$G_j = \frac{\pi d_{h,j}^4}{256 \mu R_m T_o} \left(\frac{p_{j-1}^2 - p_j^2}{L_j} \right) \tag{2.24}$$

Equation (2.24) recognizes that each segment j has its own bounding upstream (p_{j-1}) and downstream (p_j) pressures[f] and hydraulic diameter $d_{h,j}$. For there to be no change in the accumulated gas content in the rod, the pseudo-steady condition requires that $G_j = G = \text{const}$, where G is associated with the overall mass flow for a rod comprising n aggregated segments with an overall ("effective") hydraulic resistance $d_{h,e}$ such that:

$$G = \frac{\pi d_{h,e}^4}{256 \mu R_m T_o} \left(\frac{p_0^2 - p_n^2}{L} \right) \tag{2.25}$$

Comparison of Equations (2.24) and (2.25) finds:

$$d_{h,e} = \left(\sum_{i=1}^{n} \frac{w_j}{d_{h,j}^4} \right)^{-\frac{1}{4}} \qquad \text{with} \qquad w_j = \frac{L_j}{L} \tag{2.26}$$

Equation (2.26) provides a means of aggregating individual rod segment d_h results into an effective hydraulic diameter $d_{h,e}$ for the full-length rod. The format in which individual lengths are weighted involves d_h^{-4}, which means that hydraulic resistance is heavily weighted by the most resistive segments (i.e., those with the smallest hydraulic diameters). This is consistent with the underlying expectations when treating hydraulic resistance in porous media using the "single channel/capillary" approximation (see Shimskey et al. 2019b).

In total, the equations developed in Sections 2.2.1 through 2.2.4 provide a complete basis for evaluating the hydraulic properties of both individual rod segments tested in CY 2019/2020 and full-length rods tested in CY 2018 rod EOL puncture tests. The next section gives a high-level summary of SNF rod hydraulic resistance parameters derived from rod pressurization, depressurization, and gas puncture testing; equations (2.1) to (2.26) are used to provide insight on variation in hydraulic resistance between fuel types and spatially along the fuel rod itself.

2.2.5 Functional Dependence on Pressure

Gas communication testing will be completed at two nominally distinct pressures: (1) the EOL RIP and (2) 5 MPa (725 psia). The effect of test pressure on hydraulic diameter is unclear (and depends on interaction between the fuel and the cladding); however, its effect on the diameter and length of pressurized blank (empty) rods is well established; it can be found in standard reference texts on mechanics of deformable solids (e.g., Beer and Johnston 1992). Pressurization of a semi-infinite thin-

[f] Because Equation (2.23) applies only to the rod, one need not be concerned about the volume of the "upstream" and "downstream" segments.

walled rod with one fixed (unmoving) end and a second unbound/floating end (such that the axial stress $\sigma_z = 0$) yields the following hoop strain: ε_θ

$$\varepsilon_\theta = \frac{p_r\, r_{r,i}}{\delta_r E} \tag{2.27}$$

where p_r is the internal rod pressure, $r_{r,i}$ is the inner radius of the rod, δ_r is the wall thickness of the rod, and E is Young's modulus. It should be noted that the ratio of fuel cladding wall inner radius $r_{r,i}$ to its thickness δ_r (namely, $r_{r,i}/\delta_r \sim 6$) does not meet the thin-walled tube criterion ($r_{r,i}/\delta_r > 10$). However, the goal of the current analysis is to provide order-of-magnitude estimates of how hydraulic diameter (not tube radius) changes as a result of increased test pressure. The accuracy of the first-order approximations provided by thin-walled tubing equations should suffice for that purpose. Furthermore, the development of Eq. 2.27 assumes the outer/atmospheric pressure $p_a \simeq 0$. For the purpose of the current evaluation, the rod pressure term p_r will be replaced by the difference in internal and external pressure $\Delta p_r = p_r - p_a$.

It is unclear if the strain relation for the free-floating rod is suitable for the fuel rod segment configuration employed in gas communication. Indeed, use of grips to seal and hold the rod segment ends are expected to impose axial loads on the rod. Alternate forms of Eq. (2.27) may be developed to accommodate the impact of axial stress. The hoop strain for a rod with a closed-end ends (such that $\sigma_z = p_r r_{r,i}/2\delta_r$) or with a fixed end (such that $\varepsilon_z = 0$) , respectively,

$$\varepsilon^*_{\theta r} = \varepsilon_{\theta r}\left(1 - \frac{\nu}{2}\right), \qquad \text{or} \qquad \varepsilon'_\theta = \varepsilon_\theta(1 - \nu^2) \tag{2.28}$$

where ν is Poisson's ratio. Here, the superscript * and $'$ have been added to distinguish hoop strain for closed and fixed rods, respectively, from that for the floating rod. The corresponding change in rod diameter Δd_r for floating, closed, and fixed rods can then be assessed by Equation (2.29):

$$\Delta d_r = 2\,\varepsilon_\theta\, r_{r,i}, \qquad \Delta d^*_r = 2\,\epsilon^*_\theta\, r_{r,i}, \text{ and} \qquad \Delta d'_r = 2\,\epsilon'_\theta\, r_{r,i} \tag{2.29}$$

Equations (2.27) through (2.29) are valid for thin-walled vessels (meeting the condition $r_{r,i}/\delta_r \gg 1$) within the elastic limit of the rod material. To check whether the rod conditions fall within the elastic limit, the maximum shear stress τ_m (not to be confused with scaled time) should fall below the material's yield strength in shear τ_y. The former can be estimated using Equation (2.30):

$$\tau_m = \frac{p_r r_{r,i}}{2\delta_r} \tag{2.30}$$

To enable prediction of all relevant strain calculations, the mechanical properties of fuel rod cladding are taken from Weck et al. (2015).

It should be stressed that the equations above predict the change in rod diameter as a function of internal rod pressure and are not directly applicable to evaluating the growth of hydraulic diameter (which is related to the internal structure of the fuel and its spacing) with test pressure. However, we assert that, short of gross mechanical failure of the fuel pellet stack, an increase in rod diameter under pressure should also be accompanied by growth in the gas communication pathway (either in circumferential gaps where the fuel-clad bond is broken or through growth of cracks in the fuel where the fuel-clad bond is intact). Given this assertion linking gas communication pathways to rod diameter increase, it is posited that the increase in hydraulic diameter due to internal pressure will be on the same order of magnitude as the increase of rod diameter resulting from the same pressure increase. In making these arguments, we inherently assume that the cracks in the fuel pellet and/or spacing between the fuel in the cladding form the limiting hydraulic resistance rather than inter-pellet spacing. As noted in the preceding paragraphs, Eqs. 2.27 to 2.29 are intended to provide order-of-magnitude estimates of how hydraulic diameter scales with pressure; as such the suitability of the limiting approximations used in their development, namely $r_{r,i}/\delta_r \gg 1$ and $p_a \simeq 0$, need not be fully considered or justified.

2.3 Results

Gas communication testing conducted in CYs 2019 and 2020 evaluated the hydraulic resistance of segments from rods FK (Zircaloy-4), KK (M5), KP (M5), UL (ZIRLO), and UM (ZIRLO). This analysis was further supplemented by analysis of full-rod hydraulic resistance from CY 2018 rod puncture testing. In all cases, estimates of hydraulic resistance employed the segment and total fueled-rod lengths presented in Table 2-1. For reference, the EOL RIP and rod internal volume (including the plenum volume) are also included in Table 2-1. The hydraulic diameters (d_h) and permeabilities (K_m or K_p) evaluated from both gas communication segment testing and full-rod puncture testing are listed in Table 2-2 and Table 2-3 for the five rods considered herein. Limited discussion of these results will be presented in the figures and tables that follow. A full test-by-test set of results (including pressurization and depressurization curves for all rod segments and test formats) is provided in Appendix A. In addition, Table 2-2 and Table 2-3 only include the five rods evaluated in gas communication testing; however, puncture testing was carried out on all rods and as such, rod puncture testing provides hydraulic resistance estimates for all rods evaluated in Shimskey et al. (2019a). The hydraulic diameters derived from rod puncture testing for both the current five rods and the remaining rods tested in CY 2018 may be found in Appendix B.

Representative pressure evolutions measured during gas communication testing are presented in Figure 2-4 for rods FK, KK, KP, UL, and UM. Only pressure evolution data for Segment 2 are presented, because this segment showed the least rod-to-rod length variation of ~12 mm. (When length variation is absent or negligible, differences in pressure rise/fall time scales can be attributed to differences in the fuel's hydraulic resistance and test pressure alone). In all cases, the pressure dynamics are consistent with the behavior predicted by unscaled analog of Equation (2.10) (shown as solid lines in Figure 2-4). Pressurization of the downstream volume V_2 (estimated by calculation to be roughly 25 mL) from atmospheric pressure to either the rod's EOL RIP or the standard reference test pressure of 5.0 MPa is generally complete after 20 minutes. Depressurization from either the EOL RIP or 5.0 MPa from the isolated upstream volume V_1 (approximately 24 mL) reaches 90% completion after approximately 90 minutes. Despite the difference in observed pressurization and depressurization time scales, hydraulic analysis finds that hydraulic diameters are nearly equivalent when comparing pressurization and depressurization results for the same rod and rod segment (see discussion below). This means that the differences in pressurization and depressurization time scales result solely from differences in system configuration between the two test formats (namely differences in upstream and downstream volumes V_1 and V_2).

Table 2-1. Summary of Key Rod Parameters for Gas Communication Testing.

Rod ID	Short ID	Cladding	p_r [MPa]	v_r [mL]	Tested Fueled Length (mm)				
					Seg. 1	Seg. 2	Seg. 3	Seg. 4	Rod
30AP2	AP	M5	3.36	10.8	796	914	1,029	937	3,676
F35K13	FK	Zircaloy-4	5.14	12.5	815	914	1,029	838	3,596
3F9P2	FP	ZIRLO	3.58	12.3	791	927	1,054	904	3,676
5K7C5	KC	M5	3.97	9.7	796	914	1,029	937	3,676
5K7K9	KK	M5	3.83	10.4	795	914	1,029	937	3,675
5K7P2	KP	M5	3.35	11.2	796	914	1,029	937	3,676
6U3L8	UL	ZIRLO	3.56	12.4	796	927	902	904	3,529
6U3M3	UM	ZIRLO	3.78	11.5	796	927	1,054	906	3,683
6U3O5	UO	ZIRLO	3.70	12.7	791	927	1,054	904	3,676
6U3P16	UP	ZIRLO	3.27	13.1	791	927	1,054	904	3,676

Note: Each fueled length reported here corresponds to the actual length of the rod tested in the system (after segmentation and sampling). The total length of fuel represents PNNL's best estimate of the total length of fuel within the uncut rod. Here, the EOL RIP (p_r) and rod internal volume (v_r) are taken from Shimskey et al. (2019b). Here and elsewhere in this report, rod and rod segment lengths have been rounded to the nearest 1 mm (consistent with the expected full-length uncertainty of ±2 mm). All underlying handling of lengths (and differences between lengths) employ full length precision, which may lead to ±1 mm discrepancies in lengths as-presented and as-calculated using rounded values.

From Table 2-2 and Table 2-3, the hydraulic diameters and permeabilities measured for segments from rods FK, KK, KP, UL, and UM range from approximately 65 to 110 µm and 8.6×10^{-15} and 69×10^{-15} m^2, respectively. Variation in the hydraulic diameter is most significant when comparing segments from different rod (e.g., Segment 1 from rod FK to Segment 1 from rod KK); the difference in measured diameters may be as large as 35 µm. When comparing individual rod segments (e.g., UM1 to UM3) diameters can show less intersegment variation, on the order of 18 µm. As noted above, variation in hydraulic diameter associated with the test format (i.e., depressurization versus pressurization tests) is typically 2.0 µm or less. Finally, variation in hydraulic diameter with the test pressure (EOL RIP versus 5.0 MPa) is less than 1 µm.[g]

Because the test matrix defines a total of 80 parametric combinations for the rods, rod segments, test formats, and test pressures evaluated, only a subset of the results will be discussed in detail below. In particular, subsequent discussion of hydraulic resistance will focus almost entirely on trends observed in depressurization testing. Depressurization (decay) results are representative of both pressurization and depressurization test formats (as is indicated by the similarity between pressurization/depressurization d_h and K_m shown in Table 2-2 and Table 2-3). These are expected to be the more accurate (of the two test formats) because (1) upstream volume is well characterized and (2) special analysis is not required to determine downstream volume (rather, it can be assumed to be infinite). While it may be argued that the test format results show greater variation than can be observed between results from the two gas communication test pressures (i.e., the EOL RIP and the standard 5.0 MPa), comparison of the latter are included because rod diameter is expected to vary naturally with pressure (see Section 2.2.5).

[g] The test format comparison made in this paragraph excludes rod puncture testing because these tests were not specifically designed to measure hydraulic resistance. Estimates of d_h and K_m that derive from rod puncture testing should be considered opportunistic and the assumptions that underpin analysis increase uncertainty in the results.

Table 2-2. Hydraulic Diameter d_h for the Five Rods Tested in CY 2019/2020 Gas Communication Testing.

Segment	Hydraulic Diameter (um)				
	FK	**KK**	**KP**	**UL**	**UM**
Puncture					
Expansion rC	99.8	64.1	67.2	68.4	66.2
Expansion rCB	89.7	83.5	92.7	78.3	93.9
Pressurization to EOL RIP					
1	107.6	84.4	91.6	74.6	79.4
2	101.6	78.0	87.6	71.4	69.3
3	91.5	75.2	83.8	65.1	68.5
4	95.3	83.8	87.3	75.8	76.5
Rod	**97.6**	**79.6**	**87.1**	**70.7**	**72.3**
Depressurization from EOL RIP					
1	108.4	84.8	92.8	75.5	81.5
2	100.9	76.7	86.5	70.6	68.5
3	90.1	74.4	82.4	64.6	67.9
4	94.7	83.4	85.1	78.0	74.0
Rod	**96.9**	**78.9**	**86.0**	**70.8**	**71.6**
Pressurization to 5.0 MPa					
1	107.3	84.8	92.3	75.6	80.3
2	101.5	78.5	88.2	72.0	70.0
3	91.4	75.9	84.5	65.6	69.1
4	95.3	84.4	88.3	75.7	77.2
Rod	**97.5**	**80.2**	**87.9**	**71.2**	**73.0**
Depressurization from 5.0 MPa					
1	108.4	84.8	93.2	75.7	81.8
2	100.9	76.7	86.5	70.8	68.6
3	89.9	74.5	82.5	64.8	68.1
4	94.8	83.3	85.3	78.2	74.1
Rod	**96.8**	**79.0**	**86.1**	**71.0**	**71.8**

Note: Results are accompanied by hydraulic diameter estimates derived from CY 2018 rod puncture testing. The reported d_h for the "Rod" represent effective diameters for the full-length rod estimated by Eq. (2.26).

Table 2-3. Rod Permeability K_m for the Five Rods Tested in CY 2019 Gas Communication Testing.

	$K_m \times 10^{15}$ [m^2]				
Segment	**FK**	**KK**	**KP**	**UL**	**UM**
Puncture					
Expansion rC	49.1	8.4	10.1	10.9	9.5
Expansion rCB	32.1	24.1	36.6	18.6	38.6
Pressurization to EOL RIP					
1	66.5	25.2	34.9	15.4	19.7
2	52.8	18.3	29.2	12.9	11.5
3	34.7	15.9	24.4	8.9	10.9
4	41.0	24.5	28.8	16.4	17.0
Rod	**45.0**	**19.9**	**28.5**	**12.4**	**13.6**
Depressurization from EOL RIP					
1	68.6	25.6	36.8	16.1	21.9
2	51.4	17.1	27.7	12.3	10.9
3	32.7	15.2	22.9	8.6	10.5
4	39.9	24.0	26.1	18.4	14.9
Rod	**43.7**	**19.2**	**27.1**	**12.5**	**13.0**
Pressurization to 5.0 MPa					
1	65.8	25.7	36.0	16.2	20.7
2	52.7	18.9	30.0	13.4	11.9
3	34.6	16.5	25.3	9.2	11.3
4	40.9	25.1	30.1	16.3	17.6
Rod	**44.9**	**20.5**	**29.6**	**12.8**	**14.1**
Depressurization from 5.0 MPa					
1	68.4	25.7	37.4	16.3	22.2
2	51.4	17.2	27.8	12.4	11.0
3	32.4	15.3	23.0	8.7	10.7
4	40.0	23.9	26.2	18.5	15.0
Rod	**43.5**	**19.3**	**27.3**	**12.6**	**13.2**

Note: Results are accompanied by permeability estimates derived from CY 2018 rod puncture testing. All permeability estimates are derived from the hydraulic diameter using Eq. (2.3).

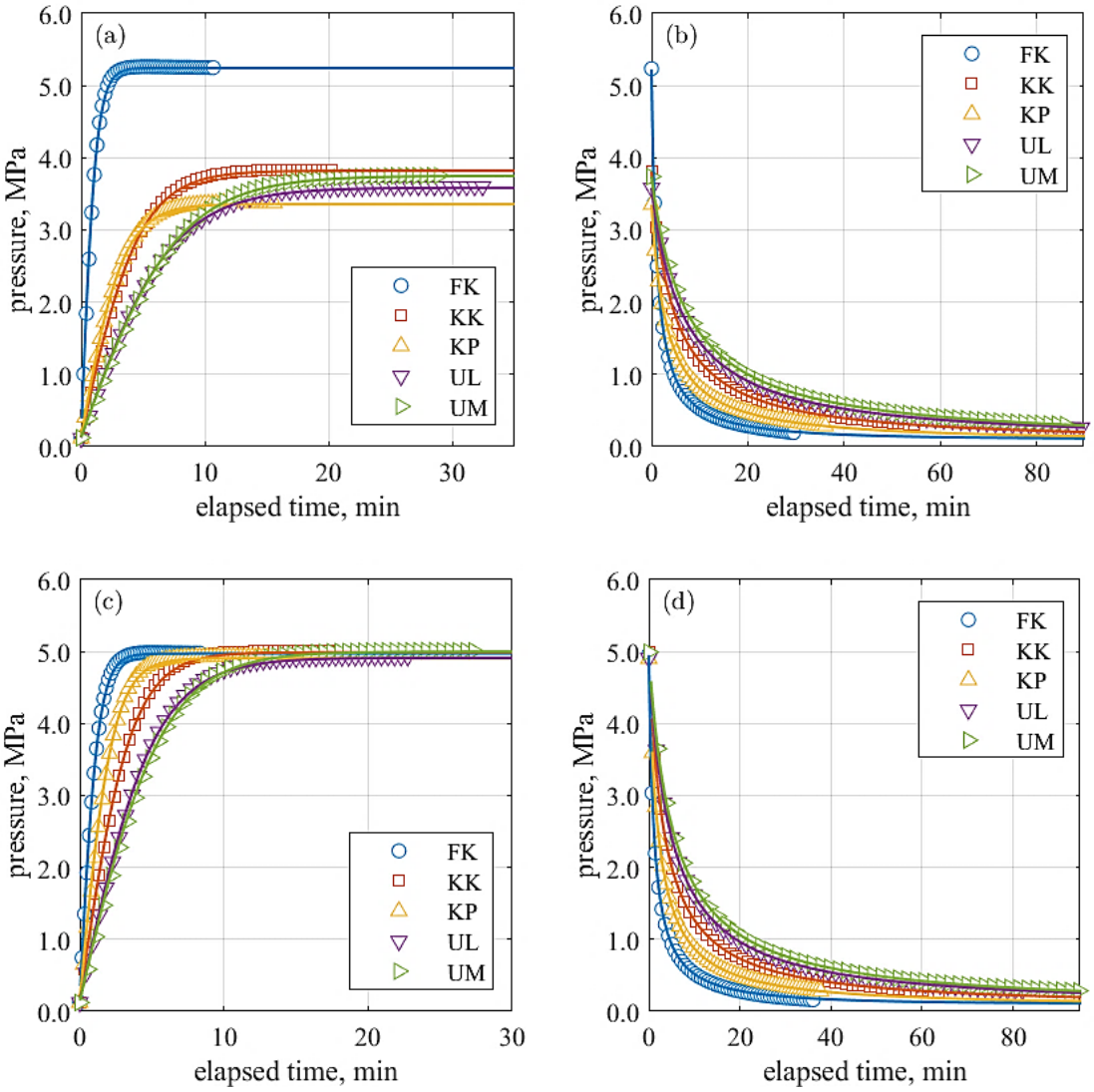

Figure 2-4. Comparison of Select Pressure Evolutions for the Five Rod Segments Tested During Gas Communication. Showing Rod Segment (a) Pressurization to the EOL RIP, (b) Depressurization from the EOL RIP, (c) Pressurization to 5.0 MPa, and (d) Depressurization from 5.0 MPa.

Note: All evolutions correspond to Segment 2 for the listed rod (this segment shows the least rod-to-rod variation in length: 914 to 927 mm). Symbols correspond to measured data (not all points are plotted to reduce point density); solid lines correspond to best-fit pressure evolutions using scaled versions of Eq. (2.10) and the hydraulic diameters listed in Table 2-2.

The greatest variation in hydraulic diameter is observed when comparing individual rods to each other (approximately 35 µm, as noted previously). Figure 2-4 and Figure 2-6 show rod-to-rod comparisons of d_h and K_m, respectively, evaluated for rods FK, KK, KP, UL, and UM. The results show that rod FK (Zircaloy-4) is the most permeable and the ZIRLO rods (UL and UM) are the least permeable. Both M5 rods (KK and KP) fall between the two extremes.

This preliminary result set suggests that hydraulic resistance can be grouped largely according to cladding type. This is to be expected, because both M5 and ZIRLO were designed to be more resistant to creep and

growth than Zircaloy-4. ZIRLO is a stress-relief annealed alloy containing tin, whereas M5 is fully recrystallized and has no tin. Given these differences in cladding texture and chemistry, it is expected that, for hydraulic diameter and gas permeability, Zircaloy-4 >M5 > ZIRLO. In addition, the Zircaloy-4 sibling pin was irradiated for four cycles and could potentially experience more fragmentation than the other rods, which were irradiated for only three cycles.

Evaluation of the hydraulic resistance against other rod parameters such as burnup, EOL RIP, and EOL volume demonstrates unclear functional dependence (which is not surprising given the limited set of test rods evaluated in the current study). However, it should be noted that rod FK, found to have the largest hydraulic diameter (nearly 100 µm, as compared with 70 to 85 µm for other rods), was also found to have the largest EOL RIP (~5.2 MPa) of all rods tested. Rod FK's EOL RIP is nearly 1 MPa greater than those of the four other rods tested herein, though that is largely because it had an initial helium fill gas pressure at least 0.5 MPa higher than the other rods. Rod FK was also irradiated for four cycles, so it is possible that the FK hydraulic diameter reflects internal crack growth caused by increased pressure and gas content. However, this possibility is moderated by the fact that current testing did not evidence a dramatic increase in hydraulic diameter with increased test pressure (i.e., the results at 5.0 MPa are similar, if not identical when measurement uncertainty is considered, to those at the EOL RIP).

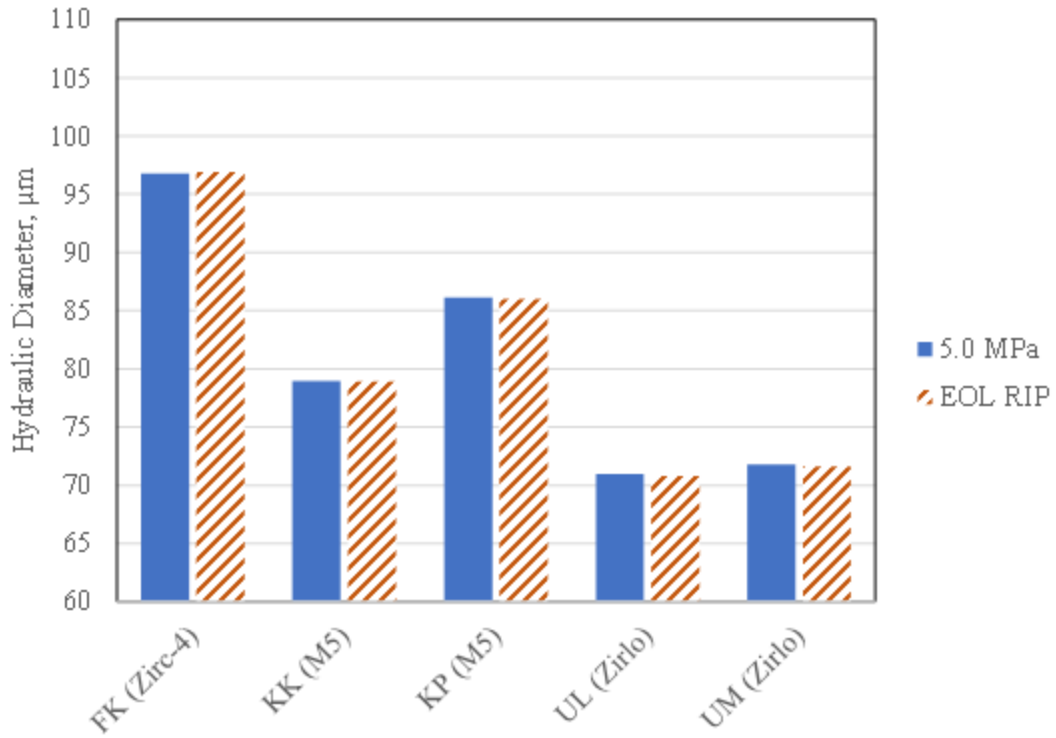

Figure 2-5. Effective Hydraulic Diameter $d_{h,e}$ for Gas Communication Tested Rods. All results derive from depressurization testing.

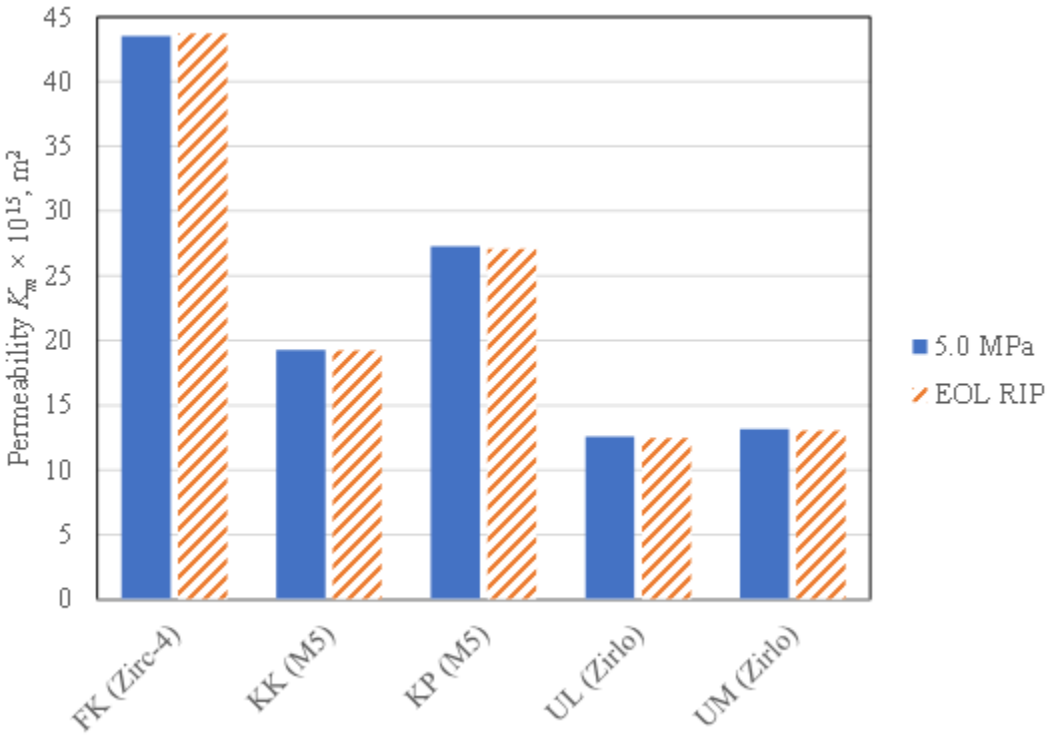

Figure 2-6. Effective Permeability K_m for Gas Communication Tested Rods. All results derive from depressurization testing.

As noted previously, testing of the hydraulic diameter at two typically distinct pressures, namely the EOL RIP (see Table 2-1) and 5.0 MPa, provides an opportunity to evaluate the pressure functionality of hydraulic resistance. Figure 2-7 shows the change in hydraulic diameter Δd_h observed with the change in gas communication test pressure Δp_o. For comparison, the dashed lines show the change in rod diameter expected from Eqs. (2.27) to (2.29). Although the Δd_h results are subject to significant scatter, the observed increase (or decrease, for the case of rod FK) in hydraulic resistance appears to be near or below the predicted changes in cladding diameter with test pressure. In particular, pressurization results typically fall around the predictions (floating, closed, and fixed), whereas depressurization results fall below those predictions. This suggests that the change in hydraulic diameter, if significant, appears to be tied to the change in cladding diameter and may ultimately reflect either hydraulic channel expansion/formation at the cladding-fuel interface or internal crack growth caused by axial and/or radial movement of cladding-bound fuel. At this point, it is also important to note that assessments of blank (empty) cladding radial growth measured by optical micrometers during rod segment pressurization also agree well with the cladding diameter growth predictions (see Figure 2-8). predictions for closed and fixed rod configurations Likewise, measurements of fueled-rod expansion for segments from rods FK, KK, KP, UL, and UM taken during gas communication (Figure 2-9) using optical micrometers show behavior consistent with that observed in Figure 2-7, albeit with a greater degree of uncertainty because of the radiation-induced degradation in the performance of the optical micrometers (to the point where one failed completely during testing).

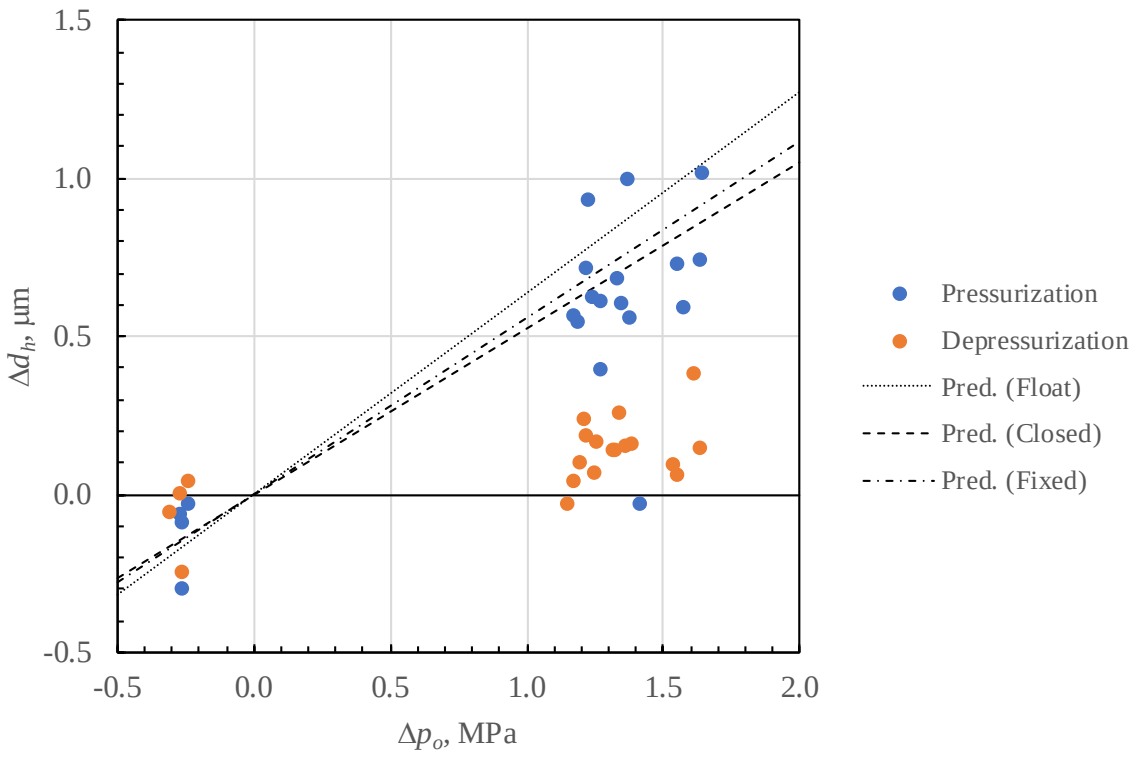

Figure 2-7. Difference in Rod Hydraulic Diameter Measured At 5.0 MPa and at the EOL RIP. *Note: Measurements were taken with an optical micrometer. Predictions are based on Eqs. (2.27) through (2.29) and physical properties from Weck et al. (2015). Specifically, the prediction uses* $r_{r,i} = 4.7625\ mm\ (\frac{3}{16}\ in.)$, $\delta_r = 0.79375\ mm\ (\frac{1}{32}\ in.)$, $E = 89.7\ GPa$, *and* $\nu = 0.35$.

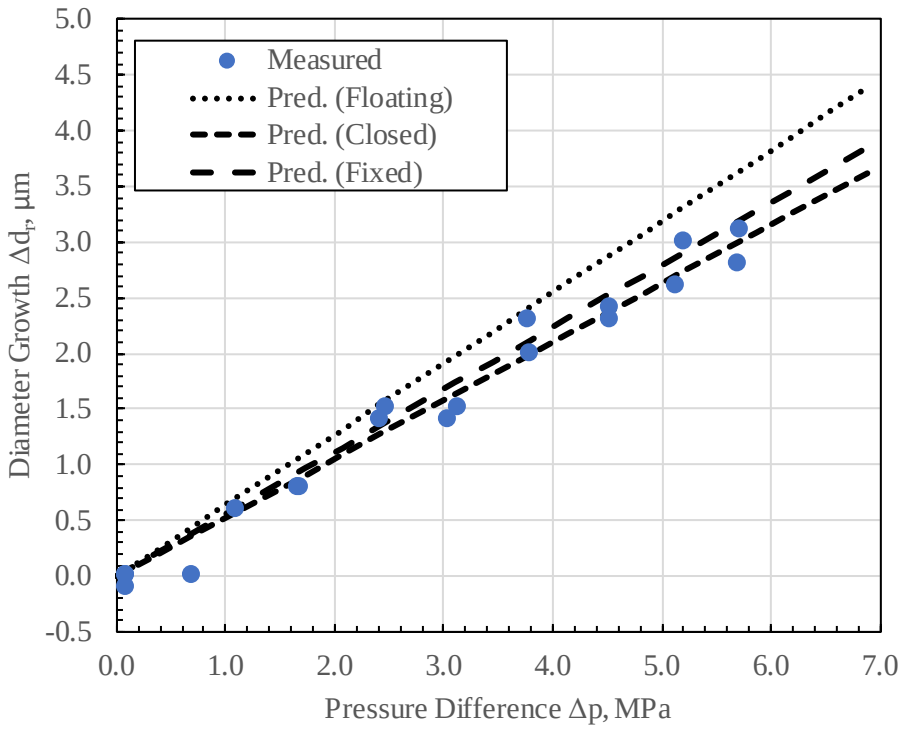

Figure 2-8. Evaluation of Blank Rod Diameter Growth as a Function of Pressure.
Note: Measurements were taken with an optical micrometer. Predictions are based on Eqs. (2.27) through (2.29) and the same physical parameters used in the predictions shown in Figure 2-7.

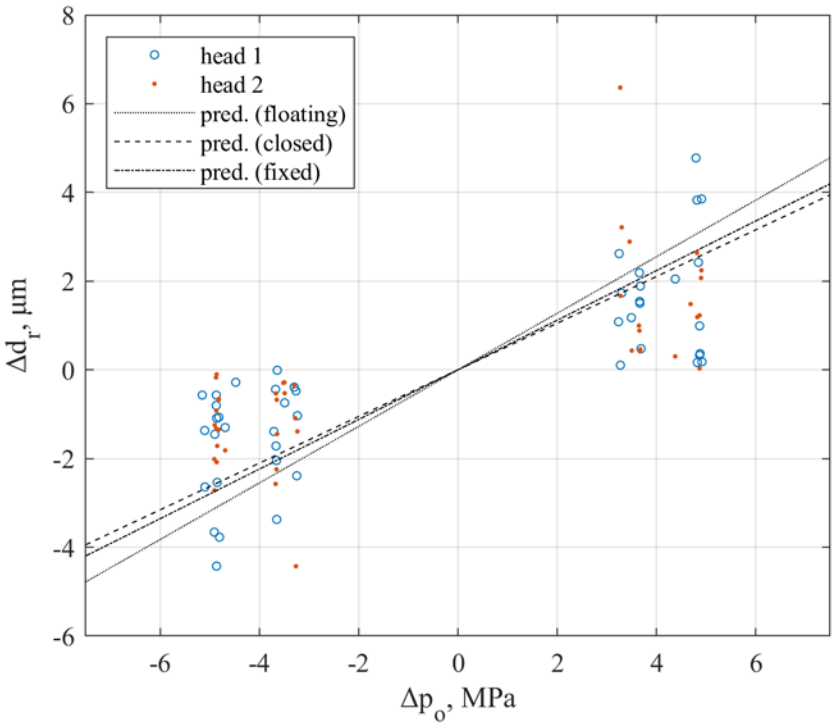

Figure 2-9. Fueled-Rod Diameter Change (Δd_r) as a Function of Change in Pressure (Δp_o) Measured during CY 2019/2020 Gas Communication Testing.

Note: Measurements taken using two optical micrometers (head 1 and head 2). The predicted (pred.) lines uses expressions, Eqs. (2.27)-(2.29), and parameters as the predictions in Figure 2-7.

With respect to the result in Figure 2-7, it is unclear why change in pressure and diameter correlate more strongly with pressurization than with depressurization. While one could speculate that the difference may relate to irreversibility in crack growth upon pressurization, there is generally insufficient data to support testing this hypothesis because replicate gas communication tests were only run when initial testing encountered problems (such as the Airmo grips not creating a seal to hold system pressure). Furthermore, the only rod segment that was extensively tested was UM-4 because it yielded anomalous pressure evolutions (i.e., the data suggested either no gas communication or failure of the gas seals somewhere along the rod ahead of the downstream reservoir). Analysis of UM-4 data suggests that gas communication did occur, because the inferred hydraulic diameters on "failed" tests with slow upstream pressure decay gave hydraulic diameters equivalent to those from "successful" UM-4 tests. If one takes the repeated tests of UM-4 as valid measurements (despite the unexpected pressure evolution behavior), then it is possible to assess the effect of repeated testing. Figure 2-10 shows the hydraulic diameters measured for the seven sequential pressurization/depressurization tests performed (over the span of several days) on rod segment UM-4. For consistency, results are only reported for depressurization events (with the caveat that pressurization events with no apparent gas communication could also be treated as though they were depressurization tests from the full upstream volume). The trend in d_h with increasing test iterations does not provide clear evidence that repeated pressurization/test cycles irreversibly increase hydraulic diameter. Of the seven tests, four fell near 75 μm and three fell in the 76.5 to 77.0 μm range. While the final two tests exhibited the largest diameters, it is unclear whether this increase reflects nominal test uncertainty, because test iteration 3 also shows increase in diameter relative to iterations 1, 2, 4, and 5. As such, the limited testing conducted on rod UM does not support the proposition that repeated gas communication testing progressively alters the hydraulic channels of the fuel.

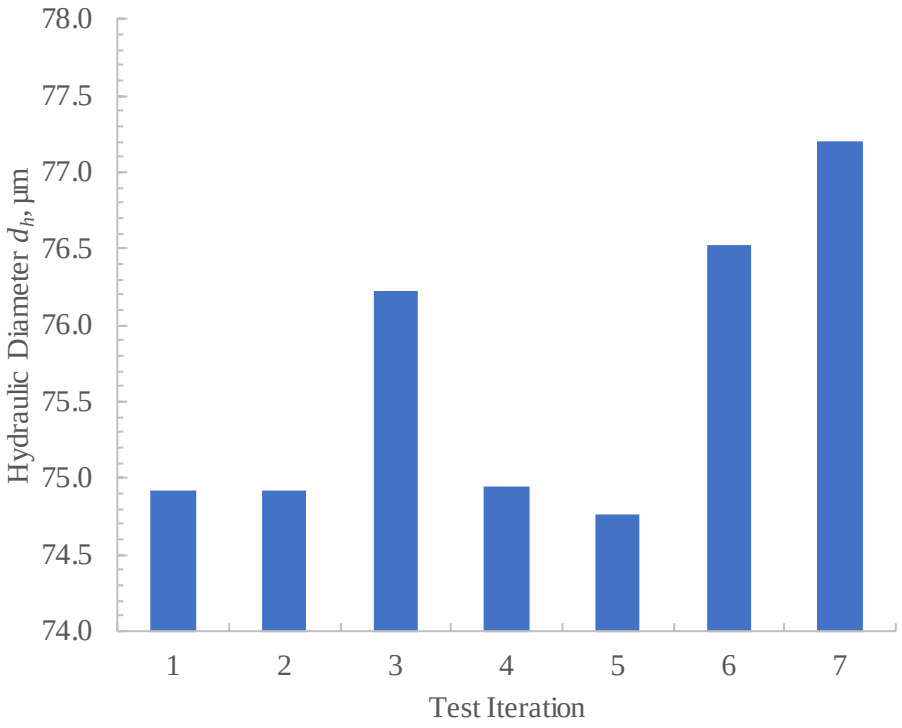

Figure 2-10. Hydraulic Diameter d_h Measured for Rod Segment UM-4 Over Seven Test Iterations.

As a final comparison of the current results, the hydraulic diameters derived from pressurization and depressurization were compared to those derived from rod puncture analysis. Figure 2-11 compares the length-averaged effective hydraulic diameters $d_{h,e}$ as determined by CY 2018 rod puncture, CY 2019/2020 depressurization, and CY 2019/2020 pressurization testing (at the EOL RIP) for the five rods tested. As noted previously, hydraulic diameters measured by pressurization and depressurization testing were self-consistent, agreeing to within ±1 µm. In contrast, hydraulic diameters inferred from CY 2018 rod puncture testing typically fell below their gas communication equivalents (except for that for rod FK). Agreement between rod-puncture and gas-communication hydraulic diameters is best for rods FK, UL, and UM (within 6 µm, which is near, albeit slightly above, the accuracy expected of the rod puncture method of 5%). In contrast, rod puncture diameters for both of the M5-clad rods (KK and KP) fell 15 µm below their respective gas communication-derived values. The cause of this difference is not clear, but it should be noted that the M5 rod puncture results stand out in one other respect: the internal upstream volumes of both M5 rods (0.7 to 0.8 mL) were much lower than the other rods (1.0 to 1.2 mL for the ZIRLO rods and 12.4 mL for the FK rod).[h]

One possibility is that sectioning of the M5 rods increased the size of internal cracks or broke the fuel-cladding bond. However, this assertion is not supported by independent evidence that sectioning and subsequent gas communication damaged the fuel and/or the fuel-cladding. Indeed, the most compelling case of loss/damaged fuel was observed in testing of Segments UL-4 and UM-4 (where loose fuel and fuel migration were observed – see Section 2.4); neither of these tests showed increase in either UL-4 or UM-4 diameters that was inconsistent with other bottom rod segments. Furthermore, UL and UM gas puncture diameters are more-or-less equivalent to their gas communication counterparts. As such, there is

[h] That rod FK's internal volume, as determined by rod puncture analysis, is one order of magnitude larger than that of all the other rods tested simply reflects its reversed orientation in the cask. That is, rod FK's "internal" volume includes the plenum volume.

not strong evidence to support that handling of the M5 rods in preparation for gas communication altered their hydraulic diameter.

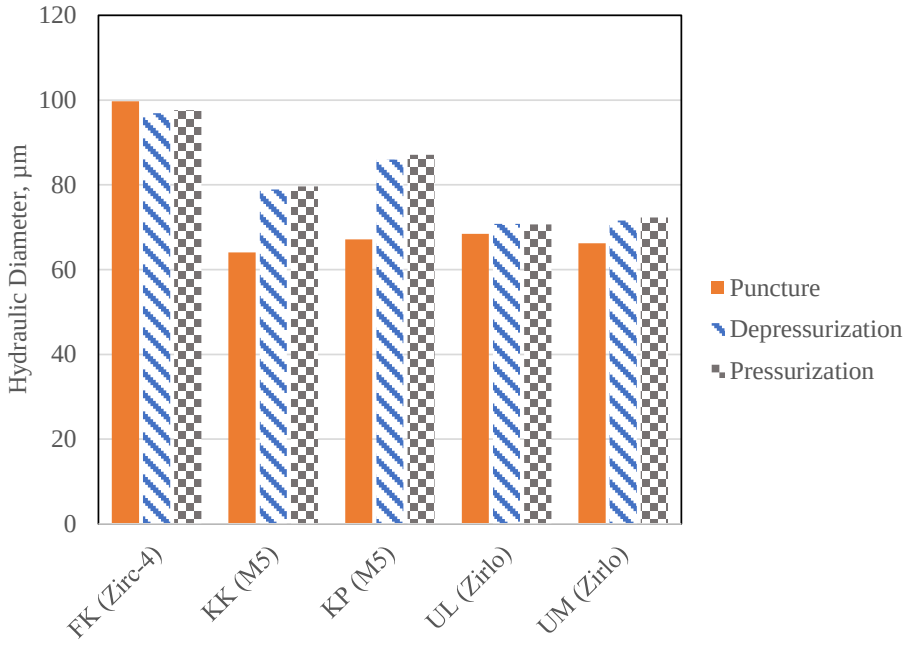

Figure 2-11. Comparison of Effective Hydraulic Diameter ($d_{h,e}$) at the EOL RIP Derived Using CY 2019/2020 Pressurization and Depressurization, and CY 2018 Rod Puncture Test Formats.

Another possible explanation for the difference in rod M5 gas puncture/communication diameters is that the hydraulic resistance in rod puncture testing reflects the size of the breach created by the impingement tool rather than the resistance of the pores in the fuel itself. The latter assertion would explain the similarity observed in hydraulic diameters determined by rod puncture for the M5 and the ZIRLO rods (i.e., all fall in the 64 to 70 µm range). Here, rod FK's outlying diameter could be attributed to having tested this rod in the reversed orientation (whereby a fueled region of the rod had to be "drilled-out" rather than simply puncturing the rod's plenum with the "pinch" tool).

However, the overall case for such breach-limited flow is not compelling, as both gas puncture- and communication-derived hydraulic diameters are consistent (they fall within the same range of 65 to 100 µm). Likewise, if flow were truly breach-limited, gas communication testing (which opens the entire cross-section of the fuel) would be expected to exhibit hydraulic diameters substantially larger than their corresponding gas puncture counterparts. Moreover, gas puncture tests evidence the expected rapid decrease in pressure upon puncture (that can be attributed to plenum depressurization) and a slower subsequent release (attributable to gas release from the fueled portion of the rod). Finally, difference in rod FK hydraulic diameter relative to other rods could be similarly attributed to its distinct cladding type (Zircaloy-4) and cooling history (~30 years versus ~10 years for the other four rods). Taken together, these observations provide strong evidence gas-puncture tests are not flow-limited by the size of the breach effected by rod puncture.

With respect to the results shown in Figure 2-11, the exact nature and cause of variation in hydraulic diameter cannot be determined from the current test program. While unsatisfying, this conclusion is not unexpected given that assessment of hydraulic diameter from gas puncture data was purely opportunistic. However, the current attempt at extracting hydraulic information from gas puncture testing shows promise (in that results from 3 of the 5 rods compare well with their gas communication counterparts). It

is expected that improved confidence in gas-puncture hydraulic diameter results could be attained through careful, deliberate design of the gas puncture system with gas communication assessments as an end-goal.

In terms of overall assessment, all hydraulic diameters reported in Table 2-2 fall within the range previously assessed for SNF of its type. First, the results agree well with the hydraulic resistances for the sibling pins reported in Montgomery and Morris (2019); (see Table 2-4, which reproduces both the K_m originally reported in Table 2.6 of Montgomery and Morris [2019] and also recasts[i] these results in terms of hydraulic diameter for direct comparison to the result format used here). Analysis found hydraulic diameters spanning 68.0 to 119 µm for the rods evaluated by Montgomery and Morris (2019). This span compares well to the range of hydraulic diameters derived from gas communication testing in the current study (70.7 to 97.6 µm based on full-length rod estimates). While there is no direct overlap of rods tested between the current study and Montgomery and Morris (2019), rods in both studies share the same age, history, and cladding, and as such, should show similar hydraulic structure.

Table 2-4. Hydraulic Resistance of Sibling Pins Tested by Montgomery and Morris (2019).

Full Rod ID	Alloy	$K_m \times 10^{15}$ [m^2]	d_h [µm]
3A1F05	Low Tin Zircaloy-4	83.2	114
F35P17	Zircaloy-4	99.6	119
3F9N05	ZIRLO	73.0	110
3D8E14	ZIRLO	40.8	95.2
6U3K09	ZIRLO	18.9	78.6
30AK09	M5	10.6	68.0
30AD05	M5	11.5	69.4
30AE14	M5	24.0	83.4

Note: Normalized permeabilities are taken directly from Table 6 in Montgomery and Morris (2019). Hydraulic diameters were calculated using Eq. (2.3).

Current PNNL testing of SNF rod hydraulic properties represents a significant expansion of testing relative to that previously reported in Shimskey et al. (2019b). Previous testing of rod segment UL-4 reported in Shimskey et al. (2019b) identified disparate hydraulic diameters for pressurization and depressurization: 46.2 and 75.2 µm, respectively. Shimskey et al. (2019b) speculated on the cause of the disparity and raised possible issues with the test configuration (namely poorly quantified system volumes and possible leaks) and also the possibility of debonding of the fuel-clad bond (leading to an increase in diameter from the initial pressurization to the subsequent depressurization). With respect to the former, issues surrounding the system geometry (including the use of flexible tubing in the system) were resolved prior to the current phase of gas communication testing. That resolution, coupled with increased testing, appears to have resolved the disparity in diameters observed in preliminary UL-4 testing. That is, current testing no longer finds a ~30 µm disparity in pressurization and depressurization; rather, both test formats give largely the same result (to within 2 µm). Indeed, current testing shows no significant increase in diameter between pressurization and depressurization. Likewise, repeated testing of rod segment UM-4 did not provide conclusive evidence that pressurization leads to substantive increases in hydraulic diameter (fuel crack width). While some of the current test results prevent the authors from entirely eliminating the possibility that pressurization of the rods during gas communication testing alters rod hydraulic resistance (see Figure 2-10 and its corresponding discussion), the current test data largely

[i] Conversion from K_m to d_h is accomplished by assuming a cladding outer diameter of 3/8 in. (0.375 in.) with a wall thickness of 1/32 in. (0.03125 in.).

suggests that the test protocol (i.e., the cycling rod pressure up to 5.0 MPa to evaluate resistance to flow) has no effect on hydraulic resistance.

2.4 Notable Observations

During gas communication testing in FY 2019 of the bottom rod segment of 6U3L08 (UL-4, 21–926 mm from bottom), fuel from the bottom of the segment was observed to have fallen out during storage after initially being observed to be firmly in place after cutting. During gas communication testing, fuel fragments were seen to move or fall out of the bottom segment of 6U3M03 (UM-4, 21–927 mm from the bottom). Also noted was the movement of fuel into the plenum section at the very top of the rod (UM-1, 2910–3857 mm from bottom). Below are images of segments UM-4 (Figure 2-12) and UM-1 (Figure 2-13) before and after gas communication testing was completed.

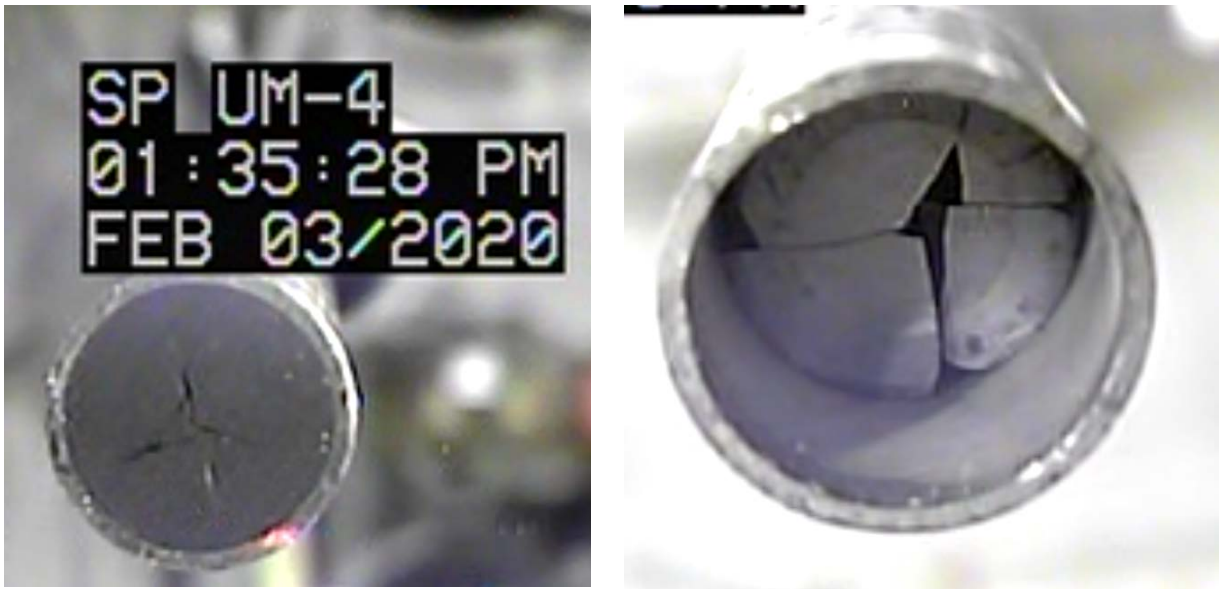

(a) End of UM-4 Before Testing Started (b) End of UM-4 After Testing was Completed

Figure 2-12. Image of End of Segment UM-4 before (a) and after (b) Gas Communication Testing.

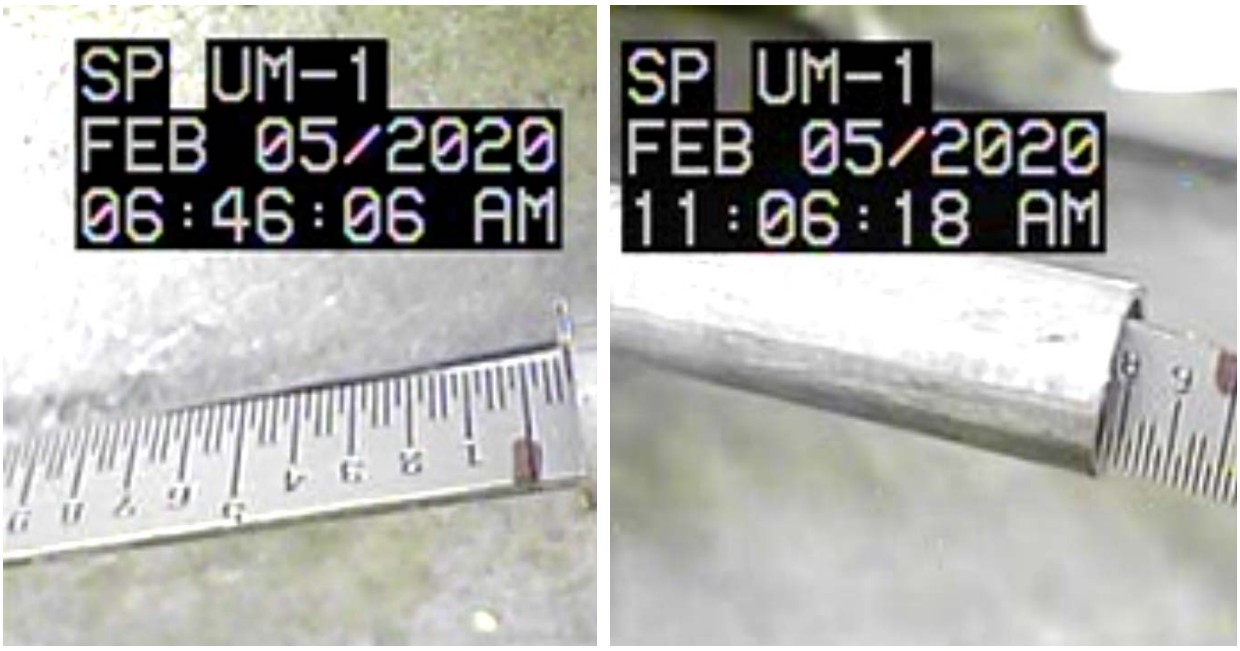

(a) Plenum Measurement Before Testing (b) Plenum Depth Measurement After Testing

Figure 2-13. Plenum Measurements of UM-1 Before (a) and After (b) Gas Communication Testing.

2.5 Summary

The hydraulic resistance of segments cut from five SNF sibling pins—rods F35K13, 5K7K9, 5K7P2, 6U3L8, and 6U3M3 (abbreviated to FK, KK, KP, UL, and UM, respectively)—was evaluated using gas communication and rod puncture data collected during testing in CY 2018 and CY 2019/2020. Interpreted using a single hydraulic flow channel, testing found SNF hydraulic diameters that spanned 70.7 to 97.6 µm. Of the observed variation in hydraulic diameter, the large differences (on the order of 30 µm) were observed when comparing individual rods to one another: rod FK (Zircaloy-4) showed the largest hydraulic diameter, rods UL and UM (both ZIRLO rods) showed the smallest diameters, and those for rods KK and KP (both M5 rods) fell in between those of Zircaloy-4 and ZIRLO rods. Smaller variation in hydraulic diameter, approximately 17 µm on average, was observed along the lengths of the fuel rods. Here, the middle two rod segments typically showed the smallest diameter and greatest hydraulic resistance to gas flow. On average, the third rod segment (which typically spans 1000 to 2000 mm from the bottom of the rod) is the most resistive to gas flow. It is postulated that increased resistivity in Segment 3 arose from the combination of high local burnup and higher lithostatic load borne by the bottom rod segments. Variation in hydraulic diameter with test pressure was small (below 2 µm) and generally fell within the range expected for nominal expansion of the cladding under pressure. Current testing largely (but not conclusively) suggests that the gas communication methodology applied herein does not significantly alter the hydraulic properties of the fuel. In particular, rod puncture data collected from “pristine” (untested) rods found largely equivalent diameters (within 2 to 5 µm) for three of the five rods tested.

3. SECTIONING OF SISTER ROD SEGMENTS

Previously, the sibling pins were cut into four segments (quarters) and the top and bottom closures (plugs) cut from the rods as documented in Shimskey et al. (2019a). Except for rod F35/K13, the rods were segmented starting at the top of the rod. A custom block with a tolerance of ±0.005 in. (~±0.13 mm) was fabricated for each rod based on the rod lengths reported by ORNL (Montgomery et al. 2018). By butting the rod up to its custom block, securing it in place, and making the cut, each of the first segments of the same cladding type was segmented such that the bottom of each segment was virtually the same height from the bottom of the rod. Repeated mock-up testing showed cut location accuracy to be ±1/16 in. (±1.6 mm). A similar process guaranteed that Segment 2 of each cladding type was the same length from the same location relative to the bottom of the rod. This was repeated for Segment 3 of each cladding type. The remaining length, Segment 4, was the remainder of the rod including the end plug. The length of Segment 4 for all rods of the same cladding type was the same length within the ±1/16 in. (±1.6 mm) accuracy. Segment 1 for each rod then had the upper approximately 1.5 in. (~38 mm) cut to remove the top plug and the puncture hole and to remove the hold down spring. The end plugs were then cut from the bottom of Segment 4 based on estimated lengths provided by the ORNL gamma scans (Montgomery et al. 2018). Figure 3-1 is an example of the cut diagram for 6U3/L8 (UL) used to design the blocks, but the end plug lengths were assumed and rounded to the nearest 0.5 in. (~13 mm).

After gas communication testing was completed, the modifications for the saw were installed, inside the cell, to convert the saw to cutting subsamples from the pin segments. After installation, the modified cutting system was functional tested with a section of as-manufactured Zircaloy cladding to confirm operation. Once the system was deemed operational, the 20 segments from the five of the sibling pins used for gas communication testing in Section 2 were sectioned into individual samples, following a prescribed cut plan, to compare physical properties of the pin at different axial locations.

3.1 Sectioning Equipment

After gas communication testing, the segmenting saw was modified to section each segment into samples for testing. As seen in Figure 3-1, the samples ranged from ~0.5 in. (~13 mm) for PIE (metallography including optical microscopy, microhardness, LECO total hydrogen analysis, and scanning electron microscopy as necessary) to ~6 in. (~152 mm) physical property (axial tube tensile, four-point bend, and burst) testing. Each of the five rods under the Phase 1 test plan (Saltzstein et al. 2018) was sectioned.

The sectioning saw was constructed by modifying the custom segmenting saw used previously. An isometric drawing of the assembled system is shown in Figure 3-2. The drawing shows the original cut saw with a shorter strong-back and now incorporating a notching saw used to mark the axial and radial position of each cut sample on the parent rod. The cutting saw uses a 5 in. diameter × 0.020 in. thick Buehler diamond wafering blade attached to a 24 VDC (volts direct current) motor. Except for the saw motor, the saw assembly was entirely mechanical and used machined physical stops and spacers to position the fuel rods as required to cut them into pre-determined segment lengths. The accuracy of the desired cut lengths was verified during remote operational testing using the hot cell manipulator mock-up with simulated spent fuel test articles (composed of stainless-steel tubing with ceramic inserts). All required lengths were verified by the quality engineer and conformed to the design standard of ±1/16 in. (±1.6 mm). Measurements taken during dry runs identified the thickness of each cut (kerf) ranges from 0.022 to 0.024 in. (0.6 mm), which is considered for the sectioning cutting plan.

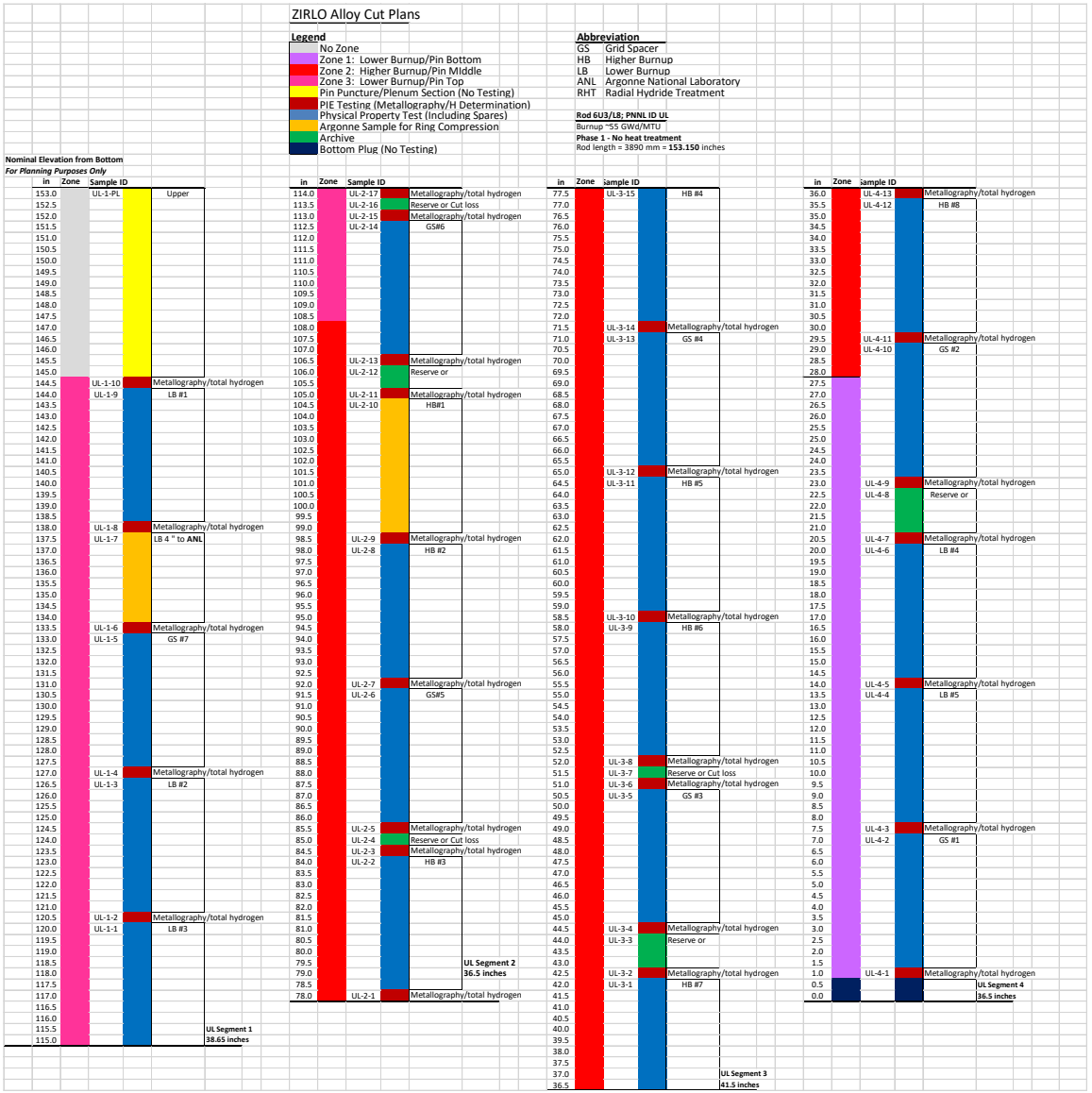

Figure 3-1. Segmenting Planning Diagram for Rod 6U3/L8.

Key features of the sectioning saw include:

- The saw assembly is mounted on jack stands to align the saw and rod supports (strong-back). This minimized flexing of the fuel rod.
- The force of the sawing is controlled by hanging weights on a cable that is connected to the saw and routed over a pulley. Different weights could be selected to provide the force that provided the best cut.
- The saw speed (including on/off functions) is controlled remotely from outside the hot cell and the saw motor is powered by 24 VDC to minimize electrical hazards to the manipulator operators.
- Machined physical stops and spacers were used to position the rod in the correct location for the cut for samples ranging a nominal length of 0.5 in. (~13 mm) up to 6 in. (~152 mm). The lengths of the stop block were established for the cut blade kerf to be split between the sample and the segment, so the length of each sample is slightly under the nominal length. Figure 3-3 provides isometric drawings of the 0.5 in. and 6-in. sample blocks and how they looked installed on the saw frame during cutting operation in cell.
- Water was used as the cutting fluid as shown in Figure 3-4. The bottom of the saw blade was submerged in a small tub of water and the rotation of the wetted blade carried the water to the cut location. The saw was designed with features that were effective in capturing and channeling most of the water back into the tub. The basin also collects the cutting fines and stores them wet for easy disposal afterward.
- The notching saw uses a similar DC motor and the same size and type diamond blade. Once the stop blocks are removed, the cut segment or sample can be moved into the tip of the notching blade to mark the axial and circumferential position of the sample as shown in Figure 3-5. The cutting of the notch is performed dry leaving a partial cut through the cladding wall that does not reach the fuel, as shown in Figure 3-6.

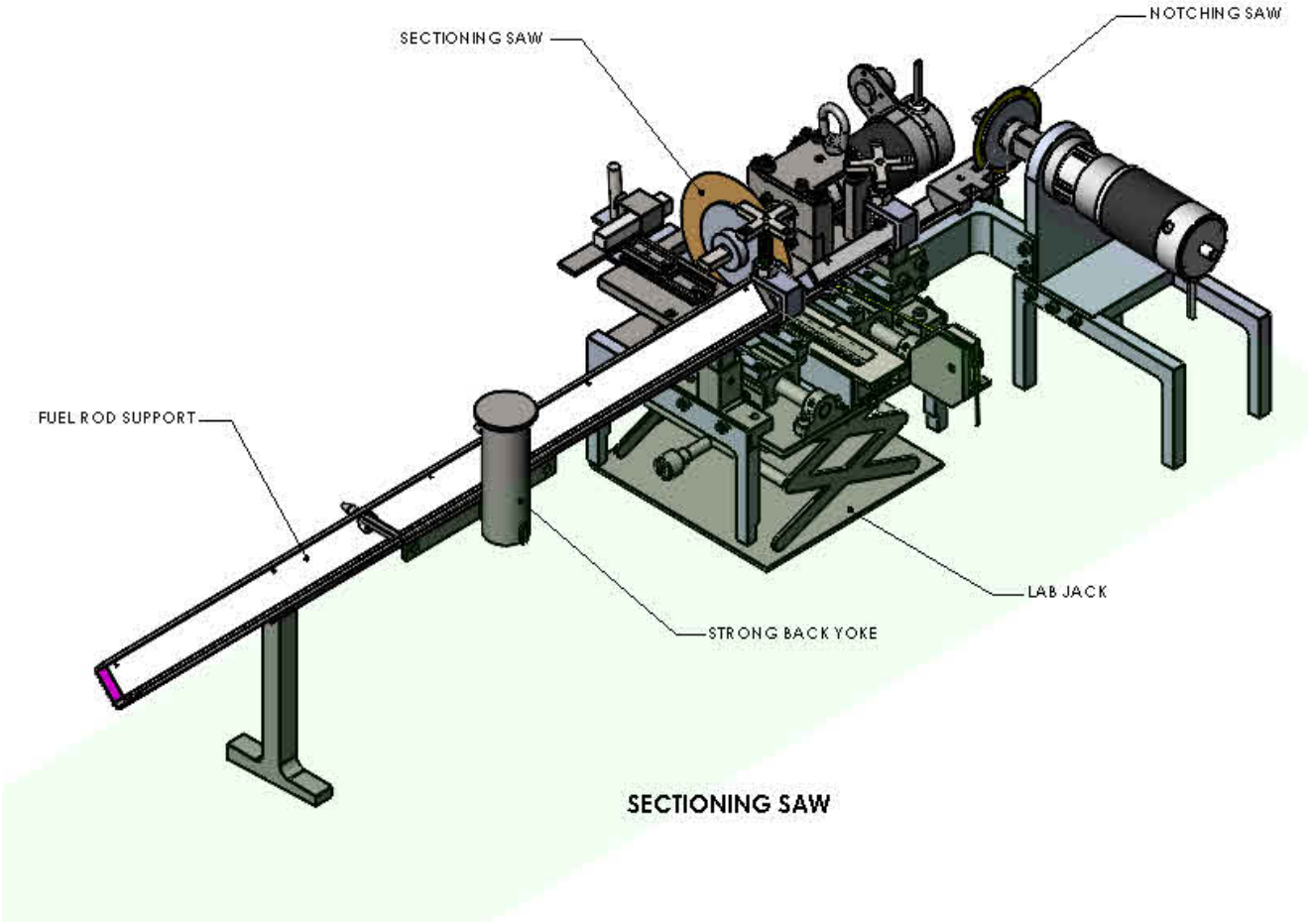

Figure 3-2. Sectioning Saw Assembly.

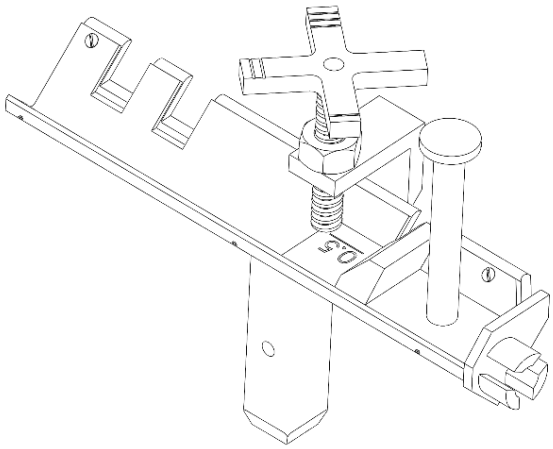

CUT LENGTH: 0.5 in.

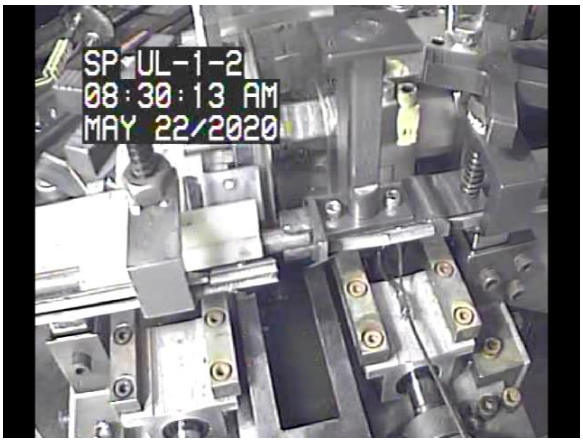

CUT LENGTH: 0.5 in.

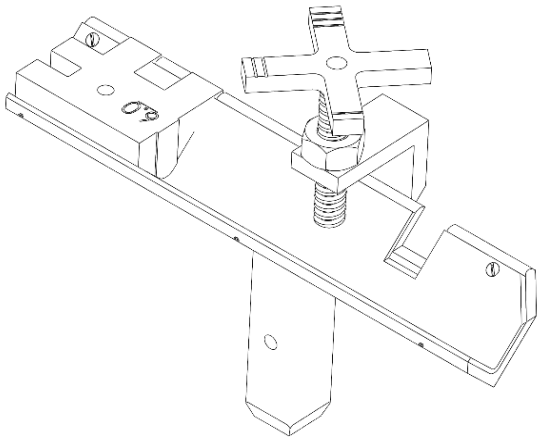

CUT LENGTH: 6.0 in.

CUT LENGTH: 6.0 in.

Figure 3-3. Examples of Common Blocks Used.

Figure 3-4. Sectioning Saw Water Basin used to Wet the Cutting Blade and Collect Cutting Fines.

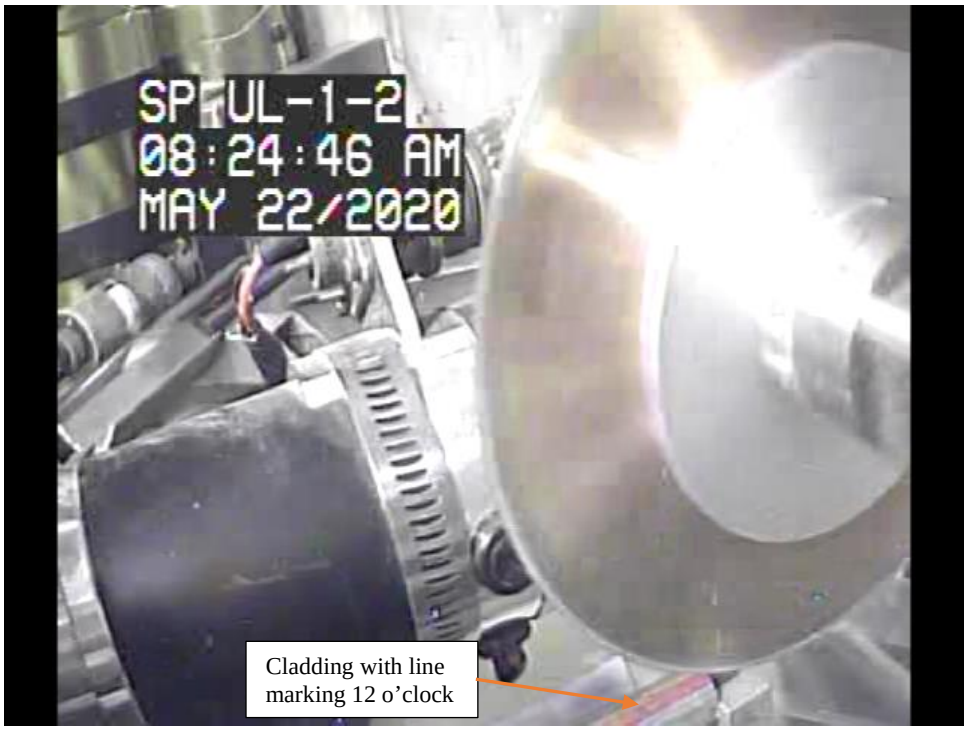

Figure 3-5. Notching Saw Marking Segment UL-1 before Cutting Sample UL-1-2.

Figure 3-6. Image of Notch Mark on Sample UL-1-1.

3.2 Sectioning Procedure and Maintaining Orientation

During the initial segmenting of the pin, markings were applied to indicate the orientation of each segment before cutting as discussed in Shimskey et al. (2019a). With the rod secured on the saw, an orange paint pen applied a lateral mark on the pin segment indicating the side where the puncture occurred (Figure 3-7a) and was considered 12 o'clock. Afterward, a white paint pen applied a dot on the end of the segment closest to the top of the pin (Figure 3-7b). Once the markings were independently verified, the segment was then cut and placed into storage.

For each of the 20 segments used for gas communication, an approved cutting plan was established for each segment to subsample the segments using the gauge blocks described in Section 3.1 and into nominal lengths varying between 0.5 to 6 in. (Appendix D). Cutting operations started from the bottom end of each segment with the axial white mark on the opposite end and with the orange lateral mark facing up as shown in Figure 3-7. Before cutting, the bottom of the segment was notched to match the location of the orange lateral mark. Once the notch was made and verified, the segment was pulled back and the prescribed gauge block was installed as directed by the cut plan. Once the block was installed, the notched segment was pushed into the block and secured in place. Once secured, the saw blade was energized, and weight was applied to the pulley to pull the cutting blade into the segment. After the cut was made, the notch on the sample was re-examined and placed into storage. This process was repeated until the final sample was cut from the segment and its length verified.

(a) Orange Lateral Mark on Segment UL-2 (b) White Axial Mark on Segment UL-2

Figure 3-7. Paint Markings on Segment Indicating Position.

3.3 Sectioning Results

As discussed in Shimskey et al. (2019a), the sibling pins were quartered into four segments before being sectioned into multiple samples. Samples were uniquely identified from a segment cutting diagram such as in Figure 3-1. Appendix D shows the cutting diagrams for each of the five rods included in Phase 1 testing. Using blocks as a cutting aid in the hot cells resulted in low variability of sample lengths, minimized user error in the cutting process, and allowed for calculations to predict the top and bottom positions of each sample and overall segment within ±0.079 in. (±2 mm).

This same approach was used with sectioning, using stop blocks to cut samples to repeatable lengths that were within ±0.0079 in. (± 0.2 mm) of each other. This minimal error results in the location of each sample (section) relative to the bottom of the fuel rod to have the same accuracy as the location for the original segment (within ±0.079 in. or ±2 mm). Tables showing the starting and ending locations relative to the bottom of the rod for each sample are given in Appendix D. Cut losses and uncertainty associated with the saw kerf (<0.024 in. or <0.6 mm) were accounted for when determining sample length and location.

4. FUEL DISSOLUTION

As outlined in Saltzstein et al. (2018), PNNL is performing destructive testing on defueled cladding. To support this activity, equipment has been fabricated to perform this task and a process developed to remove the fuel and decontaminate it sufficiently to work with the samples outside of the hot cell.

Section 4.1 describes the dissolution system and provides a general processing overview for the dissolution of fuel from 10 fuel rods delivered to the hot cells in the High-Level Radiochemistry Facility (HLRF) at the PNNL Radiochemical Processing Laboratory (see Shimskey et al. 2019a). Section 4.2 provides more details on how the dissolutions were conducted. Section 4.3 describes the equipment used to measure the cladding outside diameter (d_o) and inside diameter (d_i) and measurement results. Section 4.4 provides dose measurements of two cladding samples selected to estimate worker dose during handling of irradiated cladding samples outside the hot cell.

4.1 Dissolution Apparatus and Processing Overview

A fuel dissolution system was designed and fabricated as depicted in Figure 4-1 through Figure 4-3. The system includes a ~1-liter dissolution vessel (8.5 in. × 3.65 in. × 4.0 in., width, depth, height [WDH]) machined out of 304L stainless steel (SS). Attached to the dissolution vessel are two 8 in. Watlow SGA1J8AO9 400-W strip heaters for elevated temperature dissolution. A temperature controller with overtemperature protection is used to control the temperature during dissolution.

The dissolution vessel is sized to dissolve up to four 6 in. fuel rod samples (or equivalent) in one batch. A SS basket, which holds fuel cladding samples between 0.5 and 6 in. long, is placed inside the dissolution vessel. The basket holds the fuel samples in specific locations and maintains configuration control during the dissolution process. A photograph of the basket is shown in Figure 4-3.

The dissolution vessel is mounted on a scissor jack stand that has approximately 6 in. of vertical travel. The jack stand is mounted on a SS sliding drawer, which provides approximately 6 in. of horizontal travel. With the jack stand lowered and the drawer slid into the forward position, the basket holding the fuel rods can be placed into the dissolution vessel. Once loaded, the dissolution vessel is slid back to the rear position and the jack stand is raised to contact a 0.25-in.-thick stationary SS plate, which forms a seal during the dissolution process. Five attachments are mounted to the stationary plate: a thermocouple to monitor temperature, a funnel to add reagents, a sonicator to aid in mixing, and two condensers that are cooled with chill water.

Nitric acid is added to the dissolution vessel through the addition funnel; 6 M HNO_3 was selected as the nominal acid charge based on work done by Johnson and Stone (1980). At this acid concentration and a solution temperature of 100 °C, the corrosion potential of zirconium is 1030 mV vs. the standard hydrogen electrode (SHE), slightly lower than the redox potential of the nitric acid solution at 1070 mV/SHE (Fauvet 2012). This value is within the passivity region of zirconium. Reducing the dissolution temperature below 100 °C reduces the potential for zirconium corrosion. This initial acid charge should provide adequate excess nitric acid to prevent the formation of insoluble plutonium products. The dissolution follows these formulas:

$$UO_2 + 2.7\ HNO_3 \rightarrow UO_2(NO_3)_2 + 0.7\ NO + 1.35\ H_2O \quad (4\text{-}1)$$

$$UO_2 + 4\ HNO_3 \rightarrow UO_2(NO_3)_2 + 2\ NO_2 + 2\ H_2O \quad (4\text{-}2)$$

where reaction 4-1 occurs predominantly at lower acid concentrations and reaction 4-2 occurs at acid concentrations greater than 8 M.

The dissolution vessel is maintained under slight vacuum (via an air-operated venturi vacuum system) and off-gas (calculated to not exceed 1 liter/min) is drawn from the dissolution vessel through the off-gas

system to reduce the acid vapors in the hot cell. The off-gas system is composed of a condenser, condensate knockout pot, two NaOH scrubbers, and silica gel to adsorb NO_2.

When dissolution is complete, the dissolved fuel is drained from the dissolution vessel directly into a 1-liter SS container (Eagle Stainless Model BTB-10 316L SS 1L) for safe storage until disposal. The fuel cladding undergoes two additional cleanup steps to help remove fuel residue and reduce cladding dose to workers.

In the leach step, the cladding is contacted with fresh nitric acid for one hour. The leachate is subsequently drained and stored for dissolution of the next batch. The final step is a rinse with 1 M HNO_3. Both steps take place with sonication.

The final rinse step is performed using a clean basket and glass cylinder that have never been exposed to concentrated dissolution or leach solution. The cladding in the rinse solution is sonicated for ~1 hour. A photograph of this basket and graduated cylinder is shown in Figure 4-4. The dissolution, leach, and rinse steps occur as indicated in Figure 4-5. Such a process helps to reduce liquid waste volume in the hot cell while producing clean cladding.

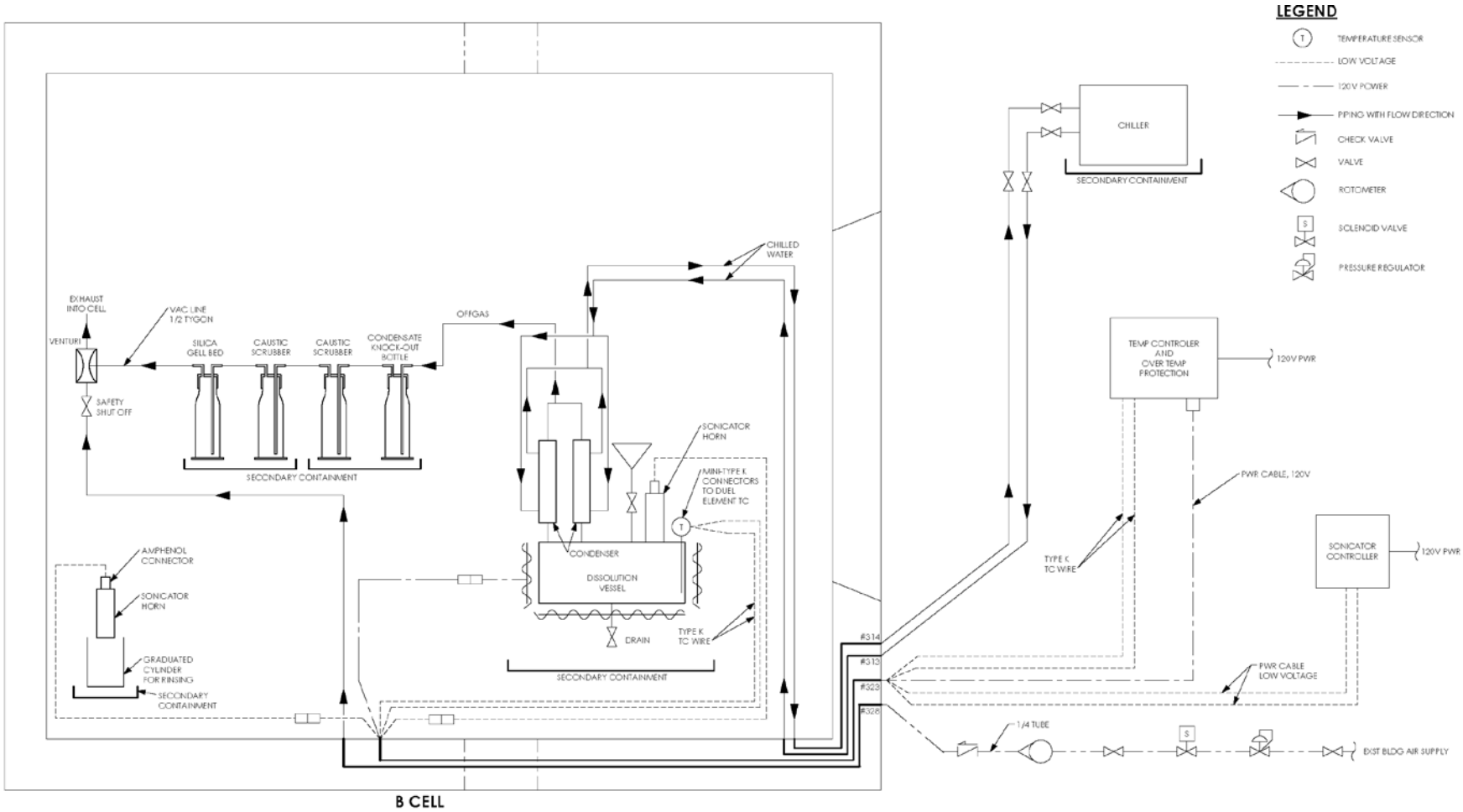

Figure 4-1. Simplified Dissolution System Piping and Instrumentation Diagram.

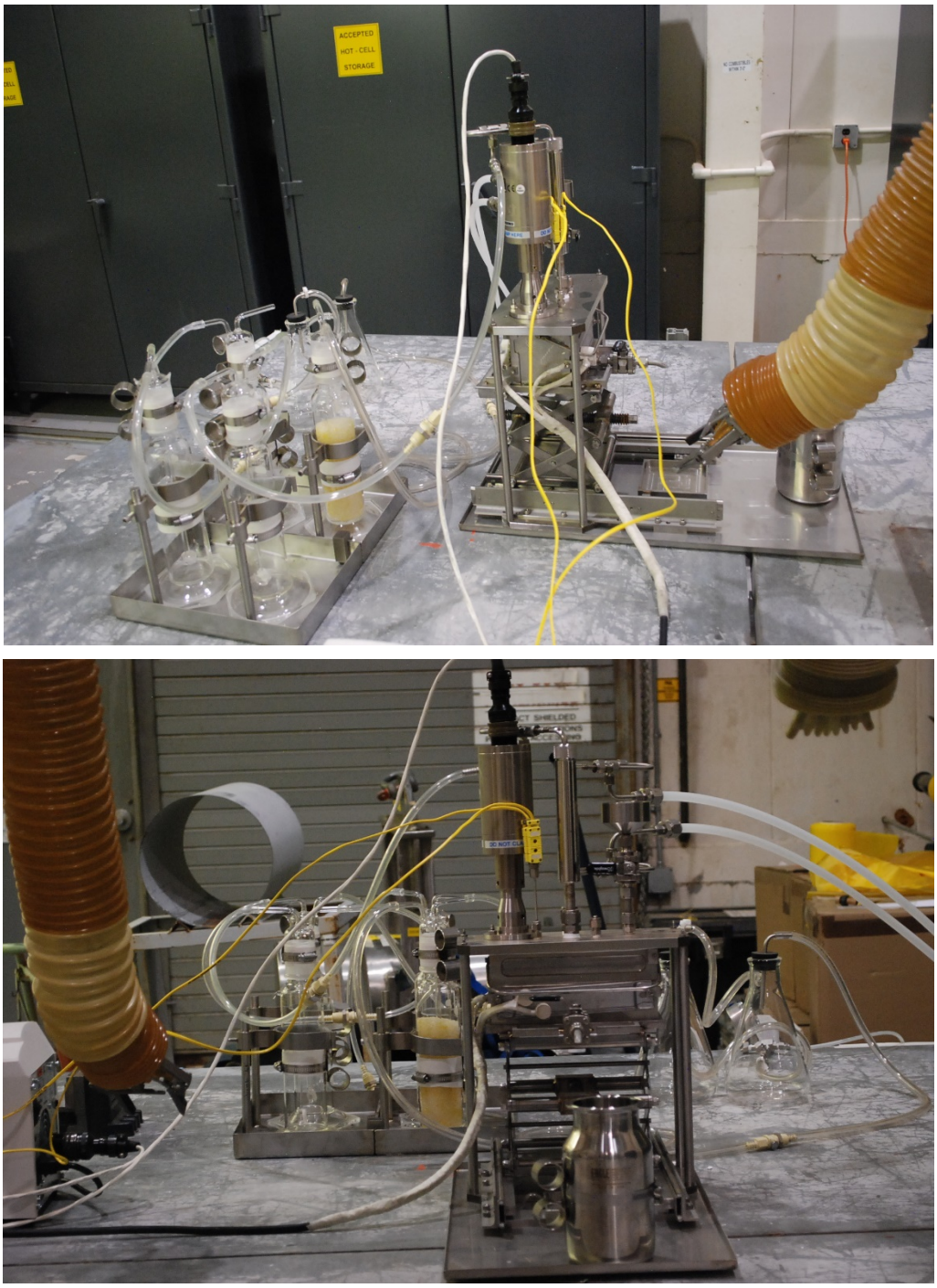

Figure 4-2. Photos of Dissolution System. Top: Side View; Bottom: Front View

Figure 4-3. Dissolution Basket.

Note: Samples 0.5 in. long are placed vertically in the 12 available cylindrical slots. Longer samples are placed horizontally (10° incline) and there are four available positions. SS Tubing (3/8 in. diameter × 6 in. long) is shown in one of the horizontal positions.

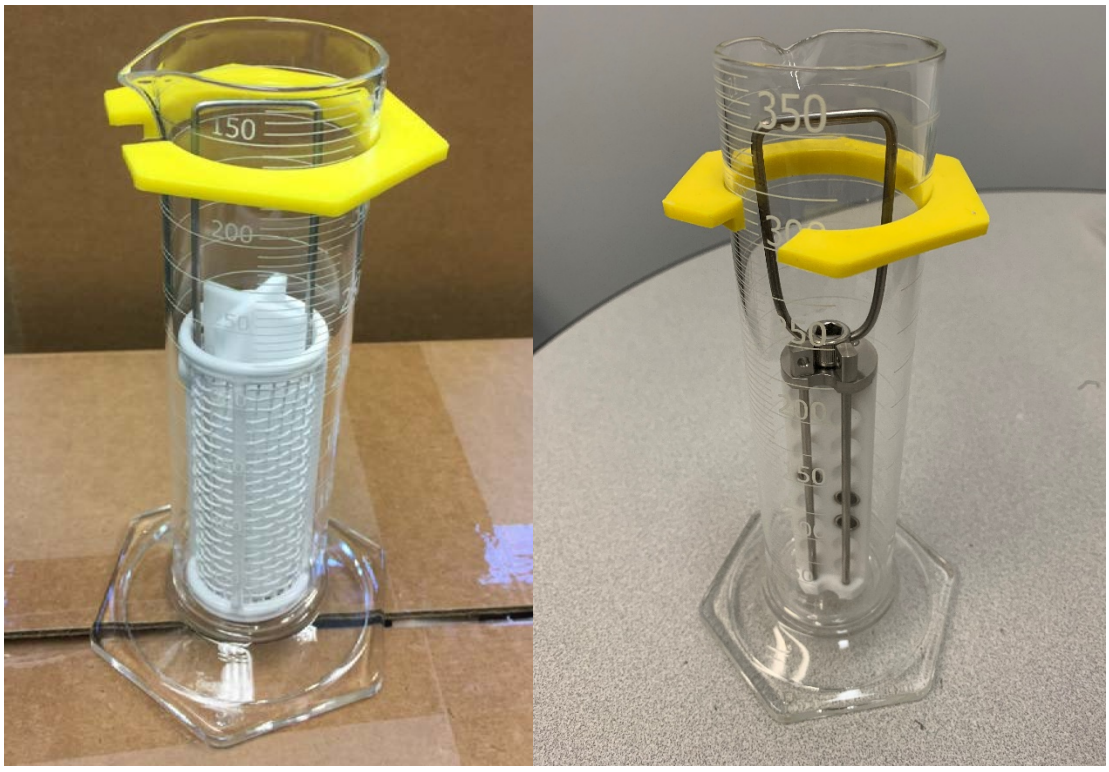

Figure 4-4. Rinse Basket and Rinse Cylinder.

Note: Left: Up to four 6 in. cladding pieces are placed between the dividers in the basket. (Cladding pieces are notched to maintain configuration control). Right: Half-inch cladding samples are placed in a jig, in which positions are uniquely numbered to maintain configuration control. A sonicator horn is lowered into the rinse solution and run for ~1 hour.

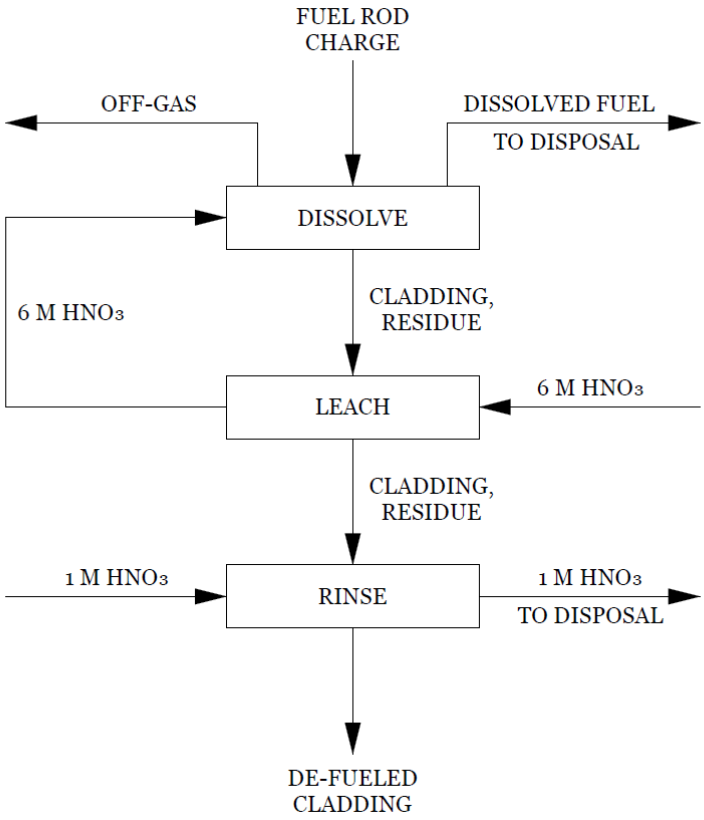

Figure 4-5. Batch Dissolution Flowsheet. (nominal acid molarity is shown)

4.2 Dissolution Evolutions

The dissolution of each fuel rod was performed in six batches. Dissolution conditions are provided in Table 4-1. Photographs of the dissolution process in the hot cell are shown in Figure 4-6 through Figure 4-9.

The steps used to dissolve a single batch of fuel from the cladding and subsequent cleaning of the cladding batch (dissolution, leach, and rinse steps) are outlined below:

1. Samples designated for dissolution were staged for processing.
2. One-by-one and sequentially, the following actions were taken:
   a. The sample was removed from its individually labeled storage container.
   b. The sample was weighed.[j,k] Weights before and after dissolution are provided in Table 4-2.
   c. For 6 in long samples only: the d_o of the sample was measured with the optical micrometer.[l]
   d. The sample was placed in a designated location in the dissolution basket to maintain configuration control.

[j] Daily checks of the balances were conducted using calibrated weight standards.

[k] The high dose in the hot cell rendered the balance nonfunctional after five days. Because of this, weighing the samples was discontinued.

[l] Daily checks of the optical micrometer were conducted with calibrated ring gauge standards.

3. After all samples were loaded, the dissolution basket was placed in the dissolver tub and the tub and basket were raised into position using the jack stand.
4. The off-gas system was turned on.
5. The dissolution acid was added to the dissolution tub, and the solution was heated and periodically sonicated.
6. After dissolution was complete, the dissolved fuel was drained into a 1-liter SS container so that the acid would be securely held until disposal (see Figure 4-6).
7. Next, a leach solution of fresh nitric acid was added to the tub and the cladding was contacted with this solution for ~1 hour with periodic sonication.
8. The leach solution was drained (and later used as the dissolution solution for the next batch).
9. The cladding was flushed with 0.1 M NaOH to neutralize the acid and the cladding was allowed to dry.
10. One-by one and sequentially, the following actions were taken:
    a. The cladding sample was removed from the basket; then video and observations were recorded (see Figure 4-7 and Figure 4-8).
    b. The sample was weighed.
    c. For 6 in. cladding samples only: The d_o and d_i were measured using an optical micrometer and an air gauge, respectively.
    d. For 6 in cladding samples only: the sample was deburred.
    e. The cladding was placed in an individually labeled storage capsule.
11. Just before a cladding sample was removed from the hot cell, it was removed from the storage capsule, contacted with 1 M HNO_3, and sonicated. The final rinse step was performed in a clean basket and glass cylinder never been exposed to concentrated dissolution or leach solution. A photograph of a sample basket and a graduated cylinder is shown in Figure 4-4 and Figure 4-9.

Dissolution of each fuel rod was conducted in six batches. Note that some samples from each rod were not dissolved but were held in reserve. (See Appendix D for tables identifying sample identification and test assignment.) Table 4-1 provides the dissolution conditions for the 14 batches that were completed in fiscal year 2020 (all samples designated for dissolution from rods UL and KP, and two batches from rod FK). Dissolution times varied from 26 hours to 98 hours. The dissolution system had no capability to monitor the extent of dissolution in real time, so the times of dissolution listed have a “less than” sign included and indicate when the batch was visually inspected. We generally found that either end of the rod dissolved faster than the middle.

Figure 4-6. Dissolution Solution Draining from Dissolver Tub at the Conclusion of Dissolution (UL Batch 3).

Note: The SS container shown was used to store the dissolved fuel until the grouting process.

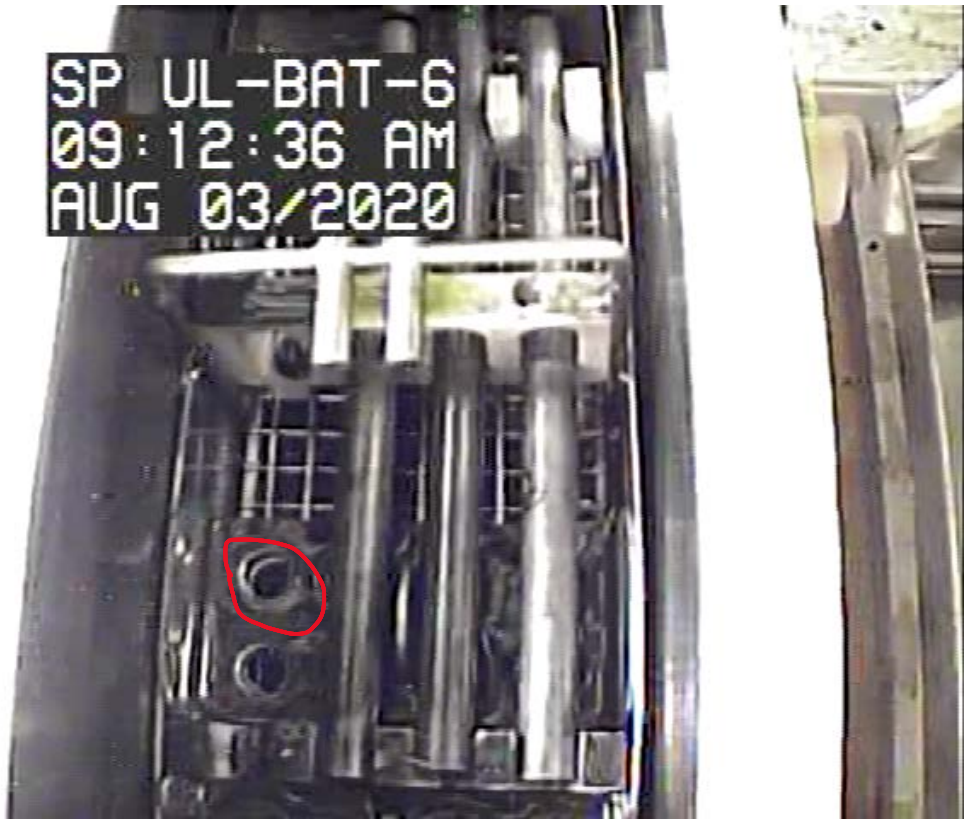

Figure 4-7. UL Batch 6 After Dissolution.
Note: Batch 6 comprised three 6 in. long samples and twelve 0.5 in. samples. One of the 0.5 in. cladding samples is visible under the sample holder and is circled in red. Each cladding piece is placed in a specified location to maintain configuration control.

Figure 4-8. KP Batch 10 After Dissolution, Looking Down the Barrel of a 6 in. Long Cladding Section After Leaching. (left and right).

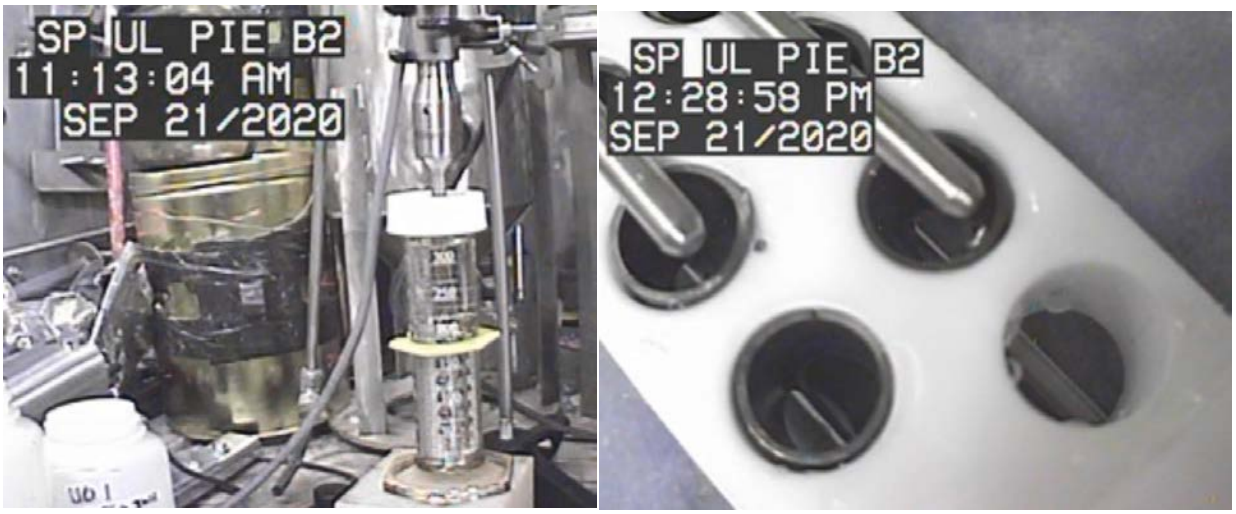

Figure 4-9. Final Rinse of 11 Samples of 1/2 in. Cladding from Rod UL.
Note: (Left) Cladding is held in jig inside a graduated cylinder with a sonicator horn at top. The white cap on top of the graduated cylinder helps keep the system clean. (Right) After final rinse.

Table 4-1. Dissolution Conditions.

	Rod UL						Rod KP						Rod FK	
	Batch 1	Batch 2	Batch 3	Batch 4	Batch 5	Batch 6	Batch 7	Batch 8	Batch 9	Batch 10	Batch 11	Batch 12	Batch 13	Batch 14
Total Fuel Charge (in.)	18	18	18	24	24	24	22	21	20.5	20.5	20.5	20.5	21.36	22
Oxide Fuel Charge (g)	248.0	248.0	248.0	330.6	330.6	330.6	303.1	289.3	282.4	282.4	282.4	282.4	294.3	303.1
Initial Acid Concentration, M	4.8	6.0	6.0	6.4	6.4	6.4	6.5	6.5	6.5	6.5	6.5	6.5	7.6	6.5
Solution Volume, L	0.85	0.85	0.85	0.95	0.95	0.95	0.89	0.89	0.88	0.88	0.88	0.88	0.85	0.88
Final Acid Concentration, M	3.0	3.2	3.2	3.1	3.1	3.1	3.3	3.4	3.5	3.5	3.5	3.5	4.3	3.3
Uranium Concentration, g/L	243	243	243	290	290	290	284	271	267	267	267	267	288	287
Heating Set Point, °C	65	65	65	65	65	65	65	65	65	65	65	65	65	65
Time of Dissolution, hr	<26	<51	<69	<68	<68	<98	<66	<97	<65	<93	<41	<47	<42	<42

Table 4-2 proves available masses measured before and after dissolution. Note that because the radiation dose rate in the hot cell was high, the balance was nonfunctional after five days. As a result, obtaining sample weights was discontinued.

Table 4-2. UL-1 Sample Weights.

Sample ID	Sample Length Dissolved (inches)	Mass before Dissolution (grams)	Mass after Dissolution and Leach (grams)	Mass of Fuel Dissolved (grams)	Mass of Fuel per inch of sample g/inch	Fuel Density** g/cc
UL-3-1	6	98.42	15.90	82.52	13.75	10.06
UL-1-1	6	98.23	15.97	82.26	13.71	10.03
UL-1-2	0.5	7.88	1.29	6.59	13.18	9.64*
UL-1-3	6	98.47	N/A	N/A	N/A	N/A
UL-1-4	0.5	8.19	1.33	6.86	13.72	10.03
UL-1-6	0.5	8.19	1.33	6.86	13.72	10.03
UL-1-7	4	65.53	10.65	54.88	13.72	10.03
UL-1-8	0.5	8.17	1.33	6.84	13.68	10.00
UL-1-9	6	98.53	N/A	N/A	N/A	N/A
Average						10.03

**Not used in average; it is suspected that a small amount of fuel fell out of the cladding during sample cutting.*

***Calculated based on average d_i of 8.2791 mm.*

N/A - High radiation dose in the hot cell rendered the balance nonfunctional after five days. As a result, weighing samples was discontinued.

4.3 Cladding d_o and d_i Measurements

Cladding d_o measurements were taken with a Keyence optical micrometer (model LS-9030) installed in the hot cell.[m] The manufacturer-stated precision of the optical micrometer is ±2 µm[n]. Cladding d_i measurements were taken with a Western Gage Corp. air gauge (Model AEQ-42-11-10) that has a manufacturer-stated precision of ±0.00005 in. (1 µm). These measurements were made on 6 in. long cladding samples only.

A pneumatically operated sled, shown in Figure 4-10, was used to mount the cladding and take d_o measurements. The sled moved the cladding across the optical micrometer's field of view and measurements were taken during motion in both directions. The cladding was then rotated 90 degrees, using the notch cut into the top of the cladding as an orientation guide, and the measurements were repeated. d_o in both directions and both radial orientations are averaged together and reported in Table 4-3 and Table 4-4. The averages reported are based on approximately 40 measurements for UL cladding samples. The sample frequency was increased, and the FK sample averages are based on approximately 400 measurements per 6 in. sample. The jig used to hold the cladding in the sled (see Figure 4.10) prevented measuring the ends of the cladding, so measurement of possible cutting burrs was not an issue. The standard deviation reported in Table 4-3 and 4-4 are one standard deviation of the mean.

The team had also planned to use the pneumatically operated sled for cladding d_i measurements with the air gauge. However, the clamp that held the cladding in place caused a slight deformation of the cladding and the practice was abandoned. The project settled on taking d_i measurements at 1, 3, and 5 in. axial locations; averages of these three d_i measurements are reported. Daily checks of the optical micrometer were performed with pin gauge standards. The air gauge was user calibrated prior to each use with standard ring gauges. Post calibration checks indicated that measurements fell within ± 1 µm of standards.

Table 4-3 and Table 4-4 provide average d_o and d_i measurement results for rods UL and KP, respectively. The tables relate the axial position of the rod to the sample ID. The tables include average ORNL d_o measurements (with the rod pressurized before puncture) obtained from Montgomery et al. (2018). Also included in the tables are the PNNL average d_o measurements of samples before and after dissolution, as well as average d_i measurements taken after dissolution. Only 6 in. long samples were measured by PNNL.

[m] The high dose in the hot cell limited the life span of the optical micrometer to approximately one month.

[n] Uncertainty based on measurements taken in the hot cell was higher as discussed in text below.

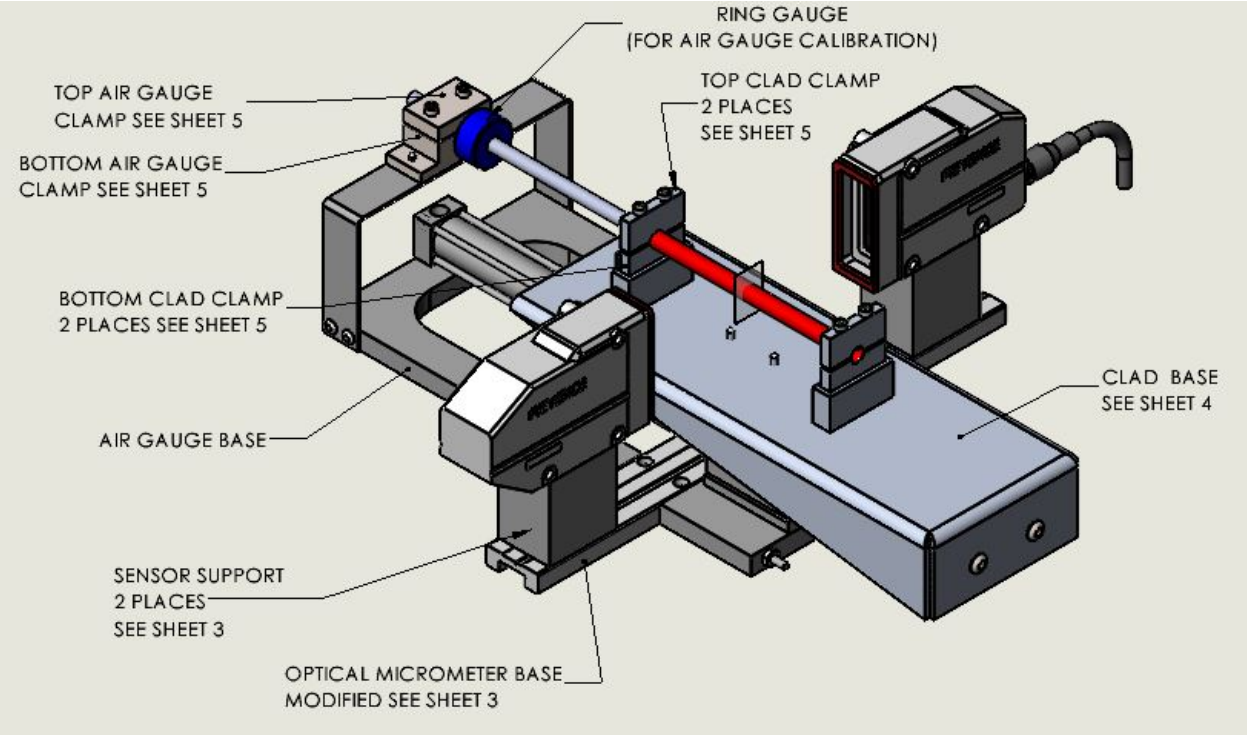

Figure 4-10. Schematic and Photo of the Pneumatically Operated Sled Used for OD Measurements in the Hot Cell.

Note: The air gauge is mounted on the upper left side. Cladding mounted on the sled in the photo is a surrogate.

Table 4-3. Rod UL d_o and d_i Measurements.

SECTIONING	SECTIONING	SECTIONING	SECTIONING	SECTIONING	ORNL NDA	ORNL NDA	PNNL NDA	PNNL NDA	PNNL NDA	PNNL NDA	PNNL NDA	PNNL NDA
Sample Length (in.)	Test	Sample ID	Bottom Position (mm)	Top Position (mm)	Avg d_o Measure (mm)	STD d_o Measure (mm)	Avg d_o Measure before fuel dissolution (mm)	STD d_o Measure (mm)	Avg d_o Measure after fuel dissolution (mm)	STD d_o Measure (mm)	Avg d_i Measure after fuel dissolution (mm)	STD d_i Measure (mm)
		UL-1										
6.6	PUNCTURE	UL-1-PL	3683	3852								
0.5	PIE	UL-1-10	3671	3683								
6.0	BEND 25°C	UL-1-9	3518	3670	9.4293	0.0045	9.4303	0.0092	9.4240	0.0078	8.2639	0.0018
0.5	PIE	UL-1-8	3505	3518								
4.0	ANL	UL-1-7	3404	3505	9.4408	0.0047	NA	NA	NA	NA	NA	NA
0.5	PIE	UL-1-6	3391	3403								
6.0	SPARE	UL-1-5	3239	3391								
0.5	PIE	UL-1-4	3226	3238								
6.0	BURST 25°C	UL-1-3	3074	3225	9.4547	0.0041	9.4610	0.0046	9.4455	0.0029	8.2760	0.0007
0.5	PIE	UL-1-2	3061	3073								
6.0	BURST 200°C	UL-1-1	2909	3060	9.4574	0.0032	9.4550	0.0055	9.4494	0.0049	8.2715	0.0000
		UL-2										
0.5	PIE	UL-2-17	2896	2908								
0.5	ARCHIVE	UL-2-16	2883	2895								
0.5	PIE	UL-2-15	2870	2883								
6.0	TENSILE 25°C	UL-2-14	2717	2870	9.4492	0.0053	9.4539	0.0087	9.4409	0.0034	8.2736	0.0007
0.5	PIE	UL-2-13	2705	2717								
1.0	ARCHIVE	UL-2-12	2679	2704								
0.5	PIE	UL-2-11	2667	2679								
6.0	ANL	UL-2-10	2514	2666	9.4524	0.0025	9.4616	0.0122	9.4455	0.0028	8.2812	0.0019
0.5	PIE	UL-2-9	2502	2514								
6.0	SPARE	UL-2-8	2349	2501								
0.5	PIE	UL-2-7	2336	2349								
6.0	TENSILE 25°C	UL-2-6	2184	2336	9.4456	0.0051	9.4439	0.0052	9.4368	0.0041	8.2798	0.0050
0.5	PIE	UL-2-5	2171	2183								
0.5	ARCHIVE	UL-2-4	2159	2171								
0.5	PIE	UL-2-3	2146	2158								
6.0	TENSILE 25°C	UL-2-2	1994	2145	9.4501	0.0031	9.4446	0.0027	9.4404	0.0029	8.2820	0.0006
0.5	PIE	UL-2-1	1981	1993								

Note: ORNL d_o measurements are on pressurized rods prior to puncture. PNNL d_o measurements are on rod segments after the rod was punctured and sectioned, first before the fuel was dissolved and then after.

Table 4-3. Rod UL d_o and d_i Measurements (continued).

SECTIONING	SECTIONING	SECTIONING	SECTIONING	SECTIONING	ORNL NDA	ORNL NDA	PNNL NDA	PNNL NDA	PNNL NDA	PNNL NDA	PNNL NDA	PNNL NDA
Sample Length (in.)	Test	Sample ID	Bottom Position (mm)	Top Position (mm)	Avg d_o Measure (mm)	STD d_o Measure (mm)	Avg d_o Measure before fuel dissolution (mm)	STD d_o Measure (mm)	Avg d_o Measure after fuel dissolution (mm)	STD d_o Measure (mm)	Avg d_i Measure after fuel dissolution (mm)	STD d_i Measure (mm)
		UL-3										
6.0	TENSILE 200°C	UL-3-15	1828	1980	9.4423	0.0031	9.4448	0.0023	9.4426	0.0085	8.2800	0.0032
0.5	PIE	UL-3-14	1815	1827								
6.0	BURST 25°C	UL-3-13	1663	1815	9.4421	0.0050	9.4493	0.0186	9.4365	0.0029	8.2783	0.0019
0.5	PIE	UL-3-12	1650	1662								
6.0	BURST 25°C	UL-3-11	1498	1649	9.4516	0.0045	9.4582	0.0124	9.4460	0.0038	8.2868	0.0025
0.5	PIE	UL-3-10	1485	1497								
6.0	BURST 200°C	UL-3-9	1333	1484	9.4513	0.0039	9.4503	0.0066	9.4414	0.0036	8.2812	0.0007
0.5	PIE	UL-3-8	1320	1332								
0.5	ARCHIVE	UL-3-7	1307	1319								
0.5	PIE	UL-3-6	1294	1307								
6.0	BURST 200°C	UL-3-5	1142	1294	9.4405	0.0055	9.4378	0.0044	9.4337	0.0038	8.2770	0.0029
0.5	PIE	UL-3-4	1129	1141								
1.5	ARCHIVE	UL-3-3	1091	1129								
0.5	PIE	UL-3-2	1079	1091								
6.0	BEND 25°C	UL-3-1	926	1078	9.4426	0.0028	NA	NA	NA	NA	NA	NA
		UL-4										
0.5	PIE	UL-4-13	913	926								
6.0	BEND 200°C	UL-4-12	758	913	9.4390	0.0037	9.4494	0.0124	9.4352	0.0025	8.2821	0.0039
0.5	PIE	UL-4-11	745	757								
6.0	BEND 25°C	UL-4-10	593	744	9.4403	0.0049	9.4447	0.0111	9.4308	0.0031	8.2766	0.0058
0.5	PIE	UL-4-9	580	592								
2.0	ARCHIVE	UL-4-8	529	579								
0.5	PIE	UL-4-7	516	529								
6.0	TENSILE 25°C	UL-4-6	364	516	9.4386	0.0058	9.4425	0.0080	9.4319	0.0057	8.2745	0.0078
0.5	PIE	UL-4-5	351	363								
6.0	TENSILE 200°C	UL-4-4	199	351	9.4283	0.0059	9.4292	0.0070	9.4238	0.0051	8.2669	0.0063
0.5	PIE	UL-4-3	186	198								
6.0	BEND 200°C	UL-4-2	34	186	NA	NA	9.4264	0.0151	9.4258	0.0082	8.2745	0.0085
0.5	PIE	UL-4-1	21	33								

Note: ORNL d_o measurements are on pressurized rods prior to puncture. PNNL d_o measurements are on rod segments after the rod was punctured and sectioned, first before the fuel was dissolved and then after.

Table 4-4. Rod KP d_o and d_i Measurements.

SECTIONING	SECTIONING	SECTIONING	SECTIONING	SECTIONING	ORNL NDA	ORNL NDA	PNNL NDA	PNNL NDA	PNNL NDA	PNNL NDA	PNNL NDA	PNNL NDA
Sample Length (in.)	Test	Sample ID	Bottom Position (mm)	Top Position (mm)	Avg d_o Measure (mm)	STD d_o Measure (mm)	Avg d_o Measure before fuel dissolution (mm)	STD d_o Measure (mm)	Avg d_o Measure after fuel dissolution (mm)	STD d_o Measure (mm)	Avg d_i Measure after fuel dissolution (mm)	STD d_i Measure (mm)
		KP-1										
6.6	PUNCTURE	KP-1-PL	3685	3845								
0.5	PIE	KP-1-10	3672	3684								
6.0	BEND 25°C	KP-1-9	3520	3672	9.4233	0.0099	9.4286	0.0113	9.4197	0.0060	8.2787	0.0258
0.5	PIE	KP-1-8	3507	3519								
4.5	ANL	KP-1-7	3393	3506	9.4244	0.0035	NA	NA	NA	NA	NA	NA
0.5	PIE	KP-1-6	3380	3392								
6.0	SPARE	KP-1-5	3228	3379								
0.5	PIE	KP-1-4	3215	3227								
6.0	BURST 25°C	KP-1-3	3063	3214	9.4540	0.0050	9.4533	0.0049	9.4475	0.0035	8.2948	0.0015
0.5	PIE	KP-1-2	3050	3062								
6.0	BURST 200°C	KP-1-1	2897	3049	9.4522	0.0048	9.4536	0.0064	9.4480	0.0111	8.2986	0.0007
		KP-2										
0.5	PIE	KP-2-16	2885	2897								
0.5	ARCHIVE	KP-2-15	2872	2884								
0.5	PIE	KP-2-14	2859	2871								
6.0	TENSILE 25°C	KP-2-13	2706	2859	9.4445	0.0043	9.4498	0.0062	9.4473	0.0050	8.2959	0.0022
0.5	PIE	KP-2-12	2694	2706								
1.0	ARCHIVE	KP-2-11	2668	2693								
0.5	PIE	KP-2-10	2656	2668								
6.0	ANL	KP-2-9	2503	2655	9.4547	0.0053	9.4544	0.0073	9.4480	0.0033	8.2910	0.0148
0.5	PIE	KP-2-8	2490	2503								
6.0	SPARE	KP-2-7	2338	2490								
0.5	PIE	KP-2-6	2325	2337								
6.0	TENSILE 200°C	KP-2-5	2173	2325	9.4457	0.0097	9.4450	0.0036	9.4435	0.0028	8.2870	0.0092
0.5	PIE	KP-2-4	2160	2172								
0.5	ARCHIVE	KP-2-3	2148	2160								
6.0	TENSILE 25°C	KP-2-2	1995	2147	9.4505	0.0082	9.4518	0.0081	9.4442	0.0019	8.2969	0.0000
0.5	PIE	KP-2-1	1982	1995								

Note: ORNL d_o measurements are on pressurized rods prior to puncture. PNNL d_o measurements are on rod segments after the rod was punctured and sectioned, first before the fuel was dissolved and then after.

Table 4-4. Rod KP d_o and d_i Measurements (continued).

SECTIONING	SECTIONING	SECTIONING	SECTIONING	SECTIONING	ORNL NDA	ORNL NDA	PNNL NDA	PNNL NDA	PNNL NDA	PNNL NDA	PNNL NDA	PNNL NDA
Sample Length (in.)	Test	Sample ID	Bottom Position (mm)	Top Position (mm)	Avg d_o Measure (mm)	STD d_o Measure (mm)	Avg d_o Measure before fuel dissolution (mm)	STD d_o Measure (mm)	Avg d_o Measure after fuel dissolution (mm)	STD d_o Measure (mm)	Avg d_i Measure after fuel dissolution (mm)	STD d_i Measure (mm)
		KP-3										
6.0	TENSILE 200°C	KP-3-14	1829	1982	9.4452	0.0029	9.4477	0.0062	9.4538	0.0047	8.2986	0.0015
0.5	PIE	KP-3-13	1817	1829								
6.0	BURST 25°C	KP-3-12	1664	1816	9.4397	0.0044	NA	NA	9.4477	0.0062	8.2948	0.0039
0.5	PIE	KP-3-11	1652	1664								
6.0	BURST 25°C	KP-3-10	1499	1651	9.4503	0.0046	NA	NA	9.4511	0.0060	8.2978	0.0012
0.5	PIE	KP-3-9	1487	1499								
0.5	ARCHIVE	KP-3-8	1474	1486								
0.5	PIE	KP-3-7	1461	1473								
6.0	BURST 200°C	KP-3-6	1309	1461	9.4540	0.0036	NA	NA	9.4528	0.0058	8.2980	0.0024
0.5	PIE	KP-3-5	1296	1308								
6.0	BURST 200°C	KP-3-4	1144	1295	9.4401	0.0051	9.4494	0.0038	9.4426	0.0058	8.2944	0.0020
0.5	PIE	KP-3-3	1131	1143								
1.0	ARCHIVE	KP-3-2	1106	1130								
6.0	BEND 25°C	KP-3-1	953	1105	9.4498	0.0030	9.4518	0.0025	9.4480	0.0021	8.2999	0.0032
		KP-4										
0.5	PIE	KP-4-13	940	953								
6.0	BEND 200°C	KP-4-12	790	940	9.4525	0.0037	9.4561	0.0077	9.4572	0.0119	8.3018	0.0033
0.5	PIE	KP-4-11	777	789								
6.0	BEND 25°C	KP-4-10	625	777	9.4436	0.0059	9.4505	0.0108	9.4475	0.0096	8.2992	0.0048
0.5	PIE	KP-4-9	612	624								
3.5	ARCHIVE	KP-4-8	523	612								
0.5	PIE	KP-4-7	511	523								
6.0	TENSILE 25°C	KP-4-6	358	510	9.4341	0.0033	9.4550	0.0101	9.4462	0.0070	8.2929	0.0009
0.5	PIE	KP-4-5	345	358								
6.0	TENSILE 200°C	KP-4-4	193	345	9.4417	0.0043	9.4384	0.0042	9.4409	0.0093	8.2848	0.0023
0.5	PIE	KP-4-3	180	192								
6.0	BEND 200°C	KP-4-2	28	180	NA	NA	9.4511	0.0154	9.4386	0.0120	8.2948	0.0137
0.5	PIE	KP-4-1	15	27								

Note: ORNL d_o measurements are on pressurized rods prior to puncture. PNNL d_o measurements are on rod segments after the rod was punctured and sectioned, first before the fuel was dissolved and then after.

After examining the daily checks data for the optical micrometer (PNNL instrument used to measure fuel rod outer diameters), it was determined that the measurements from the optical micrometer were biased high, as shown in Figure 4-11. That is, all daily check measurements were greater than the corresponding pin gauge standard (nominal target) values. The mean difference from the nominal value over all daily checks with the optical micrometer was 9.5 µm, and the median was 8.3 µm. Because the optical micrometer daily check values included two outliers, it was decided to use the median difference from the nominal value as the bias correction amount and apply that bias to the statistical analysis presented below.

The daily checks data were also used to quantify measurement uncertainty (i.e., random variability in measured values obtained using the optical micrometer at PNNL). This measurement uncertainty may be estimated (calculated) in different ways. It is important to note that in quantifying this uncertainty, we are not quantifying the variability in the measured values, we are quantifying the variability in the differences between the measured values and their respective nominal (target) values based on the daily checks data. One of the simplest ways to quantify the measurement uncertainty is to calculate the standard deviation (SD) of the differences between the measured values and their respective nominal values[o]. This calculated value is 5.1 µm. Based on this, we estimate the measurement uncertainty of the optical micrometer to be approximately ±5 µm, with a bias of 8 µm. Note that this overall measurement uncertainty describes the combined effect of different sources of variability (including the instrument uncertainty discussed above) associated with optical micrometer measurements at PNNL.

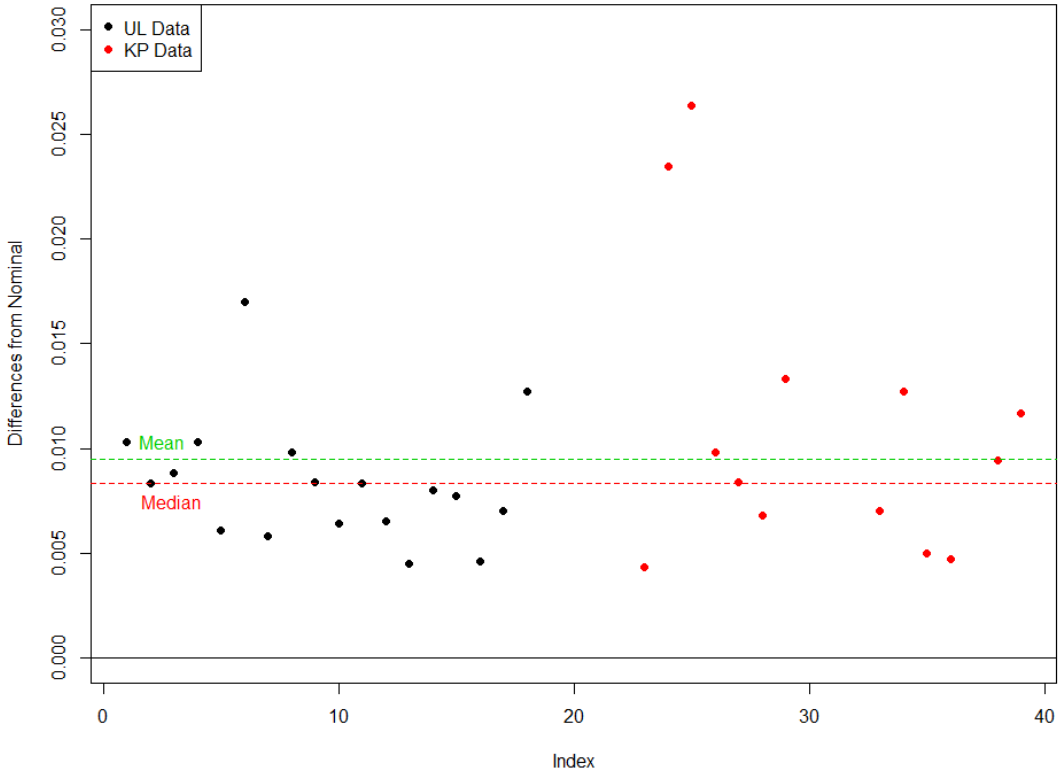

Figure 4-11. Optical Micrometer Daily Check Data.

[o] Other ways to estimate measurement uncertainty include the mean absolute deviation from the mean difference, or the mean absolute deviation from the median difference. These calculated values are 3.4 µm and 3.2 µm, respectively.

The following figures and analyses describe fuel rod outer diameter (d_o) results obtained from ORNL and PNNL. The ORNL measurements are on pressurized rods prior to puncture; the PNNL measurements are on rod segments after the rod was punctured and sectioned. The PNNL results include measurements taken both before and after dissolution. The PNNL results graphed below were bias corrected by subtracting 8.3 µm from each measured value.

Figure 4-12 and Figure 4-13 are plots of the average d_o measurements over each sample length listed in Table 4-3 and Table 4-4, respectively. The uncertainties represent one standard deviation of the mean without accounting for instrument uncertainty. Measurements taken after dissolution were generally smaller than those from before dissolution, suggesting that either the fuel itself exerts a minimal stress on the cladding or the fuel dissolution process may be removing an oxide layer or debris present on the surface of the cladding. This measured result is consistent with visual observations that the cladding appeared smoother after fuel dissolution.

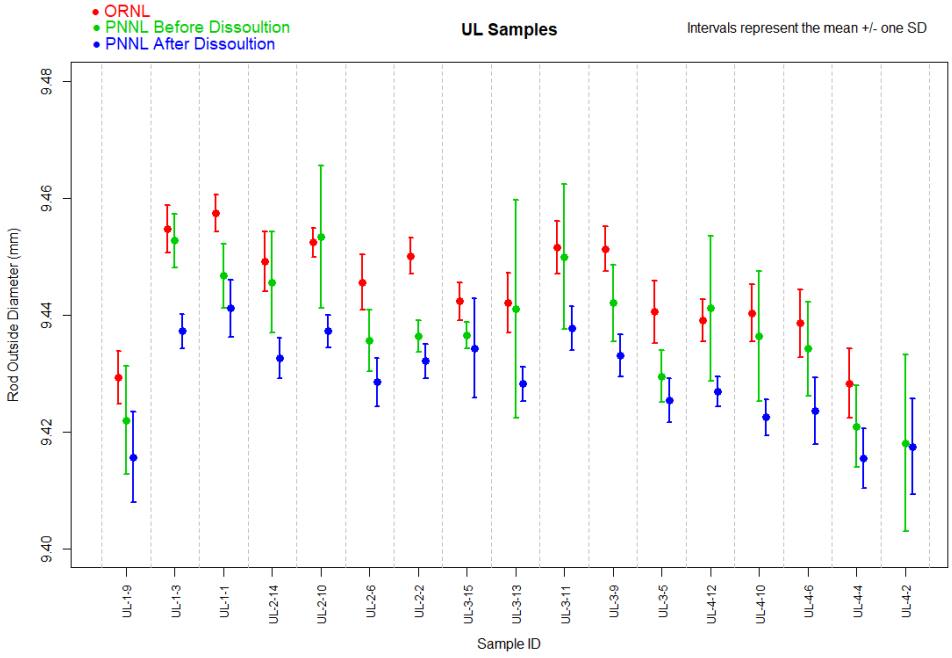

Figure 4-12. d_o Measurements of Rod UL Cladding Samples.

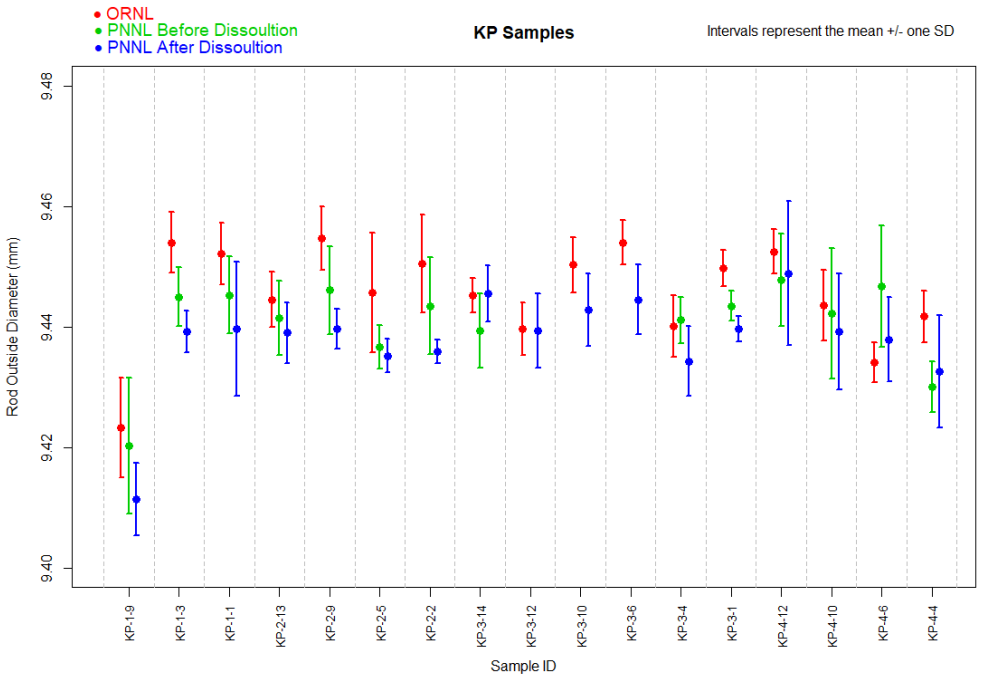

Figure 4-13. d_o Measurements of Rod KP Cladding Samples.

To check this observation, a statistical comparison was done using paired *t*-tests based on the mean diameters obtained from PNNL before and after dissolution. Under this approach, differences between the mean diameters of the various samples are considered. The null hypothesis for this approach is that the diameters are not statistically significantly different on average. However, the paired *t*-tests indicated that the diameters were statistically significantly different on average.

Figure 4-14 and Figure 4-15 show the differences between mean diameters for rod UL and rod KP before and after dissolution, respectively. The black horizontal line at zero in each figure represents the null hypothesis, i.e., no significant difference. The solid, colored horizontal line in each figure identifies the mean difference across the various samples. The dashed, colored horizontal line in each figure identifies a 95% lower confidence limit on the mean difference across the various samples. The interpretation of the lower confidence limit values is that with 95% confidence, the true overall average difference between diameters would be expected to be at least as large as the lower confidence limit for each comparison. Since each of the dashed lines (the lower confidence limit on the average difference) is greater than zero in both comparisons, the conclusion is again that there is a statistically significant difference between mean diameters for the comparisons conducted. On average the differences between the PNNL pre-dissolution and post-dissolution measurements were approximately 9 and 4 µm for the UL and KP rods, respectively. Table 4-5 lists the *t*-statistics and *p*-values from the actual paired *t*-tests, as well as the actual 95% lower confidence limits (LCLs) resulting from each comparison.

Table 4-5. Statistical Comparison Results for Rod Diameters Before and After Dissolution.

	***t*-statistic**	***p*-value**	**95% LCL (mm)**
Rod UL	7.5380	<0.00001	0.0069
Rod KP	3.3737	0.00227	0.0020

Note that additional d_o and d_i measurements will be made using an optical microscope for PIE samples when these samples are removed from the hot cell and evaluated.

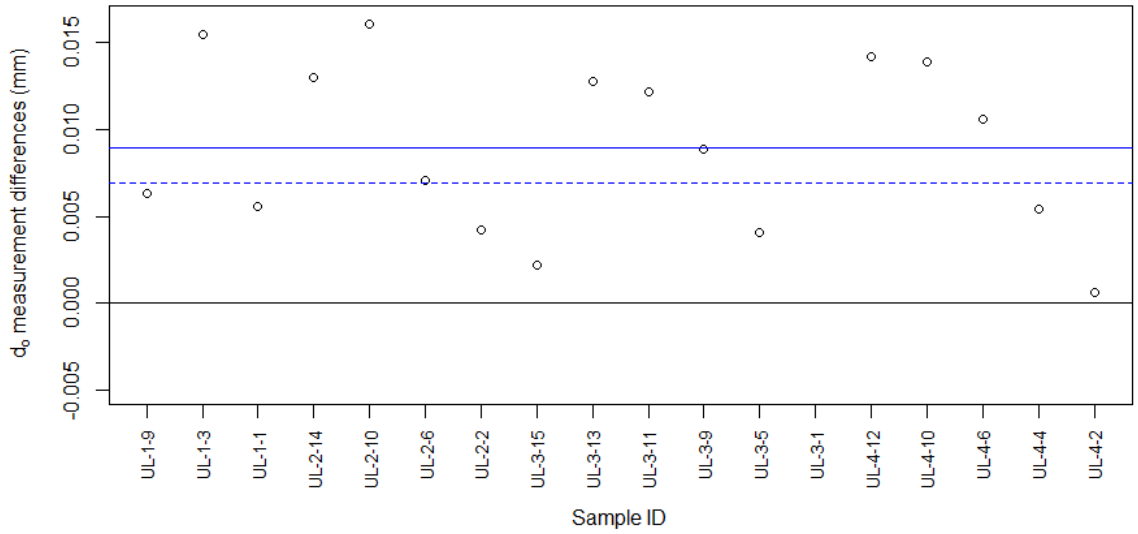

Figure 4-14. Depiction of Paired *t*-Test Comparing d_o Before and After Dissolution for Rod UL.

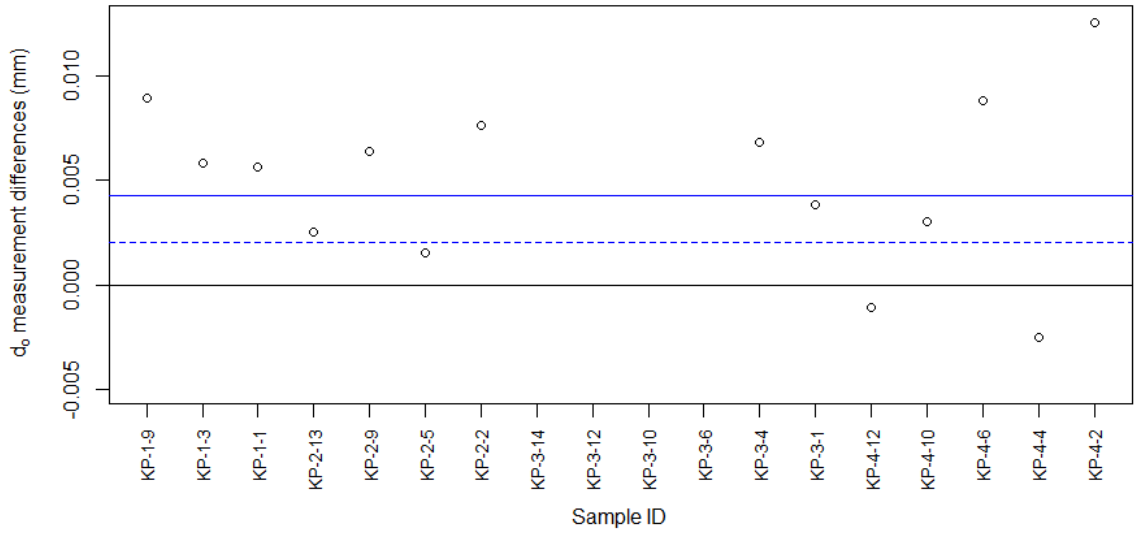

Figure 4-15. Depiction of Paired t-Test Comparing d_o Before and After Dissolution for Rod KP.

Similarly, based on inspection of Figure 4-11 and Figure 4-12, it appears that ORNL d_o measurements (taken while the rod was still intact, pressurized, and containing fuel) were larger than PNNL d_o measurements before dissolution (taken after the rod was punctured and cut). To check this observation, a statistical comparison was done using paired t-tests based on the mean diameters obtained from ORNL and PNNL before dissolution. Under this approach, differences between the mean diameters of the various samples are considered. The null hypothesis for this approach is that the diameters are not statistically significantly different on average. However, the paired t-tests indicated that the diameters were statistically significantly different on average.

Figure 4-16 and Figure 4-17 show the differences between mean diameters measured by ORNL and PNNL for rod UL and rod KP before dissolution, respectively. The black horizontal line at zero in each figure represents the null hypothesis, i.e., no significant difference. The solid, colored horizontal line in each figure identifies the mean difference across the various samples. The dashed, colored horizontal line in each figure identifies a 95% lower confidence limit on the mean difference across the various samples. The interpretation of the lower confidence limit values is that with 95% confidence, the true overall average difference between diameters would be expected to be at least as large as the lower confidence limit for each comparison. Since each of the dashed lines (the lower confidence limit on the average difference) is greater than zero in both comparisons, the conclusion is again that there is a statistically significant difference between mean diameters for the comparisons conducted.

Table 4-6 lists the t-statistics and p-values from the actual paired t-tests, as well as the actual 95% lower confidence limits (LCLs) resulting from each comparison. Different methods were used for the d_o measurements; PNNL used an optical micrometer (with an 8.3 µm bias applied) whereas ORNL used linear variable differential transformers and reported an accuracy within 20 µm (Montgomery et al. 2018). On average the differences between the ORNL and PNNL pre-dissolution measurements were approximately 6 and 4 µm for the UL and KP rods, respectively. Although these measured differences may not be of practical importance, especially considering the instrument uncertainties, it makes sense that the ORNL data would be larger than the PNNL data (before dissolution), as the former was measured with the rod pressurized before puncture.

Table 4-6. Statistical Comparison Results for ORNL and PNNL Rod Diameters Before Dissolution.

	t-statistic	*p*-value	95% LCL (mm)
Rod UL	4.8180	0.00011	0.00354
Rod KP	2.8126	0.0073	0.00166

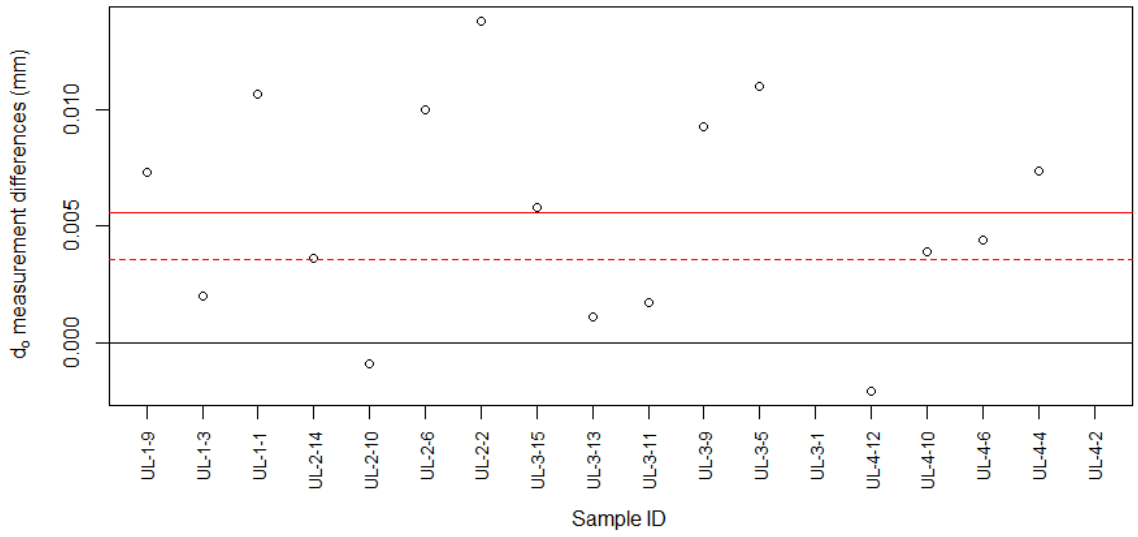

Figure 4-16. Depiction of Paired t-test Comparing ORNL and PNNL Before Dissolution for Rod UL.

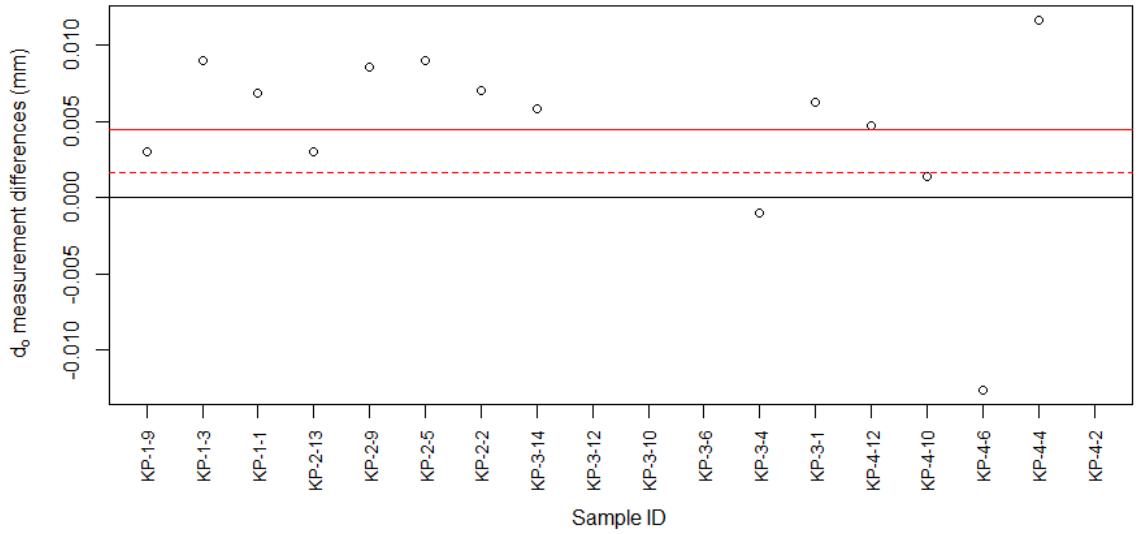

Figure 4-17. Depiction of Paired t-test Comparing ORNL and PNNL Before Dissolution for Rod KP.

4.4 Cladding Dose Measurements of UL-3-1 and FK-4-1

Multiple measurements were taken to develop an estimated radiation dose to workers handling irradiated cladding samples outside of the hot cells. Dose measurements were taken at 1 in., 8 in., and 1 ft from the side and end of each defueled cladding sample with a Thermo Scientific Model RO-20 Ion Chamber Survey Meter (see Figure 4-18). Measurements were repeated, with the beta window closed and then open, to determine the beta radiation contribution to the total dose. Results from this survey are given in Table 4-7 and Table 4-8. Note that the acid molarity used in the leach for these samples was higher than used in Batch 1 through 14, above.

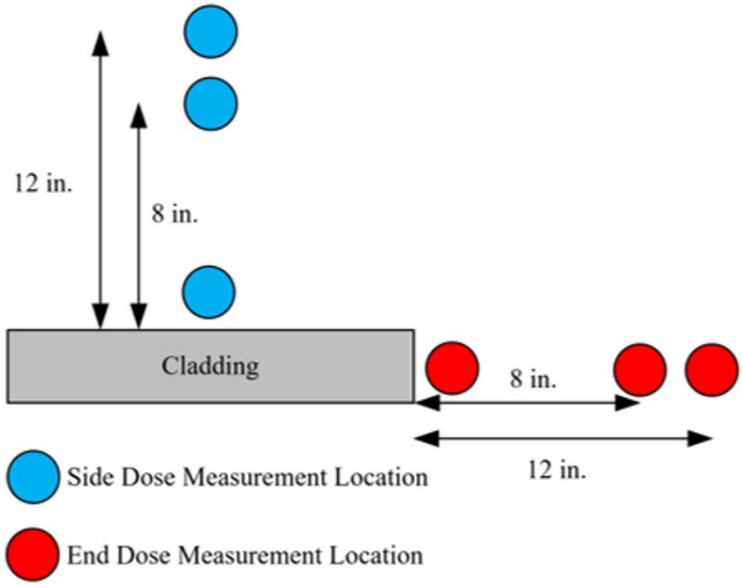

Figure 4-18. Dose Measurement Location Diagram.

Table 4-7. Measured Dose Rates for Sample UL-3-1. (6 in. long cladding sample)

		End			Side		
	Distance	**Open Window (mR/h)**	**Closed Window (mR/h)**	**Beta Contribution (mR/h)**	**Open Window (mR/h)**	**Closed Window (mR/h)**	**Beta Contribution (mR/h)**
After 1 M HNO_3 Rinse	1 ft	350	80	270	800	80	720
	8 in.	2500	100	2400	1500	150	1350
	1 in.	>50000	1200	>50000	12000	2000	10000
After 10 M HNO_3 Leach	1 ft	1000	80	920	800	100	700
	8 in.	2500	120	2380	1000	150	850
	1 in.	>50000	1000	>50000	10000	2000	8000
After Dissolution Only	1 ft	-	-	-	1000	100	900
	8 in.	-	-	-	2000	300	1700
	1 in.	-	-	-	15000	2000	13000

Table 4-8. Measured Dose Rates for Sample FK-4-1. (3.36 in. long cladding sample)

	Distance	End			Side		
		Open Window (mR/h)	Closed Window (mR/h)	Beta Contribution (mR/h)	Open Window (mR/h)	Closed Window (mR/h)	Beta Contribution (mR/h)
After 1 M HNO_3 Rinse	1 ft	400	8	392	150	8	142
	8 in.	1000	15	985	300	20	280
	1 in.	10000	100	9900	2800	200	2600
After 10 M HNO_3 Leach	1 ft	200	8	192	100	8	92
	8 in.	500	100	400	200	15	185
	1 in.	12000	150	11850	5000	350	4650
After Dissolution Only	1 ft	250	5	245	100	8	92
	8 in.	500	12	488	200	15	185
	1 in.	15000	100	14900	2500	180	2320

The effectiveness of the leach and rinse steps at reducing dose are quantified[p] as decontamination factors (DFs) given by Equation (4-3):

$$DF = \frac{D_{before}}{D_{after}} \tag{4-3}$$

where D_{before} is the measured dose before the process step and D_{after} is the measured dose after the process step. Higher values denote more effective decontamination. These DF values are provided in Table 4-9 and Table 4-10. On average, the leach step was better at reducing open-window dose, while the rinse step on average reduced the closed-window dose more effectively.

Table 4-9. Decontamination Factors for Sample UL-3-1.

	Distance	End		Side	
		Open Window DF	Closed Window DF	Open Window DF	Closed Window DF
After 1 M HNO_3 Rinse	1 ft	2.86	1.00	1.00	1.25
	8 in.	1.00	1.20	0.67	1.00
	1 in.	-	0.83	0.83	1.00
After 10 M HNO_3 Leach	1 ft	-	-	1.25	1.00
	8 in.	-	-	2.00	2.00
	1 in.	-	-	1.50	1.00

*Shaded boxes indicate DF < 1.

[p] It must be acknowledged that the dose measurements were taken by different personnel and distances were estimated. Based on observation during the dose measurements, the listed distances have a likely uncertainty of ±30%.

Table 4-10. Decontamination Factors for Sample FK-4-1.

	Distance	End		Side	
		Open Window DF	Closed Window DF	Open Window DF	Closed Window DF
After 1 M HNO_3 Rinse	1 ft	0.50	1.00	0.67	1.00
	8 in.	0.50	6.67	0.67	0.75
	1 in.	1.20	1.50	1.79	1.75
After 10 M HNO_3 Leach	1 ft	1.25	0.63	1.00	1.00
	8 in.	1.00	0.12	1.00	1.00
	1 in.	1.25	0.67	0.50	0.51

*Shaded boxes indicate DF < 1.

4.5 Summary of Observations

- The dissolution system worked well, and there were no issues dissolving 6-in. long samples in nitric acid at 65 ºC.
- Dissolution times for 6-in long samples varied from 26 to 98 hours, with the ends of the rod generally dissolving faster than the middle. It is speculated that different dissolution times for the same rod are related to burnup (this observation could be examined more closely if of interest).
- The process of dissolution, leach, and final rinse produced clean cladding, as evidenced by no smearable alpha contamination found on cladding samples removed from the hot cell.
- Average d_o measurements before dissolution for Rods UL and KP:

Rod	ORNL Average d_o*, before dissolution (mm)	PNNL Average d_o*, before dissolution (mm)	Differences (mm)	Nominal As-fabricated d_o (mm)
UL	9.4445	9.4390	0.0055	9.4996
KP	9.4451	9.4407	0.0044	9.4996

**Average only includes data where both PNNL and ORNL have OD measurements listed in Tables 4-3 and 4-4. PNNL data reported were bias correct by subtracting 0.0083 mm from each measured value.*

- Average d_o measurements for before and after dissolution for Rods UL and KP:

Rod	PNNL Average d_o*, before dissolution (mm)	PNNL Average d_o*, after dissolution (mm)	Differences (mm)	Nominal As-fabricated d_o (mm)
UL	9.4378	9.4288	0.0090	9.4996
KP	9.4408	9.4366	0.0042	9.4996

**Average only includes data where both before and after dissolution measurements are listed in Tables 4-3 and 4-4. PNNL data reported were bias correct by subtracting 0.0083 mm from each measured value.*

- Average ID measurements:

Rod	Average d_i (mm)	Nominal As-fabricated d_i (mm)
UL	8.2768	8.3566
KP	8.2944	8.3566

This page is intentionally left blank.

5. POST IRRADIATION EXAMINATION (PIE) TESTING

As discussed in Section 3, multiple, nominal 0.5-in. samples were cut from each rod for PIE to characterize each rod axially and radially in support of physical property analysis of the cladding. The fuel from each sample is chemically removed as described in Section 4 and cleaned before removal from the hot cells. At this point, the sample may be analyzed for surface area non-destructive analysis using the Brunauer-Emmett-Teller (BET) method. Next, the sample is sub-divided into multiple samples based on the notch mark placed on the sample as described in Section 3. Total hydrogen determination is performed on half of the sample, which is divided into four quarters to characterize the circumferential variation in the hydrogen concentration of the cladding. The other half of the sample is mounted in epoxy and prepared for optical metallurgical observations and microhardness measurements. The samples are mounted in a manner where the orientation of the sample can be matched to individual hydrogen analysis measurements. Figure 5-1 outlines the PNNL process for this examination.

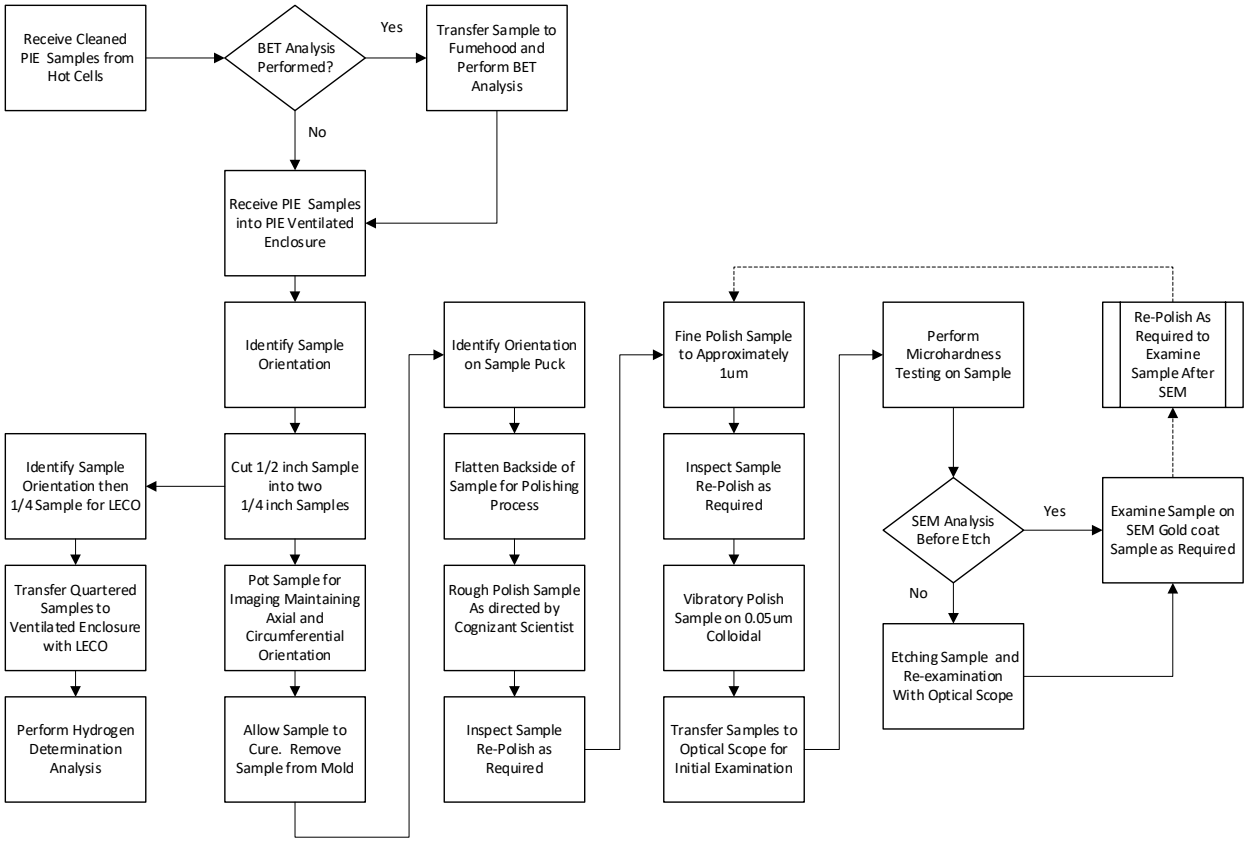

Figure 5-1. Flowchart of PIE Examination.

5.1 Preparing PIE Samples

5.1.1 Cutting Equipment

Irradiated cladding samples are sub-divided into axial and circumferential sections using a Buehler IsoMet slow-speed saw (Figure 5-2) which uses a 5 in. diameter × 0.020 in. thick Buehler diamond wafering blade, just as is used on the sectioning cutting saw in the hot cells. The cutting operations are performed wet with water which the blade picks up during cutting from the tray below the saw blade. The tray also collects cutting fines storing them wet until the tray contents are emptied at the close of operations. A weight (225 g) is used to apply pressure during cutting operations. Figure 5-2 shows how a tubular sample is cut with the saw using a jig that holds the sample in place. Figure 5-3 shows the cutting jig used to hold a tubular cross section between 6-7 mm in length and cut into four quarters.

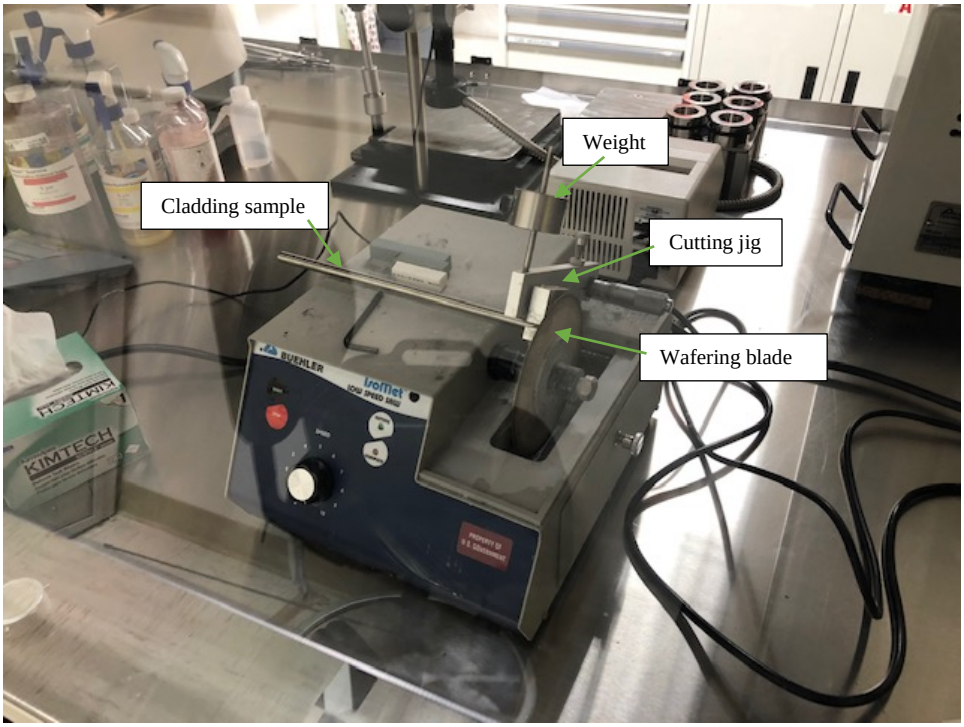

Figure 5-2. IsoMet Low-Speed Saw.

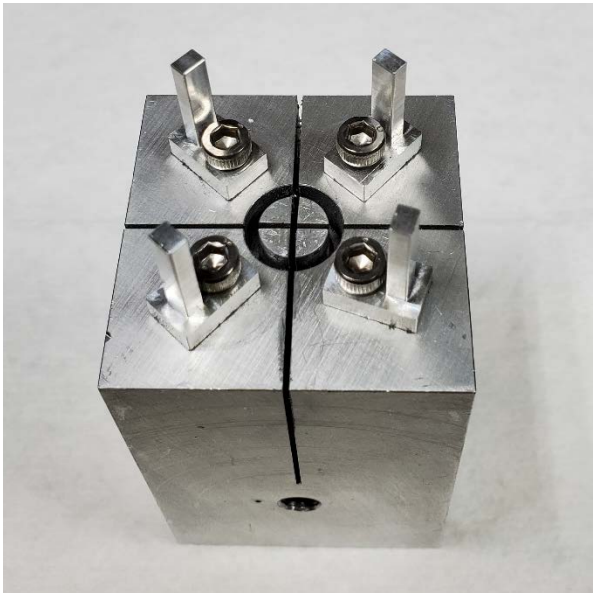

Figure 5-3. Cutting Jig Used to Quarter PIE Subsample into Circumferential Sections.

5.1.2 Cutting PIE Samples

Approximately 12 mm (~0.5 in, less cut loss) long cross sections are cut from the rod segments for PIE of the cladding with a sample notch placed on the end of the sample. The notch is located on the bottom of the sample (end facing the bottom of the rod) and at the 12 o'clock position circumferentially to indicate where the gas puncture occurred. Location of the sample position notch is maintained on all PIE sub-samples during and after cutting.

The sample is divided in half axially (Figure 5-4) to produce a 6 mm section for total hydrogen analysis with a LECO total hydrogen analyzer (Section 5.3) and a 6 mm section for optical metallurgical examination and microhardness testing (Section 5.4). The notch is maintained on the 6 mm sample for LECO, but the optical metallurgy sample orientation needs to be marked to maintain orientation. A jig for cutting has been designed to position the sample during cutting to maintain orientation of this sample after the LECO sample is removed. Before the sample is removed from the jig, the sample is marked (pen, scratch) on the side facing the bottom of the rod (should be the cut side) at the 12 o'clock position. Once removed from the jig, the optical metallurgy samples are examined looking at the *bottom side of the sample* (the side that is polished and observed) and use the applied mark to maintain orientation in the circumferential direction (12 o'clock position).

The sample for the LECO analyzer at this point is still too large and must be divided into four sections (Figure 5-4). Each section is identified as a *quadrant* and represents a circumferential region of the cladding for each axial position of the rod from which the parent PIE sample was cut. As previously discussed, the gas puncture location was selected to be the 12 o'clock position for each rod. Using the puncture as the reference point, the LECO quadrants are defined as the following circumferential locations, looking up from the bottom of rod, as:

- Quadrant A: Between 12 o'clock to 3 o'clock
- Quadrant B: Between 3 o'clock to 6 o'clock
- Quadrant C: Between 6 o'clock to 9 o'clock
- Quadrant D: Between 9 o'clock to 12 o'clock

The sample position notch is located between quadrants D and A, facing the bottom side of the sample during cutting operations as shown in Figure 5-4. This allows observed variation in total hydrogen values to be associated with observed hydride formation in the matching optical microscope (OM) sample. During the splitting operations and PIE analysis, the sub-samples are provided additional sub-samples ID to indicate if the subsample is destined for LECO analysis (-1A/B/C/D) or OM (-2). However, the results of these analyses are only reported herein to the parent PIE sample ID to prevent confusion.

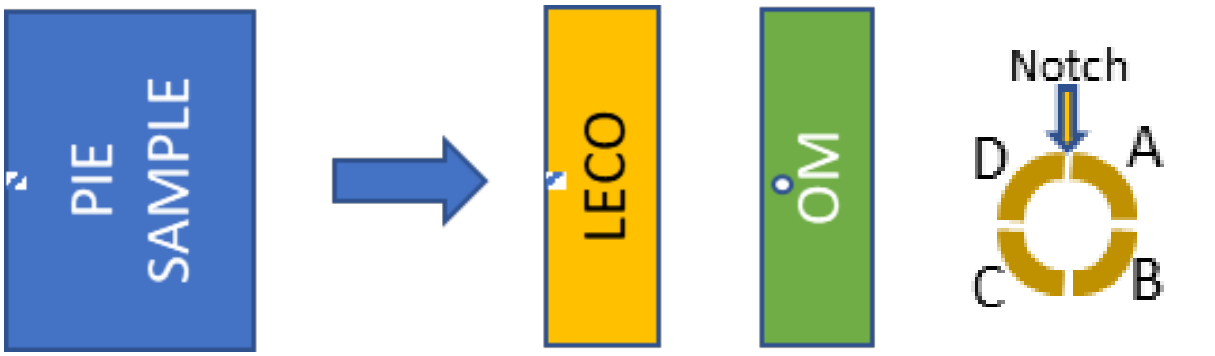

(a) Splitting PIE Sample Axially

(b) Splitting LECO Sample Circumferentially

Figure 5-4. Cutting PIE Sample (a) Axially and (b) Circumferentially.

5.1.3 Preparing PIE Samples from FK-4-1 (15 mm – 101 mm from Bottom)

Sample FK-4-1 from rod F35K13 was cut from the bottom of segment FK-4 and defueled in 2019 as described in Shimskey et al. (2019b). The bottom of rod F35K13 was punctured from the bottom 86 mm of the rod (excluding the plug) and was deemed not usable for physical properties testing because of the puncture. However, this section of the rod was used to verify dissolution operations and to verify PIE. Images of the sample before cutting are shown in Figure 5-5.

Since the sample was ~86 mm in length, the plan called out to cut the sample into six nominally sized PIE samples (~12 mm) with the remainder to be used for surface analysis and OM only (see Figure 5-6 and Table 5-1). During cutting operations, the notch located on the bottom of FK-4-1 was located and orientation was maintained by marking the bottom of each sample before cutting with a pen marking. Samples were delivered to a separate analytical lab to perform surface area measurements by BET before further splitting (Section 5.2).

Once BET was performed, six of the seven PIE samples were split into LECO samples and OM samples as shown in Figure 5-4, and Figure 5-6. The LECO samples for the first six samples were delivered for hydrogen determination (Section 5.3) while the OM samples from the first six and the remaining samples were mounted for optical microscopy and microhardness measurements (Section 5.4). More detailed results and imaging can be found in Appendix E.

(a) Sample FK-4-1 in Hot Cell After Dissolution of Fuel. Puncture location visible towards left end of sample.

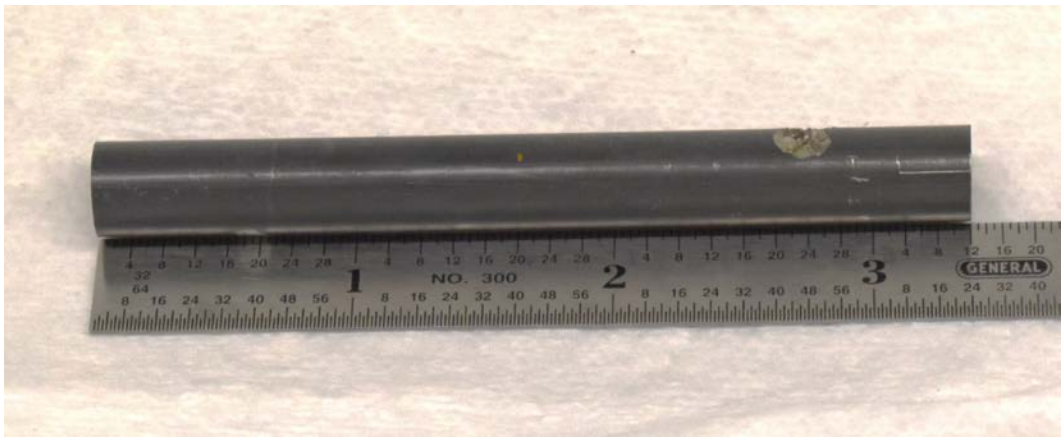

(b) Sample FK-4-1 in Ventilated Enclosure after Cleaning before Cutting. Puncture location visible towards right end of sample.

Figure 5-5. Sample FK-4-1 in (a) Hot Cell and (b) Ventilated Enclosure.

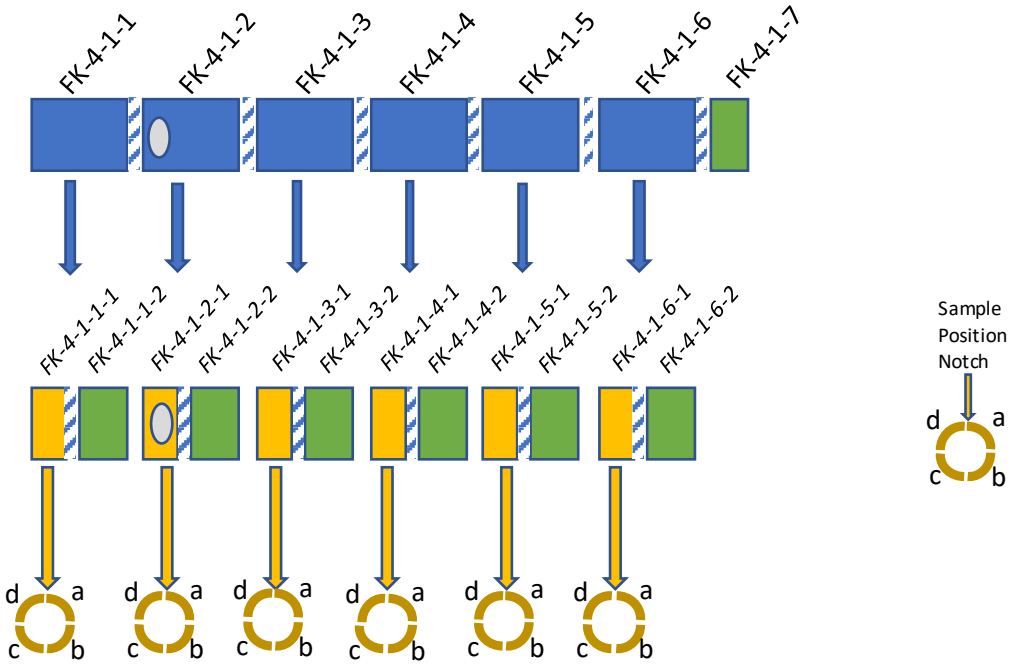

Figure 5-6. Cutting Plan Diagram for FK-4-1.

Table 5-1. Subsample Positions of FK-4-1 on Rod F35/K13 Relative to the Bottom of Rod.

Sample ID	PIE Analysis Performed	Bottom Position (mm)	Top Position (mm)
FK-4-1-1	BET, OM, LECO	15	28
FK-4-1-2	BET, OM, LECO	29	41
FK-4-1-3	BET, OM, LECO	42	55
FK-4-1-4	BET, OM, LECO	55	68
FK-4-1-5	BET, OM, LECO	69	81
FK-4-1-6	BET, OM, LECO	82	95
FK-4-1-7	BET, OM	95	101

Note: Positions are rounded to the nearest mm accounting for saw kerf and are known to ±2 mm.

5.1.4 PIE Analysis of Segment UL-1 (2909 mm – 3852 mm from Bottom)

Once PIE analysis was completed for FK-4-1, defueled PIE samples cut from the top segment from rod 6U3/L8 (segment UL-1) were cleaned and transferred for splitting and cutting operations as listed in Table 5-2. BET was not performed on these samples before cutting and destructive testing. Results are further discussed in Sections 5.3 and 5.4.

Table 5-2. PIE Sample Positions from the UL-1 Segment on Rod 6U3/L8 Relative to the Bottom of Rod.

Sample ID	PIE Analysis Performed	Bottom Position (mm)	Top Position (mm)
UL-1-2	OM, LECO	3061	3073
UL-1-4	OM, LECO	3226	3238
UL-1-6	OM, LECO	3391	3403
UL-1-8	OM, LECO	3505	3518
UL-1-10	OM, LECO	3671	3683

Note: Positions are rounded to the nearest mm accounting for saw kerf and are known to ±2 mm.

5.2 Specific Surface Area Measurement

To provide data to other areas of the program, such as drying of SNF, it is desired to know how the surface area of the cladding changes over the axial length due to the variations in oxide layer thickness and porosity. Specific surface area measurements of an entire defueled sample were collected using the BET method on a Tristar II Plus BET analyzer (Micromeritics). The instrument is designed to measure the surface area of solids and powders by measuring the adsorption of krypton or nitrogen gas to a sample over a range of pressures at a constant temperature. Krypton gas is used in the case of samples with a small amount of material available and low surface area measurements, such as the cladding samples. The BET analyzer is equipped with a large sample vial adapter, which accommodates one 30 mm outer diameter vial. This larger vial kit allows for the analysis of samples of larger size while using the krypton gas option. The instrument automatically calculates the BET surface area based on the selected data points. The BET constant, c, relates to the adsorption of the gas to the solid being measured; higher c values are indicative of a stronger interaction between the two, and typical values range between 5 and 300. User input is required to determine the data points of best fit for the BET surface area calculation, which may reduce the number of data points used in a calculation (in comparison to the number of data points collected). The accuracy of the measurement is higher with a greater number of data points. The calculation can only be performed with two or more data points, and those computed with only two points will not calculate associated error.

5.2.1 Sample Preparation

Before cutting, sample analysis in the BET analyzer was performed on 0.5-in. long cladding rings. Before analysis, cladding samples were individually degassed using nitrogen at 90°C for 1 hour, followed by room temperature degassing for 30 minutes.

5.2.2 Instrument Preparation and Sample Analysis

The BET analyzer is a vendor calibrated instrument. An alumina standard, prepared according to vendor specifications, is suitable to verify the calibration of the instrument when analyzing using krypton gas. The alumina calibration verification standard was run before sample analysis and upon completion of the batch of samples. A batch of samples is defined as a group of samples that are run continuously with the instrument sitting idle for ≤ 24 hours.

Samples FK-4-1-1 through FK-4-1-7, run individually, were loaded into the large vial and secured to the instrument. Ten points between relative pressure (P/P_o) 0.05 and 0.25 were selected for adsorption measurements, consistent with measurements of samples with low surface area. Results of the individual sample runs are shown in Table 5-3.

Table 5-3. BET Surface Area Results of Samples FK-4-1-1 through FK-4-1-7.

Sample	BET Surface Area (m^2/g)	c	Number of Datapoints Used for Calculation
FK-4-1-1	0.0016 ± 0.0008	94.58	3
FK-4-1-2	0.0130	112.33	2
FK-4-1-3	0.0135 ± 0.0003	244.64	6
FK-4-1-4	ND	ND	0
FK-4-1-5	ND	ND	0
FK-4-1-6	0.0125	27.99	2
FK-4-1-7	ND	ND	0

ND (no detection) indicates the instrument could not complete the run due to sample size limitations.
c is the BET constant and relates to the adsorption of the gas to the solid being measured

BET surface area was successfully calculated on four of the seven samples. Those samples with no error noted on the surface area measurements indicate that only two data points were suitable for the calculation of the BET surface area. While the resulting specific areas calculated do agree in surface area measurements, the c values for the samples varied, making it difficult to quantify the validity of the agreement. Furthermore, the number of data points used in the calculation was three or fewer in three of the four samples that provided analysis results, indicating that the reliability of the samples is in question. To further determine if the no detection (ND) results were due to instrument or sample issues, a verification standard was run between the ND analyses. The verification run and results passed easily within specification, indicating a sample issue.

The instrument has a minimum total surface area and mass required to successfully complete a sample analysis, which for krypton analysis is 0.01 m^2. Based on the results determined in Table 5-3, it was determined that the mass required for a successful sample analysis is approximately equal to, or greater than, the mass of the samples themselves. Thus, those results documented as ND indicate that the sample size was too small for the instrument to analyze. This also explains the large variation in data points and linearity observed in those samples with successful BET specific area analysis. Initially, samples that resulted in ND were run a second time. However, when these samples also resulted in ND, additional runs were not pursued following ND due to ALARA concerns.

To overcome the minimum mass required, two samples were prepared through degassing, and then run simultaneously in the large sample vial. Samples FK-4-1-2 and FK-4-1-3 were chosen for this due to the distinctive markings on them, making them easily identifiable between each other. As with the previous batch of samples, an opening and closing calibration verification was performed with the alumina standard. Ten points between 0.05 and 0.25 relative pressure (P/P_o) were again selected for analysis. Results from these runs are in Table 5-4.

Table 5-4. BET Surface Area Results from Two Cladding Samples FK-4-1-2 and FK-4-1-3.

Sample and Run Number	BET Surface Area (m^2/g)	c	Number of Datapoints Used for Calculation
FK-4-1-2 and FK-4-1-3 R1	0.0079 ± 0.0002	57.62	5
FK-4-1-2 and FK-4-1-3 R2	0.0051 ± 0.0002	99.08	5
FK-4-1-2 and FK 4-1-3 R3	0.0051 ± 0.0003	87.81	5

The surface area results from two samples run simultaneously (Table 5-4) did not agree well with those samples run individually (Table 5-3). However, runs 2 and 3 from the dual sample analyses agreed very well with each other in the BET surface area and the c value. It should be noted that both used a high number of datapoints as well in the surface area calculation, strengthening their validity. From this, it was inferred that running two samples simultaneously allows for better reproducibility.

However, further scoping work must be done before these results can be accepted as accurate and acceptable values. The reproducibility between runs 2 and 3 agree well in the dual samples, but there is still a discrepancy between these and run 1. Further work must be performed with non-radioactive samples of varied oxide thickness to understand minimum mass and run criteria. While this was initially planned to occur before the radioactive samples were analyzed, the COVID-19 pandemic interfered with these plans. Due to questions in sample analysis validity and ALARA concerns, further runs were not completed. BET surface area analysis may be revisited once further scoping work is performed.

After further sample examination, it was determined that the FK samples provided for BET surface area analysis had little to no oxide layer on the samples, further reducing the amount of surface area and mass.

5.3 LECO Measurement of Hydrogen, Oxygen, and Nitrogen in Cladding Samples

The ONH836 Oxygen/Nitrogen/Hydrogen Analyzer is designed for wide-range measurement of oxygen, nitrogen, and hydrogen content of steel, refractory metals, and other inorganic materials. A pre-weighed sample is placed in a graphite crucible, which is heated in an impulse furnace to release analyte gases. An inert gas carrier, helium (He), sweeps the liberated analyte gases out of the furnace, through a mass flow controller, and to a series of detectors. Oxygen present in the sample reacts upon combustion with the graphite crucible to form carbon monoxide (CO) and carbon dioxide (CO_2), which are detected using non-dispersive infrared (NDIR) cells.

Since analyte gas molecules absorb infrared (IR) energy at unique wavelengths within the IR spectrum, incident IR energy at these wavelengths is absorbed as the gases pass through the NDIR absorption cells. The gas continues through a heated copper oxide bed, where CO is oxidized to CO_2 and hydrogen gas (H_2) is oxidized to water (H_2O). The gas then passes through another set of NDIR cells where H_2O and CO_2 are detected. H_2O and CO_2 are then scrubbed out of the carrier gas stream and a dynamic flow compensation system is used to add carrier gas as a makeup for the gas lost during the scrubbing process.

The final component in the flow stream is a thermal conductivity (TC) detector, which is used to detect nitrogen. TC detection takes advantage of the difference in TC between carrier and analyte gases. Resistive TC filaments are placed in a flowing stream of carrier gas and heated by a bridge circuit. As analyte gas is introduced into the carrier stream, the rate at which heat transfers from the filaments will change, producing a measurable deflection in the bridge circuit.

5.3.1 Instrument Modifications

The instrument is designed to sit on a countertop (Figure 5-7a) but, because of the instrument dimensions, it was necessary to turn it 90° and remove several instrument covers to fit into the radioactive fume hood. Contamination and dose control modifications to the system and fume hood were completed and include the following:

1. a containment box was designed to fit over the piston/furnace chamber (Figure 5-7b) to contain dispersible radioactive material generated during the combustion of the sample.
2. the supplied vacuum for graphite cleanup was replaced with a high-efficiency particulate air vacuum.
3. arm holes were cut into the side of the fume hood (Figure 5-7c) for easier access to the sample piston. This sped up sample manipulations and reduced time handling the samples. Future plans include adding glove box gloves to the armholes for greater contamination control.

a)

b)

c)

Figure 5-7. (a) As Manufactured LECO ONH 836 instrument, (b) LECO ONH 836 Fit into Fume Hood 90°, Reagent Covers Removed, fitted with containment box around furnace, and (c) Arm Holes Cut in the Side of the Fume Hood

5.3.2 Sample Preparation

Samples are prepared by taking 0.25-in. cladding rings and quartering the rings using an IsoMet slow-speed saw (Figure 5-2) and a quartering jig (Figure 5-8). Orientation is maintained on each quarter so samples can be traced back to a location on the fuel rod. The sample notch, which indicates the bottom of the rod, is faced up and set at the 12 o'clock position. Each quarter sample is labeled either "a," "b," "c," or "d" based on the 12 o'clock position in a clockwise manner (Figure 5-9). Samples are cleaned with acetone and placed in pre-tared sample vials. The vials are weighed with the quartered samples, and a sample mass is determined. Each quarter ring is ~0.05-0.10 g and fits within the ~1-cm^3 LECO crucible and through the LECO sample drop chamber.

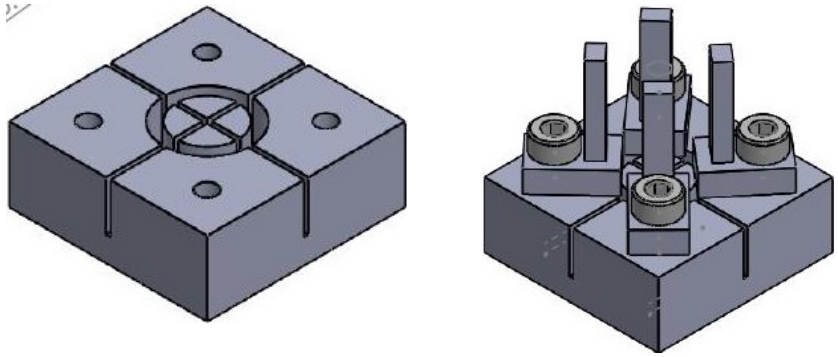

Figure 5-8. Sample Quartering Jig.

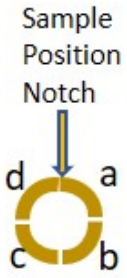

Figure 5-9. Sample Quartering Scheme.

5.3.3 Instrument Calibration and Sample Analysis

Unless otherwise stated, all samples are run using a graphite crucible with tin and nickel flux (to accelerate sample combustion) by an accepted method for sample analysis of zirconium metal in LECO analyzers.

Before sample analysis, a blank calibration is established for the instrument by running 3-5 crucibles with flux but without sample; this sets the instrument "zero." After the blank calibration, a series of certified standard metals are run, and an instrument calibration curve is generated based upon total analyte mass. Unknown samples are compared against the calibration curve to determine total hydrogen, oxygen, and nitrogen values and concentrations are determined using the sample mass. Typical calibrations contain standard materials in the following ranges:

Table 5-5. High and Low LECO Calibration Values.

Analyte	Low Calibration Standard (total grams)[1,2]	High Calibration Standard (total grams)[1,2]
Hydrogen	0.000388	0.001238
Nitrogen	0.001250	0.055700
Oxygen	0.003600	0.014500

[1] *Sample curve typically forced through zero*
[2] *The instrument is calibrated by total analyte grams. However, by entering sample mass, the results are given as concentration.*

Samples are run in batches of eight. After each batch a calibration verification sample (a certified standard) is performed to verify the continued validity of the calibration curve. After the final sample has been run for the day a closing verification sample is performed.

5.4 Optical Metallography Sample Preparation and Examination

5.4.1 ASTM Methods Comparison

In the development of the methods used to prepare and examine samples for optical metallography, the following ASTM methods were followed:

- ASTM E3-11 Standard Guide for Preparation of Metallographic Specimens
- ASTM E92-17 Standard Test Method for Vickers Hardness and Knoop Hardness of Metallic Materials
- ASTM E384-17 Standard Test method for Microindentation Hardness of Materials
- ASTM E1951-14 Standard Guide for Calibrating Reticles and Light Microscope Magnifications

Some of the ASTM requirements are called out in Table 5-6. A comprehensive list of ASTM methods and requirements is included in Appendix C.

Table 5-6. Summary of ASTM Methods Comparison.

	Section	Summary	Comment
ASTM E3	5.1.3	Sampling: Dictated by needs of study.	See Section 5.1.3 and 5.1.4
	11.2.2	Grinding and Polishing: Grinding should be done with the finest paper, platen, or stone capable of removing effects of prior operations in a short time.	See Section 5.4.2
	11.3.3	Polishing and Cleaning: Cleaning mandatory between stages. Ultrasonic cleaning recommended.	See Section 5.4.2
ASTM E92	1.4	Scope: Covers Knoop Hardness tests made using test forces from 1 gf to 2 kgf.	See Section 5.4.3
	6.2	Preparation: The test should be performed on a flat specimen with a polished or otherwise suitable surface.	See Section 5.4.2

	Section	Summary	Comment
	6.2.2	Preparation: The specimen should not be etched.	See Section 5.4.3
	7.1	Verification: Verification should be performed daily.	See Section 5.4.3
	7.7.3	Force Application: Force shall be applied for 10 to 15 seconds.	See Section 5.4.3
	7.11	Spacing of Indentations: The spacing between indentations is large enough so that adjacent test does not interfere with one another.	See Section 5.4.3

5.4.2 Sample Preparation

The samples that undergo optical metallography are approximately 6 mm in length. The sectioning of these samples is described in Section 5.1.2. The samples are mounted such that the polished face is the part of the sample toward the end of the rod. The 12 o'clock position is marked by a black line on the outer surface of the sample. The quadrants of the polished face match the quadrants of the LECO samples, as seen in Figure 5-9.

To mount the samples, each sample is placed in an individual cup before pouring the resin in. The samples are mounted in Buehler EpoThin epoxy resin. Once each cup is filled, the samples are placed under vacuum for several minutes to allow any gas trapped in the resin to escape. The resin is then allowed to cure overnight at room temperature.

Once the resin is cured, the samples are taken out of the cups and moved to the Pace Technologies multistage grinder-polisher (Figure 5-10). Before grinding begins, the samples first undergo backing. This refers to the grinding of the back side of the sample puck, resulting in a flat surface that is parallel to the sample surface. The samples are backed using 240 grit silicon carbide paper for 30 seconds. Next, the samples are ground using silicon carbide paper. Each silicon carbide paper is used for between 30 and 60 seconds. For each grit, multiple papers are used. The samples are cleaned in an ultrasonic deionized water (DIW) bath after each run. A typical ultrasonic rinse runs for a minimum of 30 seconds. The samples are then examined by a video microscope to determine if they are ready to move onto the next step (Figure 5-11). Table 5-7 details the typical grinding and polishing times. Polishing is done with a polishing cloth with a diamond suspension. After a polishing step is complete, the samples are cleaned in a soap and water ultrasonic bath, rinsed in DIW, and rinsed in ethanol before being air dried. The samples are examined under a video microscope to determine if more time is needed at the current step or if they are ready to proceed to the next step. The samples are polished down to 1 µm on the grinder-polisher.

Table 5-7. Grinding and Polishing Times.

Grit	Diamond Suspension (µm)	Polishing Paper/Cloth	Time (sec)
240		Silicon Carbide	90
400		Silicon Carbide	180
600		Silicon Carbide	120
800		Silicon Carbide	90
	9	Pace TexPan Pad	120
	6	Pace TexPan Pad	60
	3	Pace Atlantis Pad	60
	1	Pace Atlantis Pad	60
	0.5	Pace Microcloth	4 hours

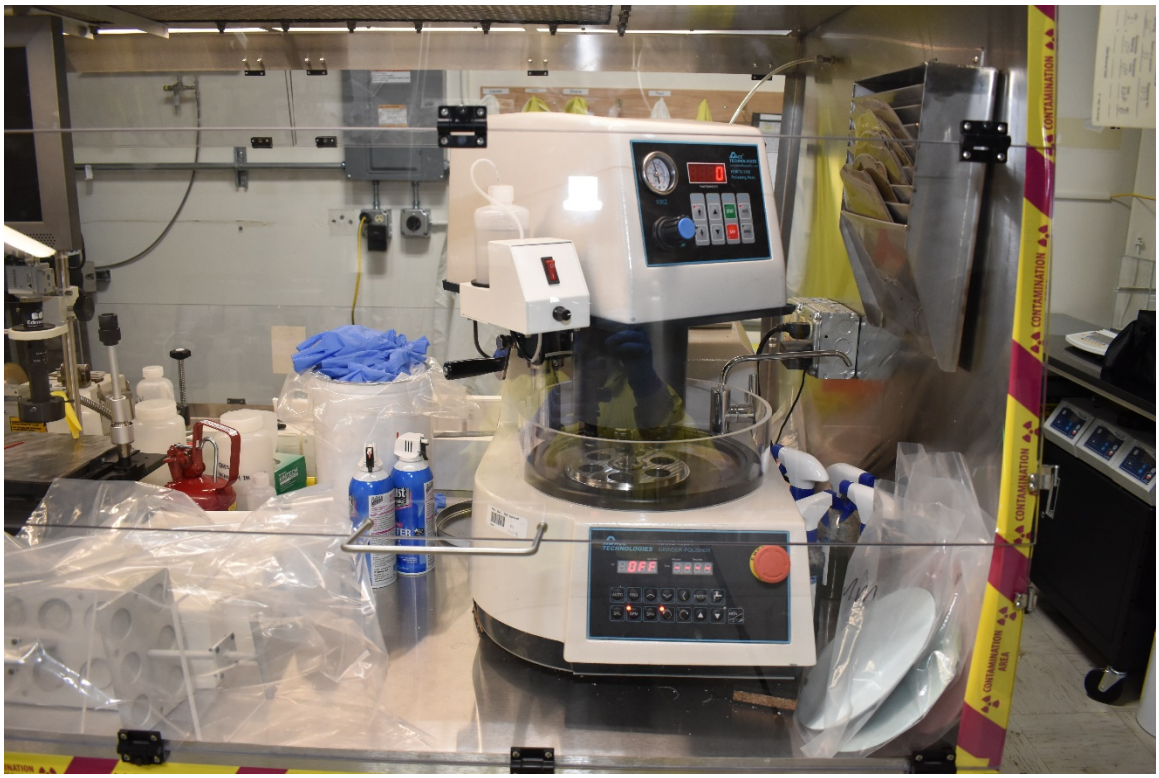

Figure 5-10. Pace Technologies Multistage Grinder-Polisher.

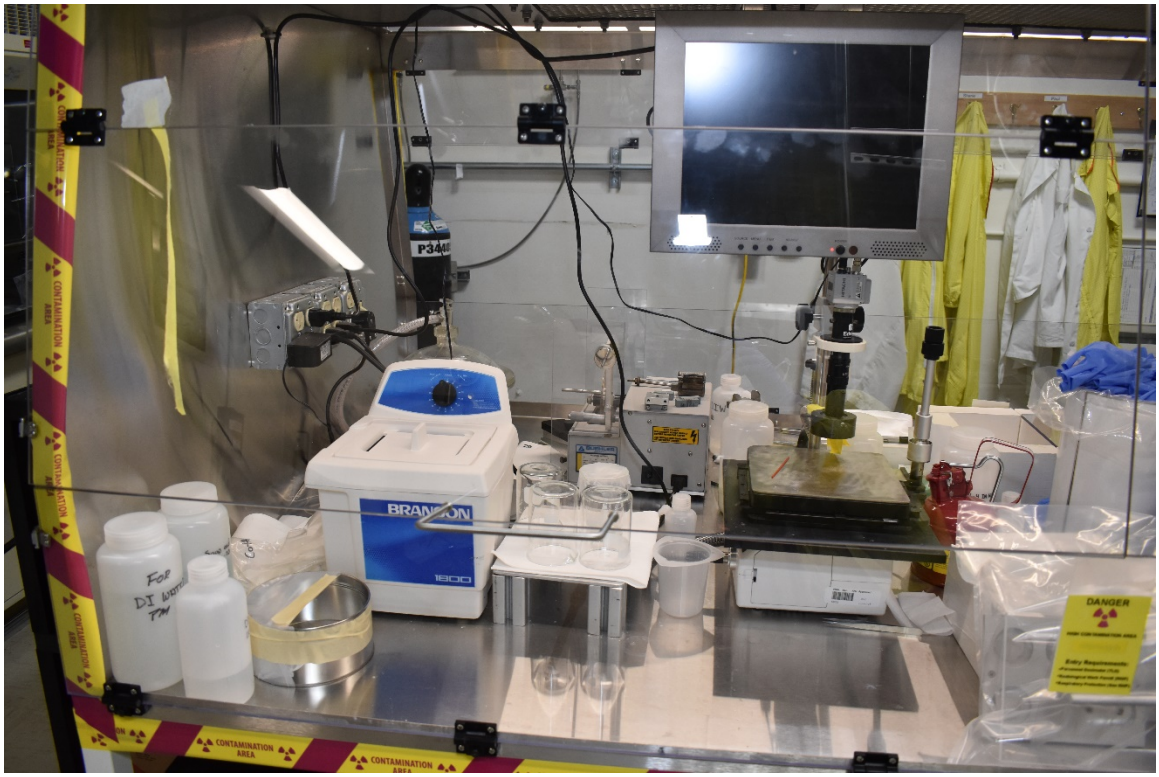

Figure 5-11. Branson Ultrasonic Cleaner and Video Microscope.

The final polishing step is performed on a Pace vibratory polisher (Figure 5-12). The samples are placed in a metal mount. A screw is used to secure the mount to the sample. This mount provides weight to the sample to help the polishing process. The samples are placed in the vibratory polisher with a diamond suspension for four hours. Once this step is complete, the samples are removed from the metal mount and cleaned in an ultrasonic bath of soap and water and then rinsed with DIW (Figure 5-12). If additional cleaning is required, cotton or microcloth can be used to scrub the polished sample surface. Additional ultrasonic rinses can be used, or the sample may be cleaned with ethanol. For this final cleaning step, allowing the samples to sit in the ultrasonic bath for several minutes provided the best results. After this cleaning step, the samples are ready for optical microscopy and microhardness testing (detailed in Section 5.4.3).

Figure 5-12. Pace Technologies Vibratory Polisher.

Figure 5-13. Branson Ultrasonic Cleaner and Etching Station.

After examination of a polished sample is complete, the sample is etched. Etching is performed in a fume hood (Figure 5-13). To etch a sample, the polished sample surface is submerged in etchant. The sample is then rinsed in a beaker of DIW, then rinsed in a second beaker of DIW, then moved to a DIW ultrasonic bath for a minimum of one minute. The etchant solution used is 47% volume concentrated nitric acid, 47% volume of 30% peroxide, 6% volume concentrated HF. Etching time is affected by several variables. For example, a new batch of etchant etches faster than one that is hours old. As a batch of etchant is used for more samples, it becomes less effective. For this reason, a minimum of one batch per three samples is used. The cladding alloy and hydrogen concentration also affect the etching time. A higher concentration of hydrogen results in a faster etching time. Due to the high variability of etching times, samples are started at a low etching time, then examined under the optical microscope. Additional etching time is incrementally increased until the desired etch is achieved.

5.4.3 Microstructure Examination

Optical microscopy and microhardness testing are performed on every sample. Optical microscopy is completed on an Olympus scope (Figure 5-14) equipped with 5× and 20× lenses. Images are captured of each sample after polishing, and after etching. An overview of the sample is captured by stitching together 144 images taken using the 5× lens (Figure 5-15). Images of each quadrant are captured by stitching together 64 images taken using the 20× lens (Figure 5-16). Individual images, such as Figure 5-17, are also captured across the sample to show detail and areas of interest. These images are used to measure the inner diameter, outer diameter without oxide layer, wall thickness, and oxide thickness.

Figure 5-14. Olympus Optical Microscope.

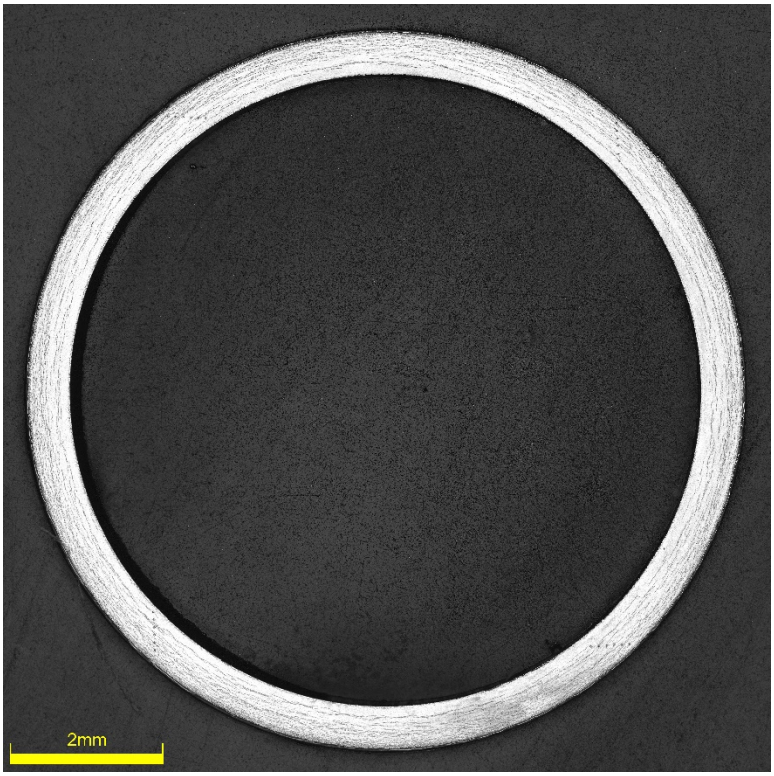

Figure 5-15. Example Overview Image of UL-1-2.

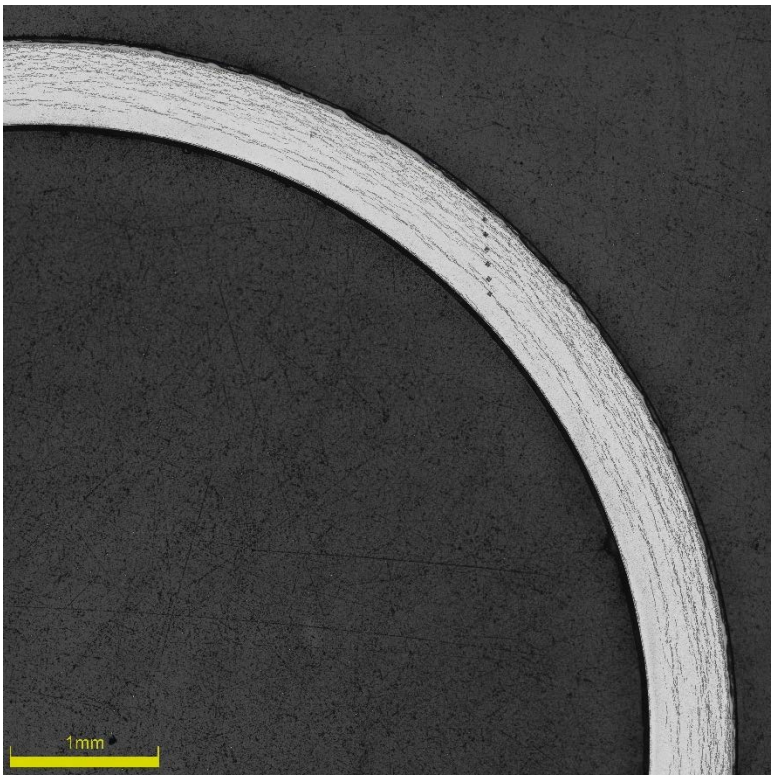

Figure 5-16. Example Quadrant Image of UL-1-2.

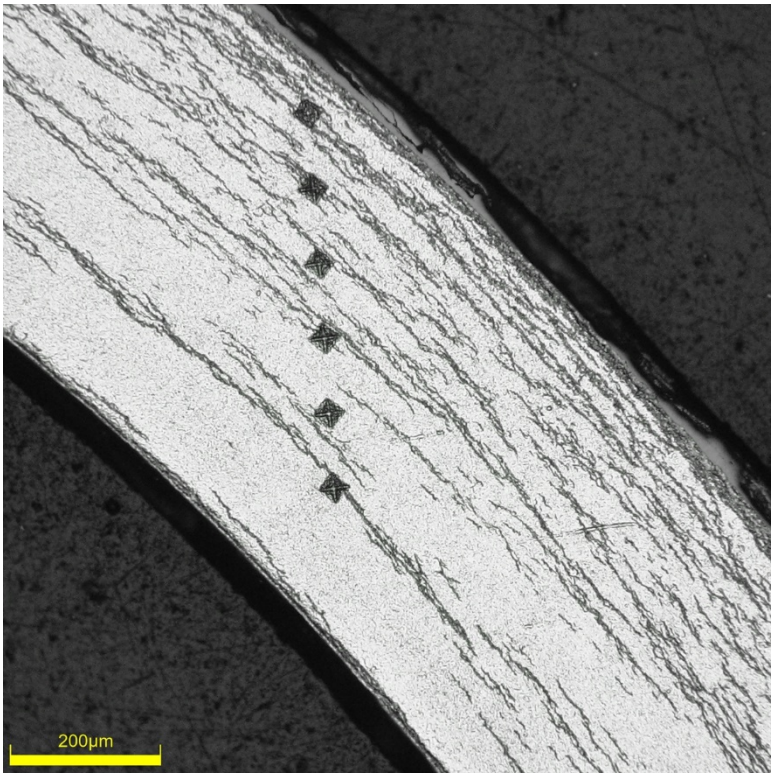

Figure 5-17. Example Individual Image of UL-1-2.

Microhardness is performed on polished samples using a Sun-Tech microhardness tester (Figure 5-18). The tester is capable of both Vickers and Knoop indentation. All testing on UL-1 and FK-4 samples was done using the Vickers indenter. Microhardness testing was completed on the polished sample, before etching. In each quadrant of each sample, six indents are made using 300g force, held for 10 seconds. For all UL-1 samples and FK-4-1-7, the six indentations are made in a line that is 45° in relation to the outer circumference. The indentations are spaced 100 µm apart. For FK-4-1-2, FK-4-1-6, and FK-4-1-5 two sets of indentations were completed, one set at 90° and the second at 60°. For FK-4-1-2, FK-4-1-4, and FK-4-1-6 two sets of indentations were completed at 90° and 45°. The spacing of the indentations for FK-4-1-1 through FK-4-1-6 was 80 µm. Microhardness testing was originally completed on these samples before moving on to UL-1 and FK-4-1-7. An angle of 45° was determined to be optimum because it allowed an increase in spacing between indentations. The recommended spacing per ASTM E92-17 is the length of the indentation diagonal multiplied by 2.5, or a distance great enough so that an adjacent test does not interfere with others. With a typical diagonal measurement of 40 µm - 45 µm, a 45° set of indentations with a spacing of 100 µm better follows these guidelines. Figure 5-17 shows an example of the microhardness indentations.

Both the optical microscope and hardness tester are calibrated and are regularly confirmed against standards. The microscope measurements are confirmed using a NIST standard reference material microscope magnification standard. A calibration check is performed at the beginning of each week that the scope is in use. The microhardness tester is checked using a certified hardness standard. A check is performed at the beginning of each workday. The measured value must be within 2% of the certified value.

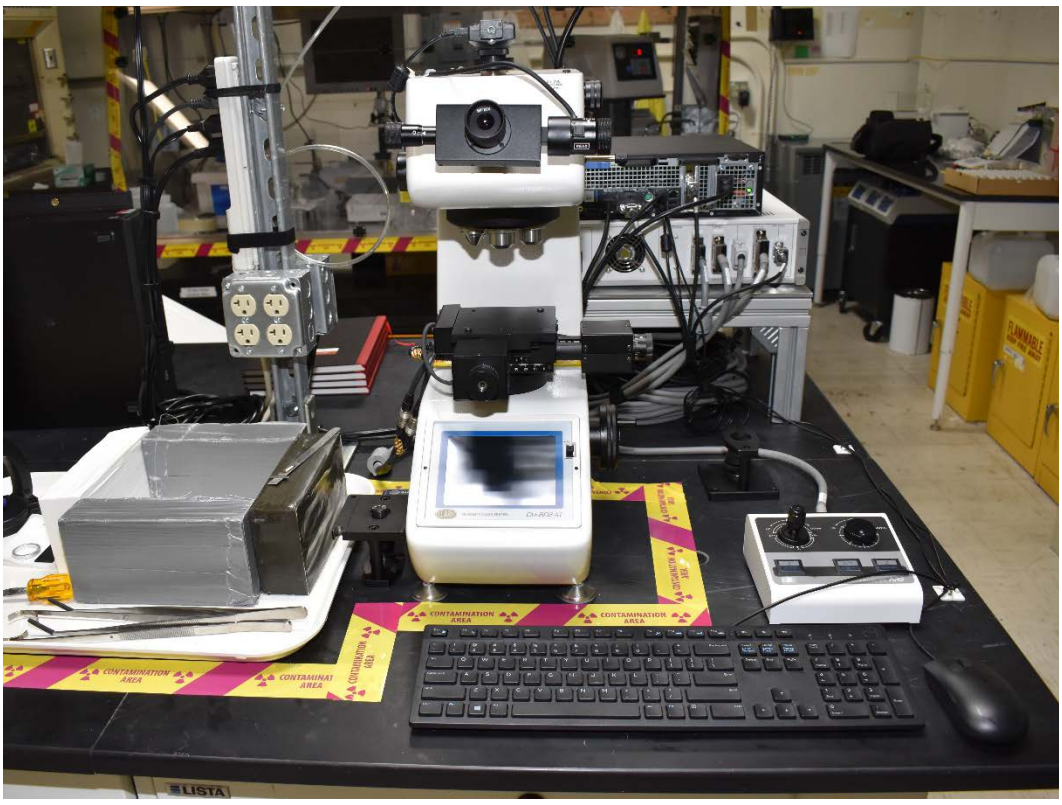

Figure 5-18. Sun-Tec Microhardness Tester.

Sections 5.4.3 and 5.4.4 include a summary of results for FK-4-1-1, FK-4-1-2, FK-4-1-3, FK-4-1-4, FK-4-1-5, FK-4-1-6, FK-4-1-7, UL-1-2, UL-1-4, UL-1-6, UL-1-8, and UL-1-10. Included are sample location, wall thickness, oxide layer, hydrogen concentrations, and Vickers microhardness. There are sample images taken from FK-4-1 and UL-1 samples. These images demonstrate how measurements were taken and show optical images of the etched and polished samples.

5.4.4 Results from Section FK-4-1 (15 mm – 101 mm) from Rod F35K13

Sample FK-4-1 is located at the very bottom of the rod (between 15 mm and 101 mm from the bottom of the rod). The sample was cut into seven PIE samples to validate PIE methodology. This section contains an overview of results, as summarized in Table 5-8. Examples of one quadrant from each of the first six samples (FK-4-1-1 through FK-4-1-6) are presented in Figure 5-19 through Figure 5-24, showing the overview with outer diameter (d_o) and inner diameter (d_i), a closeup showing representative cladding wall thickness, and a closeup showing oxide layer thickness. Figure 5-25 through Figure 5-28 show the four quadrants of sample FK-4-1-7. In addition to the information shown for the first six samples, the figures for FK-4-1 also show the microhardness results for each quadrant. Appendix E contains more details and images, including the mean wall thickness and standard deviation, mean oxide layer thickness and standard deviation, and mean microhardness and standard deviation. The oxide layer thickness and total average hydrogen concentration are quite small in these samples as the temperatures of this portion of the cladding are quite low during irradiation.

The most significant uncertainty associated with the cladding dimensions (d_o, d_i), wall thickness, and oxide layer thickness is user variability. The same user can attempt to measure the same dimension in the same location on the same sample repeatedly, but readily have observable variations of ±10 µm for d_o and d_i, ±3 µm for cladding wall thickness, and ±0.5 µm for oxide layer thickness which is performed at a much higher magnification. The project is currently performing a statistical analysis to determine quantitative values for error from user variability. Similarly, locations are known to have an uncertainty of approximately ±2 mm (see Section 3.3), although since FK-4-1 is at the bottom of the rod, the location uncertainty is approximately ±1 mm.

Table 5-8. FK-4-1 PIE Summary Table.

FK-4-1 Subsample ID	Location from Bottom of Rod (mm)[1]	Average Wall Thickness (µm)[2]	Range of Oxide Thickness (µm)[3]	Average H Concentration (ppm)	Average Microhardness (HV)
FK-4-1-1	15-28	563	3.7 - 6.2	67	283
FK-4-1-2	29-41	566	1.7 – 6.0	66	287
FK-4-1-3	42-55	562	2.3 – 6.4	46	285
FK-4-1-4	55-68	566	3.6 – 6.9	56	287
FK-4-1-5	69-82	563	1.9 – 5.4	53	285
FK-4-1-6	82-95	565	2.3 – 6.1	46	284
FK-4-1-7	95-101	573	1.1 – 3.8	NA[4]	288

[1] *Positions are rounded to the nearest mm accounting for saw kerf and are known to ±2 mm.*
[2] *Wall thickness is estimated to have an uncertainty of ±3 µm*
[3] *Oxide thickness is estimated to have an uncertainty of ± 0.5 µm*
[4] *NA = Not Analyzed (not enough sample to perform LECO total hydrogen analysis)*

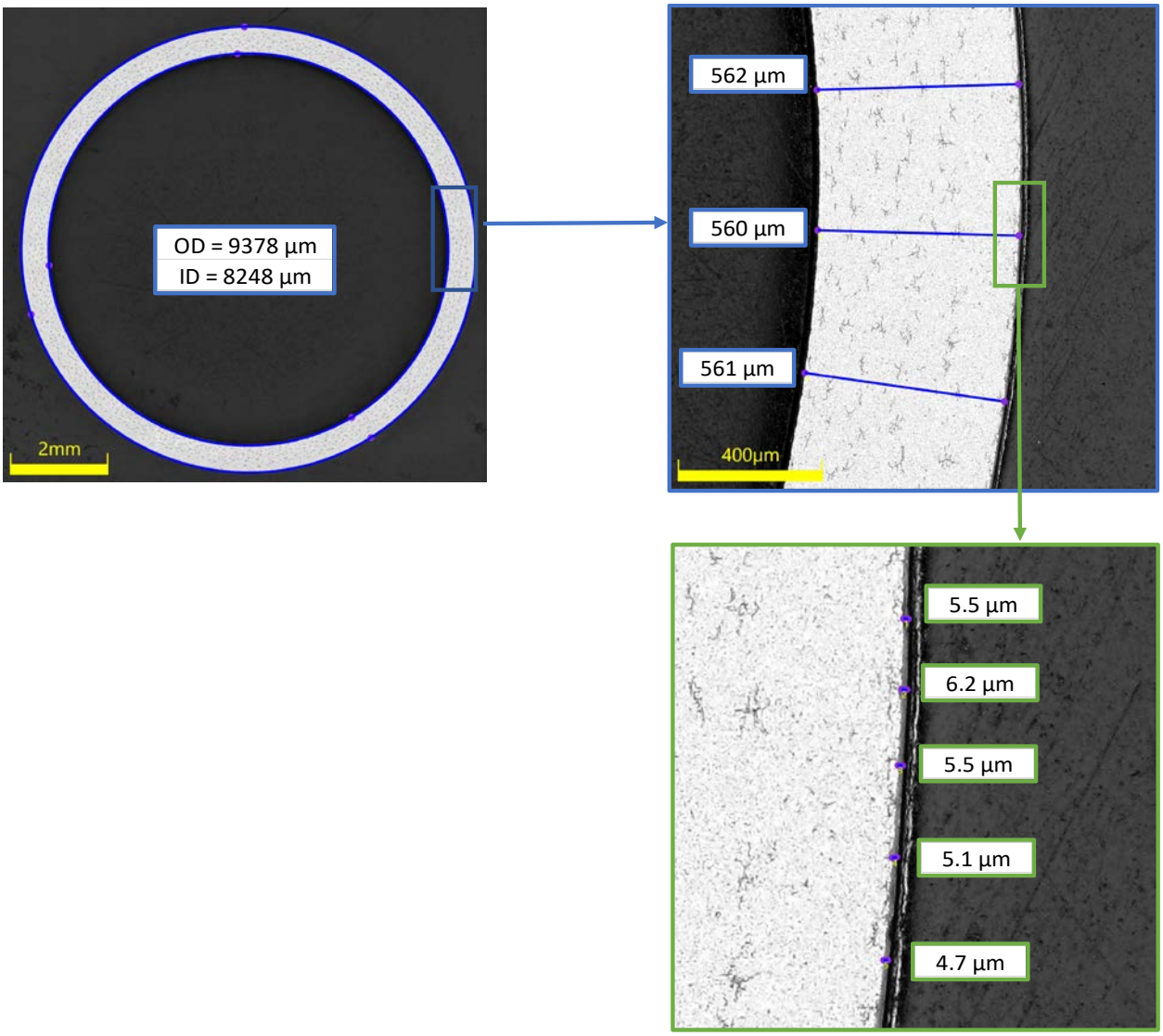

Figure 5-19. Quadrant B of Sample FK-4-1-1 (Rod Location 15 mm – 28 mm).

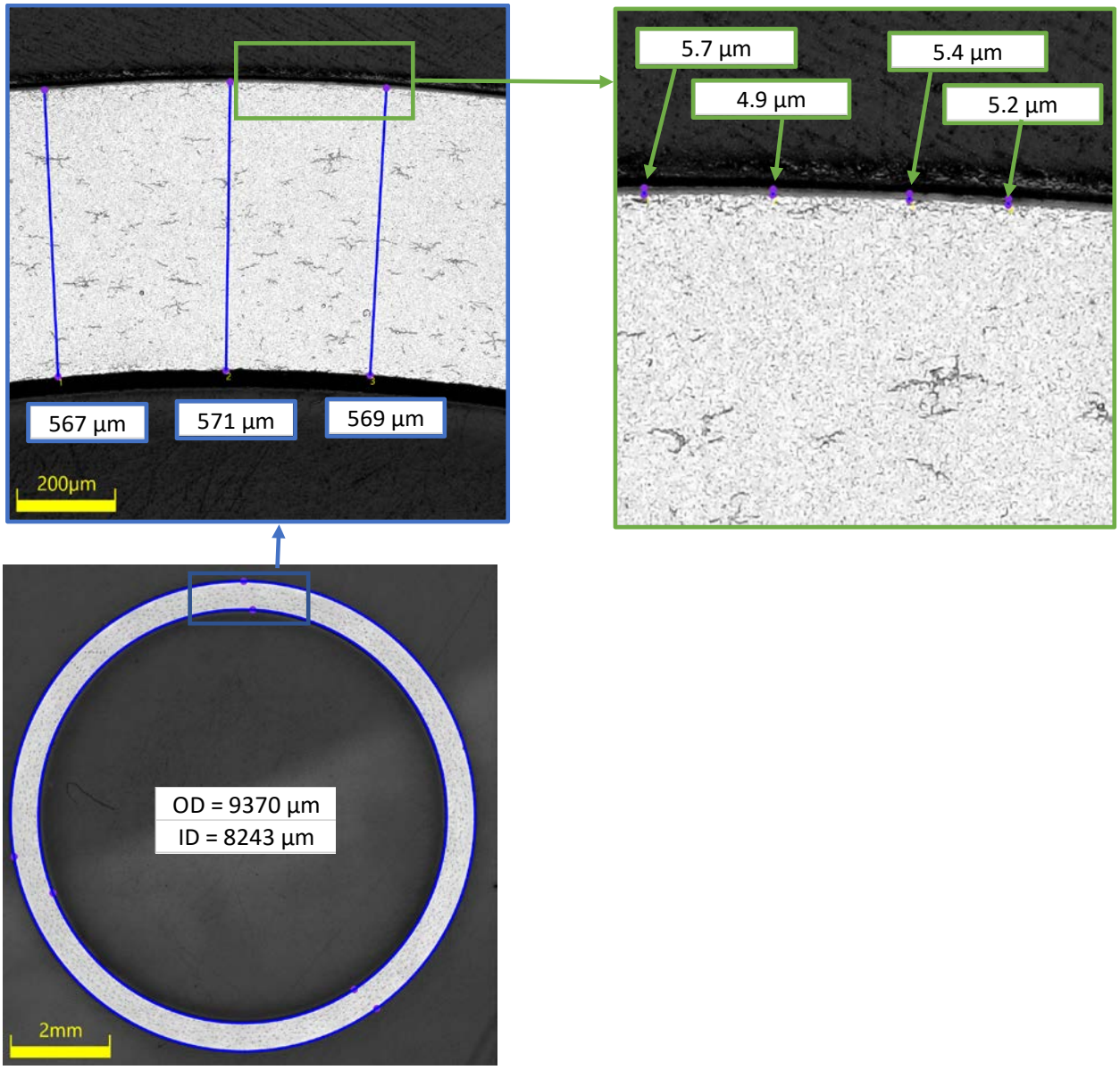

Figure 5-20. Quadrant A of Sample FK-4-1-2 (Rod Location 29 mm – 41 mm).

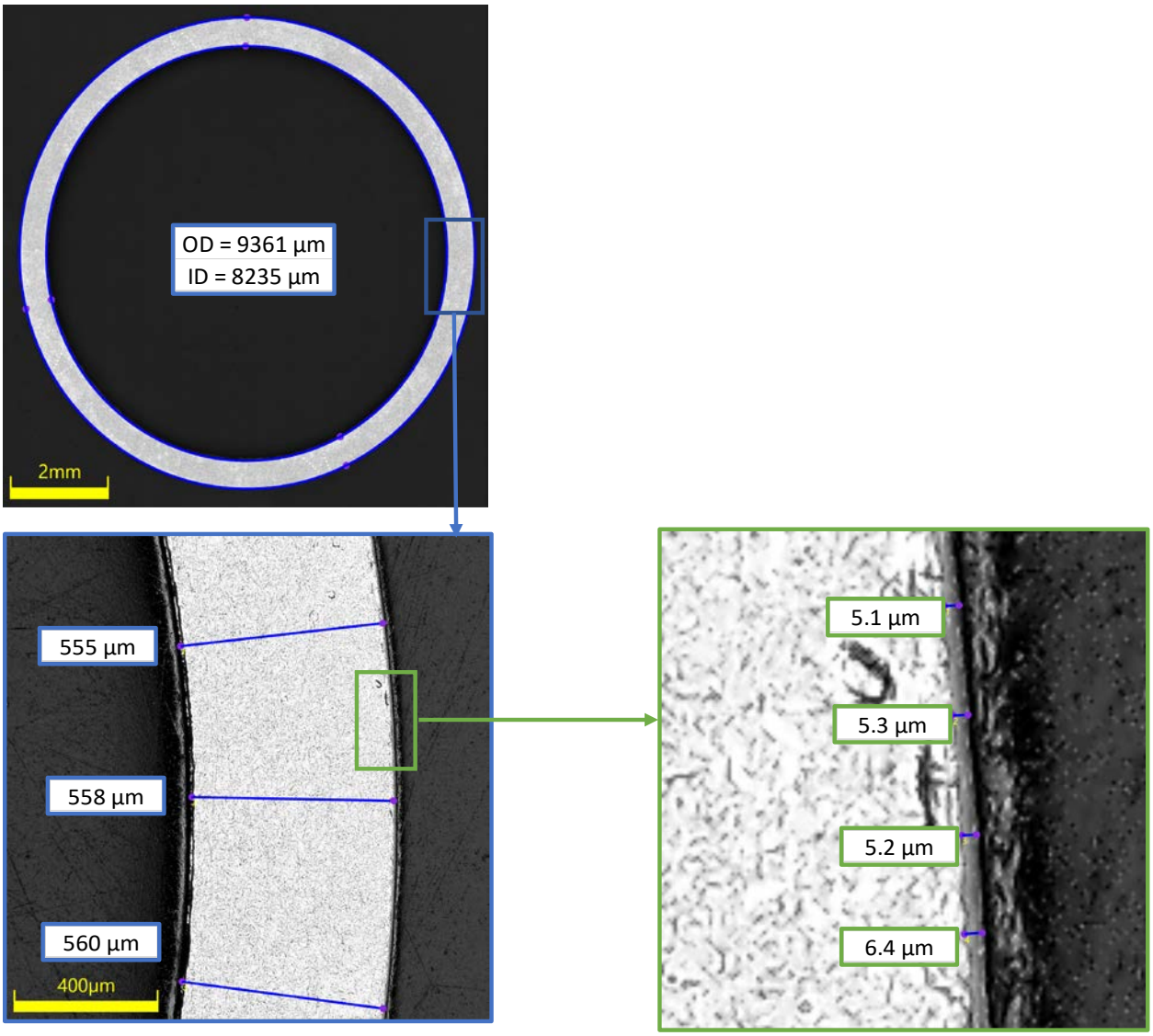

Figure 5-21. Quadrant B of Sample FK-4-1-3 (Rod Location 42 mm – 55 mm).

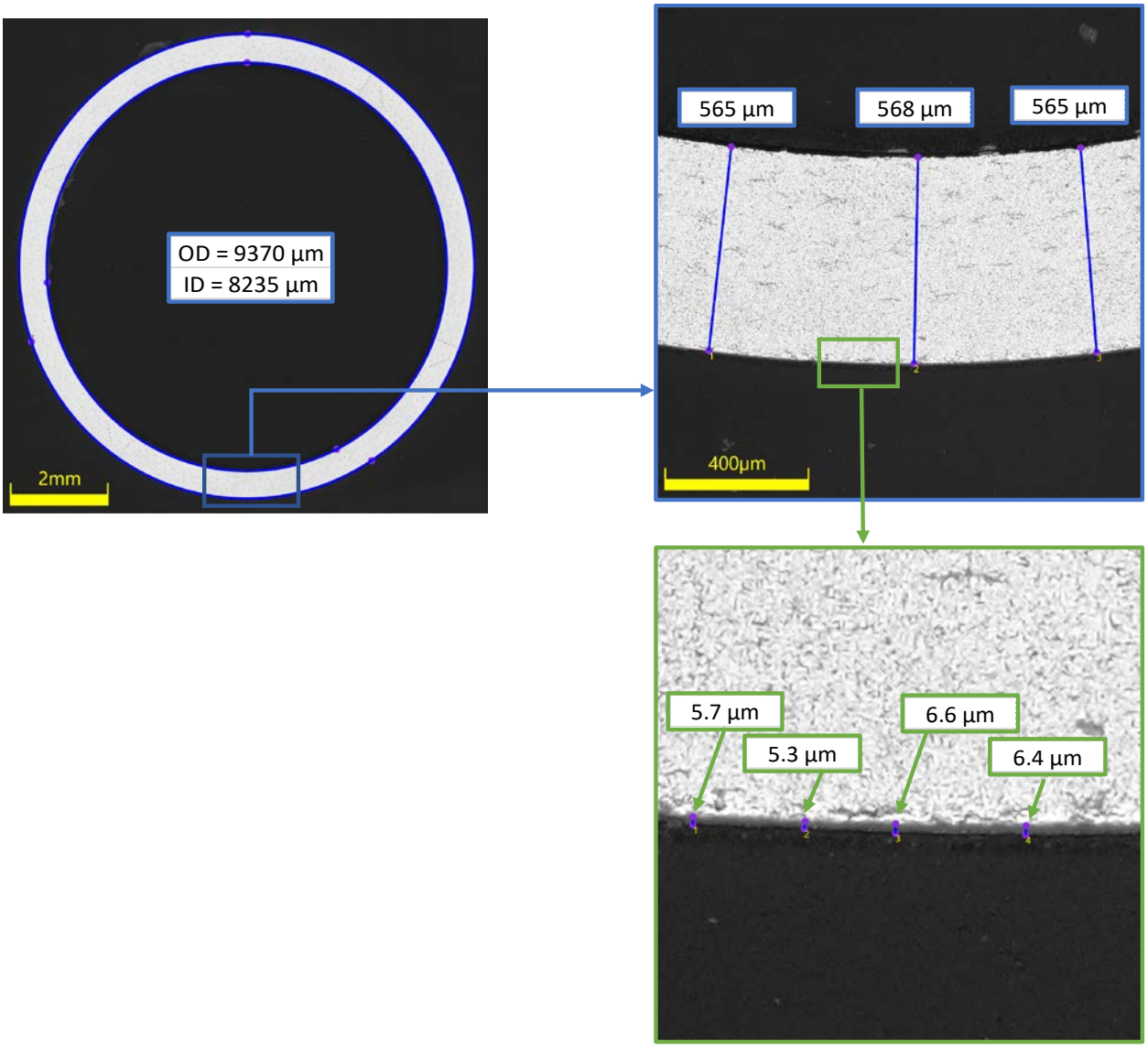

Figure 5-22. Quadrant C of Sample FK-4-1-4 (Rod Location 55 mm – 68 mm).

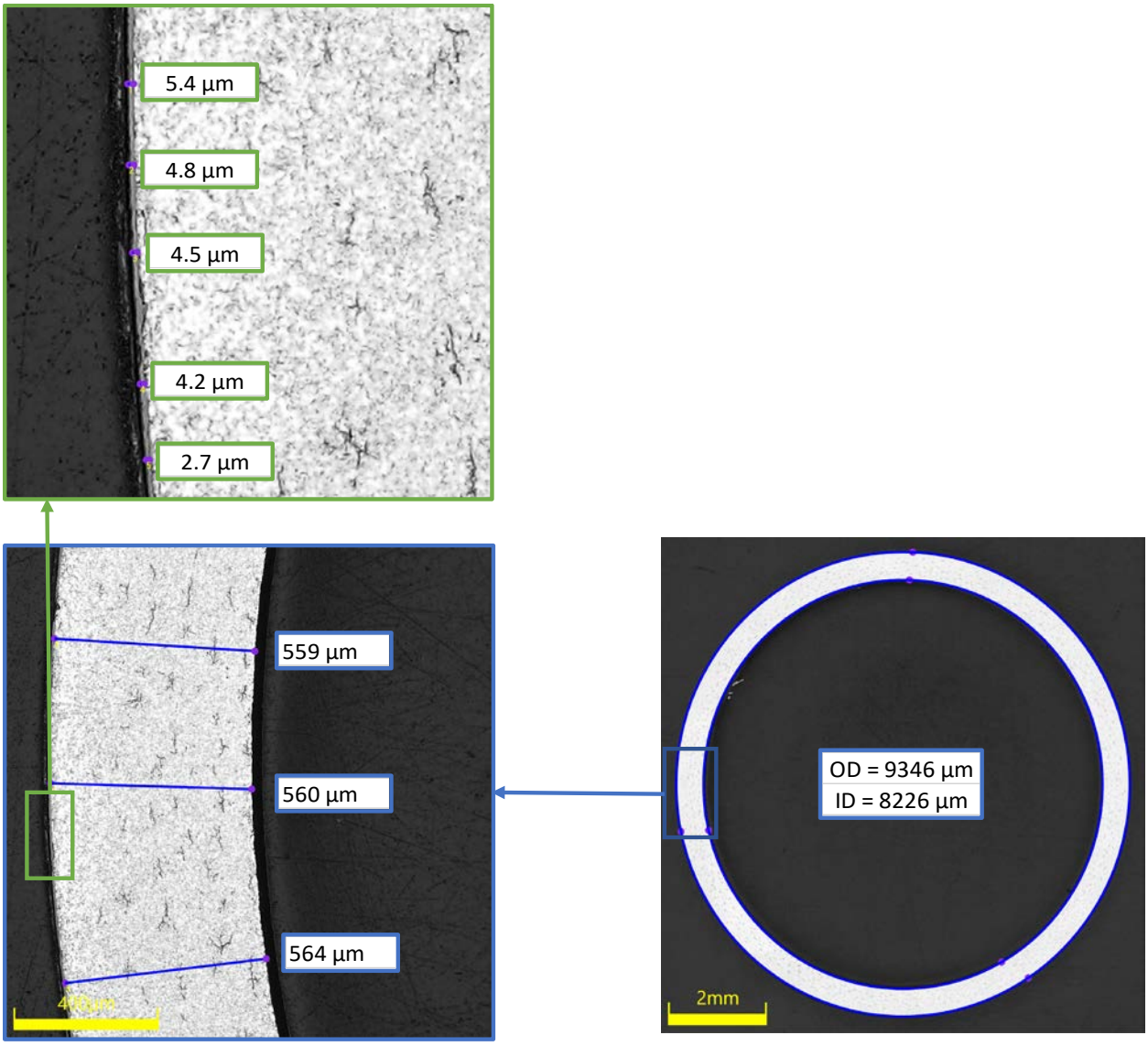

Figure 5-23. Quadrant D of Sample FK-4-1-5 (Rod Location 69 mm – 82 mm).

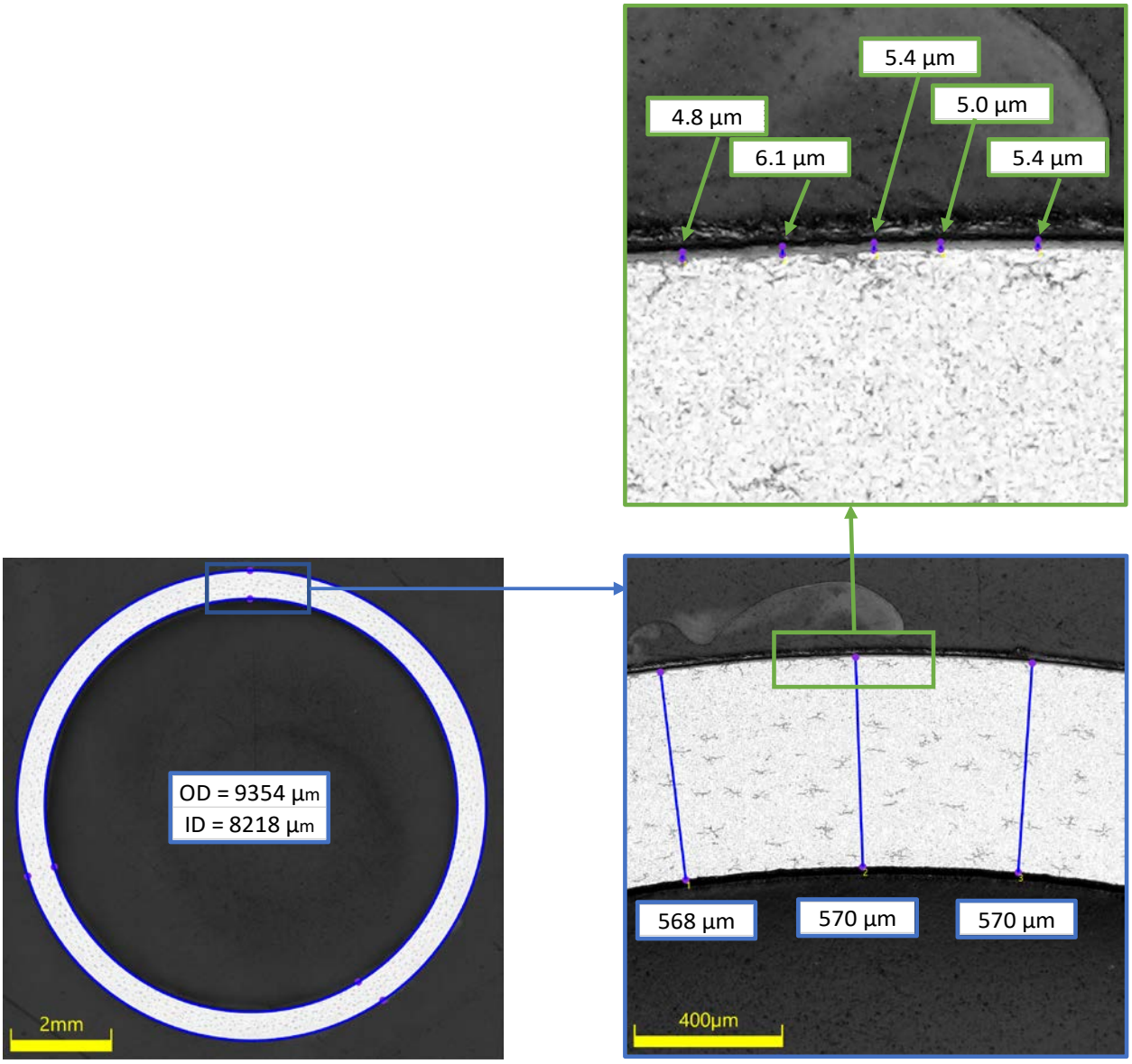

Figure 5-24. Quadrant D of Sample FK-4-1-6 (Rod Location 82 mm – 95 mm).

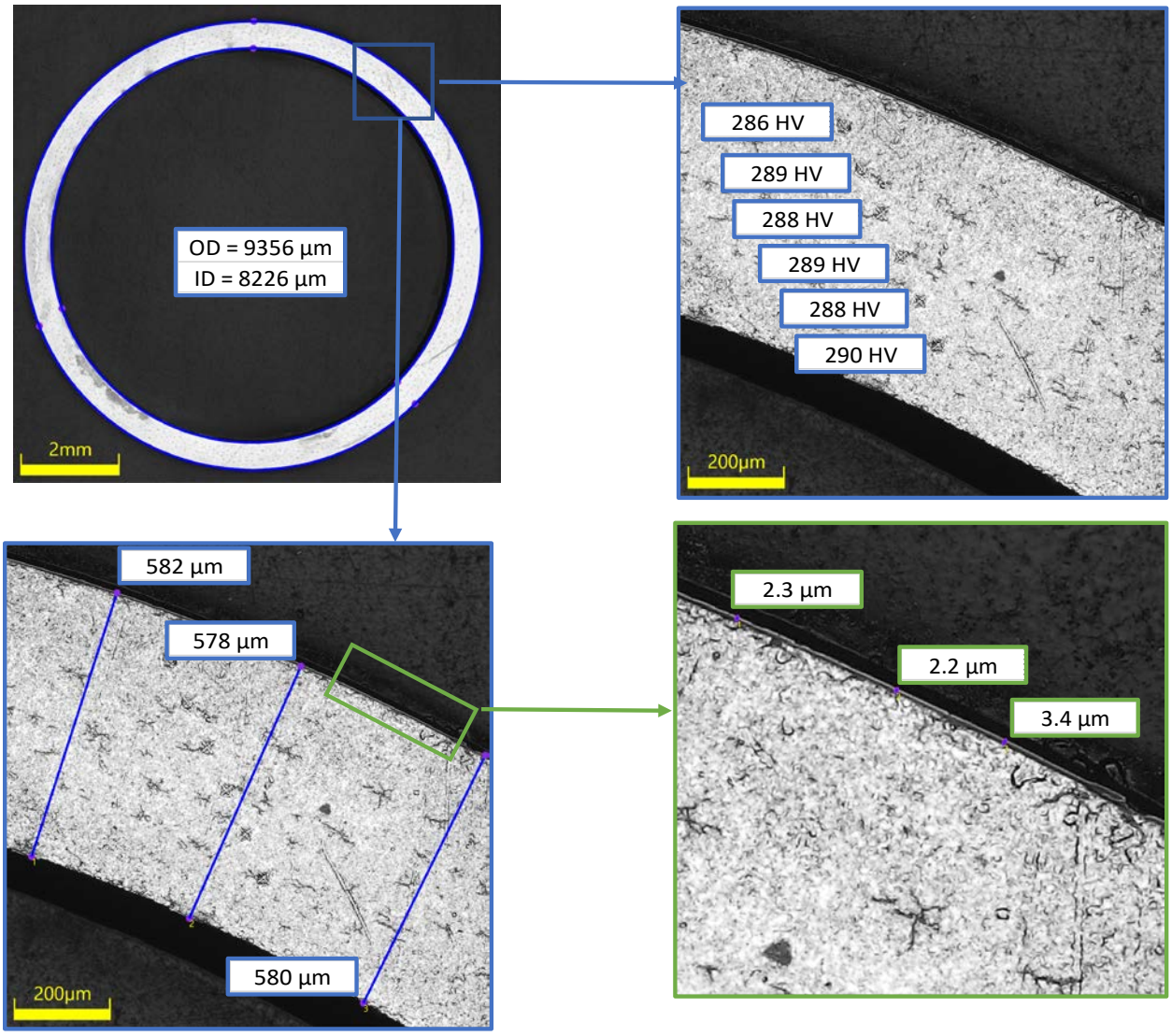

Figure 5-25. Quadrant A of Sample FK-4-1-7 (Rod Location 95 mm – 101 mm).

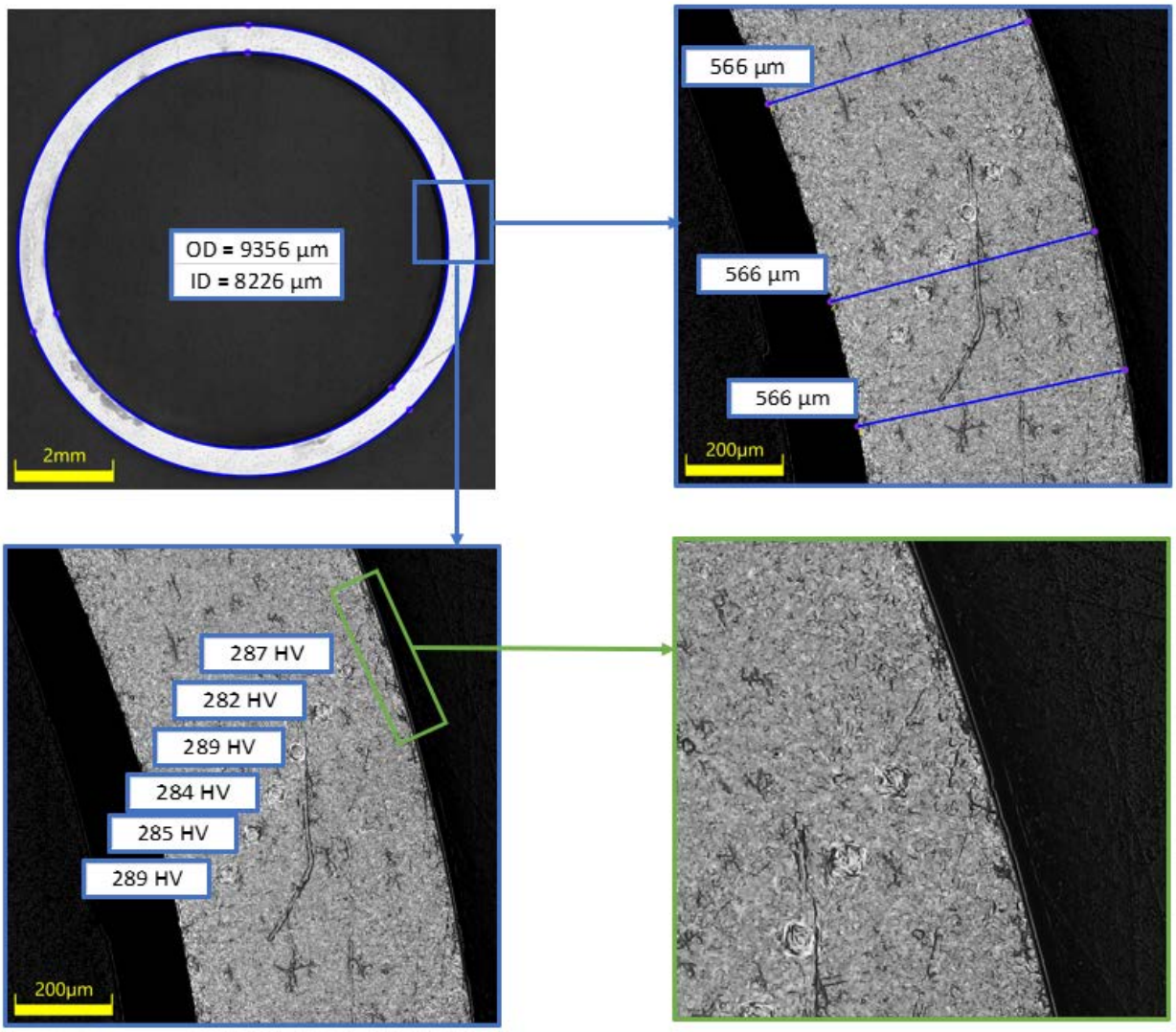

Figure 5-26. Quadrant B of Sample FK-4-1-7 (Rod Location 95 mm – 101 mm).

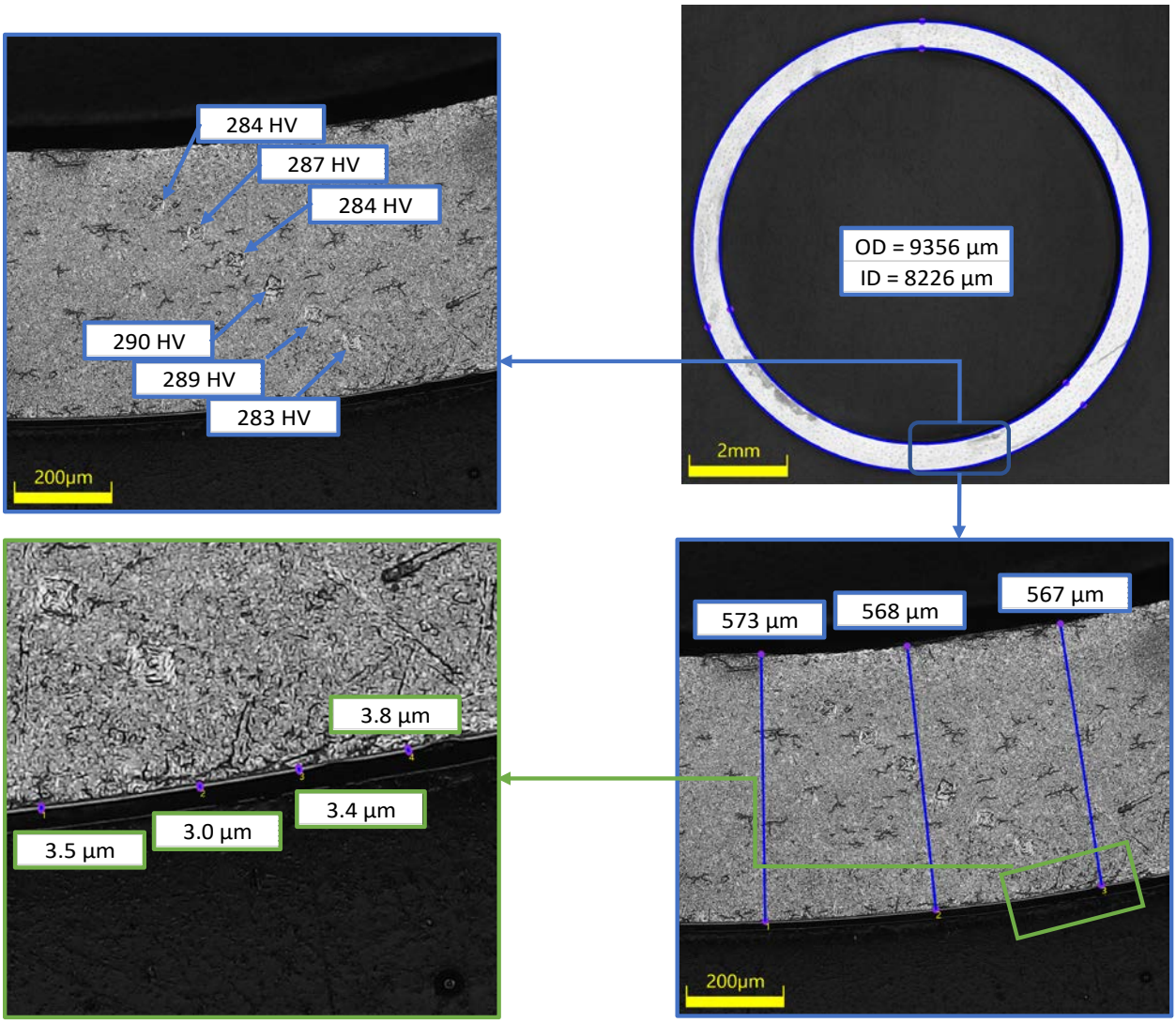

Figure 5-27. Quadrant C of Sample FK-4-1-7 (Rod Location 95 mm – 101 mm).

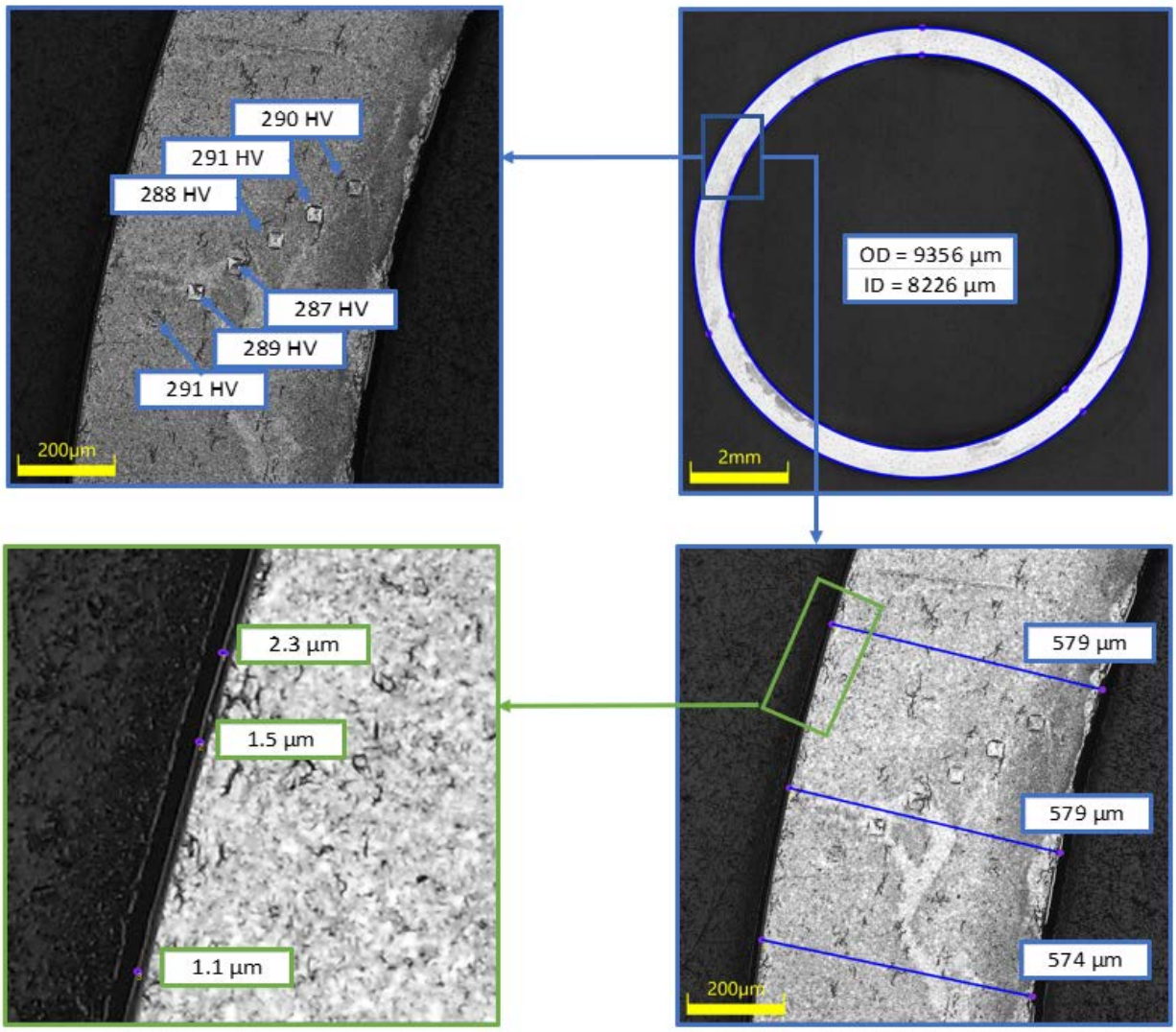

Figure 5-28. Quadrant D of Sample FK-4-1-7 (Rod Location 95 mm – 101 mm).

5.4.5 Results from Segment UL-1 from Rod 6U3L8 (2909 mm – 3852 mm)

PIE measurements of rod 6U3L8 has started, beginning with the top segment (UL-1) of the rod. Most of this segment is in the lower burnup upper end of the fuel rod, but cladding temperatures are higher than the lower portions of the rod. Optical microscopy, microhardness, and hydrogen determination has been performed on five subsamples spanning 3049 mm and 3670 mm from the bottom of the rod. This section gives an overview of the results from UL-1, as shown in Table 5-9. Figure 5-29 through Figure 5-32 show the results for the four quadrants of UL-1-2, Figure 5-33 through Figure 5-36 for UL-1-4, Figure 5-37 through Figure 5-40 for UL-1-6, Figure 5-41 through Figure 5-44 for UL-1-8, and Figure 5-45 through Figure 5-48 for UL-1-10. Appendix E contains more details and images.

The most significant uncertainty associated with the cladding dimensions (d_o, d_i), wall thickness, and oxide layer thickness) is user variability. The same user can attempt to measure the same dimension in the same location on the same sample repeatedly, but readily have observable variations of ±10 µm for d_o and d_i, ±3 µm for cladding wall thickness, and ±0.5 µm for oxide layer thickness which is performed at a much higher magnification. The project is currently performing a statistical analysis to determine quantitative values for error from user variability. Similarly, locations are known to have an uncertainty of approximately ±2 mm (see Section 3.3).

Table 5-9. UL-1 PIE Summary Table.

UL-1 Subsample ID	Location from Bottom of Rod (mm)[1]	Average Wall Thickness (µm)[2]	Range of Oxide Thickness (µm)[3]	Average H Concentration (ppm)	Average Microhardness (HV)
UL-1-2	3061-3073	542	21.5 – 26.6	*In Progress*	267
UL-1-4	3226-3238	539	24.5 – 32.3	*In Progress*	260
UL-1-6	3391-3403	542	26.3 – 36.2	*In Progress*	267
UL-1-8	3505-3518	541	24.5 – 39.3	*In Progress*	265
UL-1-10	3671-3683	545	17.7 – 23.8	*In Progress*	269

[1]*Positions are rounded to the nearest mm accounting for saw kerf and are known to ±2 mm.*
[2]*Wall thickness is estimated to have an uncertainty of ±3 µm*
[3]*Oxide thickness is estimated to have an uncertainty of ± 0.5 µm*

The outer diameter of sections from Rod UL-1 was measured by optical microscopy and an optical micrometer. The inner diameter was measured by optical microscopy and air gauge. Differences between these values are expected. The optical microscope measurements were taken at a single location. The optical micrometer and air gauge both take an average along the length of a 150 mm long sample. The optical microscope measurement does not include the oxide layer, while the optical micrometer does. Section 4.3 goes into detail about the instruments and methodology used to measure cladding d_o and d_i by optical micrometer and air gauge. All d_o and d_i measurements taken of Rod UL-1 are presented in Table 5-10.

Table 5-10. UL-1 OD and ID Measurements.

			Optical Micrometer	Optical Microscope	Air Gauge	Optical Microscope
Sample ID	**Test**	**Location from Bottom of Rod (mm)[1]**	**Avg d_o Measure after fuel dissolution (mm)[2,3]**	**Avg d_o Measure after fuel dissolution (mm)[4]**	**Avg d_i Measure after fuel dissolution (mm)[5]**	**Avg d_i Measure after fuel dissolution (mm)[4]**
UL-1-10	PIE	3671-3683		9.314		8.196
UL-1-9	BEND 25°C	3518-3670	9.4157		8.2639	
UL-1-8	PIE	3505-3518		9.307		8.183
UL-1-6	PIE	3391-3403		9.292		8.179
UL-1-4	PIE	3226-3238		9.296		8.188
UL-1-3	BURST 25°C	3074-3225	9.4372		8.2760	
UL-1-2	PIE	3061-3073		9.287		8.212
UL-1-1	BURST 200°C	2909-3060	9.4411		8.2715	

[1]Positions are rounded to the nearest mm accounting for saw kerf and are known to ±2 mm.

[2]Manufacturer-stated accuracy is ±2 µm

[3]Bias applied to d_o values taken from Table 4.3. Section 4.3 details how bias was calculated.

[4]Diameter measurements taken from optical microscope images are estimated to have an uncertainty of ±10 µm

[5] Manufacturer-stated accuracy is ±1 µm

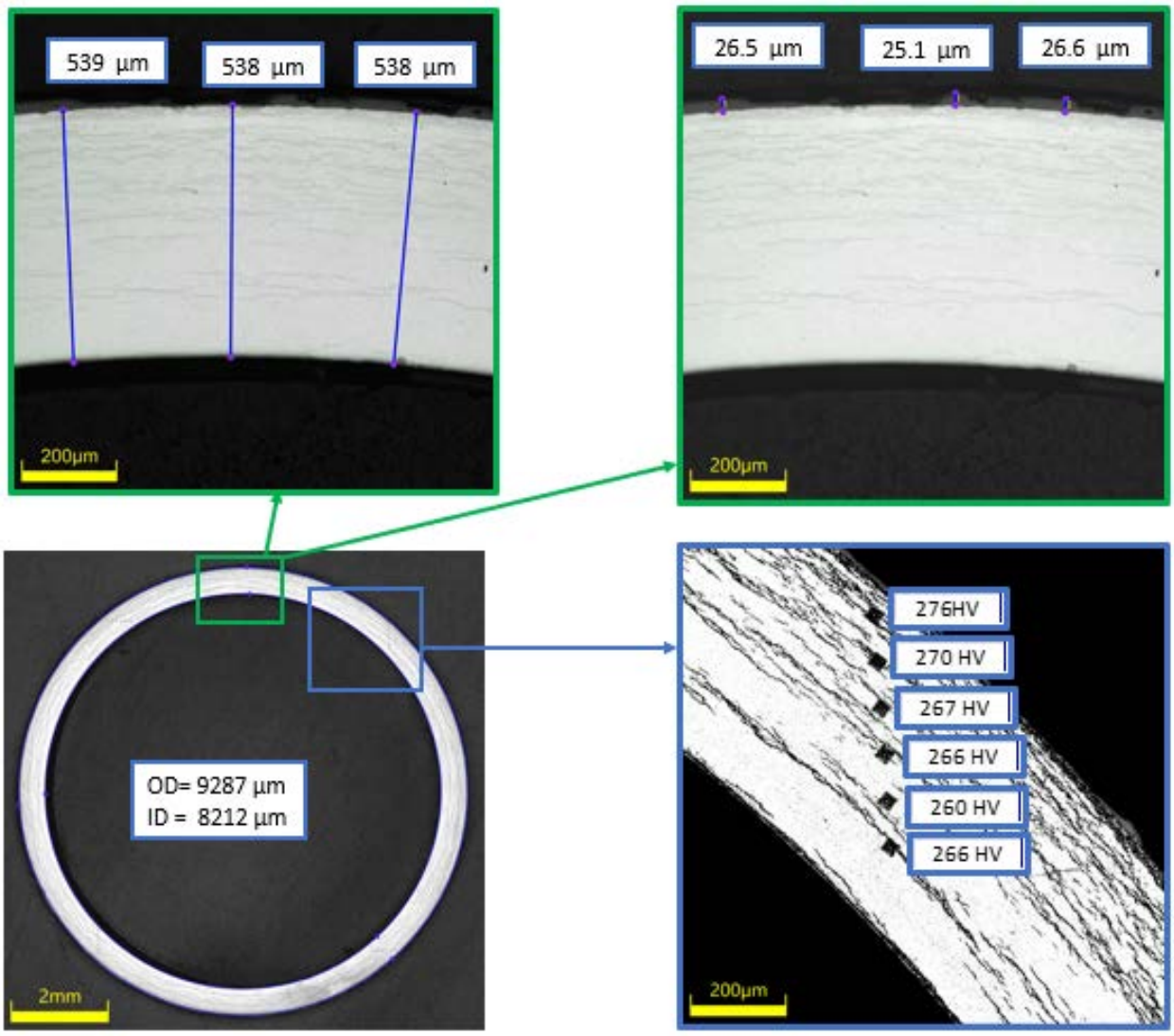

Figure 5-29. Quadrant A of Sample UL-1-2 (Rod Location 3061 mm – 3073 mm).

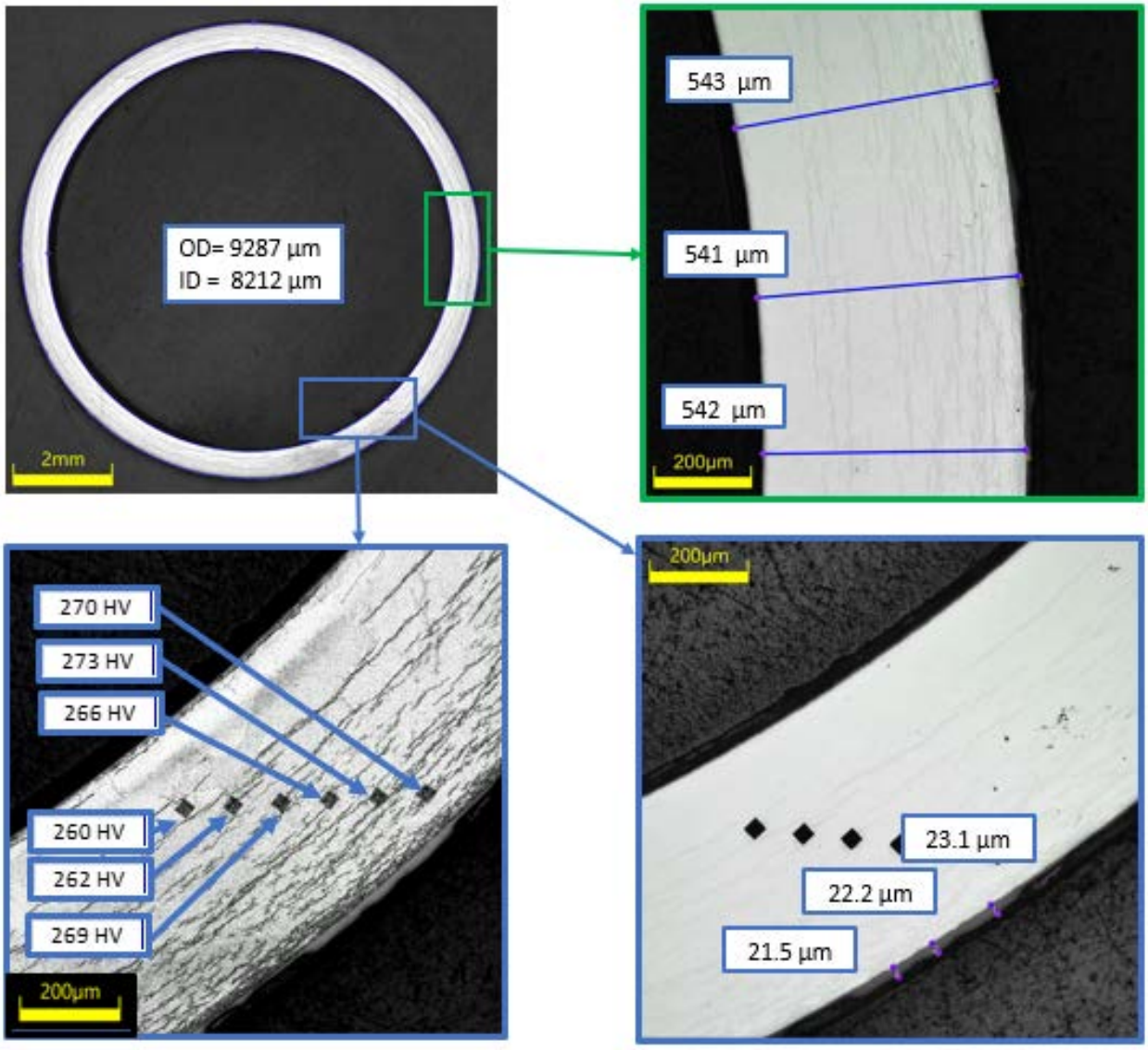

Figure 5-30. Quadrant B of Sample UL-1-2 (Rod Location 3061 mm – 3073 mm).

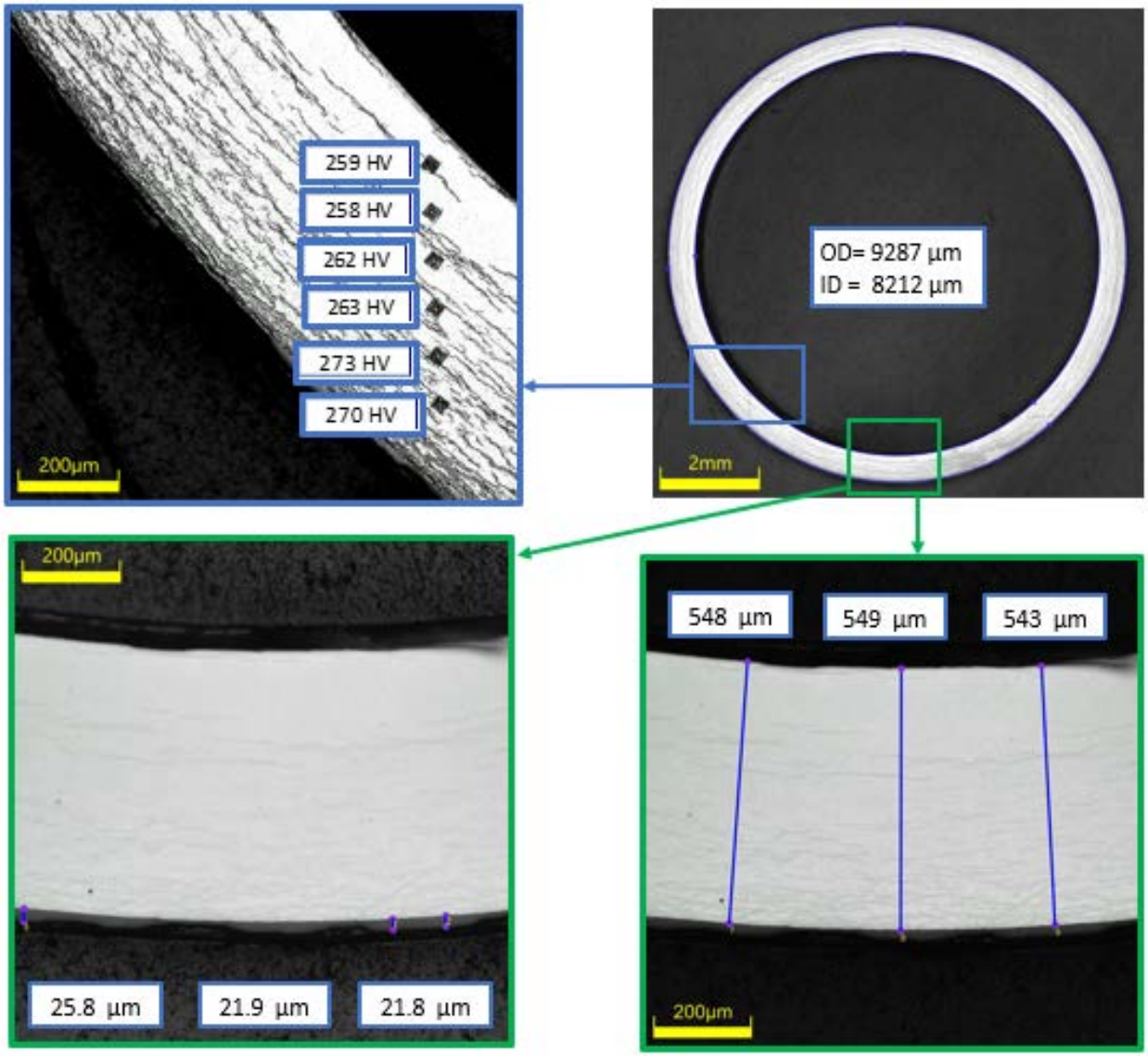

Figure 5-31. Quadrant C of Sample UL-1-2 (Rod Location 3061 mm – 3073 mm).

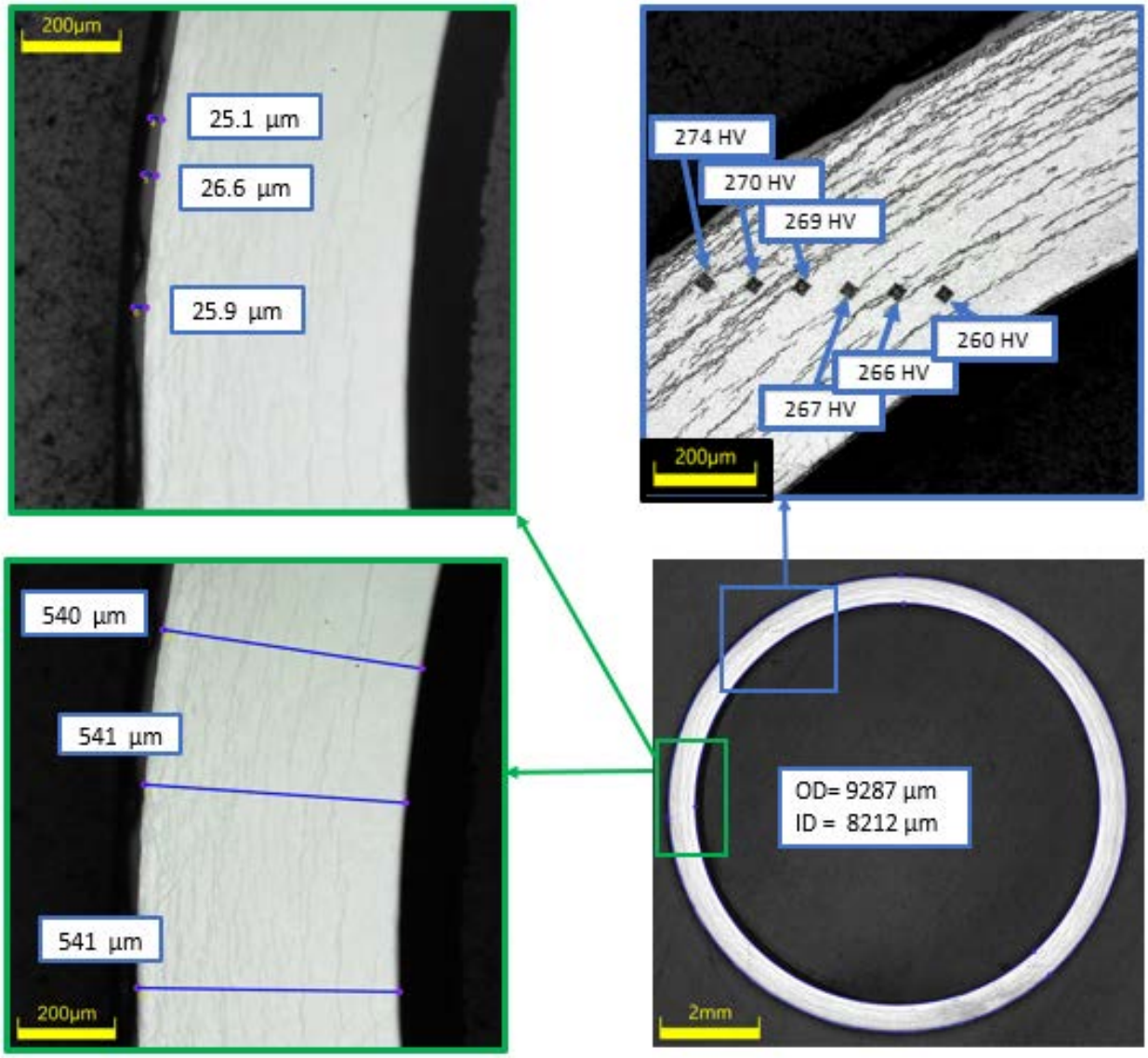

Figure 5-32. Quadrant D of Sample UL-1-2 (Rod Location 3061 mm – 3073 mm).

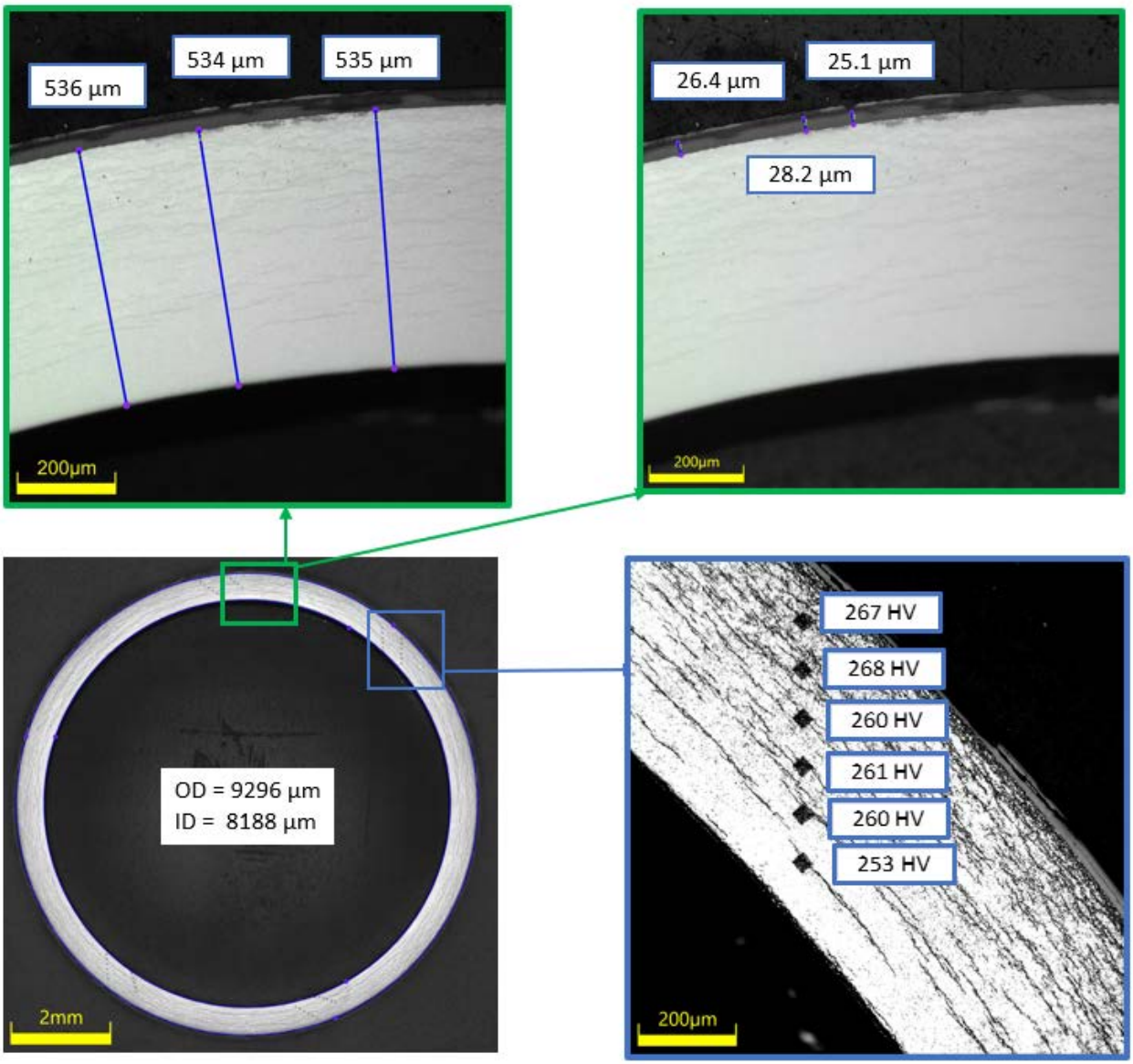

Figure 5-33. Quadrant A of Sample UL-1-4 (Rod Location 3226 mm – 3238 mm).

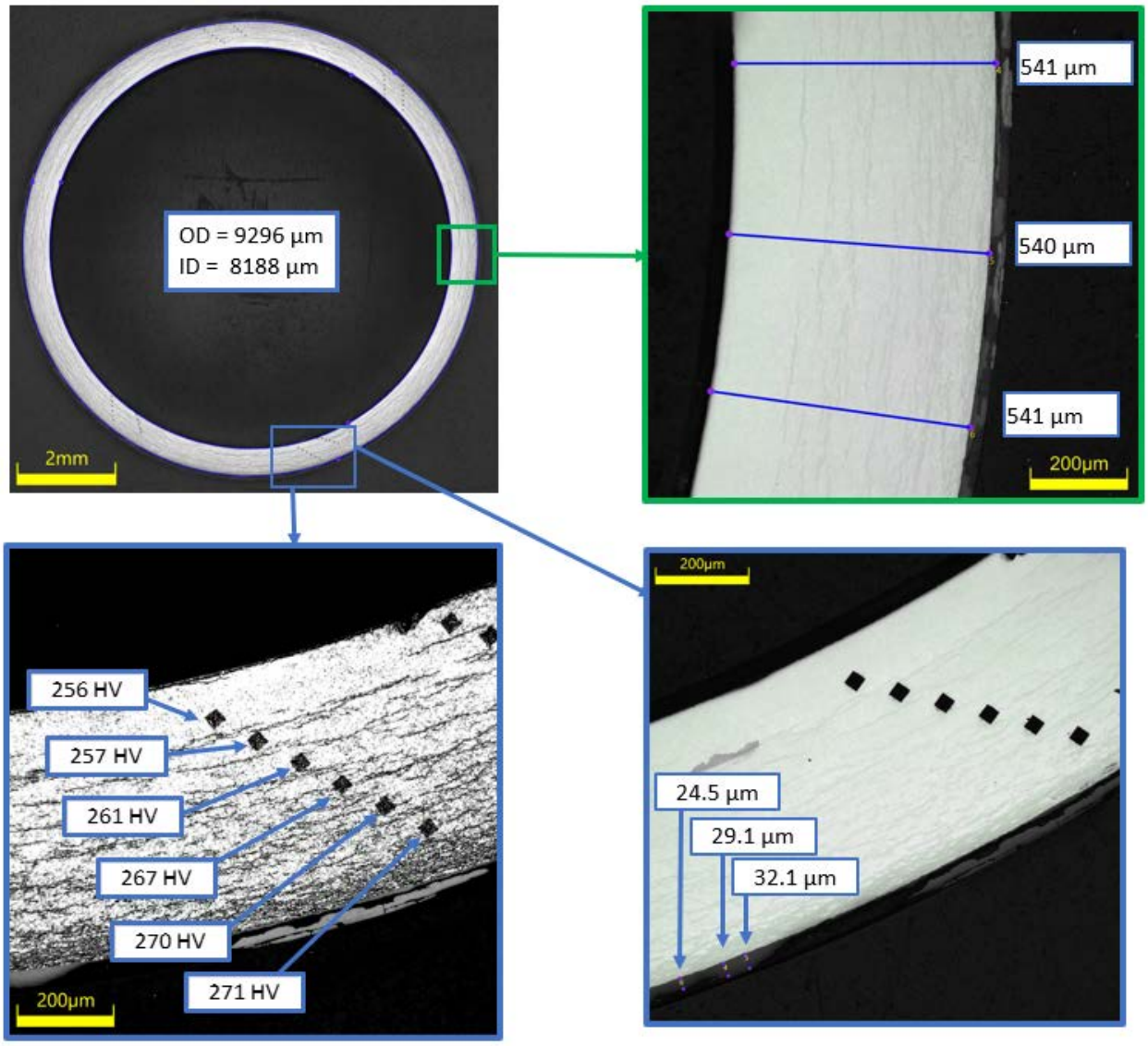

Figure 5-34. Quadrant B of Sample UL-1-4 (Rod Location 3226 mm – 3238 mm).

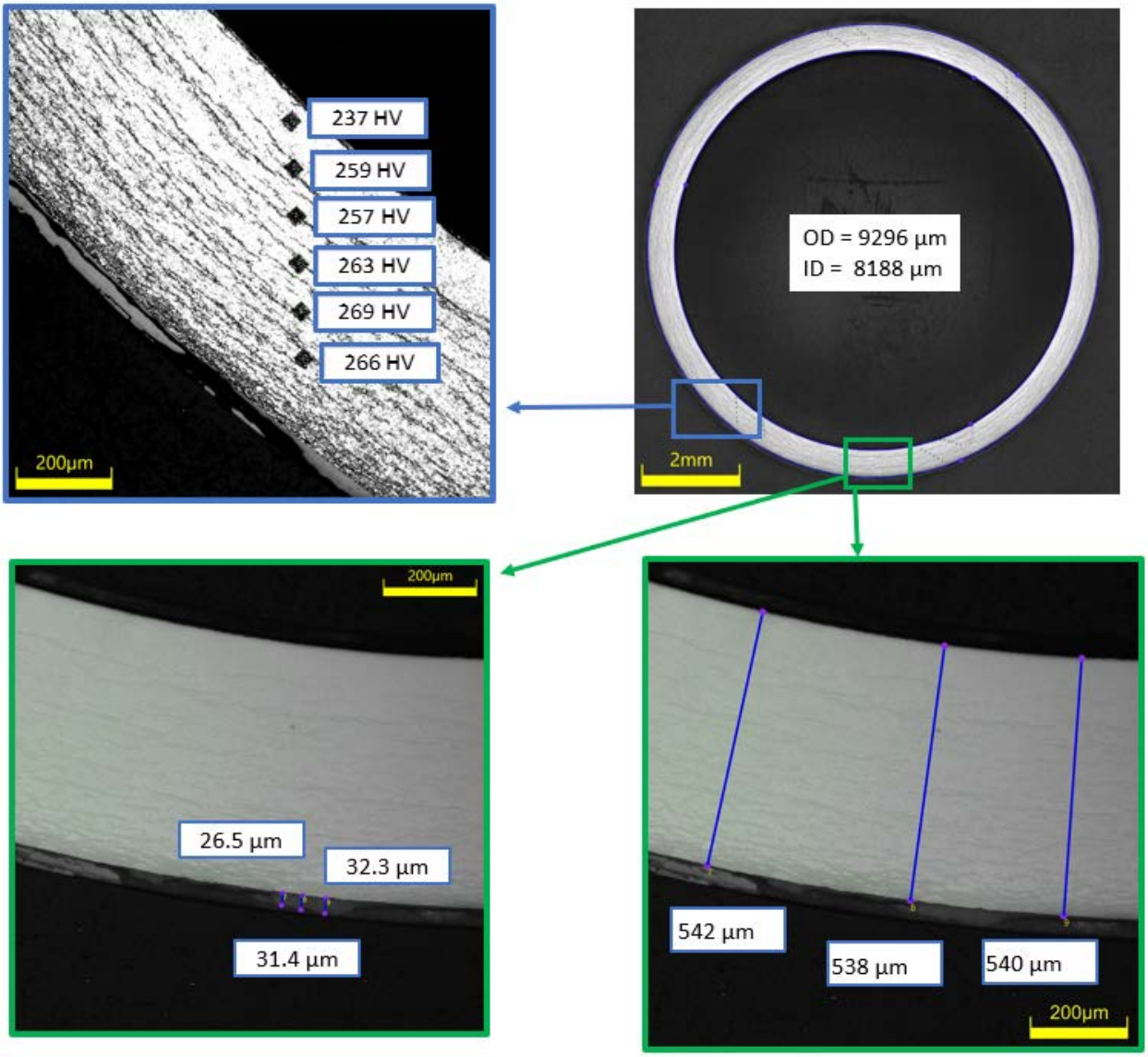

Figure 5-35. Quadrant C of Sample UL-1-4 (Rod Location 3226 mm – 3238 mm).

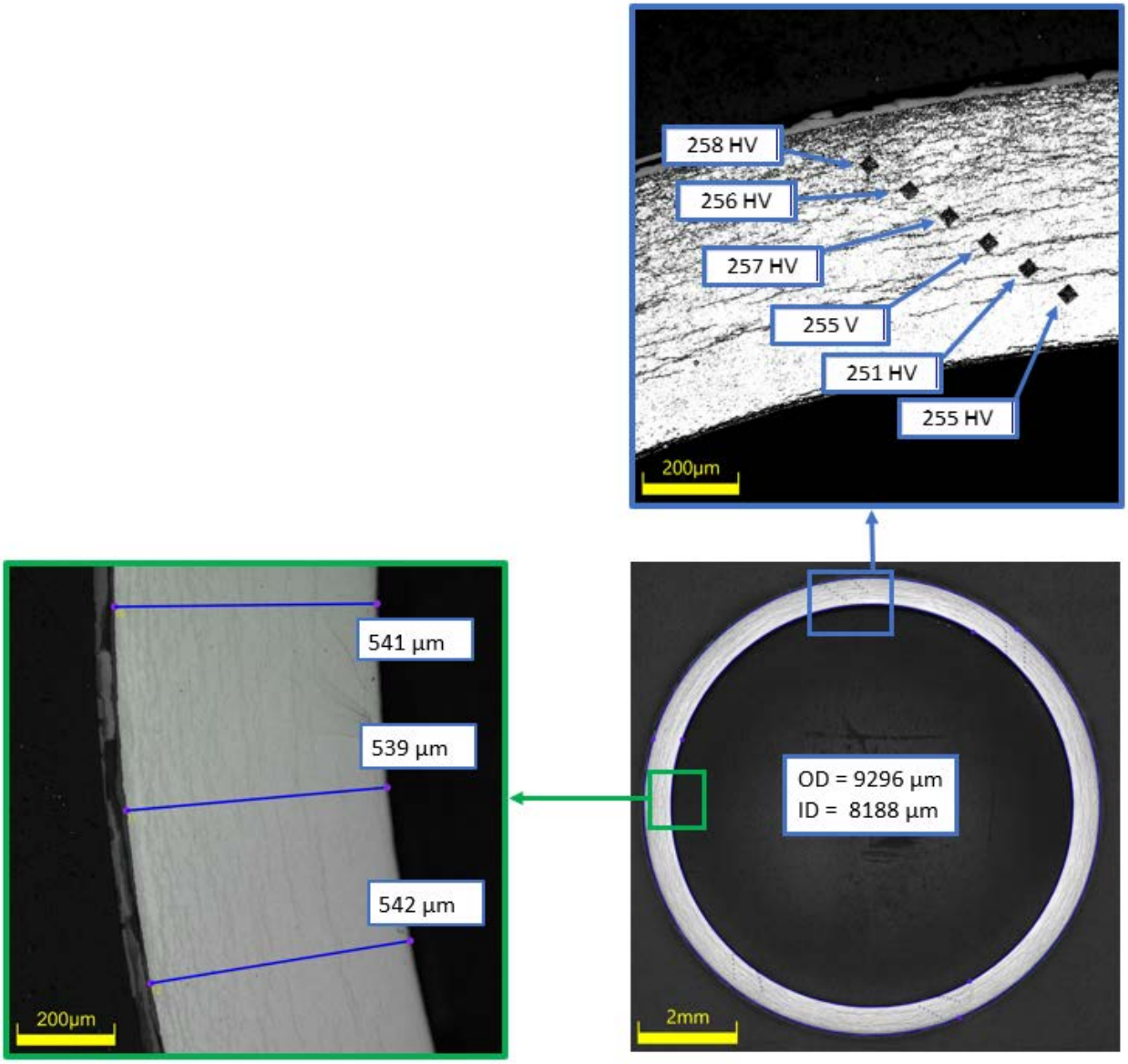

Figure 5-36. Quadrant D of Sample UL-1-4 (Rod Location 3226 mm – 3238 mm).

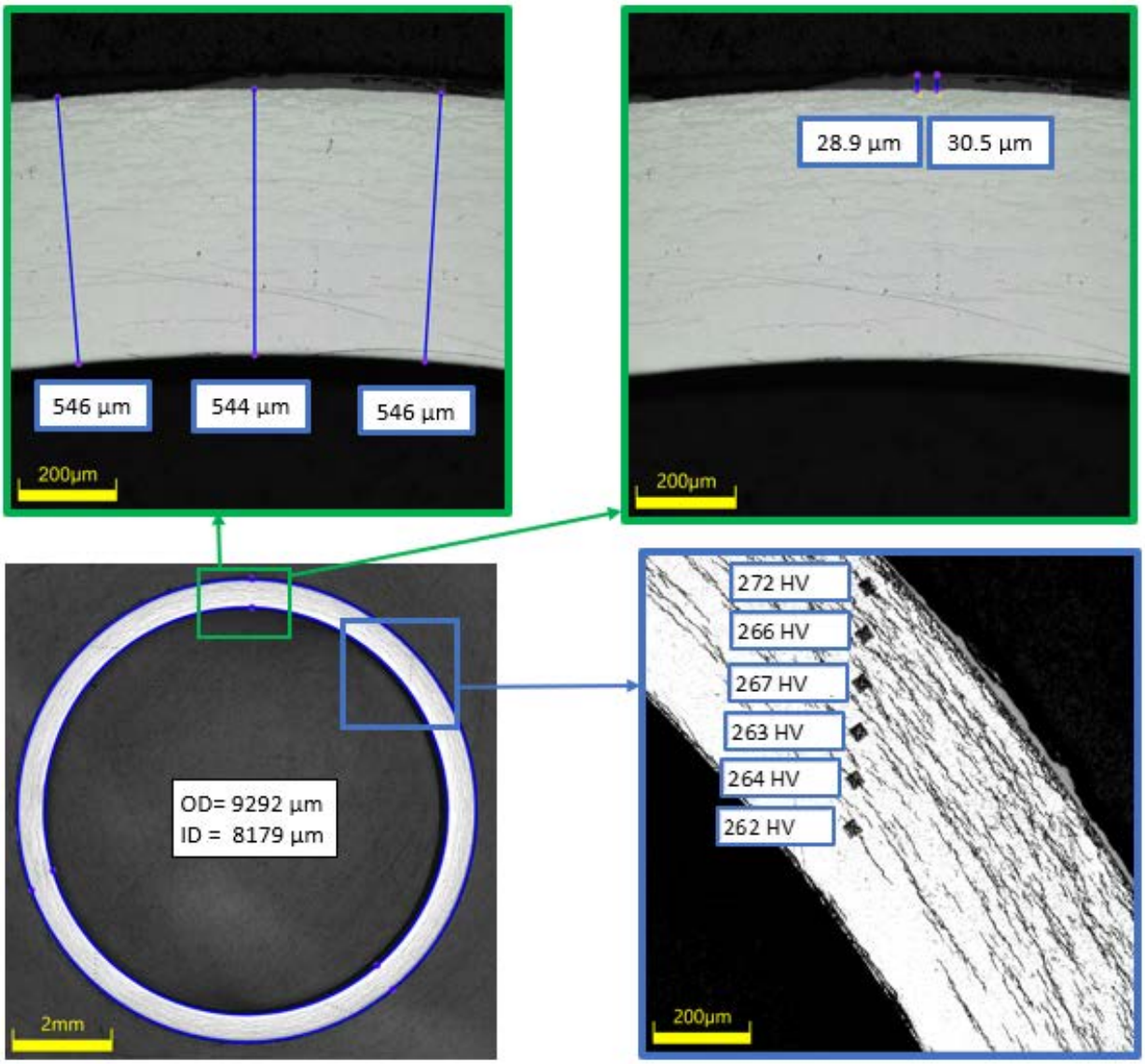

Figure 5-37. Quadrant A of Sample UL-1-6 (Rod Location 3391 mm – 3403 mm).

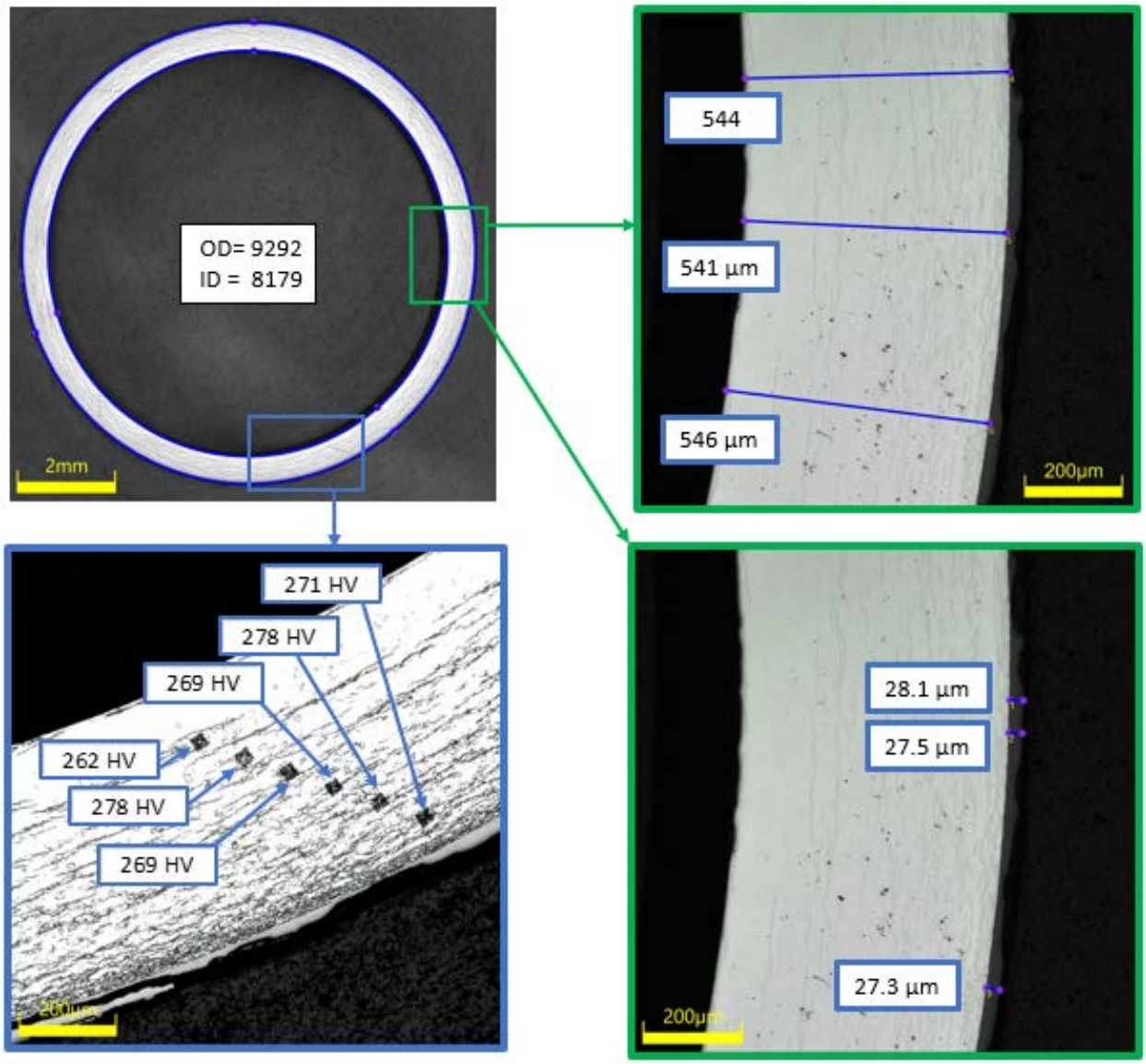

Figure 5-38. Quadrant B of Sample UL-1-6 (Rod Location 3391 mm – 3403 mm).

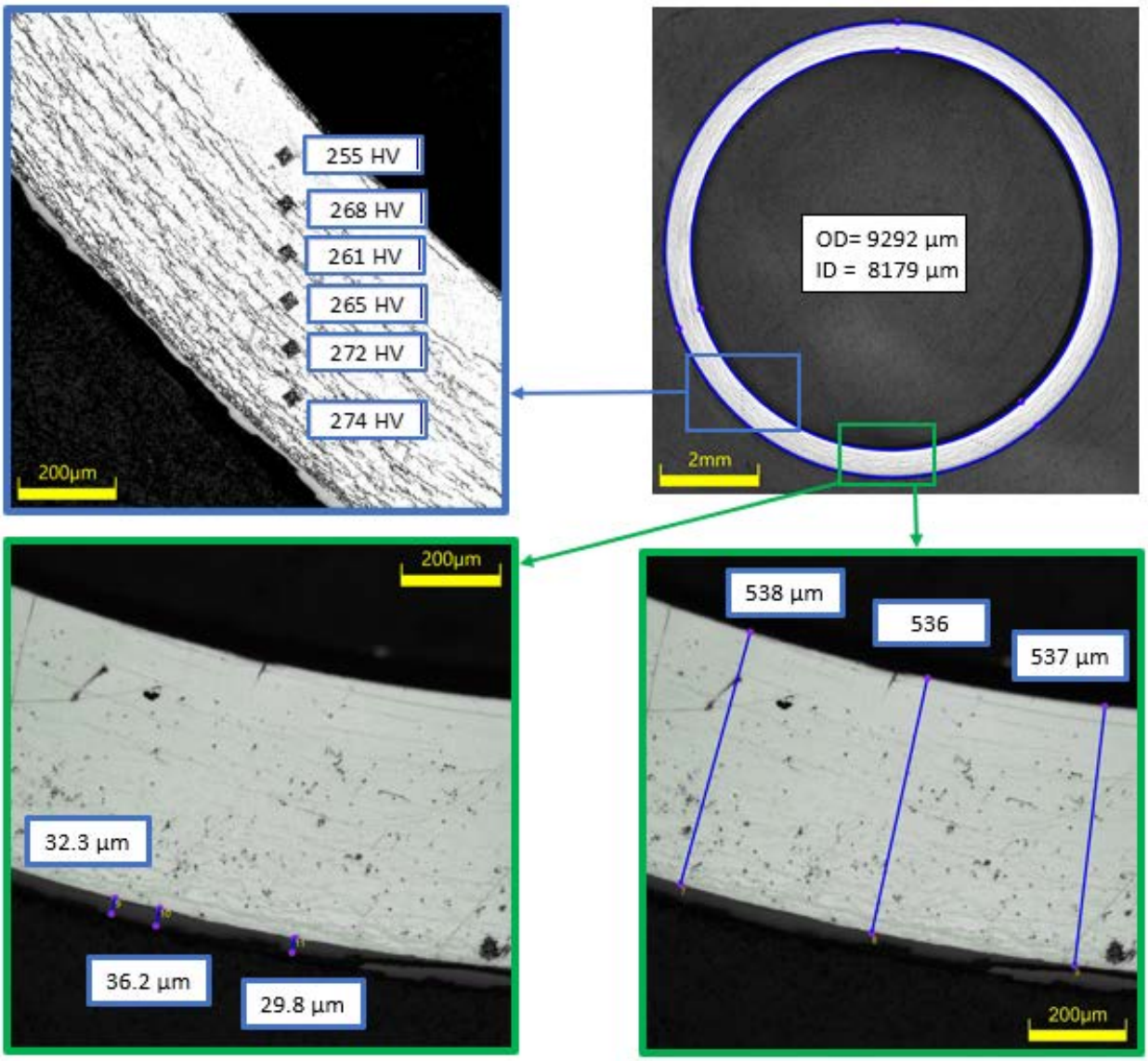

Figure 5-39. Quadrant C of Sample UL-1-6 (Rod Location 3391 mm – 3403 mm).

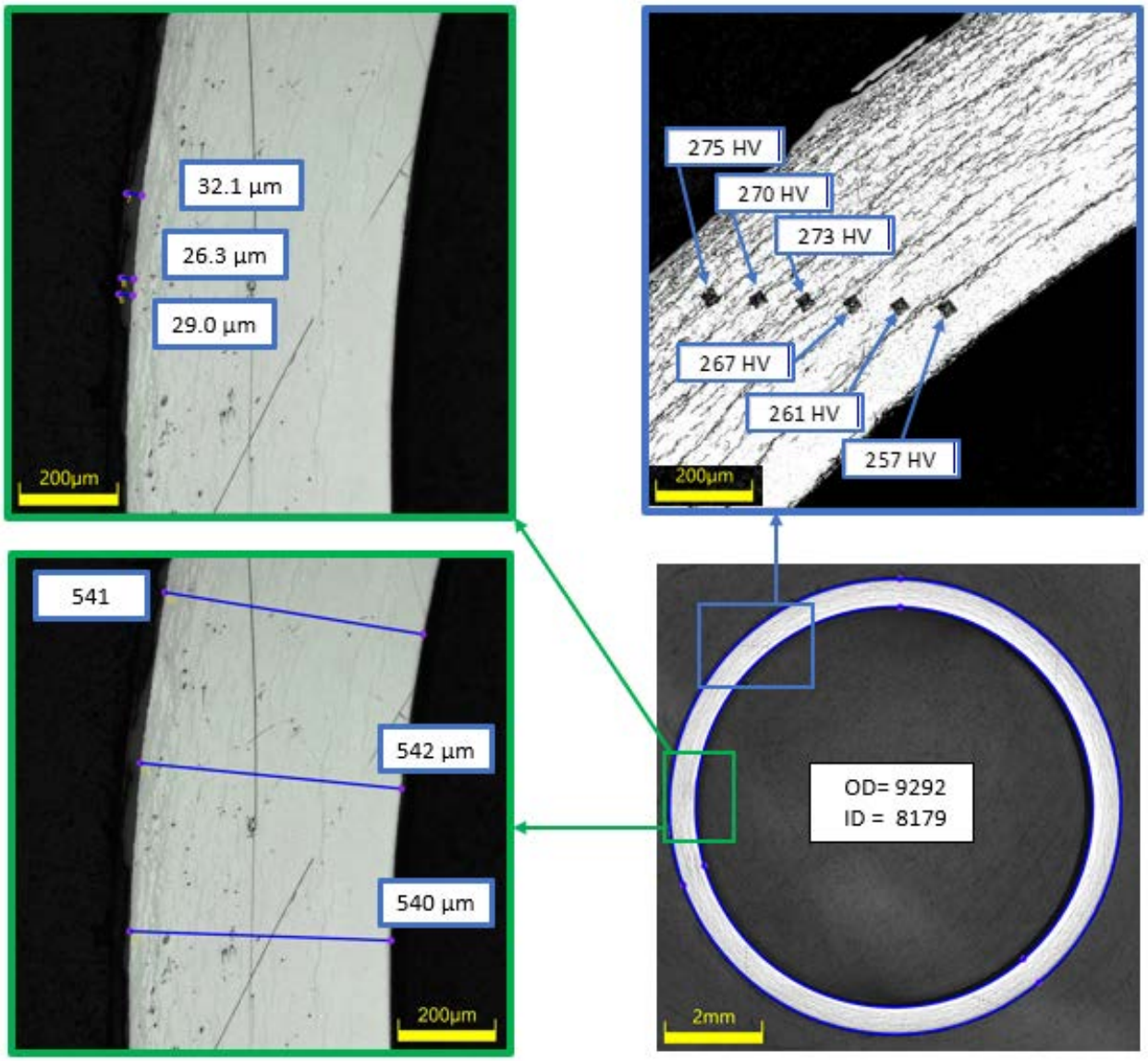

Figure 5-40. Quadrant D of Sample UL-1-6 (Rod Location 3391 mm – 3403 mm).

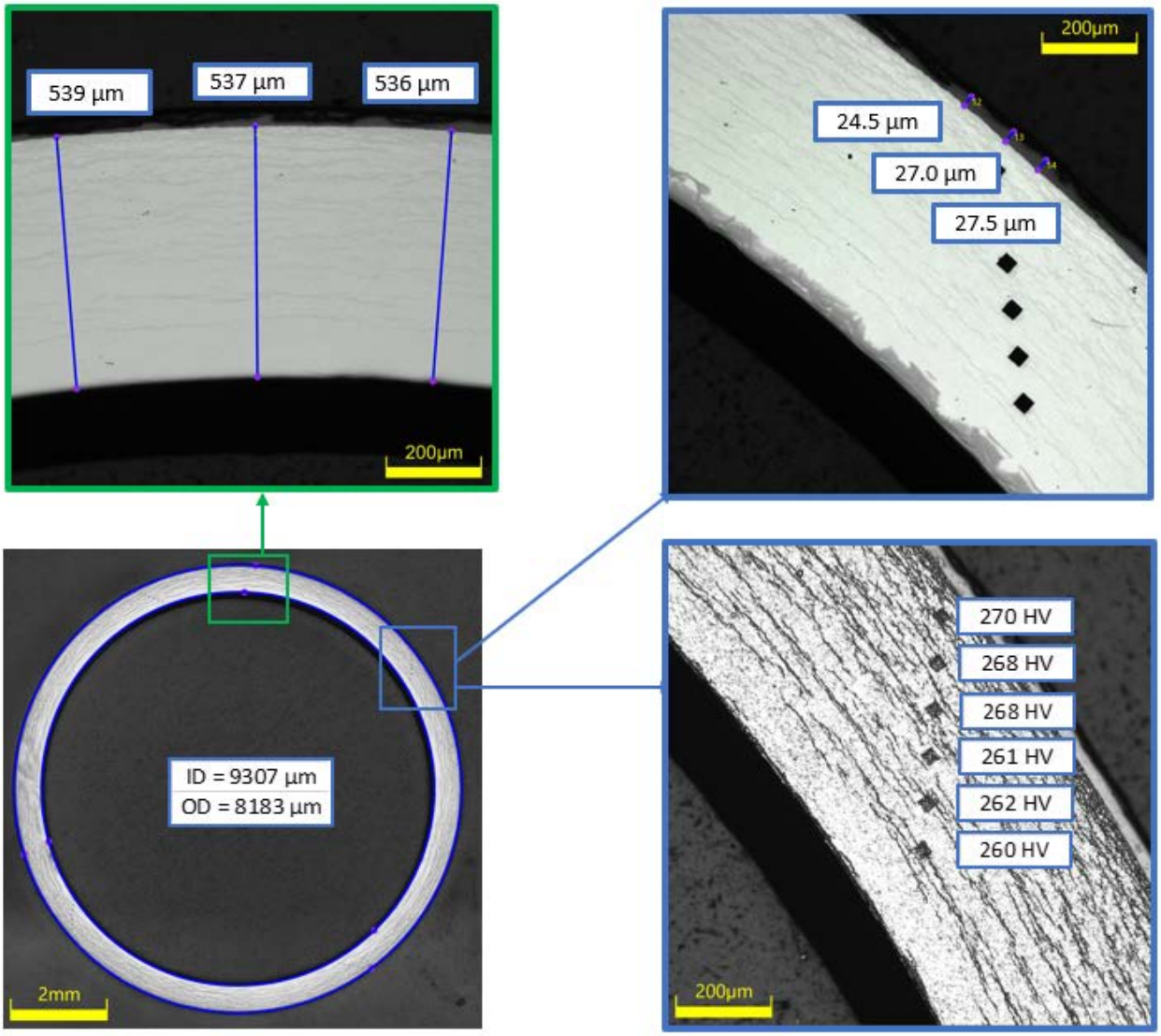

Figure 5-41. Quadrant A of Sample UL-1-8 (Rod Location 3505 mm – 3518 mm).

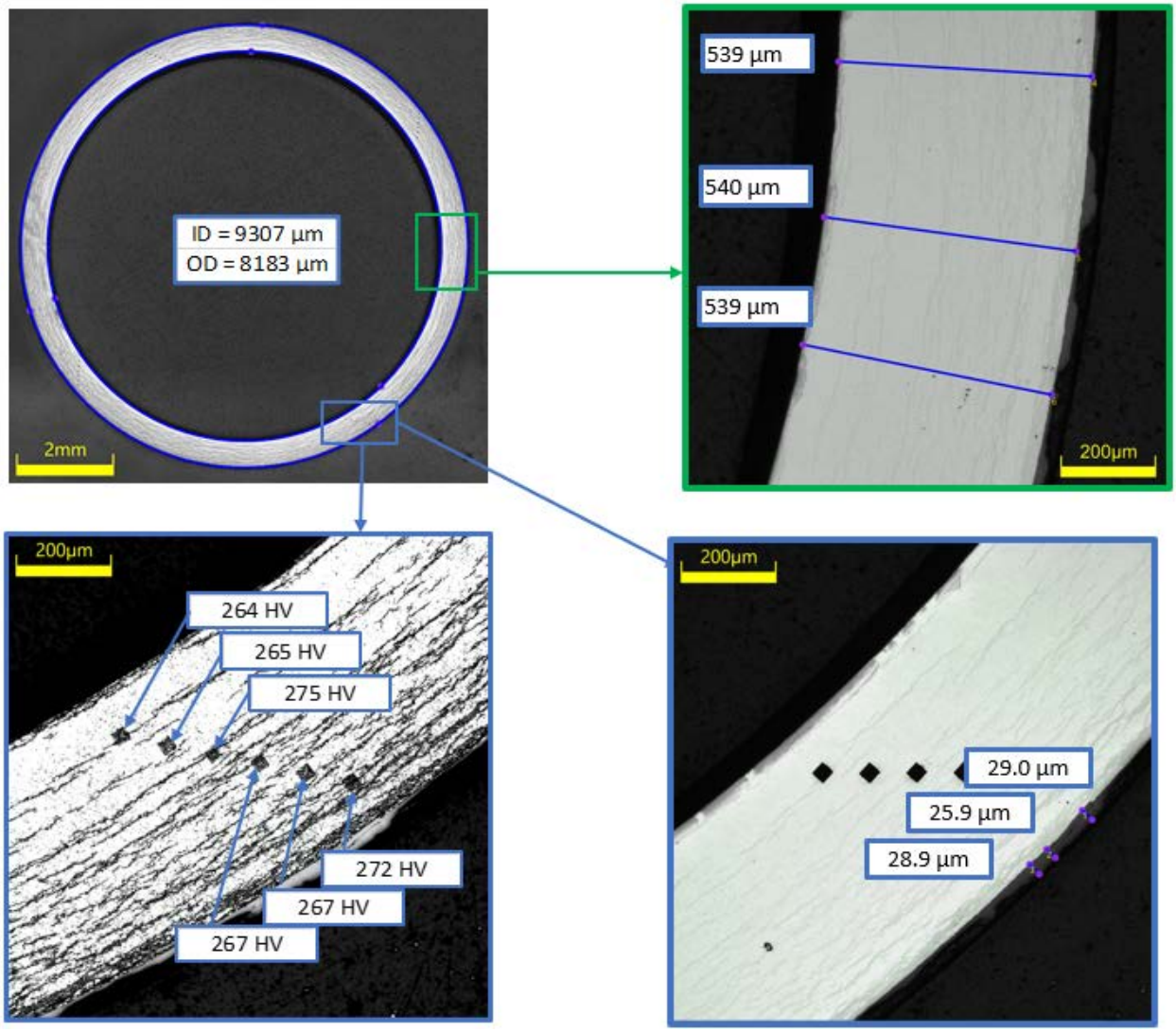

Figure 5-42. Quadrant B of Sample UL-1-8 (Rod Location 3505 mm – 3518 mm).

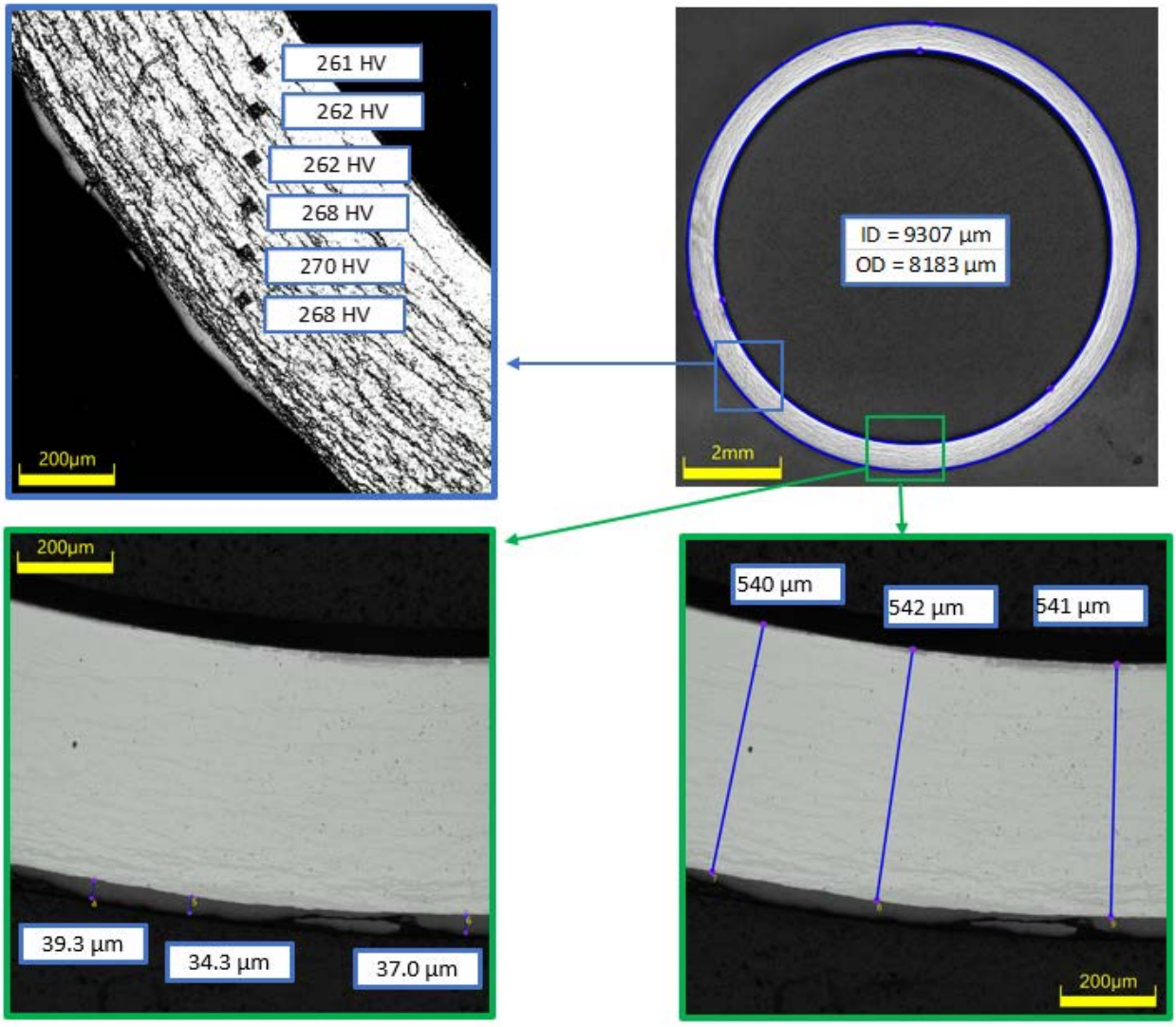

Figure 5-43. Quadrant C of Sample UL-1-8 (Rod Location 3505 mm – 3518 mm).

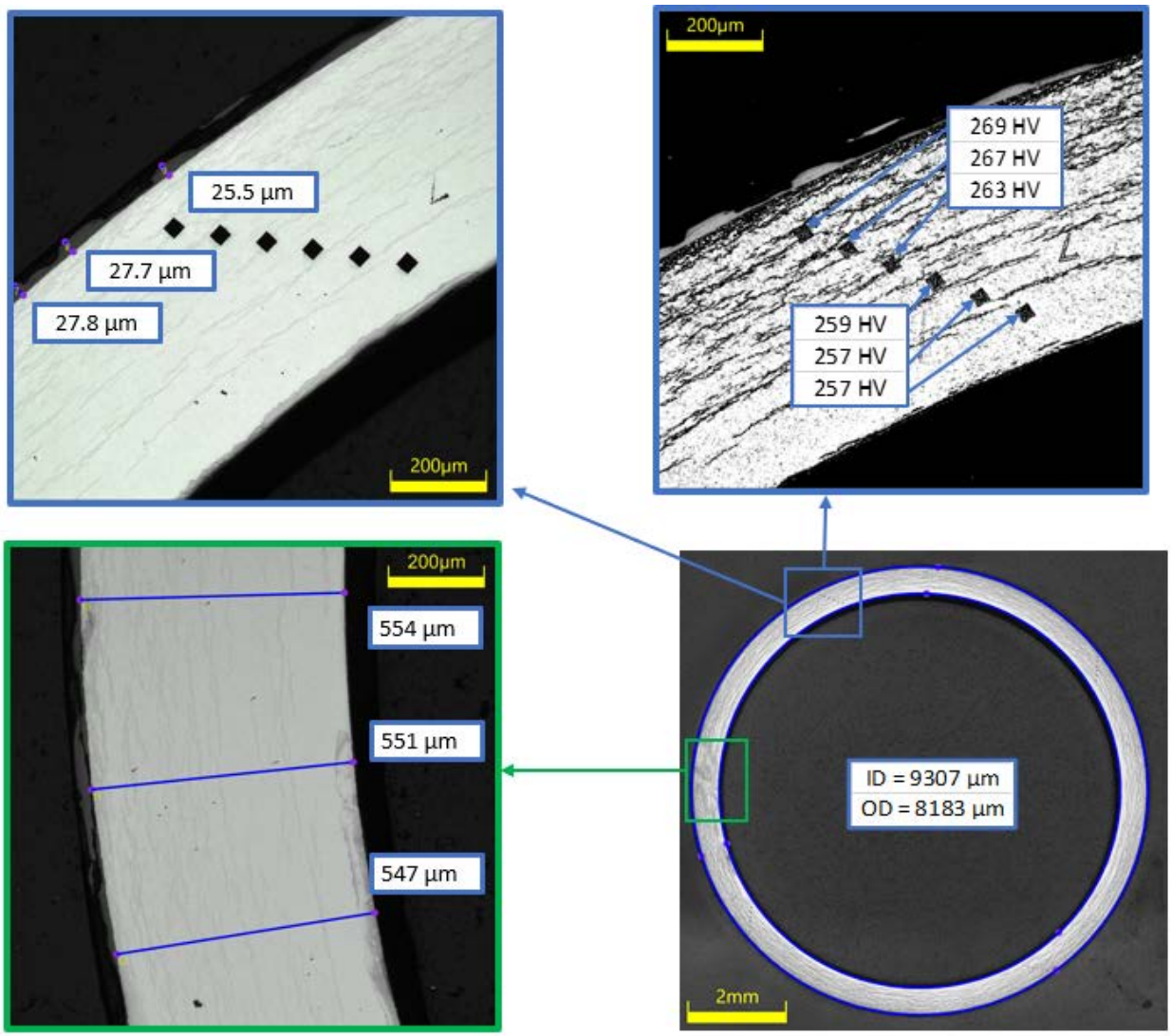

Figure 5-44. Quadrant D of Sample UL-1-8 (Rod Location 3505 mm – 3518 mm).

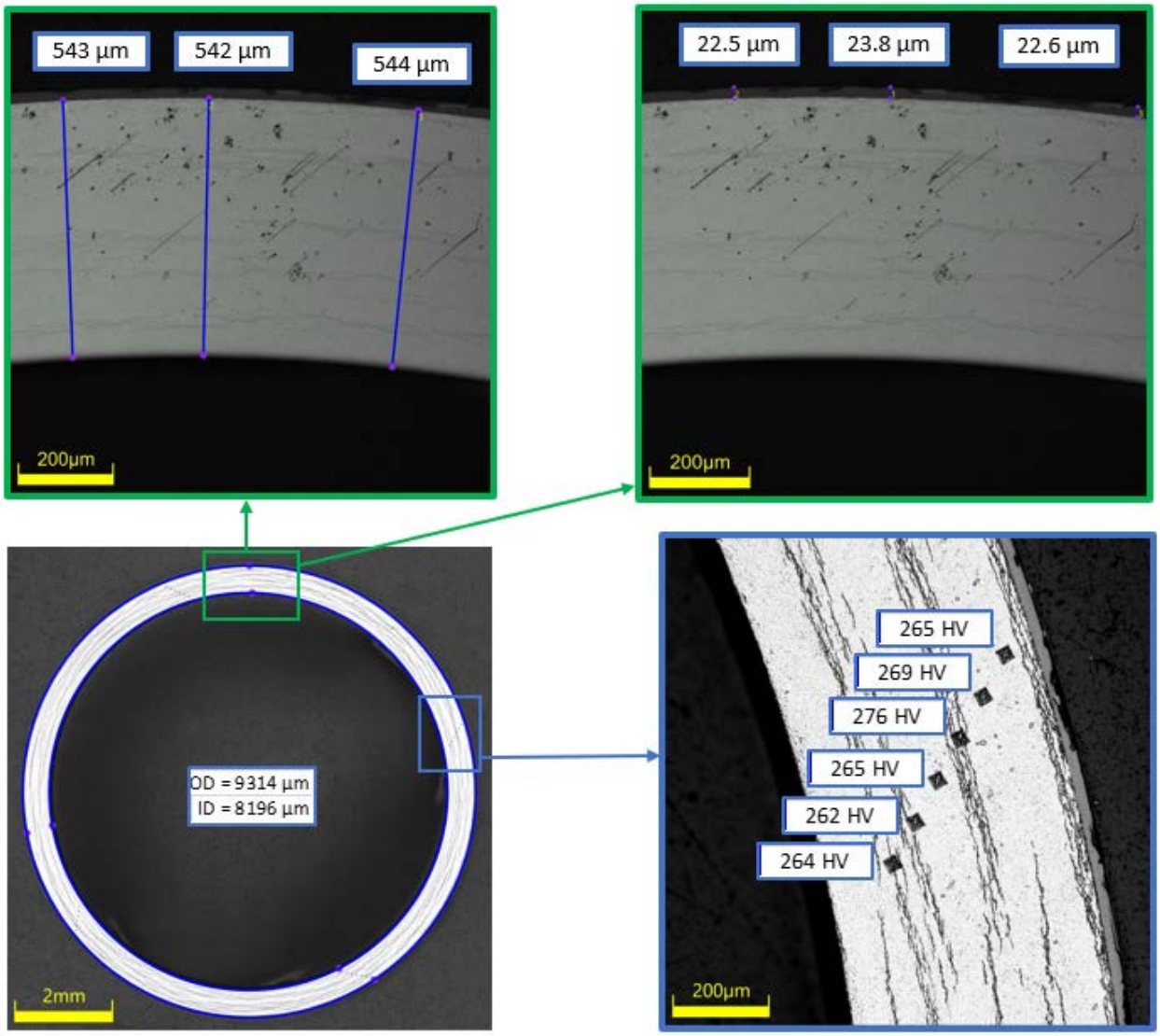

Figure 5-45. Quadrant A of Sample UL-1-10 (Rod Location 3671 mm – 3683 mm).

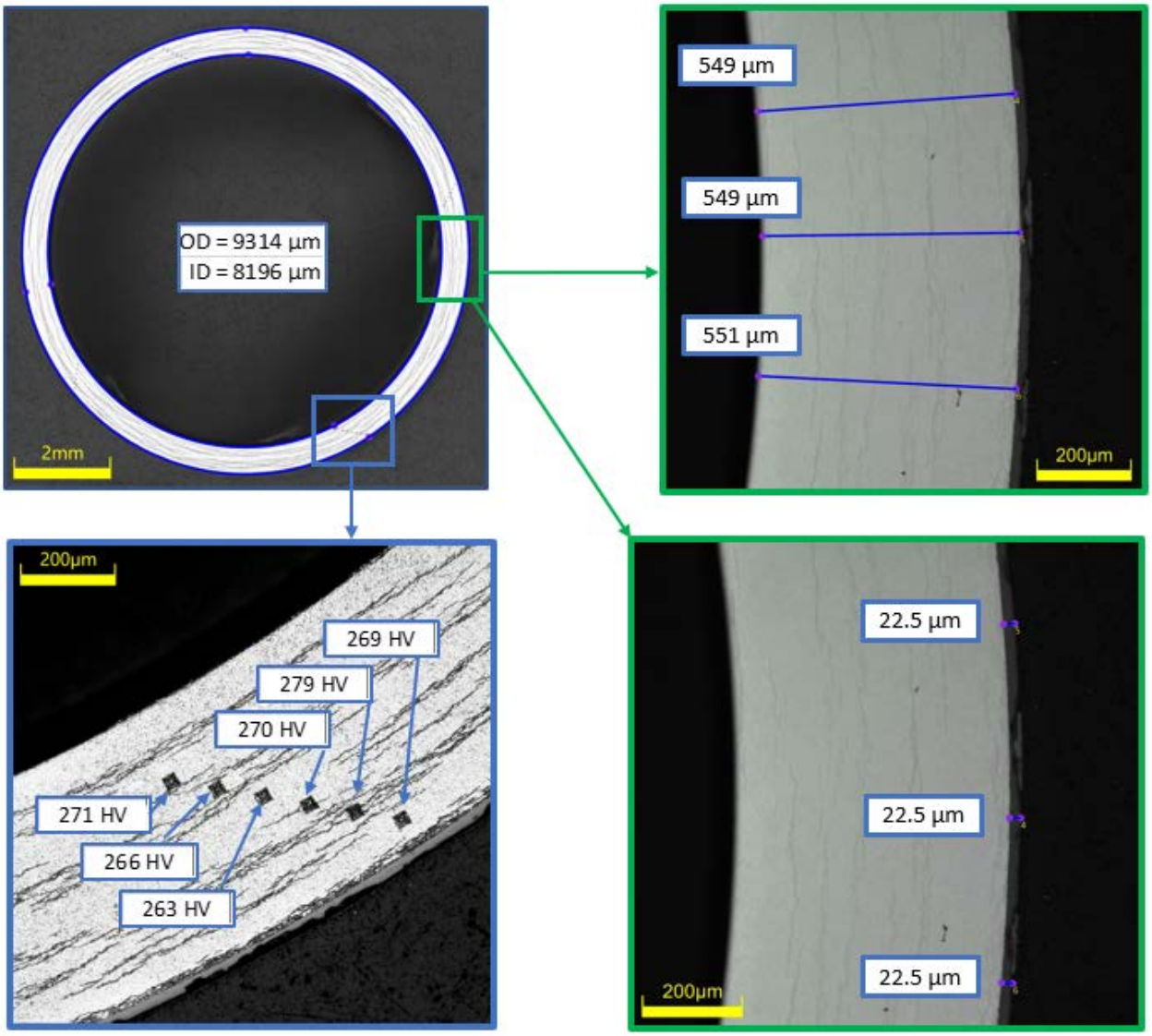

Figure 5-46. Quadrant B of Sample UL-1-10 (Rod Location 3671 mm – 3683 mm).

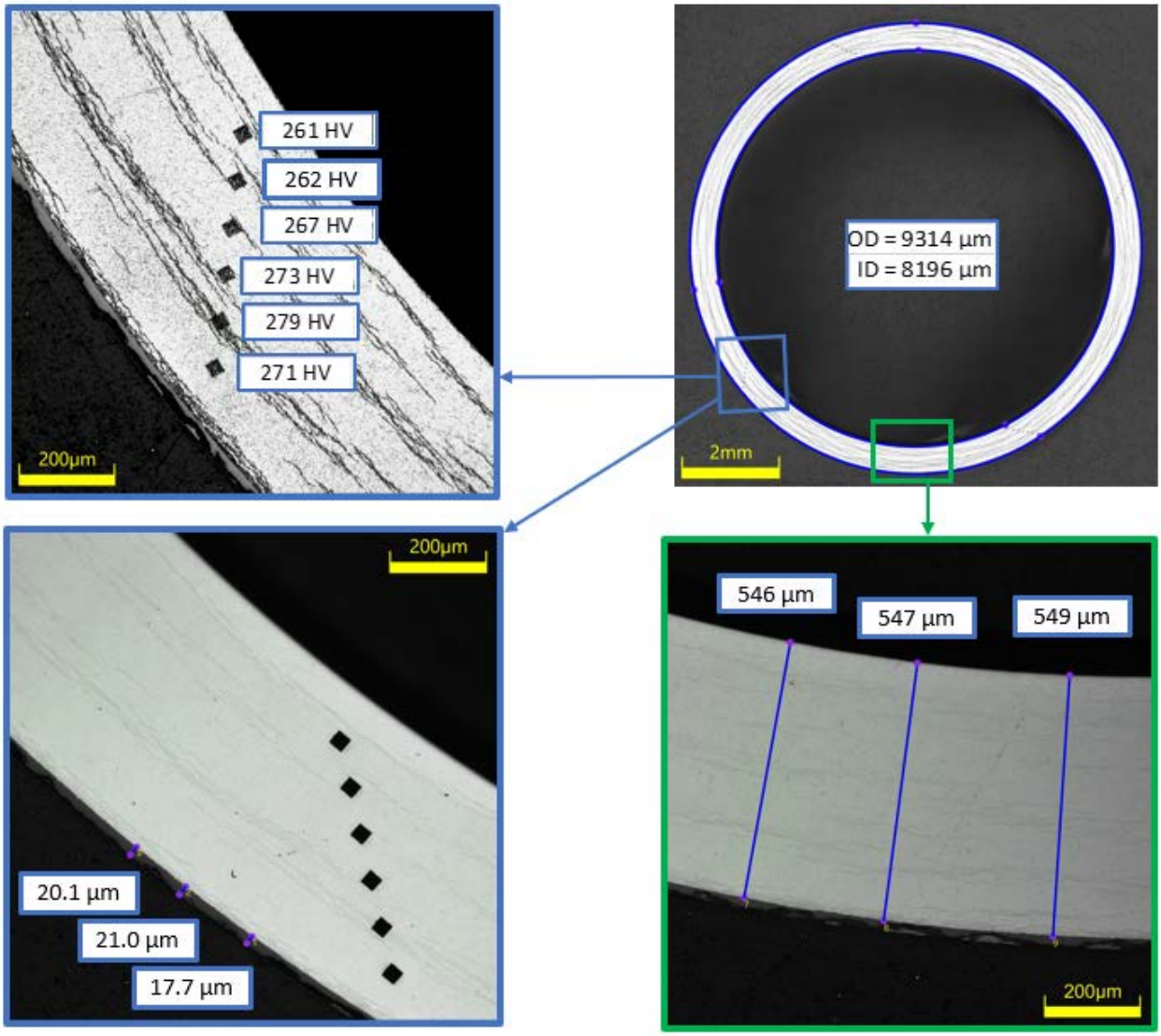

Figure 5-47. Quadrant C of Sample UL-1-10 (Rod Location 3671 mm – 3683 mm).

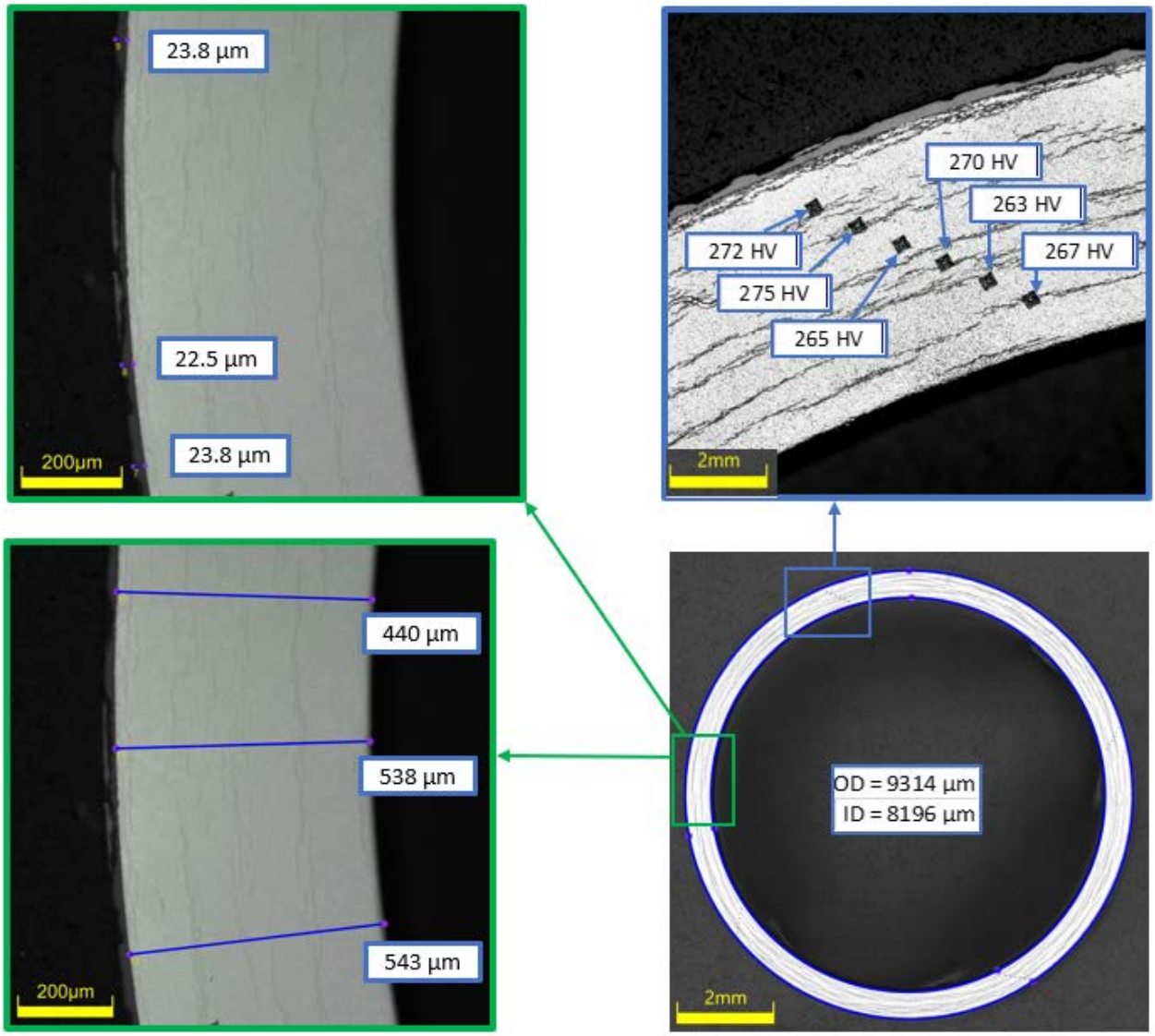

Figure 5-48. Quadrant D of Sample UL-1-10 (Rod Location 3671 mm – 3683 mm).

5.4.6 Lessons Learned and Path Forward for Optical Metallography

The variation in oxide layer thickness around the circumference of the FK-4-1 and UL-1 samples was greater than expected. Similarly, the oxide layer thickness for the FK-4-1 samples as shown in Table 5-8 are lower than expected. It appears that the process used for sample preparation, and especially the course grinding stages discussed in Table 5-7 resulted in significant oxide loss and pull-away from the cladding surface (see e.g., Figure 5-35). This in turn contributes to the largest uncertainty when determining oxide layer thickness. For future samples and analyses, the following steps will be tried to improve results and reduce variability and uncertainty:

- The sample cup filled with epoxy resin will be gently shaken to improve the contact of the resin with the cladding sample.
- Longer and/or multiple vacuum steps will be used to improve the contact of the resin with the cladding sample.
- The initial steps with the coarse silicon carbide (240 and 400 grit) may be shortened or eliminated.
- Measurements of d_o, d_i, wall thickness, and oxide layer thickness will be done on samples prior to etching.
- Oxide layer thickness will be determined in regions with the largest continuous oxide layers in each quadrant.
- Select samples will be examined with scanning electron microscopy to verify dimensions.
- The statistical analysis discussed in Sections 5.4.3 and 5.4.4 will be performed to better define the quantitative uncertainties associated with user variability.

This page is intentionally left blank.

6. PHYSICAL PROPERTY TESTING

PNNL will perform mechanical destructive tests outlined in Saltzstein et al. (2018) for defueled cladding samples nominally 152 mm in length to evaluate the strength and ductility of irradiated cladding at room temperature (RT) and at 200°C. This section describes the equipment and methods developed to perform these tests and efforts to qualify these methods before testing with sibling pin material.

6.1 Equipment

6.1.1 Burst Testing System

The system to conduct burst testing on sibling pin samples at pressures up to 20,000 psi (138 MPa) and temperatures up to 200°C was designed and fabricated as depicted in Figure 6-1. The system was designed for qualification testing of the system using as-manufactured cladding test articles that failed between 13,000 (90 MPa) to 19,000 psig (131 MPa). Hence, components of the burst system are rated for 20,000 psi or higher.

Testing began by filling the system tubing with water to remove residual air from the system and the cladding specimen. When the system is heated for an elevated-temperature test, pressure increases with the thermal expansion of the water, but a relief valve keeps the pressure below 500 psig.[q] Once the heating phase and thermal expansion were complete, the relief valve was isolated and the system was pressurized in a controlled manner (in accordance with Annex A.1 of ASTM B811, *Standard Specification of Wrought Seamless Tubes for the Nuclear Reactor Fuel Cladding,* [ASTM 2017]) until the test article burst.

When testing was conducted at RT, a small amount of water was released from the test article to the oven (~34 mL). When testing was conducted at elevated temperature, a water/steam mixture was released. When the cladding ruptures, energy is dissipated rapidly because the compressibility of water is low and the volume of steam produced is small.

A video image system took pictures of the cladding every 0.5 s during testing to produce synchronized stress-strain curves (see Section 6.1.3). The test article was contained inside an oven that controlled the temperature and provided shielding from the burst. Additionally, the oven was placed inside a fume hood to provide control of any radioactive contamination.

Key features included the following:

- A positive displacement piston pump was used to fill the system with water. When all the air had been displaced from the system, the pump and water reservoir were isolated from the high-pressure portion of the burst system.
- Piston screw pumps were used to generate high pressure. Each pump can provide 10 mL volume into the system at pressures up to 60,000 psi. A pressure gauge is on the table with the pumps so that the operator can control and monitor the pressure during testing. A photograph of the pumps set up on a table is provided in Figure 6-2.
- A pressure relief valve (set at 500 psi) in the fume hood prevented the system from overpressurizing during heating. The pressure relief valve was isolated from the system during the final pressurization and bursting of the test article.

[q] Water at 200°C requires pressure greater than ~215 psig to stay in liquid form.

- Pressure was measured using a 0–30,000 psi calibrated pressure transducer (1–5 V) with a 0.25% full-scale accuracy. Measurements from a pressure transducer were fed into a data-acquisition system to record the rate of pressurization over time and provide pressure information to external strain imaging software, which correlated hoop stress measurements from the transducer with strain imaging measurements (see Section 6.1.3).
- A digital image correlation system, consisting of cameras, image correlation software, and a computer gathered 3-D strain measurements (see Section 6.1.3).
- The test article is tested in a vertical configuration with two hydrostatic grips connected to the top and bottom end of the sample. The bottom grip connects the test article to the burst pressurization system. The top grip connects to a valve with a removable polymer tube that allows air to escape while filling the tube with water. Once all air is removed, the top valve is closed, and the bleed line removed so the test article is free to expand biaxially during testing.
- Airmo model MPG series test tools were used to grip and seal both ends of the test article (Figure 6-3). The O-rings in the grips were replaced with Parker E0962-90 geothermal EDPM O-rings designed for high temperatures (up to 260°C) and compatible with water and steam. These seals can last for up to 12 burst cycles at 200°C before replacement is required, but they were replaced after each burst test.
- A custom-built convection oven equipped with lights, viewing ports for the camera system, and thermocouple was used to control and maintain the burst system temperature (see Figure 6-4). The oven is 12 in. × 12 in. × 30 in. (WDH) and was fully contained within the fume hood.
- A calibrated thermocouple inserted into thermal well was used to measure the fluid temperature. An additional calibrated thermocouple and external data logger were used to monitor the oven temperature for validation of testing temperature.
- A fume hood was used for containing and controlling any contamination resulting from the burst tests.
- Supplemental exhaust was available when needed to control contamination resulting from the burst process.

The burst system in the Radiochemical Processing Laboratory (RPL) was installed in a fume hood (to be designated a contamination area) for testing of irradiated cladding samples. The unirradiated test samples, reported herein, were used to shake down the system and for staff training.

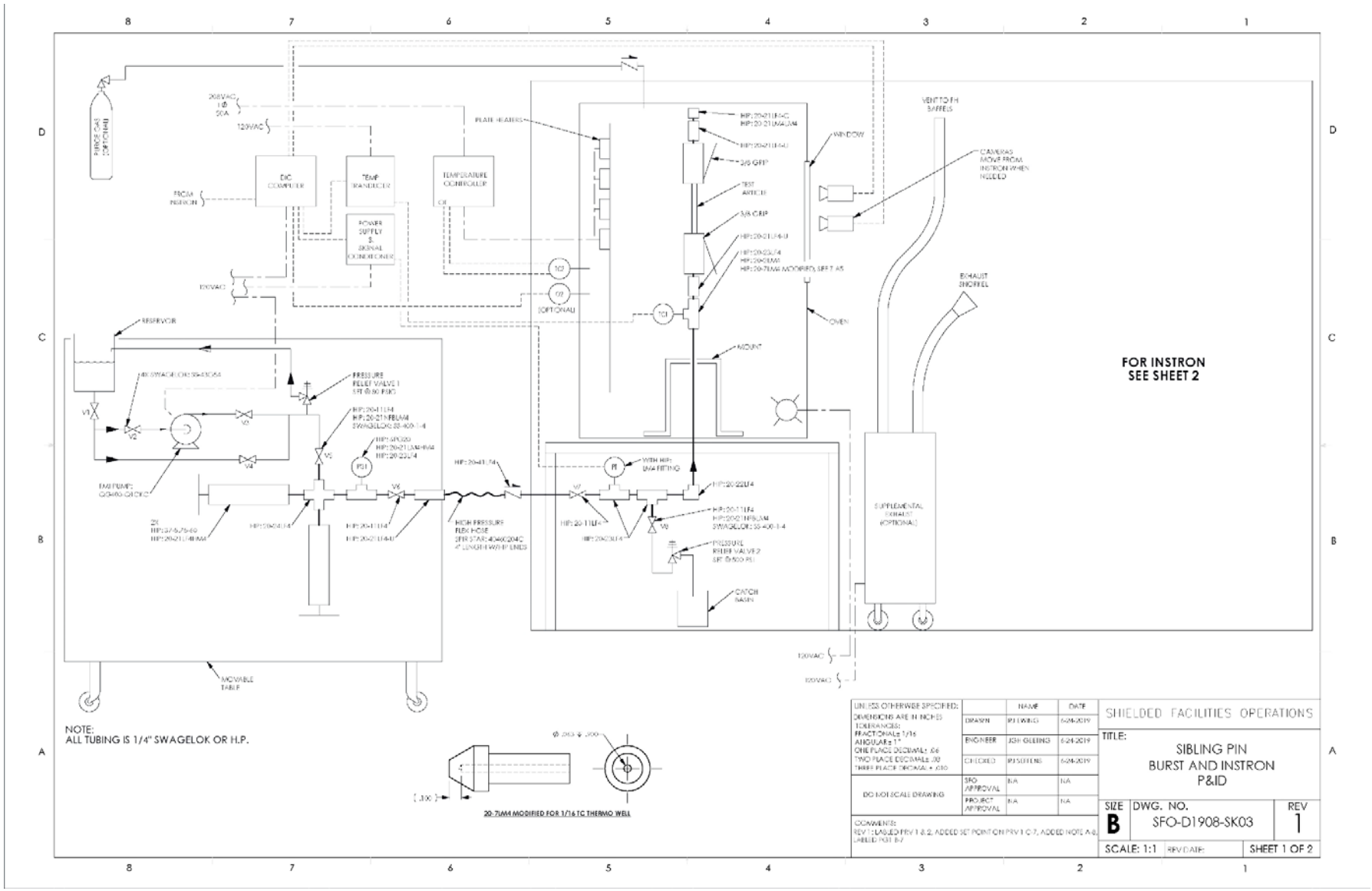

Figure 6-1. Burst System Schematic.

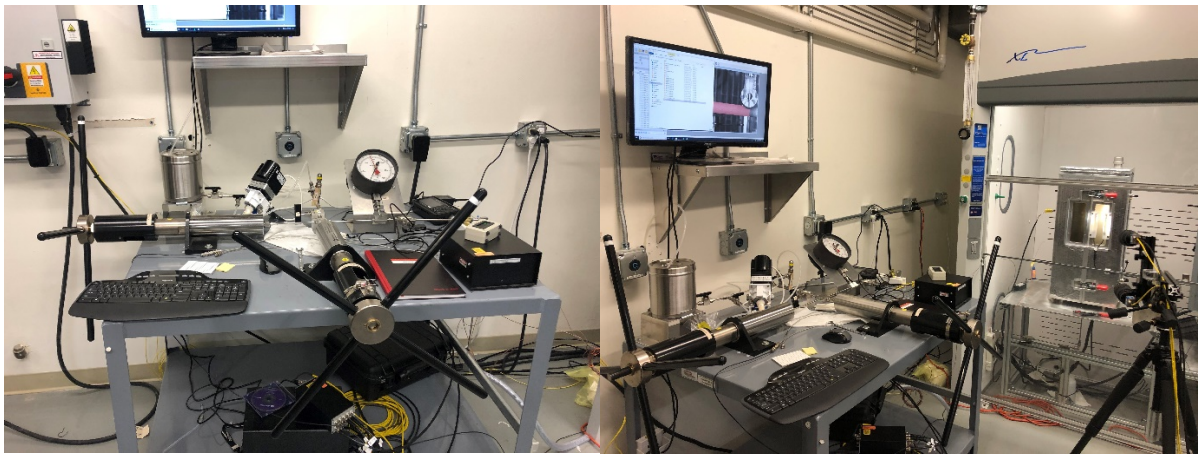

Figure 6-2. Piston Screw Pumps to Pressurize Burst System.

Figure 6-3. Airmo Model MPG Grips Used on Burst Test Samples.

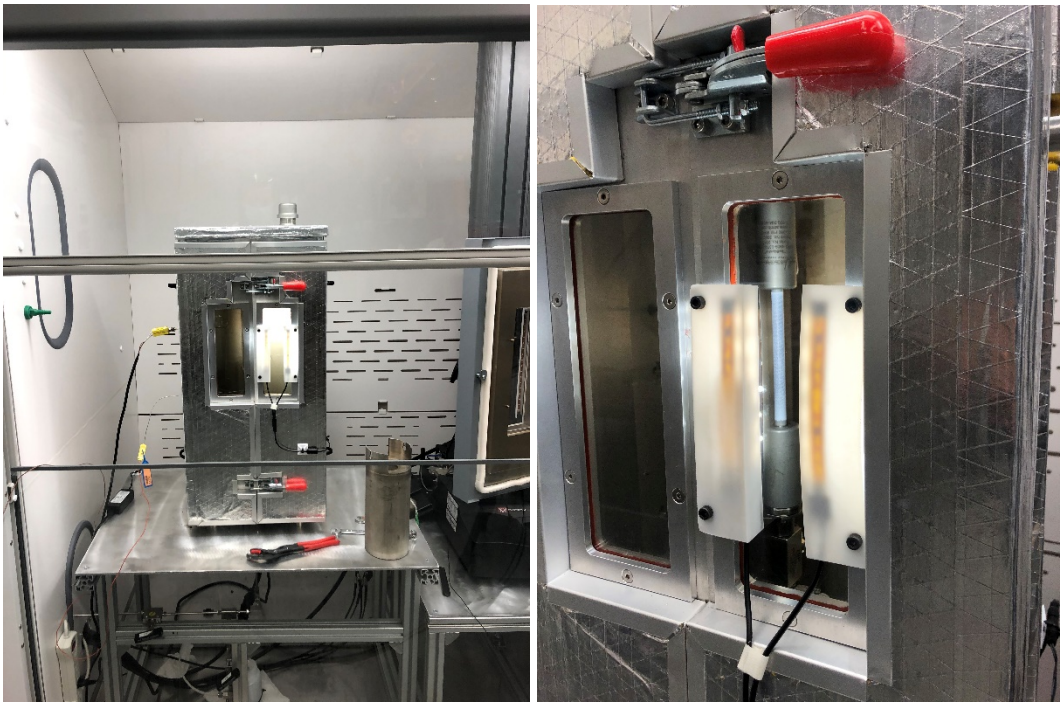

Figure 6-4. Custom Oven Insulated and Installed in Fume Hood.

6.1.2 Instron Test Frame

To perform tensile and four-point bend tests, an Instron electromechanical test frame with a 50 kN load cell was purchased and installed during 2019 (Figure 6-5). Axial tensile testing of sibling pin samples will be conducted under ASTM E8E8M, *Standard Test Methods for Tension Testing of Metallic Materials*, [ASTM 2016] and ASTM E21, *Standard Test Methods for Elevated Temperature Tension Tests of Metallic Materials*, [ASTM 2016] to compare tensile stress/strain properties at different temperatures. Four-point bend testing will be conducted under ASTM E290, *Standard Test Methods for Bend Testing of Material for Ductility*, [ASTM 2014] using the same load frame with different fixture configuration to compare flexion stress/strain properties at different temperatures. Custom fixturing was made because the supplied Instron bend-test loading and support bars are not suitable for use with tubing; it pinches the tube and produces local deformation. Custom loading rods and supports were designed as bolt-on replacements for the bars. The rods rotate, which allows the tube to slide as it is deflected and prevents the pinching effect and the resulting local deformation, and also allows the tube to expand/contract axially. The rollers and support structures are made from 304 SST. The rollers sit inside of a vee groove to allow rotation with minimal friction. Aluminum walls on both sides of the supports prevent the rollers from moving side-to-side and causing misalignment in the tube. The aluminum walls have a gap of 0.010 inches on either side to avoid additional friction on the faces of the rollers, which would inhibit their rotation as deformation proceeds. The tubing sits inside of a semi-circumferential groove on the rollers to keep alignment during testing.

Test equipment consisted of the following:

- An electromechanical Instron 5969 series dual column table frame with 50 kN load cell (see Figure 6-5) with analog output card and associated cable bundle, which outputs load and strain data to an external strain imaging system (see Section 6.1.3).
- An Instron model CP122112 environmental chamber (seen in Figure 6-5), rated to 350°C, uses an internal Type K thermocouple and a forced convection fan; the chamber has a rated temperature stability of ±2°C. The system was initially calibrated with an external calibrated thermocouple by the manufacturer. An additional calibrated thermocouple and external data logger are used to monitor the oven temperature for validation of testing temperature.
- Instron model 2716-020 wedge grips (see Figure 6-6) rated for 50 kN hold a sample in place. These have vee jaw faces grooved with 25 teeth per inch that can accommodate sample d_o between 0.28" and 0.5".
- An Epsilon model 7642-050M-125M high-temperature extensometer (see Figure 6-6) with a gauge length of 50 mm can travel +12.5 mm or −1.50 mm and is rated to 700°C. This extensometer is used specifically for axial tensile tests (see Figure 6-7).
- An Instron model 2810-403 four-point bend fixture was modified with custom rollers and supports. The supplied deflectometer plunger was also modified by replacing the factory plastic bushing with an oil impregnated bronze custom bushing (see Figure 6-8 and Figure 6-9).
- An Instron model 2630-100 clip-on extensometer has a gauge length of 25 mm and can travel +25 mm or −2.5 mm and is rated for 200°C (see Figure 6-10). This extensometer is used specifically for four-point bend tests (see Figure 6-11).
- Custom zirconium end plugs fabricated to ASTM B811 and E8M (see Figure 6-12) used to support the ends of cladding test articles within the wedge grips.

The Instron table frame's load cell was calibrated for force per ASTM E4, *Standard Practices for Force Verification of Testing Machines*, [ASTM 2020] within ±0.5% accuracy and 0.5% repeatability. The crosshead movement speed was calibrated per ASTM E2658, *Standard Practices for Verification of Speed for Material Testing Machines*, [ASTM 2015] for speeds of 0.05, 0.1, and 0.2 in./min. The

crosshead displacement was calibrated per ASTM E2309, *Standard Practices for Verification of Displacement Measuring Systems and Devices Used in Material Testing Machines*, [ASTM 2020] as a Class A displacement measurement system. Extensometers were calibrated per ASTM E83, *Standard Practice for Verification and Classification of Extensometer Systems*, [ASTM 2016] as a Class B-1 extensometer system.

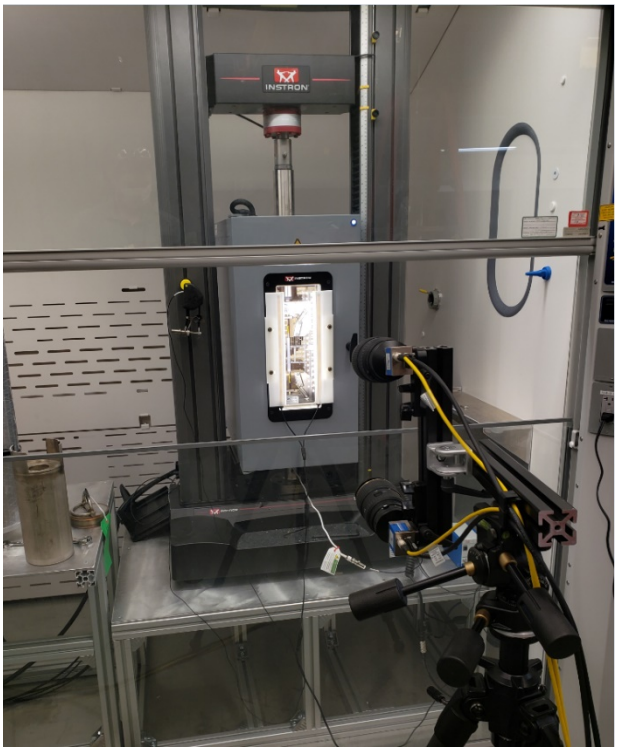

Figure 6-5. Electromechanical Load Frame with Convection Oven and Video Image System.

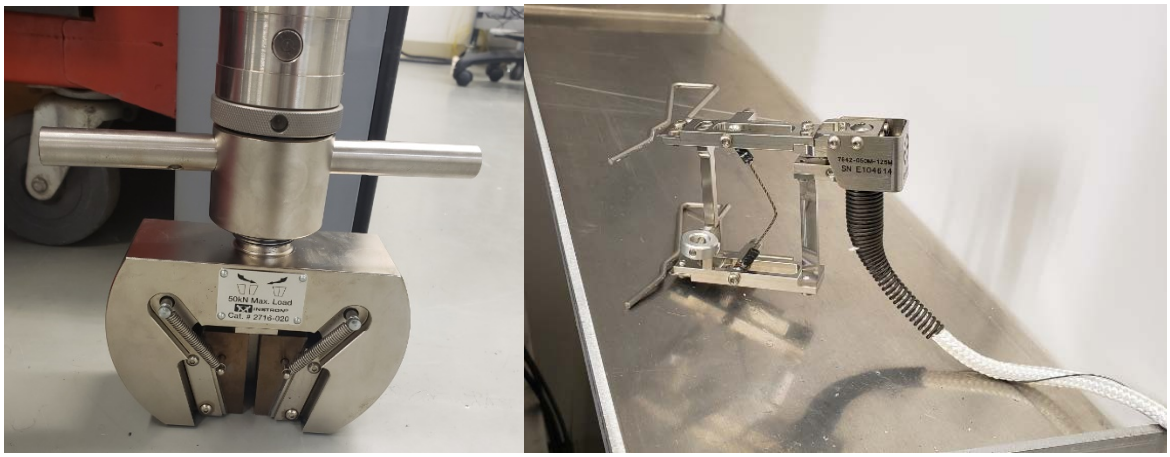

Figure 6-6. Wedge Grip (left) and High-Temperature Extensometer (right) Used in Axial Tensile Tests.

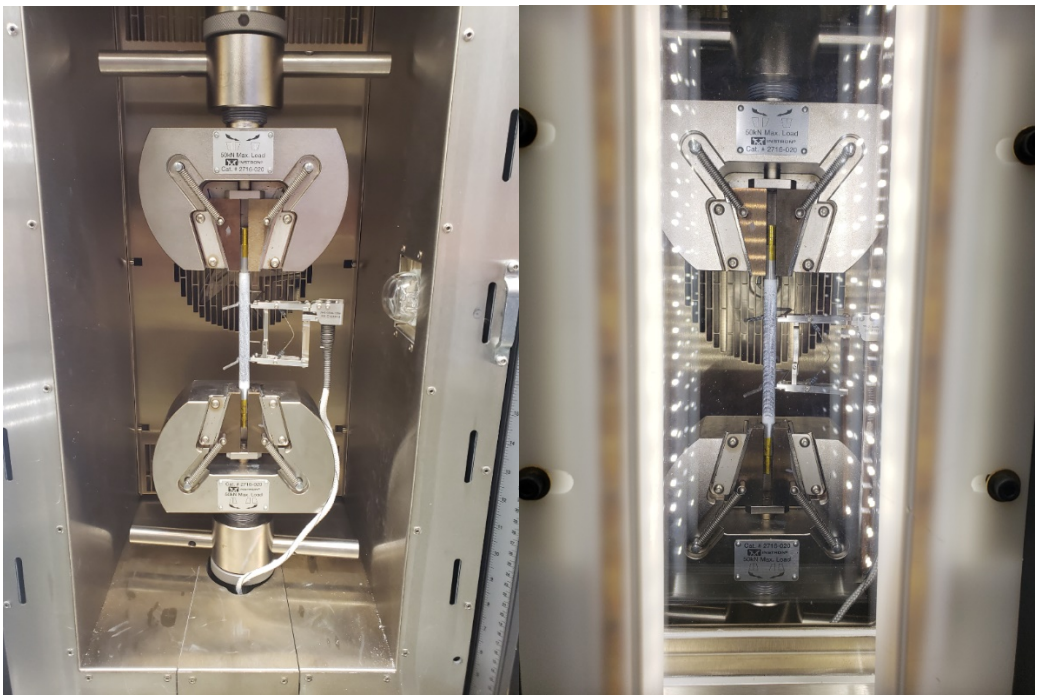

Figure 6-7. Axial Tensile Fixture Setup Inside Convection Oven.

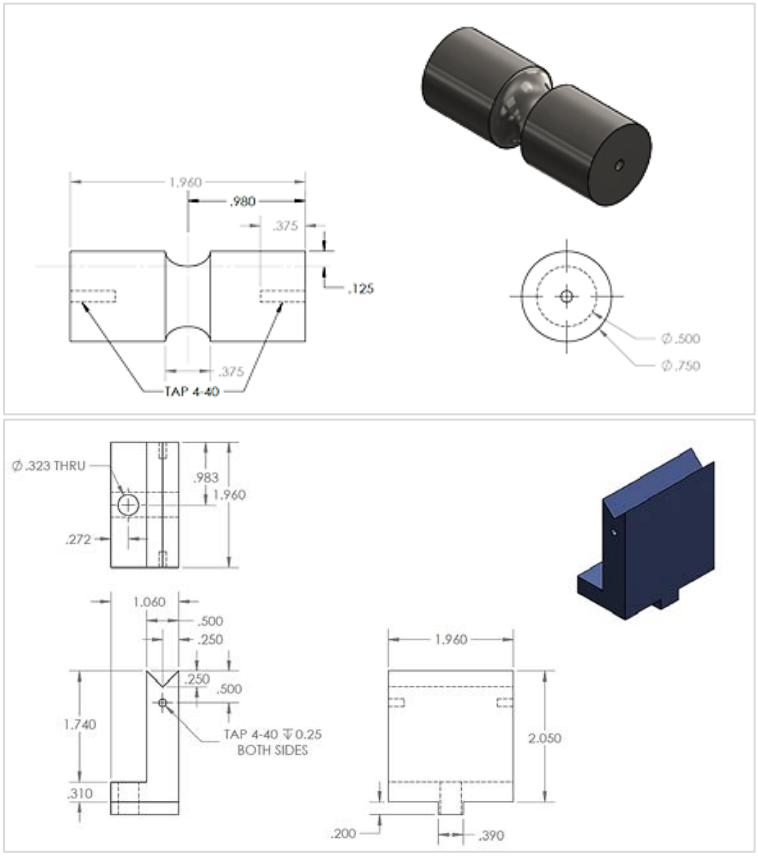

Figure 6-8. Four-Point Bend Roller (top) and Roller Support (bottom).

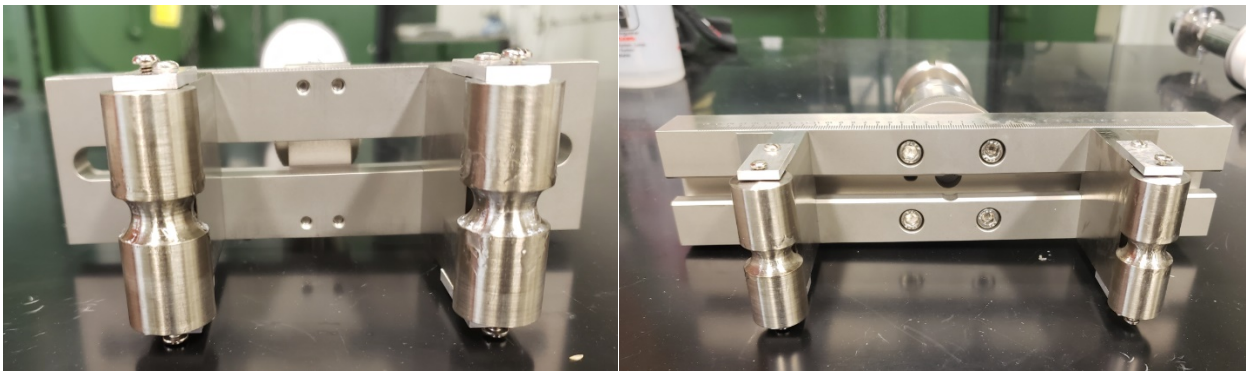

Figure 6-9. Load Fixture (left) and Support Fixture (right) Used for Four-Point Bend Testing.

Figure 6-10. Deflectometer Attached to Extensometer Used on Four-Point Bend Fixture.

Figure 6-11. Four-Point Bend Fixture Configuration Inside Environmental Chamber.

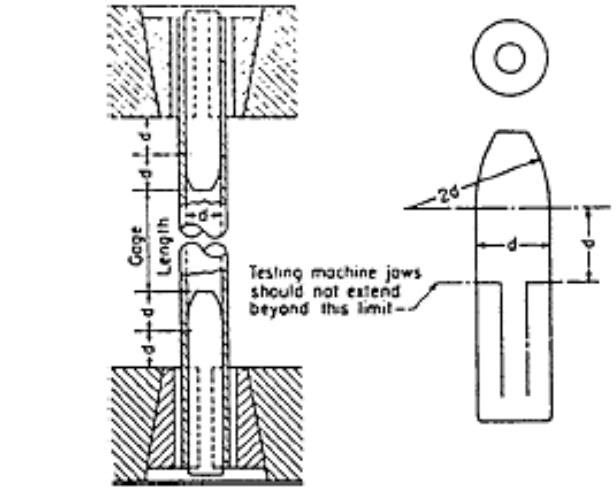

NOTE 1—The diameter of the plug shall have a slight taper from the line limiting the test machine jaws to the curved section.

Figure 6-12. End Plug Dimensional Guide from ASTM E8/E8M.

6.1.3 Digital Image Correlation and Strain Imaging Software

External strain imaging of physical property samples was collected using a digital image correlation system (DIC), which communicates with specialized software that correlates 3-D strain imaging to analog data from the test equipment to provide hoop strain data for burst testing and to supplement extensometer

data from tensile and four-point bend testing. Strain testing is a destructive physical property test. In this real-time measurement technique, a speckle pattern is applied to each specimen. A pair of digital video cameras track the strain of the test article as it develops during deformation, subsequent localization, and fracture. Strain imaging software analyzes the evolution of the speckle pattern. This method uses white-light speckle correlation to measure deformation in each image of an image sequence, where any two consecutive speckled images, captured by the digital video cameras, represent the incremental stages during deformation. Strain imaging software is then used to quantify the displacement of the speckles in the image sequence, and the strain tensor can be determined at any point on the tube surface. When the in-process displacement is known, the displacement and strain at each point on the tube can be plotted as a function of time.

Strain imaging data from the camera pair are analyzed using Correlated Solutions' *VIC-3D 8* software. Processing analysis parameters are shown in Table 6-1. The data collection rate was 2 Hz for all tests. Details on the camera setup can be found in Table 6-2. The images were acquired while viewing through the oven window, which had been wiped clean using lens cleaner. Lighting was provided by two 1.2 W 4200 K 4-inch light-emitting diode (LED) strips on polytetrafluoroethylene sheets screwed to the sides of the window. Cameras were hardware synchronized, and calibration images were taken with a calibration card multiple times with the oven doors open. The calibration must be autocorrected on every test because the image viewed through the window during testing is different from the view with the oven doors open. A photo of the calibration card is shown in Figure 6-13. Test articles were prepared by applying a high-temperature white paint coating to provide a background for the speckles. End caps are used to keep the 1 in. bands at each end free from paint so as not to interfere with the physical gripping mechanisms. Once the paint is dry, a black speckle pattern is applied using an ink stamp provided by Correlated Solutions. The ink stamp, shown in Figure 6-14, applies a 0.007 inch speckle pattern compatible with the calibration card to measure strain. An image showing an example of the speckle done on the cladding samples is shown in Figure 6-15.

Analog temperature and pressure data from the burst system are acquired from the oven thermocouple and the pressure transducer. The analog output card of the Instron test frame provides the measured load value from the 50 kN load cell and the strain/deflection measurements from the system extensometers. These analog data are collected at a rate that matches that from the strain imaging camera (2 Hz) so strain imaging values are recorded with the corresponding analog data for each test performed. Examples of DIC and straining imaging analyses are shown in Figure 6-16 for axial tensile testing, Figure 6-17 for four-point bend testing, and Figure 6-18 for burst testing.

Table 6-1. DIC Analysis Parameters.

Software Manufacturer	Correlated Solutions
Software package	VIC-3D 8, Build 660, Version 8.4.0
Subset Size	45
Step Size	11
Subset Shape Function	Center-Weighted Gaussian
Strain Formulation	Engineering
Strain Window	11 px
Virtual Strain Gauge	133 Hz

Table 6-2. DIC System Specifications.

Camera Manufacturer	Basler
Camera Model	CSI-acA4112-30um
Software Version	Vic-3D Version 8.4.0
Image Resolution	12 MP
Lens Manufacturer	Tokina
Lens Model	ATX-Pro
Focal Length	100 mm
Field of View	5.13 in.
Image Scale	801 pixels/in.
Stereo Angle	14.3 deg
Standoff Distance	40 in.
Image Acquisition Rate	2 Hz
Patterning Technique	Ink Stamp
Pattern Feature Size	0.007 in.
Aperture	5.6

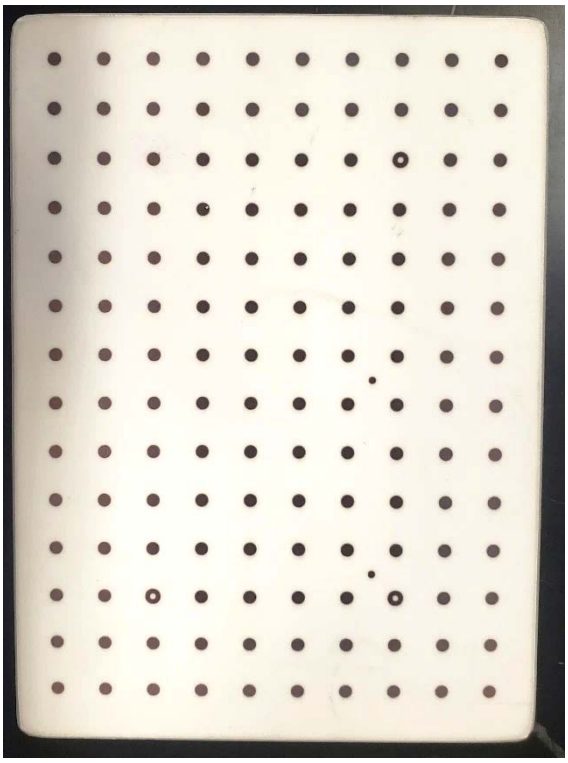

Figure 6-13. Calibration Card Used for DIC Image Calibration.

Figure 6-14. Sample Speckle Stamp (left) Being Applied to a Sample (right).

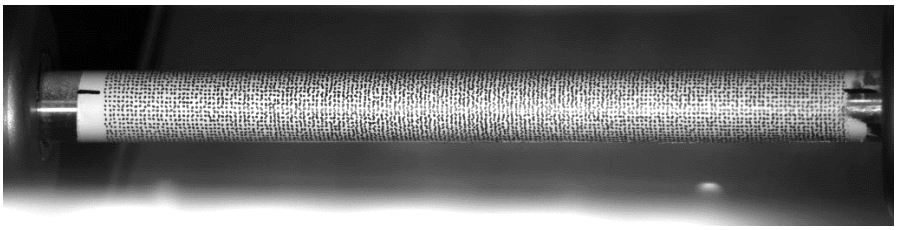

Figure 6-15. Painted and Speckled Cladding Sample.

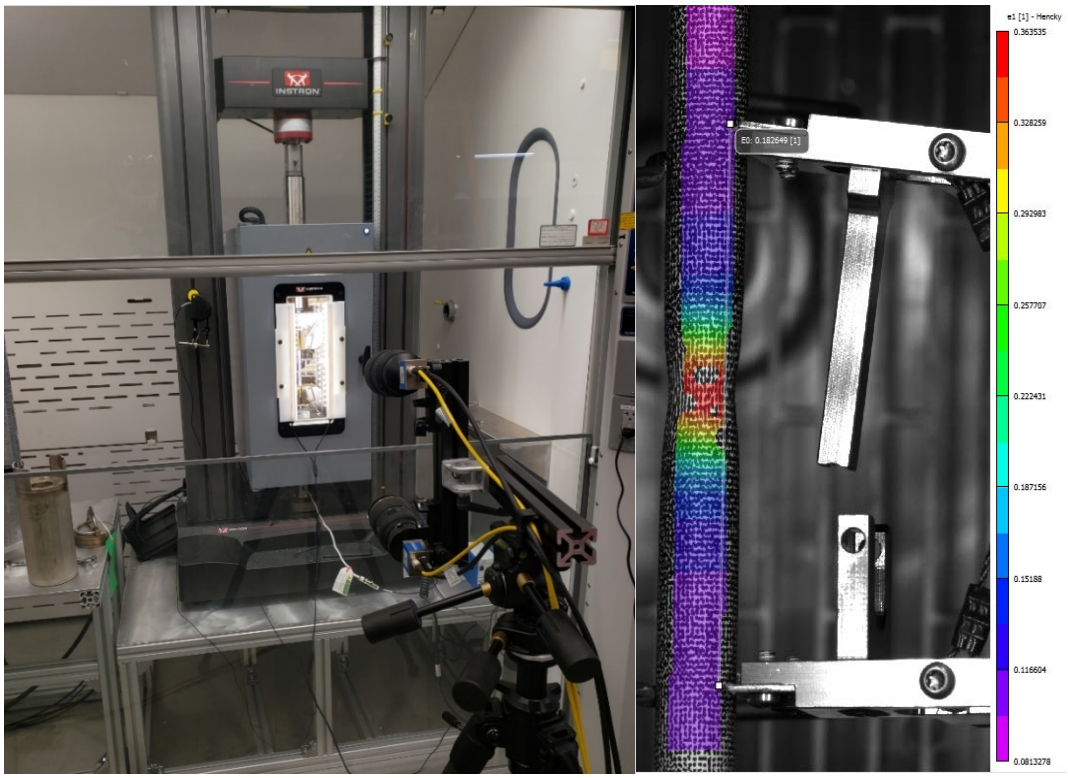

Figure 6-16. DIC System Configured for Axial Tensile Testing (left) and Strain Map Overlaid on Tensile Sample before Fracture (right).

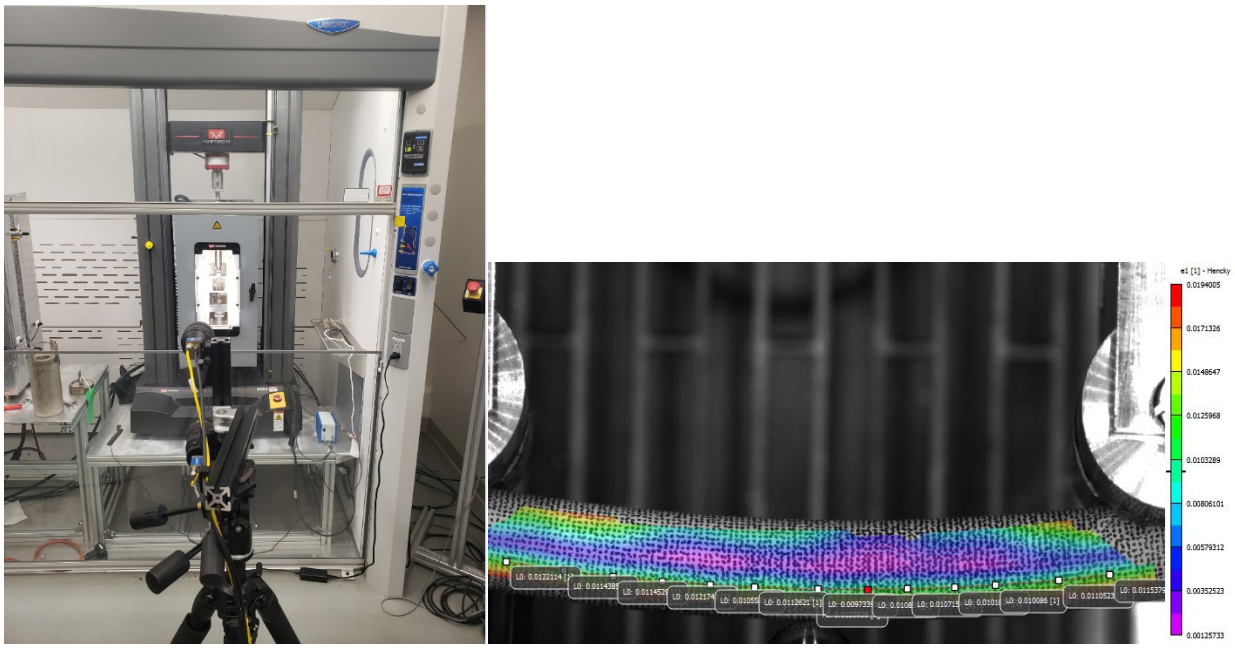

Figure 6-17. DIC System Configured for Four-Point Bend Testing and Sample Overlaid with Strain Map as Test Ends.

Figure 6-18. DIC System Configured for Burst Testing (left) and Burst Sample Overlaid with Strain Map before Burst (right).

6.2 Physical Property Testing Methods and Analysis

6.2.1 Burst Testing

The burst test uses the approach defined in ASTM B811 and uses strain imaging via DIC to measure the development of strain with increasing hoop stress, as discussed in Shimskey et al. (2015). The alternative is doing measurement of the locations after burst to only measure ultimate hoop stress and total circumferential elongation, as described in ASTM B811 Annex A1.

The general steps involved in performing a burst are the following:

a. Set up and calibrate DIC cameras.

b. Verify burst system valve line up.

c. Install cladding sample in Airmo grips.

d. Charge system with water.

e. (For high-temperature bursting) Turn on oven and allow to equilibrate at 200°C.

f. Operate syringe pump to increase system pressure at 2000 ± 200 psi per minute until cladding bursts. DIC images and data (pressure and temperature) are collected at a rate of 2 Hz over the entire pressurization.

A DIC image of a burst sample is shown in Figure 6-19. After the samples were burst, the paint and speckle were removed from the sample with acetone. Cross-sectional samples of the localization and uniform strain regions were cut from the test article and examined by OM to measure physical dimensional changes.

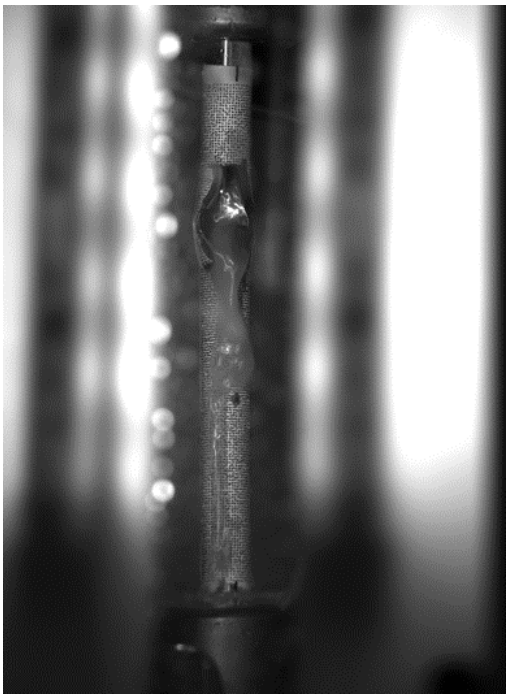

Figure 6-19. DIC Image of Burst Sample.

6.2.1.1 Methods Used and ASTM Comparison

The methods and equipment used for burst testing followed ASTM B811, *Standard Specification for Wrought Zirconium Alloy Seamless Tubes for Nuclear Reactor Fuel Cladding*. Some of the ASTM requirements are called out in Table 6-11. A comprehensive list of ASTM methods and requirements is included in Appendix C.

Table 6-3. Summary of ASTM Methods Comparison.

Section of ASTM B811	Summary	Comment
7.2.2	If elevated temperature burst test is specified, the test method and acceptance criteria shall be agreed upon between the manufacturer and purchaser.	Section 6.2.1
A1.1.3	Procedure is not appropriate for testing at elevated temperatures.	Section 6.2.1
A.1.3.1	Sample shall be tested in mill finished condition.	Section 6.1.1
A1.3.2	Minimum unsupported length shall be ten times the average outside diameter.	Section 6.2.1
A1.3.3	End fittings must produce a 2:1 circumferential to axial stress ratio.	Section 6.1.1
A1.4.1.3	Posttest circumferential elongation shall be determined at the point of maximum bulge, excluding the opening of the rupture, to an accuracy of 0.005 in (0.13 mm).	Section 6.2.2
A1.5.1	The following data should be included: measurements, maximum fluid pressure, ultimate hoop strength, and percent total circumferential elongation.	Section 6.2.2

6.2.2 Analysis of Results

Post-test circumference of the burst samples was measured at the top, bottom, and the burst localization. The burst localization, in this report, is referred to as point of maximum bulge (POMB), excluding the rupture itself. If the POMB was within 2 in. of the top of the sample, a middle circumference measurement was taken. This was performed by first cutting a 1/4 in. long subsample from the burst sample at each of the three designated locations listed above. The circumference at the cut points was then measured using an optical microscope to an accuracy of 0.13 mm (0.005").

The following data are reported for each sample, in accordance with ASTM B811-17, in Appendix H:

1. Dimensional measurements taken from test specimen
2. Internal pressure during the burst test (p_b)
3. Hoop stress (σ_θ)
4. Hoop strain (ε_θ)
5. Percent elongation
6. Hoop stress-strain curve as shown in Figure 6-20.

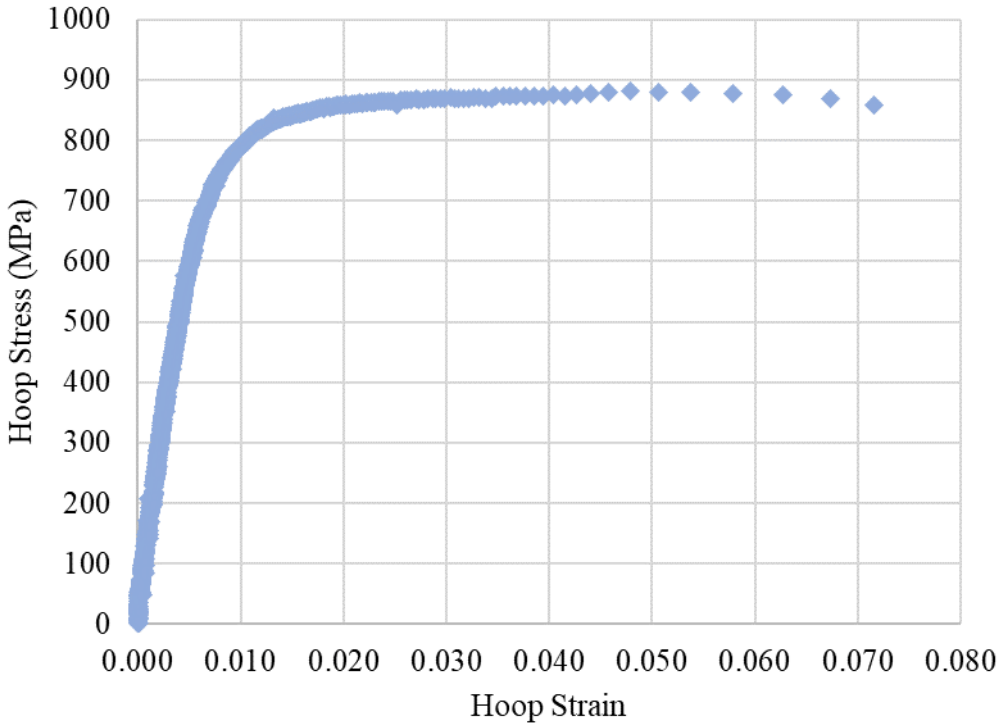

Figure 6-20. Calculated Stress vs. Strain Curve Generated from DIC Data.

Hoop stress for burst test sample is determined using Equation 6.1, using the measured inside diameter (d_i) and wall thickness (h) of the sample, and the internal gauge pressure of the sample during the test (p_b). When the ultimate hoop stress is calculated, the maximum measured pressure during the test is used.

$$\sigma_\theta = \frac{p_b d_i}{2h} \tag{6.1}$$

Dimensions of equation inputs are:

σ_θ = hoop stress (MPa)
p_b = burst gauge pressure (MPa)
d_i = measured pretest inside diameter (mm)
h = measured pretest wall thickness (mm)

Hoop strain (ε_θ) is calculated by dividing the as-tested outside diameter (d_{o2}) by the initial outside diameter (d_{o1}) and subtracting 1 as shown in Equation 6.2. DIC does this on a smaller scale by examining the motion of speckles on the test article where the initial distance between two points in the hoop direction ($\delta_{\theta 1}$) is compared to the distance in the hoop direction during the test ($\delta_{\theta 2}$) to calculate strain as shown in Equation 6.3. During the DIC analysis, the hoop strain is calculated from multiple points and averaged from a region ~25 mm from the localization. When examining the localization, it is difficult to measure the final outside diameter. In this case, the measured circumference can be substituted for the outside diameter as shown in Equation 6.4, where C_1 is the initial circumference of the sample and C_2 is the measured circumference of the sample, excluding the opening of the burst. When converting hoop strain to elongation, the strain value is multiplied by 100% as shown in Equation 6.5.

$$\varepsilon_\theta = \frac{d_{o2}}{d_{o1}} - 1 \tag{6.2}$$

$$\varepsilon_\theta = \frac{\delta_{\theta 2}}{\delta_{\theta 1}} - 1 \tag{6.3}$$

$$\varepsilon_\theta = \frac{C_2}{C_1} - 1 \tag{6.4}$$

$$percernt\ elongation = \varepsilon_\theta \times 100\% \tag{6.5}$$

Dimensions of equation variables are:

ε_θ	=	hoop strain (mm/mm)
d_{o1}	=	initial outside diameter (mm)
d_{o2}	=	test outside diameter (mm)
$\delta_{\theta 1}$	=	initial hoop distance between two speckle positions analyzed by DIC (mm)
$\delta_{\theta 2}$	=	test hoop distance between two speckle positions analyzed by DIC (mm)
C_1	=	pretest circumference (mm)
C_2	=	test circumference at burst location, excluding the opening (mm).

6.2.3 Tensile Testing

The tensile test method uses Bluehill materials testing software version 4.11, the Instron test frame, wedge grips, and a high-temperature extensometer to measure physical properties as directed by ASTM E8 and ASTM E21. Digital strain imaging cameras collected additional strain imaging as was previously performed by Shimskey et al. (2014). This allowed the performance of the DIC system to be directly compared to that of the high-temperature extensometer. Testing was performed at RT and at 200°C.

Test articles were prepared for strain imaging analysis by applying a coating of heat resistant white paint and a speckle pattern as outlined in Section 6.2.1. After the paint had dried, the sample was marked at 1 in. from either end. The gauge length (2 in.) was centered on the middle of the sample using a custom marking jig for ease of repeatability when placing the extensometer on the sample. End plugs were then installed in the sample and were secured in place using 1/4 in. wide Kapton high-temperature tape saddled over the top of the end plug (Figure 6-21).

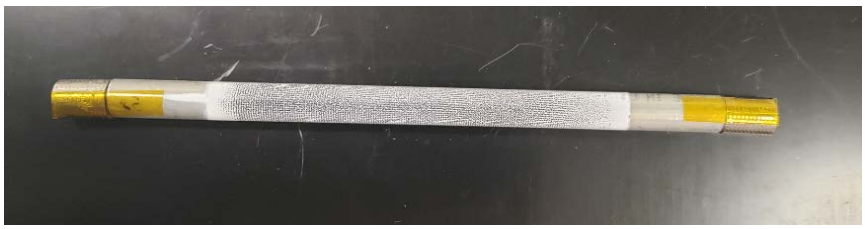

Figure 6-21. Axial Tensile Sample with End Plugs Installed.

The following are general steps involved in performing an axial tensile test:

a. Set up and calibrate the DIC cameras.

b. Zero the load cell.

c. Install the speckled test article, with end plugs in place, into wedge grips.

d. Zero the extensometer.

e. Attach the extensometer to the cladding sample.

f. For high-temperature testing: Launch the elevated-temperature routine in Bluehill, which will turn on the oven and allow the system to equilibrate at 200°C.

g. Bluehill software then preloads the sample to 22 N.

h. After preload, the test article is pulled at 0.1 mm/s crosshead displacement.

A hold point at 24.5% strain is programmed in the method to pause the test so that the extensometer can be removed if that strain level is reached. The extensometer is removed from the sample and the sample is warmed back up to the temperature set point. Then the test resumes.

DIC images and data (temperature) are collected at a rate of 2 Hz over the entire test. Instron load frame data (force, strain, and displacement) are fed into the DIC computer via an input/output cable bundle. An example of the DIC camera setup is shown in Section 6.1.2. Figure 6-22 shows an example strain map during a typical tensile test.

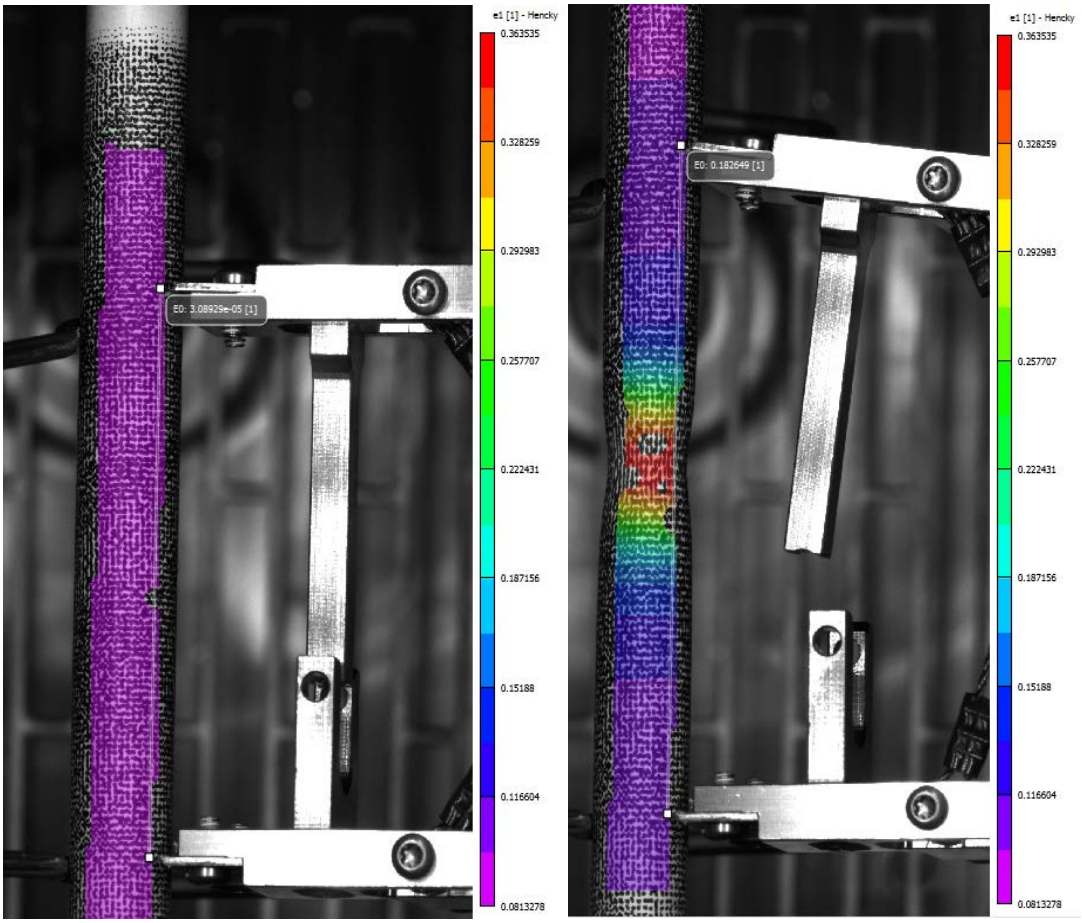

Figure 6-22. DIC Images of Tensile Sample Before Test (left) and at Fracture (right).

6.2.3.1 Methods Used and ASTM Comparison

The methods and equipment used for tensile testing followed the ASTM methods listed here:

ASTM E8/E8M	Standard Test Methods for Tension Testing of Metallic Materials
ASTM E21	Standard Test Methods for Elevated Temperature Tension Tests of Metallic Materials

ASTM E4	Standard Practices for Force Verification of Testing Machines
ASTM E83	Standard Practice for Verification and Classification of Extensometer Systems
ASTM E2309	Standard Practices for Verification of Displacement Measuring Systems and Devices Used in Material Testing Machines
ASTM E2658	Standard Practices for Verification of Speed for Material Testing Machines
ASTM B811	Standard Specification for Wrought Zirconium Alloy Seamless Tubes for Nuclear Reactor Fuel Cladding

Some of the ASTM requirements are called out in Table 6-4. A comprehensive list of ASTM methods and requirements in included in Appendix C.

Table 6-4. Summary of Axial Tensile ASTM Methods Comparison.

	Section	Summary	Comment
ASTM E8/E8M	1.2	The gauge lengths for most round specimens are required to be 4 × Diameter for E8 and 5 × Diameter for E8M.	Section 6.1.2
	5.2.2	Wedge grips are satisfactory for gripping long ductile metal specimens.	Section 6.1.2
	5.4	Extensometers used in tensile testing shall conform to the requirements of Practice E83 for the classifications specified by the procedure section of this test method. Extensometers shall be used and verified to include the strains corresponding to the yield strength and elongation at fracture.	Section 6.1.2
	6.9.1	Specimens for Pipe and Tube: Snug-fitting metal plugs shall be inserted far enough to permit the jaws to grip the specimen properly. The plugs shall not extend into the area where elongation is measured.	Section 6.1.2
	7.1	Preparation of the Test Machine: Upon startup, or following a prolonged period of machine inactivity, the test machine should be exercised or warmed up to normal operating temperatures to minimize errors that may result from transient conditions.	Section 6.3.5
	7.3.1	Gauge Length Marking of Test Specimen: Gauge length for the determination of elongation shall be stamped, scribed, or drawn with ink as preferred.	Section 6.3.5
	7.4	Zeroing of the Testing Machine: The testing machine shall be set up in such a manner that zero-force indication signifies a state of zero force on the specimen. Any force (or preload) imparted by the gripping of the specimen must be indicated by the force measuring system unless the preload is physically removed prior to testing.	Section 6.3.5
	7.6.1	Speed of Testing When Determining Tensile Strength: speed was bounded by ASTM B811. This parameter is controlled by crosshead speed.	Section 6.3.5
	7.6.2	Speed of Testing: Verification shall be done in accordance with E2658, meeting Class E or better requirements.	Section 6.1.2

	Section	Summary	Comment
	7.7.1	Determination of Yield Strength via offset method: On the stress-strain diagram draw line parallel to the elastic region equal but offset by the specified value of the offset, and thus locate the intersection of this line with the stress-strain curve. In reporting values of yield strength obtained by this method, the specified value of offset used should be stated in parentheses after the term yield strength, for example Yield strength (offset = 0.2%).	Section 6.2.3.2
	7.8	Yield Point Elongation—Calculate the yield point elongation from the stress-strain diagram or data by determining the difference in strain between the upper yield strength (first zero slope) and the onset of uniform strain hardening.	Section 6.2.3.2
	7.10	Calculate the tensile strength by dividing the maximum force, during a test carried to fracture, by the original cross-sectional area of the reduced section.	Section 6.2.3.2
	7.11.2	Measurement of elongation after fracture: When the specified elongation is greater than 3%, fit ends of the fractured specimen together carefully and measure the distance between the gauge marks to the nearest 0.25 mm [0.01 in.] for gauge lengths of 50 mm [2 in.] and under, and to at least the nearest 0.5 % of the gauge length for gauge lengths over 50 mm [2 in.]. A percentage scale reading to 0.5% of the gauge length may be used.	Section 6.2.3.2
	7.11.5.1	Report both the original gauge length, G, and the percentage increase.	Section 6.3.5
	7.12	Reduction of area is equal to the minimum cross-sectional area of the reduced section before testing minus the minimum cross-sectional area of the reduced section after testing, the difference expressed as a percentage of the area before testing.	Section 6.2.3.2
ASTM E21	8.1	The following data should be included: Reference to the standard used, Material and sample identification, Specimen type, Yield strength and the method used to determine yield strength, Yield point elongation, Tensile Strength (also known as Ultimate Tensile Strength), Elongation (report original gauge length, percentage increase, and method used to determine elongation; i.e., at fracture or after fracture), Uniform Elongation, Reduction of area, Speed and method used to determine speed of testing, Method used for rounding of test results.	Section 6.3.5
	5.1	Testing Machine: Testing machine shall follow ASTM E4.	Section 6.1.2
	5.3	Temperature-Measuring Apparatus: Temperature should be measured with calibrated thermocouples in conjunction with temperature indicating instrument.	Section 6.3.2
	9.4.2	In attaching thermocouples to a specimen, the junction must be kept in intimate contact with the specimen and shielded from radiation.	Section 6.3.2

	Section	Summary	Comment
	9.4.4	For the duration of the test, (defined as the time from the application of force until fracture), do not permit the difference between the indicated temperature and the nominal test temperature to exceed ±3ºC.	Section 6.3.2
	9.4.7	The time of holding at temperature prior to the start of the test should be governed by the time necessary to ensure that the specimen has reached equilibrium.	Section 6.3.2
	9.8	Measurements of Specimen After Test will be done at RT to the nearest 0.2 mm.	Section 6.3.5
ASTM E4	14.1	The percent error of forces within the range of forces of the testing machine shall not exceed ±1.0%.	Section 6.1.2
ASTM E83	5.7.3	Relative Error of gauge Length (max %) for a Class B-1 extensometer system is ±0.25 with a resolution of 0.00005 in./in., a fixed error of ±0.0001 in./in. or a max relative error of ±0.5%-strain.	Section 6.1.2
ASTM E2309	1.4	For a Class A displacement measurement system fixed error does not exceed ±0.025 mm or a relative error of ±0.5% of displacement with a repeatability of 0.025 mm or a relative displacement of 0.5% of displacement. Resolution is not to exceed 0.013 mm or ±0.25% of reading.	Section 6.1.2
ASTM E2658	1.6	Speed measurement values and or settings on displays/ printouts of testing machine data systems—be they instantaneous, delayed, stored, or retransmitted—which are within the Classification criteria for Class A speed application measuring systems. (Percent error of ±0.5 and a resolution of ±0.25% of reading)	Section 6.1.2
ASTM B811	A4.4.2.2	The strain rate for axial tensile tests shall be 0.003 to 0.007 in./in.-min (mm/mm-min).	Section 6.3.5

6.2.3.2 Analysis of Results

After a tensile test was complete, the raw data output from the Bluehill program and the DIC system were compiled and processed in order to calculate the following:

1. Measured diameters (d_o, d_i) and cross-sectional area (A) of test article
2. Force (F)
3. Measured Axial Elongation (ΔL_z)
4. Axial stress (σ_z)
5. Axial strain (ε_z)
6. Axial stress-strain curve coordinates

7. Yield strength, via the 0.2% offset method
8. Tensile strength (also known as ultimate tensile strength)
9. Modulus of elasticity (E)
10. Reduction of area

Using the measured force (F) during the tensile test and the cross-sectional area (A) of the test article, the axial stress (σ_z) for each sample is determined using Equation 6.6. The cross-sectional area is calculated using the measured outside diameter (d_o) and inside diameter (d_i) using geometry for a tube.

$$\sigma_z = \frac{F}{A} = \frac{4F}{\pi(d_o^2 - d_i^2)} \times (10^6\, mm^2/m^2) \tag{6.6}$$

Dimensions of equation variables are:

σ_z	=	axial stress (MPa)
F	=	force (N)
A	=	cross-sectional area (m^2)
d_o	=	outer diameter (mm)
d_i	=	inner diameter (mm)

The axial strain (ε_z) for each sample is calculated using Equation 6.7 below comparing the total axial elongation (ΔL_z) to the gauge length of the extensometer (L_{gl}) which is 50 mm. The total elongation is measured via the extensometer or by using DIC imaging by examining the contact locations of the extensometer with the sample and measuring the change in distance during the test, functioning as a "virtual extensometer". DIC imaging and analysis also examines the movement of speckles applied to the test article and measures the initial axial distance between two points (δ_{z1}) and the axial distance during the test (δ_{z2}), and calculates strain as shown in Equation 6.8. Multiple points are examined in a region ~25 mm from the localization and averaged to produce a value for axial strain to supplement the extensometer measurements. Percent elongation is reported as axial strain multiplied by 100% as shown in Equation 6.9.

$$\varepsilon_{az} = \frac{\Delta L_z}{L_{gl}} \tag{6.7}$$

$$\varepsilon_z = \frac{\delta_{z2}}{\delta_{z1}} - 1 \tag{6.8}$$

$$percent\ elongation = \varepsilon_z \times 100\% \tag{6.9}$$

Dimensions of equation variables are:

ε_z	=	axial strain (mm/mm)
ΔL_z	=	total axial elongation (mm)
L_{gl}	=	axial gauge length of extensometer (mm)
δ_{z1}	=	initial axial distance between two speckle position analyzed by DIC (mm)
δ_{z2}	=	test axial distance between two speckle position analyzed by DIC (mm)

The modulus of elasticity is calculated using a subset of data selected from the middle of the elastic region on the stress-strain curve for the sample and plotting a linear fit to that data. The slope of that line is used as the elastic modulus which becomes Equation 6.10.

$$E = \frac{\sigma_z}{\varepsilon_z} \times (10^{-3} GPa/MPa) \quad (6.10)$$

Dimensions of equation variables are:

E	=	modulus of elasticity (GPa)
σ_z	=	axial stress (MPa)
ε_z	=	axial strain (mm/mm)

Post-test metallography was performed to measure the percent reduction of area as shown in Equation 6.11. A cross-section of one side of the fracture was mounted in resin and examined via optical microscope as well as regions that were away from the localization (~ 25 mm). The outside diameter and wall thickness were measured to calculate the final cross-sectional area (A_2) and compared to the initial cross-sectional area (A_1).

$$Percent\ reduction\ in\ area = \frac{A_{12} - A_{10}}{A_{10}} * 100\% \quad (6.11)$$

Dimensions of equation variables are:

A_{12}	=	final cross-sectional area at fracture (mm^2)
A_{01}	=	initial cross-sectional area (mm^2)

6.2.4 Bend Testing

The four-point bend test method uses Bluehill software version 4.11, the Instron test frame, custom bend fixtures, and a high-temperature extensometer fitted onto a deflectometer to measure physical properties as directed by ASTM E290. Digital strain imaging cameras collected additional strain and deformation imaging as was performed by Shimskey et al. (2014). This allowed direct comparison in performance of the DIC system and the high-temperature extensometer/deflectometer. Testing was performed at RT and at 200°C.

6.2.4.1 Methods Used and ASTM Comparison

The methods and equipment used for four-point bend testing followed ASTM E290, *Standard Test Methods for Bend Testing of Material for Ductility*, [ASTM 2014]. Some of the ASTM requirements are called out in Table 6-5. A comprehensive list of ASTM methods and requirements in included in Appendix C.

Table 6-5. Summary of Bend ASTM Methods Comparison.

Section of ASTM E290	Summary	Comments
3.8	Free-Bend: The angle of the free bend is measured once the specimen is removed from the fixture.	Section 6.2.4
4.3	Significance and Use: Bend angle can be measured while the specimen is under the bending force (usually used for semi-guided tests), or after removal (for free-bend test). Product requirements determine the method used.	Section 6.2.4
5.4	Free-Bend Test: a uniaxial force is used to bend the specimen. No tension loading along the length of the specimen is permitted.	Sections 6.1.2 and 6.2.4
8.8.3	Angle of Bend: The test is complete when the conditions of the bend are achieved. If significant cracks appear in the outer surface while the force is being applied, the test shall be stopped and the material evaluated.	Section 6.2.4
8.9	Speed of Bending: The rate of motion shall conform to anticipated process application of the material.	Section 6.3.6

6.2.4.2 Analysis of Results

After a bend test is complete the raw data output from the Bluehill program and the DIC system are compiled and processed to calculate the following:

1. Midspan deflection of bend (δ_{bend})
2. Force (F)
3. Bending Moment (M)
4. Inertia (I)
5. Radius of curvature (ρ)
6. Load-displacement curves (F vs. δ_{bend})
7. Bending moment-displacement curves (M vs. δ_{bend})
8. Stiffness
9. Theoretical midspan deflection

Figure 6-23 shows a free-body diagram of the test, showing the forces acting on the tube and the distances associated with them. The support and loading span lengths are based on scaling of previous testing reported by Billone (2012). The ratios of support span to total tube length and load span to total tube length were consistent with that testing. In this case, the length of the support span (L_{bend}) is 125 mm and the distance between the support and load pin (a_{bend}) is 25 mm. Force (F) is measured as the load pins push downward upon the sample. The midspan deflection (δ_{bend}) is measured using a deflectometer attached to an extensometer. DIC imaging also measures the deflection at the center comparing the initial

position of the speckles at the center to the final position as supplemental data to the deflectometer measurement.

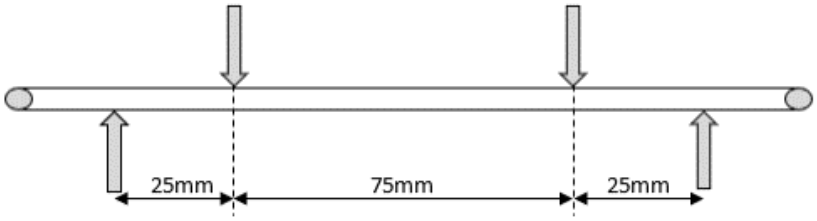

Figure 6-23. Free-Body Diagram of the Four-Point Bend Test.

The bending moment is determined from the bending force (F) and the distance between the support pin and load pin (a_{bend}) using Equation 6.12.

$$\text{Bending moment, } M = F \cdot \left(\frac{a}{2}\right) \tag{6.12}$$

Dimensions of equation variables are:

M	=	Bending moment (N-mm)
F	=	Force (N)
a_{bend}	=	Length between support and load pin (25 mm).

The tube inertia was calculated based on the tubing dimensions using Equation 6.13.

$$\text{Inertia, } I = \frac{\pi}{4} \cdot (r_o{}^4 - r_i{}^4) \tag{6.13}$$

Dimensions of equation variables are:

I	=	inertia (mm^4)
r_o	=	outer radius of tube (mm)
r_i	=	inner radius of tube (mm).

The instantaneous radius of curvature (ρ) is measured using DIC imaging analysis as shown in Figure 6-24. For the analysis, a set of speckle positions that are parallel with the sample are selected prior to the start of testing to analyze (Figure 6-24a). Once the sample starts to bend, the motion of each of these points is examined and the distance traveled is used to generate a new grid position (Figure 6-24b). This data set is then fitted to a circle using orthogonal distance regression which calculates the radius of the bend (Figure 6-24c). The radius of curvature is also measured using an inspection microscope with a magnification of 10× after the tubing was unloaded from the machine. The image from the microscope was then put into ImageJ software, where a curved line was fit to the region of the tubing between the loading pins. This yielded the radius of curvature induced by only plastic deformation since the tube had been unloaded. An example image of this measurement is in Figure 6-25.

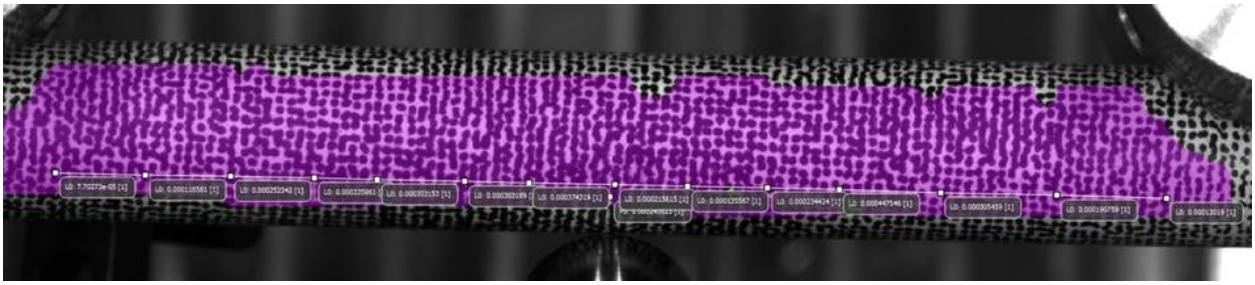

a) Initial grid selected for curvature calculation

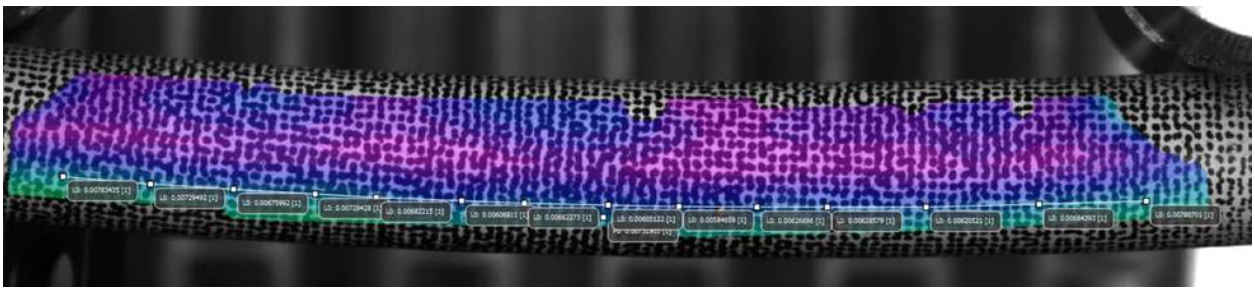

b) Final grid position used to calculate curvature

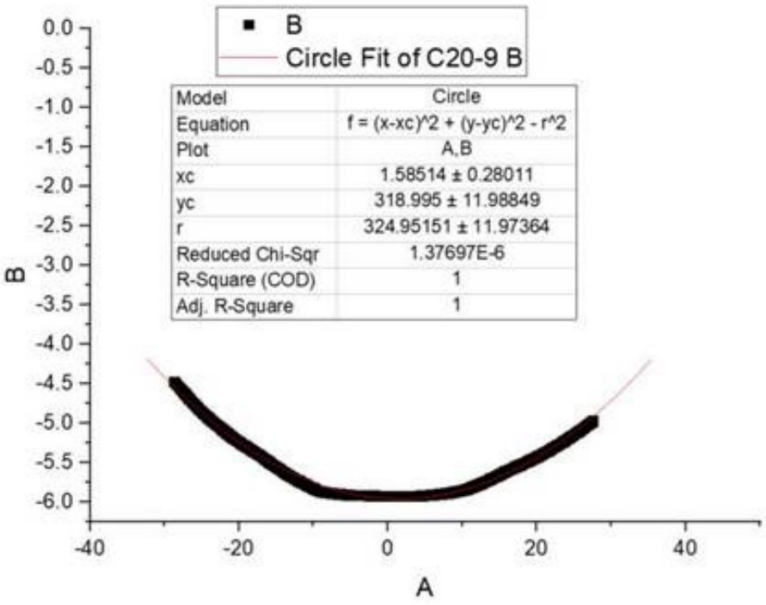

c) Orthogonal distance regression of grid positions fit curved line to circle to calculate radius of curvature

Figure 6-24. Calculation of the Radius of Curvature Using DIC by a) Selected parallel set of points prior to test b) Calculate the movement of each point during test as the bend sample curvature forms c) Use orthogonal distance regression to fit new point locations to circle and calculate radius.

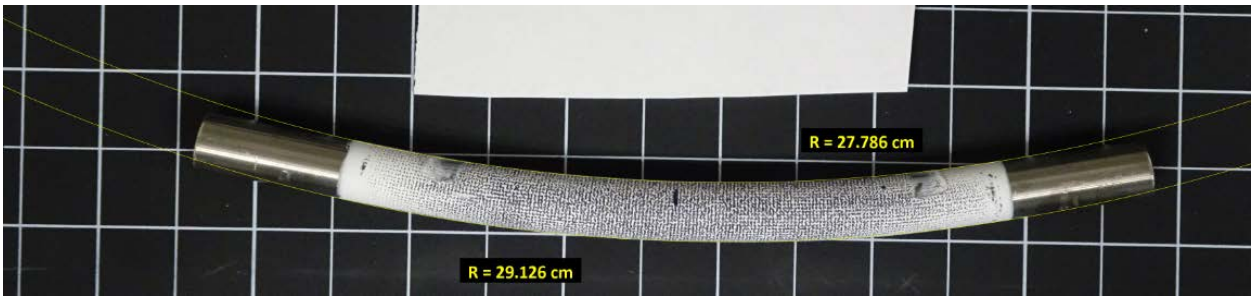

Figure 6-25. Radius of Curvature Measurement on an Unloaded Length of Tubing that Underwent Four-Point Bend Testing.The measurement was made using ImageJ software and the image taken on an inspection microscope.

The stiffness of the tube is measured by dividing the force (F) by the mid-span deflection (δ_{bend}) in the elastic region of the test as shown in Equation 6.14. This calculation is performed by calculating the slope in the elastic region of a force-displacement curve. The theoretical loading stiffness at the mid-span is calculated with Equation 6.15 using the elastic modulus (E), inertia (I), length of the support span (L_{bend}), and the distance between the load and support pin (a_{bend}) to compare to the measured stiffness. The theoretical mid-span deflection (δ_c) is also calculated in the elastic range using Equation 6.16 for comparison to the actual mid-span defection measurements (δ_{bend}).

$$\text{Stiffness, } k = \frac{F}{\delta\delta_{bend}} \tag{6.14}$$

$$\text{Theoretical Stiffness at mid-span, } Kk_c = \frac{48EI}{a_{bend}a\left(3L_{bend}^2 - 4a_{bend}^2\right)}) \tag{6.15}$$

$$\text{Theoretical Deflection at mid-span, } K\delta_c = \frac{Fa_{bend}\left(3L_{bend}^2 - 4a_{bend}^2\right)}{48EIa} \tag{6.16}$$

Dimensions of equation variables are:

F	=	Force (kN)
δ_{bend}	=	Mid-span deflection (mm)
E	=	Elastic modulus (GPa = kN/mm^2)
I	=	Inertia (mm^4)
a_{bend}	=	distance between the support and load pin (25 mm)
L_{bend}	=	length of the support span (125 mm)
k	=	Measured stiffness (kN/mm)
k_c	=	theoretical stiffness at the mid-span of the sample in elastic region (kN/mm)
δ_c	=	theoretical mid-span deflection of sample in elastic region (mm)

Unlike the burst and axially tensile test, development of stress-strain relationships is not a straightforward process due to the geometry of the sample and the direction of the force. Finite element models (FEM) with nonlinear (e.g. plastic) material behavior are needed to derive the stress-strain relationship when the test sample starts to exceed the yield strength. Development of a FEM is currently planned for analysis of this work and future testing to develop these relationships as well as supporting FEM improvements supporting transportation and seismic testing campaigns.

6.3 Qualification of Physical Property Methods and Baseline Testing

In 2013, PNNL procured representative unirradiated, nuclear-grade, zirconium-based fuel rod cladding used by the commercial industry to support the DOE program (see, e.g., Figure 6-26). The plan for this material was to perform various separate effects tests to better understand the individual processes that may affect long-term behavior during extended storage and transportation of spent fuel. Four different orders of as-manufactured cladding were acquired that were certified under ASTM B811. Each purchased set consisted of 20–40 individual zirconium alloy tubes that were

- cut to length and ready for use in an assembly
- the same diameter and wall thickness, within the tolerances of ASTM B811
- manufactured from the same ingot so variation in alloy chemistry was minimal

Figure 6-26. Procured As-Manufactured Cladding. (Shimskey et al. 2014)

Upon receipt, each tube was visually inspected, and hand scribed with an identifier. The mass, length, and d_o were measured, recorded, and entered in a project inventory database for tracking. Average wall thickness was calculated for each individual piece of cladding for physical property testing. To protect the manufacturers providing cladding, statements were included in the purchase agreement that stated that the manufacturer, cladding alloy, dimensions, and annealing conditions would not be reported, but only identified with a generic identifier such as “Group A.”

In 2014, tensile and compression testing were performed using DIC as described in Shimskey et al. (2014) followed by burst testing as in Shimskey et al. (2015). In keeping with the purchasing stipulations of the material, testing results refer to each set of cladding as Group A, B, C, or D. Baseline mechanical testing in these studies confirmed that variability of the material was very low, which demonstrated that the material was suitable for future experimental work.

Before running irradiated cladding samples under Phase 1 of the sibling pin test plan (Saltzstein et al. 2018), PNNL desired to evaluate and qualify its physical property testing equipment and DIC strain imaging systems using the as-manufactured cladding from Group C and Group D purchased in 2013. While the axial tensile and burst methods for Phase 1 testing were based on PNNL’s previous work, an understanding of how testing equipment differences and upgrades to the DIC software would affect performance was desired. Also, elevated-temperature testing and bend testing had not yet been performed with this material or with DIC, and the variability was not known. The goal of this testing was to verify and collect baseline information on the following to support the results of sibling pin testing:

- verification of DIC performance at RT and 200°C
- verification of sample thermal uniformity using convection ovens for 200°C tests
- verification of physical extensometer performance at 200°C
- verification of burst method with DIC at RT and 200°C
- verification of axial tensile method with DIC at RT and 200°C
- verification of four-point bend method with DIC at RT and 200°C

6.3.1 Digital Camera Performance at RT and 200°C

In previous testing, the DIC performance was not evaluated. The purpose of this qualification was to compare DIC strain imaging results to a secondary strain measurement (such as by an extensometer), and evaluate the accuracy of the method by examination of a stationary test article at RT and at 200°C. The qualification testing and associated results are summarized in Table 6-6.

Table 6-6. Summary of DIC Qualification Testing.

Qualification Question	Test Performed	Results
How well do DIC and strain imaging work at 200°C?	Evaluate the measurement error of a speckled test article for each test method at RT and 200°C.	Low error measured from strain imaging analysis, with some increased error at elevated temperatures.
How does the DIC compare to other strain methods?	Compare the DIC results to RT extensometers results to confirm DIC performance to calibrate instruments.	Excellent agreement between DIC imaging and extensometers. Provides additional strain imaging beyond limits of external devices and in case of equipment failure as seen with the deflectometer from initial testing.

6.3.1.1 Testing Methods

Error analysis on the burst system was performed by taking one set of approximately 250 images of a static tube at RT and a second set of images of a static tube at 200°C. In each of these image sets, it is known that there is no deformation in the tube during capture of each the image set, so any resulting strain in the analysis results from error from the system. The images were analyzed under settings identical to those for the actual specimens and over the same size area of interest.

Similarly, error analysis of the tensile and bend systems was performed by taking sets of approximately 250 images at 2 Hz of a static tube in positions for bend and tensile testing. Another set of images was taken of the specimen in the tensile configuration while moving the crosshead to displace the unstrained specimen approximately 1/2 inch. All three sets of images were then replicated at 200°C after following the standard heat and soak process. Images were captured and processed under settings identical to actual tests.

Lastly, DIC strain imaging is compared to the axial tensile strain and four-point bend deflection measurement data collected during RT testing for differences.

6.3.1.2 Results

The error in strain reported for this analysis is defined as *e1*, which is the absolute maximum amount of noise measured in the positions of the speckles placed on a test article. This error is presented in the data in Table 6-7 and Figure 6-27 for the burst system. The error in the system at 200°C was approximately five times greater than the error found at RT in both the average error found throughout the test and the maximum amount of error in any single image. Analyzing the error over the duration of the test and across the length of the tube indicates no temporal or spatial dependence of the error in this system.

Table 6-7. DIC Error Summary for Burst Testing.

Error in *e1*	RT	200°C
Average	9.59×10^{-05} in./in.	5.08×10^{-04} in./in.
Maximum	1.78×10^{-04} in./in.	1.32×10^{-03} in./in.
Standard Deviation	2.58×10^{-05} in./in.	2.18×10^{-04} in./in.

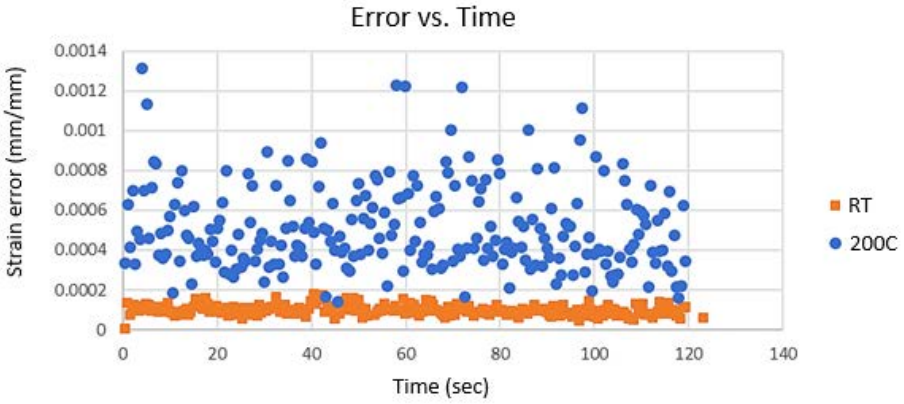

Figure 6-27. DIC Strain Error vs. Time for Burst at Room Temperature and 200°C.

Error for the tensile and bend test systems is reported here in units of strain to define the system similarly to the burst system analyzed previously, and is summarized in Table 6-8. Analysis of the static images in burst and tensile configurations indicated that error in the image does not change with respect to time or position. While this is true for a static specimen, the data from a displaced specimen, shown later, will indicate variation in the error distribution across the sample.

Table 6-8. DIC Error Summary for Bend and Tensile Testing.

	Error in *e1*	RT	200°C
Bend	**Average**	2.75×10^{-05} in./in.	2.40×10^{-04} in./in.
	Maximum	1.26×10^{-04} in./in.	5.48×10^{-04} in./in.
	St. Dev.	2.13×10^{-05} in./in.	5.96×10^{-05} in./in.
Tensile	**Average**	9.49×10^{-05} in./in.	1.84×10^{-04} in./in.
	Maximum	2.00×10^{-04} in./in.	2.91×10^{-04} in./in.
	St. Dev.	2.73×10^{-05} in./in.	3.66×10^{-05} in./in.

The images were also analyzed to show the error in the relevant measurements for each test, which may be of more interest; these are summarized in Table 6-9 and Table 6-10, and testing results are plotted

against time in Figure 6-28 and Figure 6-29. Bend testing data is given for the displacement of the tube in the direction of motion. Here, the error in these displacement measurements was shown to be an average of 0.34 µm at RT and 1.75 µm at 200°C. Tensile testing DIC data has been used to apply a virtual strain gauge (VSG) to the specimen. The error in an applied VSG on a tensile specimen was found to be 4.8×10^{-06} at RT and around 2×10^{-05} at 200°C.

Table 6-9. DIC Displacement Error for Bend Setup.

Bend Setup		
Displacement Error	**RT**	**200°C**
Average	−0.34 µm	1.75 µm
Maximum	0.88 µm	7.07 µm
Standard Deviation	0.02 µm	2.10 µm

Table 6-10. DIC VSG Error for Tensile Setup.

Tensile Setup		
VSG Error	**RT**	**200°C**
Average	-4.80×10^{-06} in./in.	2.01×10^{-05} in./in.
Maximum	5.67×10^{-05} in./in.	9.74×10^{-05} in./in.
Standard Deviation	1.83×10^{-05} in./in.	2.04×10^{-05} in./in.

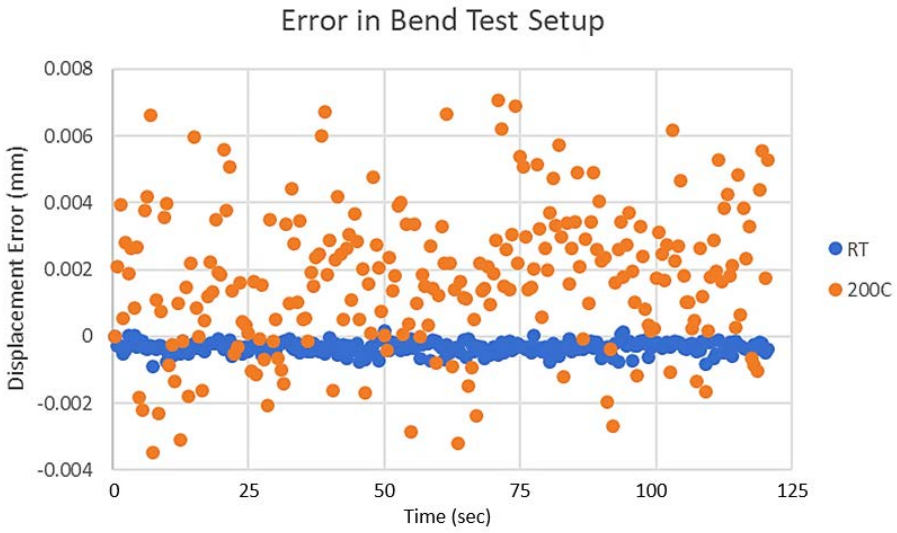

Figure 6-30. DIC Strain Error vs. Time for Four-Point Bend Tests at RT and 200°C.

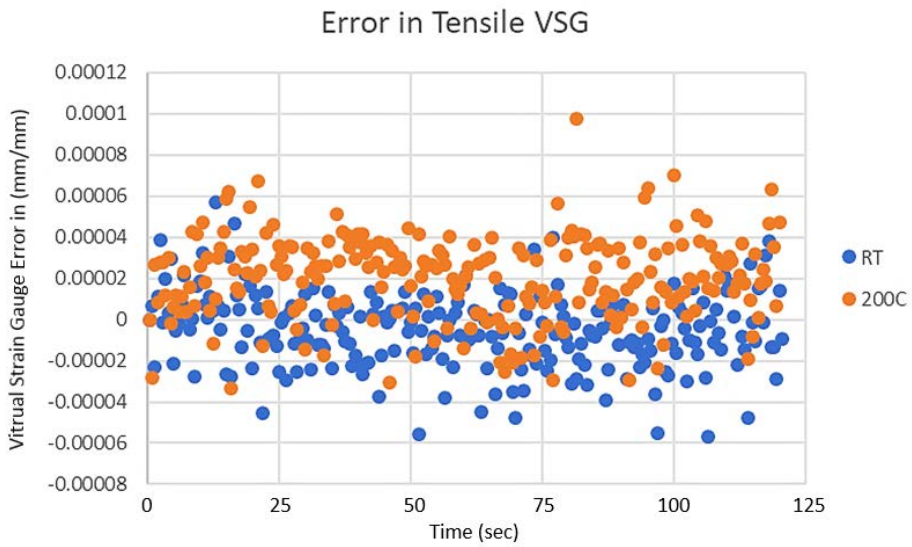

Figure 6-31. DIC Strain Error vs. Time for Tensile Tests at RT and 200°C.

The images collected while displacing the specimen added some insight into error in the tensile setup. Analysis shows there are several discrete locations on the specimen where higher strain (up to 3.5%) results from movement of the sample. These spots of high strain were found to be associated with a physical location in space rather than spots on the sample itself. This indicates that the problem lies with the setup and is most likely caused by either lighting on the sample or the image quality in that location as the specimen is viewed through the window. Outside of these certain locations, the image has a maximum error in *e1* of less than 0.15% and the VSG applied to the specimen has an average error of 2.8×10^{-05} in./in. at RT and 9.32×10^{-05} at 200°C. If the proper care is exercised when analyzing tensile tests, these locations of high strain can and should be avoided.

Figure 6-30 directly compares the differences between the extensometer and the DIC axial strain measurements over the course of a RT tensile test. Overall, there is good agreement between the two measurements until the very end of the test. At this point, imaging shows that the extensometer began to slip on the test article just before the test article failed. Typically, the extensometer is removed from the test article after the sample yields to protect the extensometer and prevent these types of errors. However, it is not desired to remove the extensometer during radiological and elevated-temperature testing, so the model used for this program was chosen because it can handle sample failures. This evaluation shows that, while the extensometer performs well through yield, using DIC strain imaging as the sample failure point develops will be a suitable alternative strain measurement for comparison. Figure 6-31 shows the difference between the displacement measured by a deflectometer and that calculated by the DIC during a typical bend test at RT. Initial tests found issues with the deflectometer that resulted in the deflectometer sticking in position during the unload cycle of the test (Figure 6-31a). Overall, the DIC and deflectometer results correlate very well until the sample stress is lowered. The difference in results during the end of the test is cause by the deflectometer sticking and not springing back when unloaded, while the strain imaging captures the correct change in deflection which required the replacement of a spring. Figure 6-31b compares the results of a RT bend test after this repair showing excellent correlation between both DIC and the deflectometer measurement during the load and unload cycle averaging between 1-3% deviation from each other.

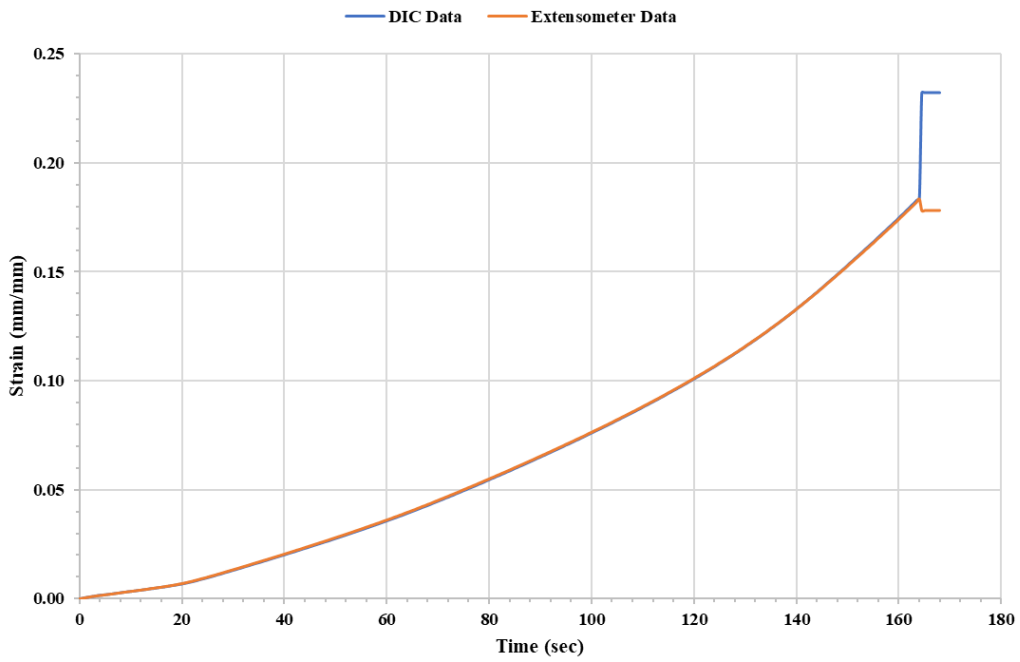

Figure 6-32. Comparison Between DIC and Extensometer Strain Outputs for Tensile Testing.

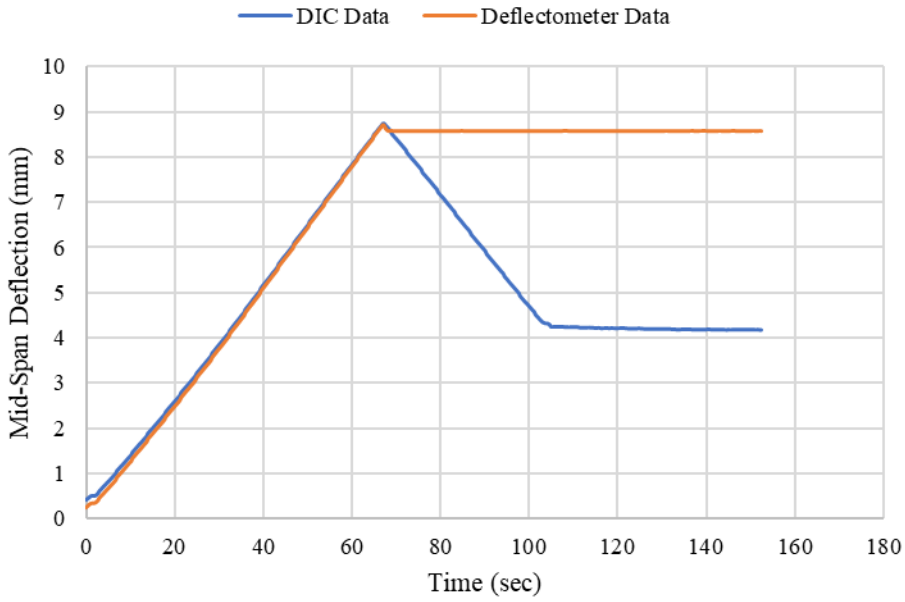

a) Before Deflectometer Repair

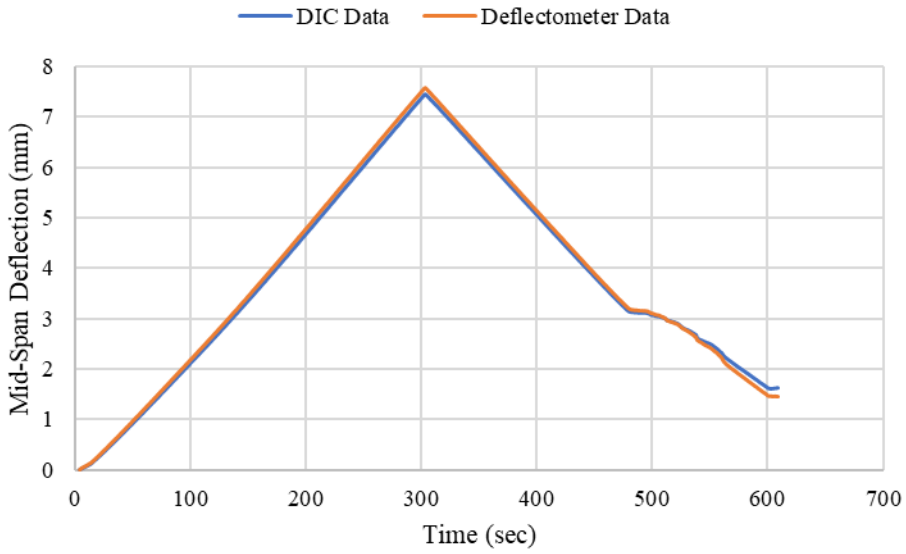

b) After Deflectometer Repair

Figure 6-33. Comparison Between DIC and Deflectometer Strain Outputs for Bend Testing a) Before Deflectometer Repair and b) After Deflectometer Repair.

6.3.2 Heating Samples for Testing at 200°C

The burst convection oven and Instron environmental chamber were used for this testing to provide better heat transfer and thermal homogeneity within our test samples than ovens without convection. The goal of this testing was to measure the heat soak required for test articles to reach equilibrium and to determine whether the measured temperature variation of the sample was within the accuracy of the thermocouples used (±2°C). A summary of the qualification testing and associated results are summarized in Table 6-11.

Table 6-11. Summary of Oven/Environmental Chamber Performance Testing.

Qualification Questions	Testing Performed	Results
How long must a thermal heat soak be to reach equilibrium?	Attach calibrated thermocouples to test articles loaded into physical property testing equipment. Heat to 200°C, and measure the time needed for the test article to reach equilibrium with the convection oven.	Based on these results, a 90-minute heat soak was selected for the axial tensile and four-point bend fixtures. A 180-minute heat soak was selected for the burst fixture. See Appendix F for temperature profiles.
Is the sample at a uniform temperature before testing?	Measure the temperature of test articles for each test at three different locations along its length to check thermal homogeneity of the sample.	Temperature readings across the sample before testing were within 0.3°C of each other.

6.3.2.1 Testing Methods

A 6 in. piece of Group C cladding was used as a test article. This sample was instrumented with three calibrated Type K thermocouples, located 2 in., 3 in., and 4 in. from the bottom of the sample (see Figure 6-32, Figure 6-33, Figure 6-34). Thermocouples were attached using high-temperature fiberglass tape. This test article was then placed in the test fixtures of the burst, axial tensile, and four-point bend systems. A calibrated data logger recorded the temperatures at these three locations, and a fourth Type K thermocouple was placed in the oven/chamber to capture ambient temperature.

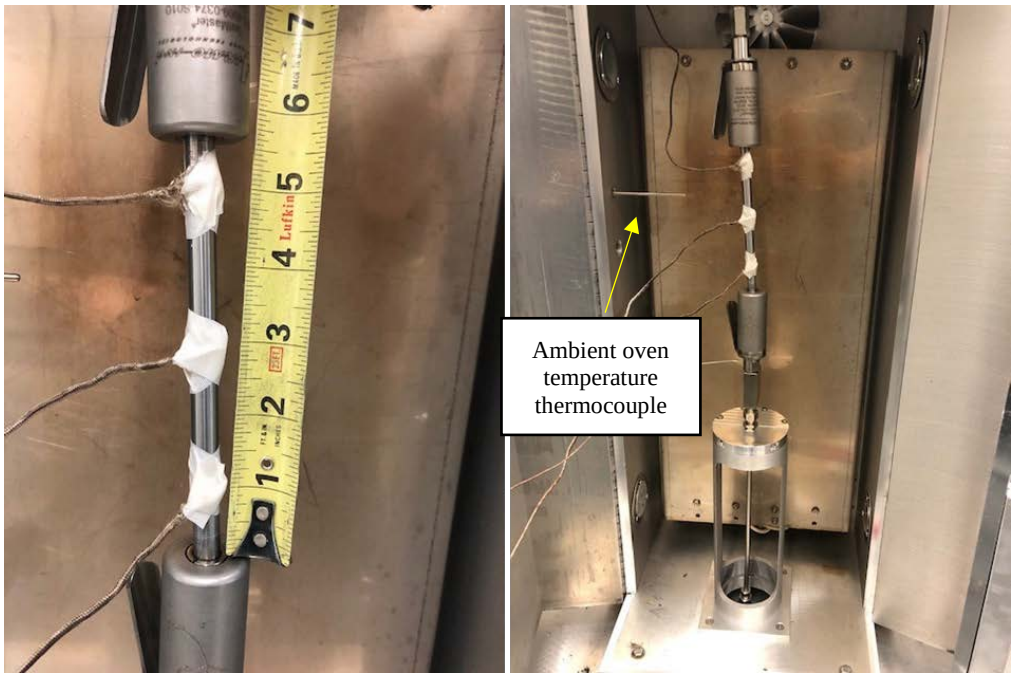

Figure 6-34. Burst-Test Oven Qualification Configuration.

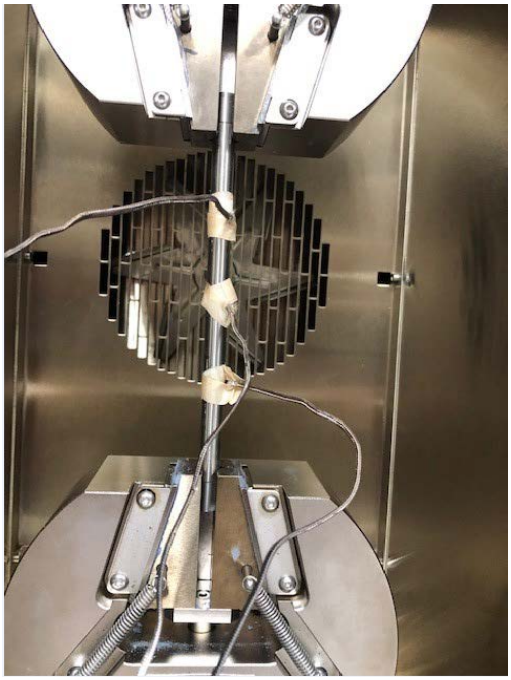

Figure 6-35. Instron Test Frame Environmental Chamber Qualification via Instrumented Tensile-Test Cladding Sample.

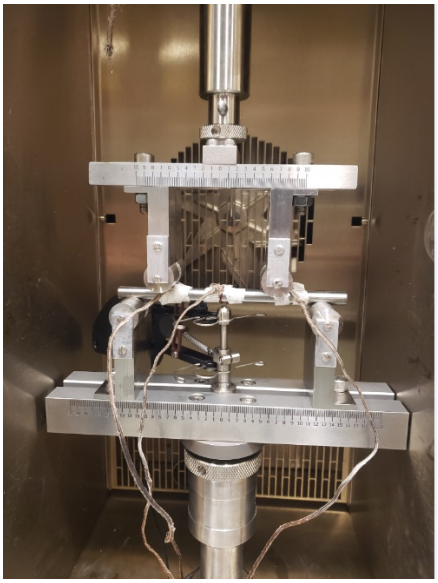

Figure 6-36. Instron Test Frame Environmental Chamber Qualification via Instrumented Four-Point-Bend Test Cladding Sample.

6.3.2.2 Results

For the Instron environmental chamber used for axial tensile and four-point bend testing, an oven set point offset of +2°C was required to reach 200°C on the sample. The burst-test oven set point remained at

200°C. However, the burst test article took longer to reach equilibrium because water was present in the sample and piping. Each fixture setup was tested five times. Table 6-12 summarizes these tests.

Table 6-12. Summary of Times Required for Ovens to Reach Thermal Equilibrium.

Fixture Setup	Average Time to Thermal Equilibrium (min)	Standard Deviation (min)
Axial Tensile	64	3
Four-Point Bend	71	9
Burst	144	16

6.3.3 Extensometer Performance at 200°C

While extensometers are calibrated and verified by ASTM methods before use, those calibrations were performed at RT and not at 200°C, so validation testing of the extensometer and deflectometer at this temperature was needed. The qualification testing and associated results are summarized in Table 6-13.

Table 6-13. Summary of Extensometer Performance at 200°C.

Qualification Questions	Answer Method	Results
How well does the extensometer perform for tensile and bend testing at 200°C?	Compare results to DIC performance for elevated-temperature tests.	The elevated-temperature testing showed DIC and extensometer values were consistent with each other. Deviations of axial strain between DIC and extensometer measurements were less than 0.2%. The deflectometer differences with DIC are an order of magnitude higher but in line with the 1-3% error measured with room temperature results

6.3.3.1 Testing Methods

To check performance of the extensometers used for tensile and bend testing at 200°C, the strain/deflection measurements from these instruments were compared to those from a “virtual” extensometer that is part of the DIC software, as was done at RT. Samples of 1/8 in. SH40 pipe steel alloy ASTM A106 grade B were used as test articles for these tests.

6.3.3.2 Results

Comparisons of axial strain measurements during an axial tensile test of a steel test article are provided in Figure 6-35 and Figure 6-36. Axial tensile-test strain measurements from the extensometer are in excellent agreement with the DIC-measured strain values: the measured difference falls below 0.2%. For the deflectometer, the differences are still small, but an order of magnitude larger. However, this difference is comparable to the 1-3% difference observed for room temperature results so operations at 200°C do not impact the measured error of deflection for bend testing.

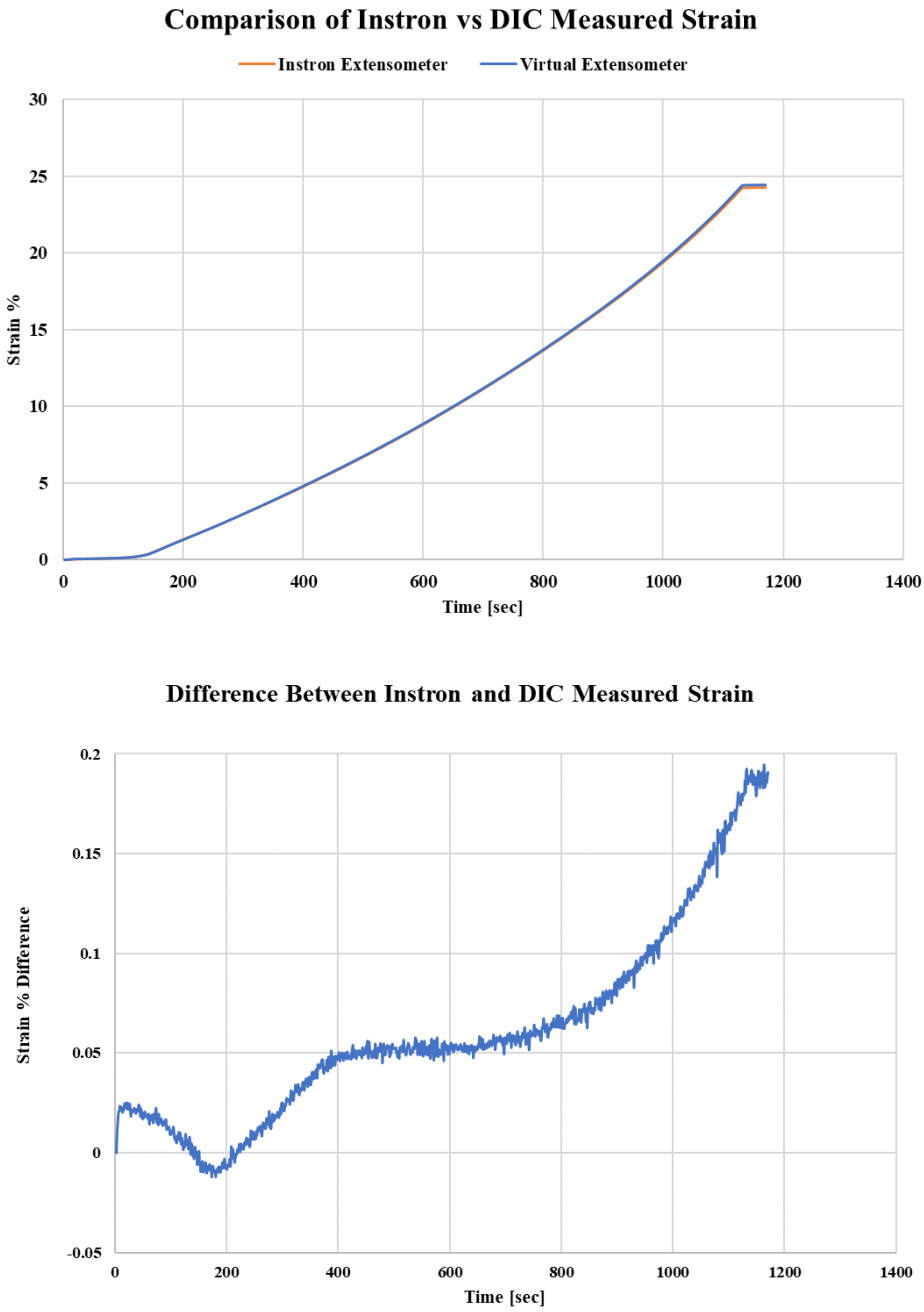

Figure 6-37. Comparison of Axial Strain Measurements of Alloy A106 Tubing and Measured Percent Difference During Axial Tensile Test at 200°C.

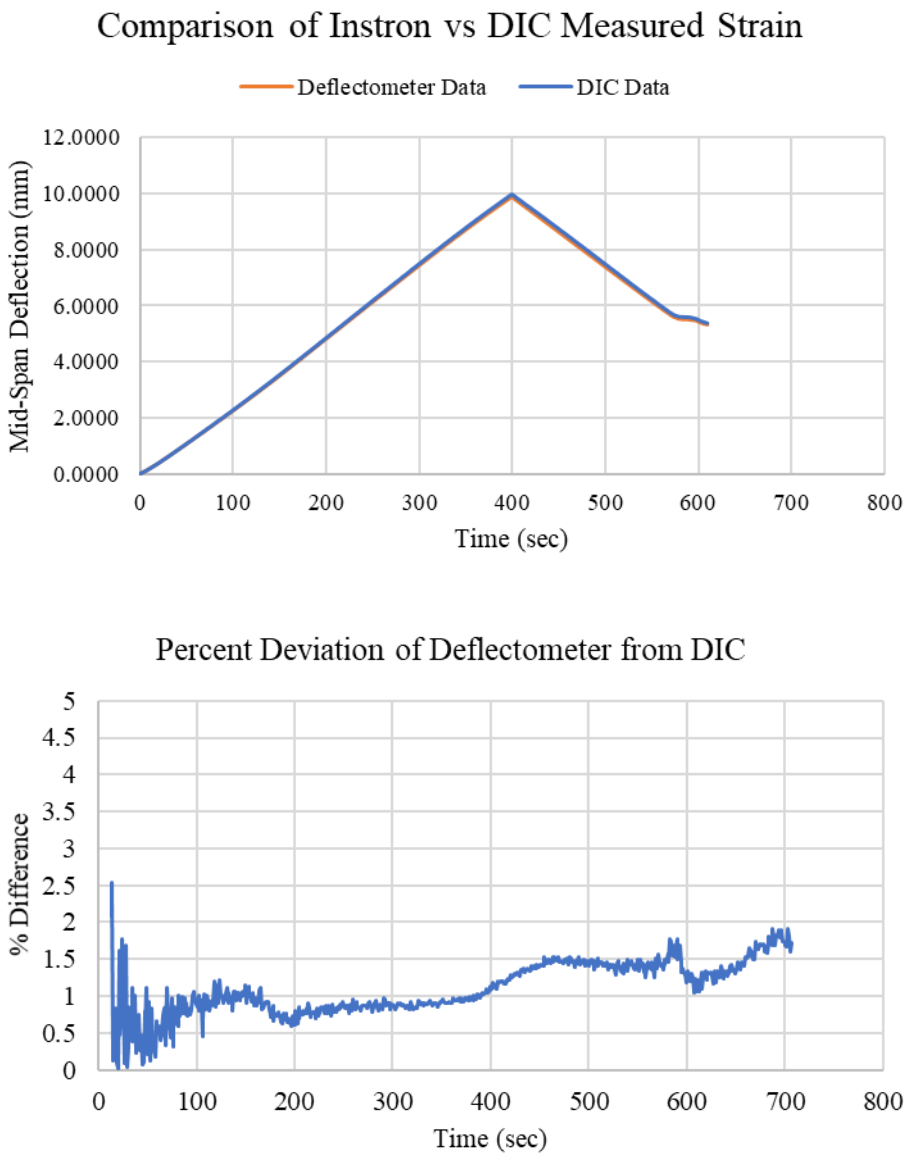

Figure 6-38. Comparison of Deflection Measurements of C Alloy Tubing and Measured Percent Difference During Four-Point Bend Test at 200°C.

6.3.4 Burst System Performance

A set of burst samples was tested using as-manufactured Zircaloy cladding certified to ASTM B811; the purpose was to evaluate variation to check the repeatability of values acquired using the measurement method. The qualification testing and associated results are summarized in Table 6-14.

Table 6-14. Summary of Burst Baseline Testing.

Qualification Questions	Test Method	Results
Is burst testing method repeatable and accurate?	Perform sample set of burst tests from certified lot of as-manufactured cladding to verify testing variation is within experimental error of system.	The burst testing method and equipment used showed excellent repeatability of results at both ambient and elevated temperatures. Metallographic analysis of the ultimate hoop stress in the uniform region validated testing results show agreement with ultimate hoop stress measurement performed using initial dimensions.

6.3.4.1 Testing Methods

Burst tests were conducted between January 30, 2020 and September 25, 2020. in the lab space that will later be used to conduct tests on irradiated samples. Tests were performed at a target ramp rate of 2,000 psi/min to onset of yielding, and then pressure was increased until failure occurred in either the specimen or the pressure delivery system. Twenty-one total specimens were tested, 16 at RT and five at 200°C. During testing of three specimens, the pressure system leaked before the specimen failed. The cause was discovered to be O-ring failure; thereafter, the O-rings were replaced for each test.

6.3.4.2 Results

Validation tests for ultimate hoop strength using unirradiated cladding yielded results that all fell within 2-3% error for Group C and 1% error for Group D as shown in Table 6-15. Additionally, Table 6-15 shows the relative percent difference (RPD) and relative standard deviation (RSD). It is important to note that pressure values displayed by the transducer were calibrated within a 2% error, so variations in data could be attributed to errors within the instrument. Elevated-temperature testing showed measurable difference in sample ductility and decreased the maximum hoop stress by nominally 25% for both groups. A stress vs. strain analysis using DIC data from Group D burst tests at RT and elevated temperature is shown in Figure 6-36. The DIC will measure the final permanent strain of the system, which is less than the maximum strain while pressurized. RT data points from raw DIC data as well as stress/strain curves for all samples are shown in Appendix H.

Table 6-15. Summary of Repeatability of Ultimate Hoop Stress Results from DIC and Initial Cladding Measurements

	Samples	RPD (%)	RSD (%)	% Error
RT Tests				
Alloy C	8	--	1.8%	2.3%
Alloy D	7	--	0.9%	0.9%
200°C Tests				
Alloy C	2	2.7%	--	--
Alloy D	2	0.3%	--	--

Note: Error is calculated from the two-tail t-confidence limit ($\alpha/2$ =2.5%) and dividing it by the average.

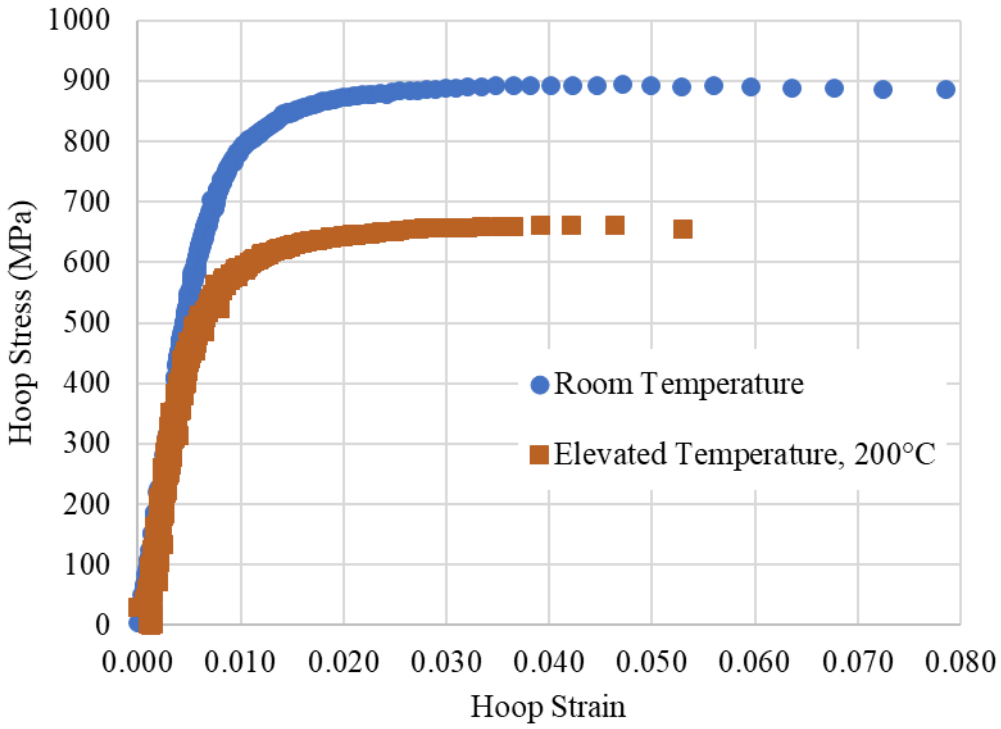

Figure 6-39. Calculated Stress vs. Strain Curve Generated from DIC Data for Burst Tests of Group D Alloy at RT and Elevated Temperature.

Post-test wall thickness and circumference were measured for each burst sample on an optical microscope to determine the ultimate hoop strength. Metallography was done to serve as baseline information for verifying the measurements that will be taken during post-irradiation testing. Table 6-16 provides the RSD/RPD and percent error (calculated from a 95% confidence interval) for the resulting measurement of the test article in the uniform strain region and of the location of the burst (POMB). The results show an increase in error which is a likely result of using the final measurements of the sample after the test which can show more variation in stress/strain in the sample versus using nominal initial dimensions for the entire test. Measurements of the diameter and wall thickness of the localization is also can be difficult. An image of an optical metallurgical sample of the burst localization with measurements of the POMB from a test article sample is shown in Figure 6-38 which is from one of the Alloy D 200°C tests. Due to the increase in ductility at the elevated temperature, the localization is large as well as the opening at the burst location.

Table 6-16. Summary of Repeatability of Ultimate Hoop Stress Results Using Final Metallographic Measurements of the Diameter and Wall.

	UNIFORM Measurement			POMB Measurement			
	Samples	RSD (%)	Error (%)	Samples	RPD (%)	RSD (%)	Error (%)
RT Tests							
Alloy C	12	5.7%	4.2%	6	--	5.0%	6.5%
Alloy D	16	3.8%	2.4%	8	--	2.0%	2.1%
200°C Tests							
Alloy C	4	2.8%	5.9%	2	1.8%	--	--
Alloy D	4	3.5%	7.2%	2	11.6%	--	--

Note: Error is calculated from the two-tail t-confidence limit ($\alpha/2$ =2.5%) and dividing it by the average.

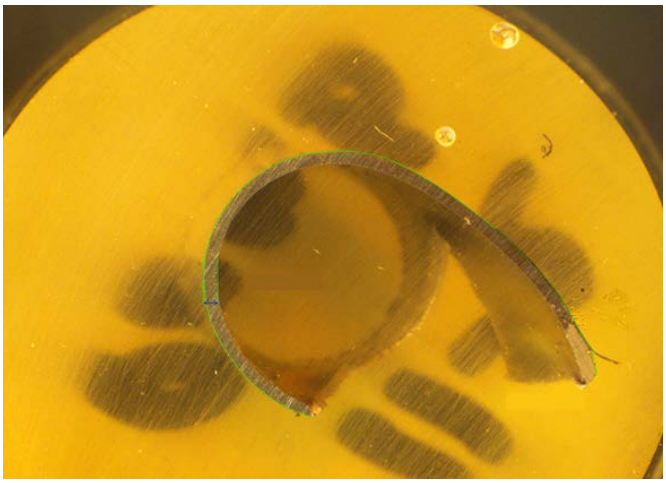

Figure 6-40. Post-Test Optical Microscope Measurement of Localization Region of Sample.

The ultimate hoop stress values in the uniform strain region of the were compared to those measured by the DIC using the initial dimensional value of the sample. The relative percent differences (RPD) between the average of each group is provided in Table 6-17, showing differences between 1-3%.

Table 6-17. Relative Percent Difference of the Average Ultimate Hoop Stress DIC and Metallography from the Uniform Strain Region

Group	Test Temperature	RPD (%)
C	Ambient	2.8
	200°C	1.5
D	Ambient	1.8
	200°C	2.3

6.3.5 Tensile Test Performance on Instron Test Frame

Samples of as-manufactured Zircaloy cladding certified to ASTM B811 were tensile tested. Sixteen were tested at RT and eight tested at 200°C, split evenly between Groups C and D and evaluated for variation of resulting tensile data to check whether the values were repeatable with the measurement method. The qualification testing and associated results are summarized in Table 6-18.

Table 6-18. Summary of Baseline Tensile Testing.

Qualification Questions	Test Method	Results
Is the tensile testing method repeatable and accurate?	Perform tensile tests on samples from a certified lot of as-manufactured cladding to check whether test result variation is within the experimental error of the system.	The tensile testing method and equipment used showed excellent repeatability of results at both ambient and elevated temperatures.

6.3.5.1 Testing Methods

Tensile tests were conducted in RPL with the Instron test frame during September 2020. Twenty-five total specimens were tested, 16 at RT and nine at 200°C, split between Group C and D cladding (see Table 6-17). Testing was controlled via crosshead displacement of the load frame at a constant speed of 0.1 mm/s for the entire test. While this corresponded to an average strain rate above the target rate outlined in ASTM B811, the strain rate used is within the rates tested by Shimskey et al. (2014) which confirmed zircaloy cladding was not sensitive to strain rate in this range. The crosshead speed will be decreased for irradiated samples to allow more data to be collected for the duration of the test.

6.3.5.2 Results

Testing showed excellent repeatability. The compiled stress-strain curves, with strain determined by extensometer and DIC virtual extensometer, can be seen in Appendix I. There were two instances in this test set where the test article in Group C failed at or very near the upper knife edge of the extensometer. The resulting data would have to be excluded if only an extensometer was used. However, the DIC virtual deflectometer could be shifted above the fracture and still collect accurate data.

RT results were compared to tensile data generated by Shimskey et al. (2014). As shown in Table 6-20, all calculated properties seemed to agree closely.

Post-test metallography subsampling allowed for the measurement of OD and wall thickness at the point of fracture and 1.5 in. from the top and bottom of the test article. From these measurements, the reduction-of-area and fracture stress values were calculated. These post-test measurements were taken via optical microscope on subsamples mounted in resin (see Figure 6-39).

Table 6-19. The 95% Confidence Interval Error for Selected Properties During Axial Tensile Testing

		95% Confidence Level Error				
Material	Temp (°C)	Elastic Modulus	Yield	UTS	Failure Strain	Average Percent Difference of Strain between DIC and Extensometer
C Group	RT	0.9%	0.8%	0.3%	2.1%	0.79

	200*	6.3%	1.7%	1.3%	10.3%	1.19
D Group	RT	2.5%	1.2%	1.1%	3.3%	0.93
	200	1.5%	3.3%	2.6%	3.9%	0.99

*Larger error is reported in this row because sample size was truncated when the sample failed at the deflectometer knife blade.
UTS is ultimate tensile strength.

Table 6-20. Percent Difference Between 2020 and 2014 Data.

	Temperature	Elastic Modulus (MPa)	Yield (MPa)	UTS (MPa)
C Group	RT	7.03%	5.86%	1.49%
D Group	RT	3.97%	2.75%	2.64%

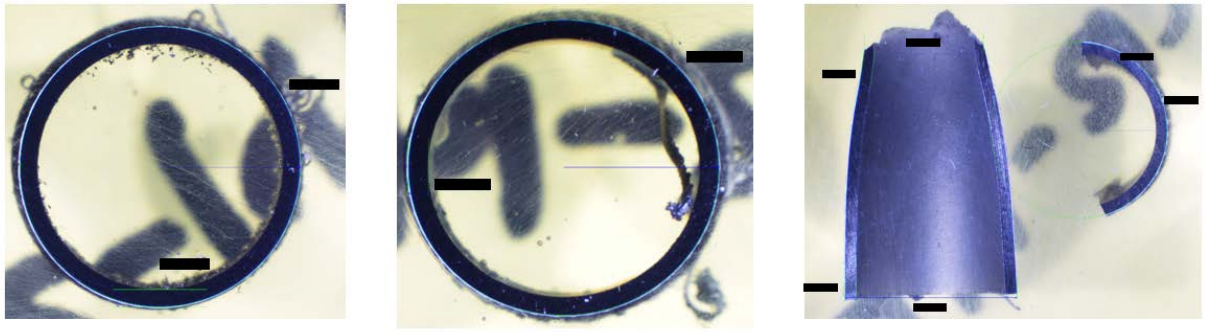

Figure 6-41. Metallography Imaging of Post-test Tensile Sample, Top (left), Bottom (middle), and at Fracture (right).

6.3.6 Bend Test Performance on Instron Test Frame

A set of bend samples were tested using as-manufactured Zircaloy cladding certified to ASTM B811 and evaluated for variation to confirm the repeatability of the measurement method developed for sibling pins (Table 6-21).

Table 6-21. Summary of Four-Point Bend Performance Testing.

Qualification Questions	Test Method	Results
Is bend testing method repeatable and accurate?	Perform a sample set of bend tests from a certified lot of as-manufactured cladding to check whether testing variation is within the experimental error of the system.	The bend testing method and equipment used showed excellent repeatability of results at both ambient temperatures and elevated temperatures.

6.3.6.1 Testing Methods

Tubing was tested in the previously described four-point bend setup for 16 RT tests and eight tests at 200°C, split evenly between the C and D tubing groups. The rollers contacting the tube were greased with silicone, which is stable to 260°C. The tube was preloaded to 2 N and then the displacement was zeroed. Then a preload was applied at 1 mm/min to 22 N. The test then proceeded at 5 mm/min to a maximum crosshead displacement of 6 mm. After the crosshead reached the 6 mm displacement, the crosshead was returned to 0 mm at the same unload rate as the loading rate.

Due to issues seen with the deflectometer during the testing described above, seven additional RT tests and three elevated temperature tests were performed from the Group C cladding. For these tests, the displacement spend was decreased to 1mm/min and the crosshead displacement was reduced to 5 mm due to pinching seen at 6 mm.

6.3.6.2 Results

The testing of the zirconium tube groups showed excellent repeatability within the temperature and alloy sets. The compiled force-displacement curves, and bending moment-displacement curves with deflection determined by deflectometer, can be seen in Appendix J. Issues with the deflectometer sticking with the first test sample group prevented it from capturing the unloading curves; therefore, the DIC was needed to capture the unloading deflection. However, the deflectometer was working well for the second set of samples and compared well with DIC mid-span deflection measurements throughout the test as discussed previously and provides two methods of measuring the mid-span deflection during testing in the event one fails unexpectedly (e.g., spring failure in the deflectometer).

This repeatability was shown during the testing of the zirconium tube groups, as seen in Appendix J. Table 6-22 indicates that the Instron frame, and tooling, were all working properly through the load cycle of the test. Re-runs from Group C performed similarly with the deflectometer working correctly for all tests. Table 6-23 summarizes the repeatability of the testing equipment and analytical techniques for the second set of tests showing excellent agreement of measured properties and comparison to theoretical properties. Comparisons of the theoretical mid-span displacement versus the measured displacement are found in Appendix J which show good agreement in the elastic range of the tests.

Table 6-22. The 95% Confidence Interval Error for Selected Properties during Four-Point Bending Initial Tests

		95% Confidence Level Error	
Material	**Temp °C**	**Max Deflection**	**Max Bending Moment**
C Group	RT	2.4%	1.1%
	200	18.2%*	6.6%*
D Group	RT	2.7%	1.2%
	200	3.9%	2.2%

* One outlier that is 16% different on deflection and 6% different on bending moment

Table 6-23. The 95% Confidence Interval Error and for Selected Properties and RPD% Comparisons of Measurements of Re-Run Four-Point Bending Tests from Group C

	95% Confidence Level Error					RPD (%)	
Temp °C	**Max Deflection**	**Max Elastic Deflection**	**Max Bending Moment**	**Max Elastic Bending Moment**	**Measured Stiffness**	**Theoretical Stiffness vs Measured Stiffness**	**Measured Radius Curvature vs DIC**
RT	1.2%	2.3%	0.5%	2.0%	1.2%	9.1%	4.64%
200	2.1%	0.7%	2.6%	4.5%	0.9%	3.6%	3.81%

6.4 Summary and Future Actions

- Installation of physical property testing equipment is now complete. The test equipment is connected to strain imaging software that can collect imaging of speckled test articles through the windows of the convection ovens of the burst system in the Instron test frame used for axial tensile and four-point bend testing.
- Qualification results can be used to check whether the system continues to work properly when irradiated cladding is tested. At predetermined intervals during the irradiated cladding testing, the unirradiated zirconium tube groups will be tested with the four-point bend methodology and compared to this original data to verify whether the system continues to function properly.
- Error of the strain imaging technique was evaluated at room temperature and at 200°C. As expected, the error at elevated temperature increases, likely because heat waves disturb the DIC speckle image being analyzed by the strain analysis software. This is apparent when comparing stress-strain curves between room temperature and 200°C for all testing. However, the signal-to-noise error is still relatively small at 200°C, and high-quality data can be retrieved at this temperature with this technique. It is recommended that the signal-to-noise error measurement be repeated if tests above 200°C are performed.

This page is intentionally left blank.

7. REFERENCES

ASTM B811-13. 2017. Standard Specification for Wrought Zirconium Alloy Seamless Tubes for Nuclear Reactor Fuel Cladding. ASTM International, West Conshohocken, Pennsylvania.

ASTM E3-11. 2017. Standard Guide for Preparation of Metallographic Specimens. ASTM International, West Conshohocken, Pennsylvania.

ASTM E4-20. 2020. Standard Specification for Force Verification of Testing Machines. ASTM International, West Conshohocken, Pennsylvania.

ASTM E8/E8M-16a. 2016. Standard Test Methods for Tension Testing of Metallic Materials. ASTM International, West Conshohocken, Pennsylvania.

ASTM E21-17. 2016. Standard Test Methods for Elevated Temperature Tests of Metallic Materials. ASTM International, West Conshohocken, Pennsylvania.

ASTM E83-16. 2016. Standard Practices for Verification and Classification of Extensometer Systems. ASTM International, West Conshohocken, Pennsylvania.

ASTM E92-17. 2017. Standard Test Methods for Vickers Hardness and Knoop Hardness of Metallic Materials. ASTM International, West Conshohocken, Pennsylvania.

ASTM E220-19. 2019. Standard Test Method for Calibration of Thermocouples by Comparison Techniques. ASTM International, West Conshohocken, Pennsylvania.

ASTM E290-14. 2014. Standard Test Methods for Bend Testing of Material Ductility. ASTM International, West Conshohocken, Pennsylvania.

ASTM E384-17. 2017. Standard Test Methods for Microindentation Hardness of Materials. ASTM International, West Conshohocken, Pennsylvania.

ASTM E453-79. 2001. Standard Practice for Examination of Fuel Element Cladding Including the Determination of the Mechanical Properties. ASTM International, West Conshohocken, Pennsylvania.

ASTM E766-14. 2019. Standard Practice for Calibrating the Magnification of a Scanning Electron Microscope. ASTM International, West Conshohocken, Pennsylvania.

ASTM E1951-14. 2019. Standard Guide for Calibrating Reticles and Light Microscope Magnifications. ASTM International, West Conshohocken, Pennsylvania.

ASTM E2282-14. 2019. Standard Guide for Defining the Test Result of a Test Method. ASTM International, West Conshohocken, Pennsylvania.

ASTM E2309-20. 2020. Standard Practices for Verification of Displacement Measuring Systems and Devices Used in Material Testing Machines. ASTM International, West Conshohocken, Pennsylvania.

ASTM E2658-15. 2015. Standard Practices for Verification for Speed for Material Testing Machines. ASTM International, West Conshohocken, Pennsylvania.

Beer, FP and ER Johnston Jr. 1992. Mechanics of Materials. McGraw-Hill, 1221 Avenue of the Americas, New York, NY 10020.

Billone, M.C. 2012. Assessment of Current Test Methods for Post-LOCA Cladding Behavior. 2012. ANL-11/52. Argonne National Laboratory. Argonne, IL 60439.

Churchill, S. 1977. “Friction Factor Spans All Fluid-Flow Regimes.” Chemical Engineering 84(24):91-92.

EPRI (Electric Power Research Institute). 2014. High Burnup Cask Research and Development Project: Final Test Plan. Palo Alto, California. February 27, 2014.

Fauvet, P. 2012. “Corrosion Issues in Nuclear Fuel Reprocessing Plants.” Nuclear Corrosion Science and Engineering, pp. 679–728.

Johnson, D.R. and J.A. Stone. 1980. Light Water Reactor Fuel Reprocessing: Dissolution Studies of Voloxidized and Non-voloxidized Fuel. Savannah River Laboratory, Aiken, South Carolina. doi:10.2172/711324.

Montgomery, R., B. Bevard, R.N. Morris, J. Goddard, Jr., S.K. Smith, J. Hu, J. Beale, and B. Yoon. 2018. Sister Rod Nondestructive Examination Final Report. SFWD-SFWST-2017-000003, Rev. 1; ORNL/SPR-2017/484, Rev. 1, Oak Ridge National Laboratory, Oak Ridge, Tennessee.

Montgomery, R. and R. Morris. 2019. “Measurement and modeling of the gas permeability of high burnup pressurized water reactor fuel rods.” Journal of Nuclear Materials 523, 206-215. https://doi.org/10.1016/j.jnucmat.2019.05.041.

Saltzstein, S.J., M. Billone, B. Hanson, and J. Scaglione. 2018. Visualization of the High-Burnup Spent Fuel Rod Phase 1 Test Plan: Technical Memo. SAND2018-8042 O, Sandia National Laboratories, Albuquerque, New Mexico.

Shimskey, R.W, B. Hanson, C. Lavender, S. Pitman, E. Stephens, P. MacFarlan, and M. Dahl. 2014. FY 2014 PNNL Zr Cladding Testing Status Report. PNNL-23594. Pacific Northwest National Laboratory, Richland, Washington.

Shimskey, R.W., P.J. MacFarlan, L. Lin, B.D. Hanson, C. Lavender, S. Pitman, E. Stephens, and M Dahl. 2015. Effects of Hydrides on Mechanical Properties of Unirradiated Cladding. PNNL-24872. Pacific Northwest National Laboratory, Richland, Washington.

Shimskey, R.W., M.K. Edwards, J. Geeting, J.R. Allred, S.K. Cooley, R.C. Daniel, and R.M. Cox, et al. 2019a. Initial Results of Destructive Examination of Ten Sister Rods at PNNL. PNNL-28548. Pacific Northwest National Laboratory, Richland, Washington.

Shimskey, R.W., J.R. Allred, R.C. Daniel, M.K. Edwards, J. Geeting, P.J. MacFarlan, L.I. Richmond, T.S. Scott, and B.D. Hanson. 2019b. PNNL-29179. Pacific Northwest National Laboratory, Richland, Washington.

Weck PF, E Kim, V Tikare, and JA Mitchell. 2015. “Mechanical properties of zirconium alloys and zirconium hydrides predicted from density functional perturbation theory.” Dalton Transactions 44: 18769-18779